———————————————————————————

D O C T O R A L   T H E S I S

Elasticity tensor determination by means of ultrasonic pulse transmission: Application ranges in terms of specimen geometry and microstructure, off-diagonal tensor components, as well as different engineering and biomedical materials

———————————————————————————

D I S S E R T A T I O N

Bestimmung von Elastizitätstensoren mittels Übertragung von Ultraschallimpulsen: Anwendungsbereiche bezüglich Probengeometrie und -mikrostruktur, (Poisson-)Querdehnungseffekten sowie verschiedener Materialien aus Technik und Medizin

———————————————————————————

ausgeführt zum Zwecke der Erlangung des akademischen Grades eines
Doktors der technischen Wissenschaften

eingereicht an der Technischen Universität Wien
Fakultät für Bauingenieurwesen

von

Dipl.-Ing. Christoph Kohlhauser
Geburtsname: Nagl
Matrikelnummer 9825700
Laudach 11, 4817 St. Konrad, Österreich

Referent: Ao.Univ.Prof. Dipl.-Ing. Dr.techn. Christian Hellmich
Institut für Mechanik der Werkstoffe und Strukturen
Technische Universität Wien
Karlsplatz 13/202, 1040 Wien, Österreich

Koreferent: Univ.Prof. Dipl.-Ing. Dr.techn. Ewald Benes
Institut für Allgemeine Physik
Technische Universität Wien
Wiedner Hauptstraße 8-10/134, 1040 Wien, Österreich

Wien, im Juli 2009   ....

Acknowledgments

Abstract

Ultrasonics is a well-established method for the determination of elastic properties of solids. Depending on the application, it may have advantages over classical quasi-static tests, in terms of its non-destructive nature, of simpler specimen preparation, of easy and fast experimental realization, and of high precision measurements of normal and shear ('diagonal') elasticity tensor components. These advantages, however, rely on the appropriate application of the method within specific ranges, the elucidation of which is the primary focus of this thesis. The application ranges concern specimen geometry and microstructure (Publication 1), Poisson's ratios and off-diagonal elasticity tensor components (Publication 2), and different dense and porous glass-ceramic, biological, and metal-based materials from the engineering and biomedical fields (Publication 1 – 5).

Publication 1 covers the influence of specimen shape and porosity on elastic wave velocity and stiffness determination through ultrasonic contact pulse transmission. It turns out that bar-shaped specimens with a slenderness ratio larger than ten, excited by low-frequency signals, transmit (1D) extensional or bar waves, whereby the specimen needs to be the more slender the higher the signal frequency to be transmitted as extensional wave. Beyond a quite narrow extensional-bulk-wave transition regime, less slender bar-type specimens excited by higher frequency signals transmit (3D) bulk waves, whereby specimens need to be the less slender the lower the frequency to be transmitted as bulk waves. As for porous non-slender specimens, the wave propagation type depends on the 'pore-diameter-over-wavelength' ratio and on the porosity. Cube-shaped porous specimens excited by low frequency signals transmit bulk waves relating to the effective porous medium (long-wavelength-limit), whereby the specimen needs to be the more porous, the higher the frequency to be transmitted as effective wave 'feeling' the porous medium. Beyond a long-to-short wavelength transition period, which is increasing with increasing porosity and with decreasing direction-dependent wave propagation velocity, cube-shaped porous specimens excited by higher frequencies transmit bulk waves relating to the solid matrix (short-wavelength-limit). Thereby, specimens need to be the less porous, the lower the frequencies to be transmitted as waves 'feeling' the solid matrix.

Publication 2 deals with the determination of Poisson's ratios in isotropic, transversely isotropic, and orthotropic materials by means of combined ultrasonic-mechanical testing of normal stiffnesses. Poisson's ratios of isotropic, transversely isotropic, and orthotropic non-axially auxetic materials are expressed as functions of normal elastic stiffnesses, considering the positive definiteness of the stiffness and compliance tensors. The relevance of our method is shown by comparing Poisson's ratios computed from normal elastic stiffnesses given in the literature, to experimentally given Poisson's ratios, for a range of materials including (isotropic) aluminum, (transversely isotropic) aluminum matrix-fiber composite and (orthotropic) stainless-steel weld metal. Finally, the method is applied to (orthotropic) wood (namely spruce), by measuring four normal stiffnesses, and relying on a spruce-specific universal constant involving longitudinal Poisson's ratios and on reasonable estimates for the radial Young's modulus. Resulting ranges of Poisson's ratios agree well with ranges of Poisson's ratios obtained from direct mechanical measurements on spruce.

In porous materials, especially such with very high porosity, the determination of material stiffness may be strongly biased by inelastic deformations occurring in the material specimens. In contrast, ultrasonic waves propagating through a material generate very small stresses and strains (and also strain rates lying in the quasi-static regime). Therefore, elastic properties of such materials can be reliably accessed through ultrasonics, which we used for multiple-scale elastic characterization of porous biomaterials (Publication 3) and of titanium scaffolds for biomedical applications (Publication 4). Ultrasonically determined elastic properties finally helped us to understand the micromechanics of bioresorbable porous CEL2 glass ceramic scaffolds for bone tissue engineering (Publication 5). Interesting details on various aspects of ultrasonic testing are collected in Appendices A – H.

Kurzfassung

Ultraschall ist eine etablierte Methode zur Bestimmung der elastischen Eigenschaften von Festkörpern. Abhängig von der Anwendung hat sie Vorteile gegenüber klassischen quasi-statischen Tests in Bezug auf ihre zerstörungsfreie Durchführbarkeit, die einfachere Prüfkörpervorbereitung, die einfache und schnelle experimentelle Umsetzung und die hohe Präzision der Messung von Normal- und Schubkomponenten (Diagonalkomponenten) des Elastizitätstensors. Diese Vorteile sind jedoch auf die korrekte Durchführung dieser Methode innerhalb bestimmter Anwendungsbereiche angewiesen, deren Bestimmung die Zielsetzung dieser Arbeit ist. Die Anwendungsbereiche betreffen Aspekte, die von der Probengeometrie und -mikrostruktur (Publikation 1), über Poissonzahlen und nicht-diagonale Elastizitätstensorkomponenten (Publikation 2), bis hin zu verschiedenen dichten und porösen biologischen und metallischen Materialien und Glas-Keramiken aus Technik und Medizin (Publikation 1 – 5) reichen.

Publikation 1 behandelt den Einfluss der Probengeometrie und -porosität auf die Bestimmung elastischer Wellengeschwindigkeiten und Steifigkeit durch Kontaktübertragung von Ultraschallimpulsen. Es stellt sich heraus, dass stabförmige Probekörper mit einer Schlankheit größer zehn bei Anregung durch niederfrequente Signale (1D) Dehn- oder Stabwellen übertragen, wobei der Probekörper umso schlanker sein muss, je höher die als Stabwelle zu übertragende Signalfrequenz ist. Jenseits eines recht schmalen Übergangsbereichs zwischen Stab- und Volumenwellen übertragen weniger schlanke, von höherfrequenten Signalen angeregte, stabförmige Probekörper (3D) Volumenwellen, wobei der Probekörper umso gedrungener sein muss, je geringer die als Volumenwelle zu übertragende Signalfrequenz ist. Bei porösen gedrungenen Probekörpern hängt die Art der Wellenausbreitung vom Verhältnis 'Porendurchmesser-zu-Wellenlänge' und der Porosität ab. Würfelförmige poröse Probekörper, die von niederfrequenten Signalen angeregt werden, übertragen dem effektiven porösen Medium zugehörige Volumenwellen (langwelliger Grenzwert), wobei der Probekörper umso poröser sein muss, je höher die als Effektivwelle zu übertragende Frequenz ist, die das poröse Medium 'spürt'. Jenseits eines Übergangsbereichs von Lang- auf Kurzwellen, der mit zunehmender Porosität und mit abnehmender, richtungsabhängiger Wellenausbreitunggeschwindigkeit zunimmt, übertragen von höheren Frequenzen angeregte würfelförmige poröse Probekörper Volumenwellen in der festen Grundmasse oder Matrix (kurzwelliger Grenzwert). Dabei müssen die Probekörper umso weniger porös sein, je geringer die als eine die feste Matrix 'spürende' Welle zu übertragende Frequenz ist.

Publikation 2 befasst sich mit der Bestimmung von Querdehnungszahlen in isotropen, transversal isotropen und orthotropen Materialien mittels Kombination von aus quasistatischen Messungen und Ultraschallversuchen gewonnenen Normalsteifigkeiten. Die Querdehnungszahlen von isotropen, transversal isotropen und orthotropen, axial nicht auxetischen Materialien werden als Funktionen der Normalsteifigkeiten angegeben, wobei die positive Definitheit der Steifigkeits- und Nachgiebigkeitstensoren berücksichtigt wird. Die Bedeutung der Methode wird durch den Vergleich von Querdehnungszahlen, welche mittels aus der Literatur entnommener Normalsteifigkeiten berechnet werden, mit direkt experimentell bestimmten Querdehnungszahlen gezeigt, und zwar für (isotropes) Aluminium, (transversal isotrope) Aluminium-Matrix Faserverbundmaterial und (orthotropes) Edelstahl-Schweißgut. Schließlich wird die Methode auf (orthotropes) Holz (genauer Fichte) angewandt, durch Messung von vier Normalsteifigkeiten und auf Basis einer durch Längs-Querdehnungszahlen definierten fichtenspezifischen universellen Konstanten sowie vernünftiger Abschätzungen für den radialen Elastizitätsmodul. Die sich daraus ergebenden Querdehnungszahlen passen gut mit solchen aus quasistatischen Messungen an Fichte überein.

In porösen Materialien, insbesondere in hochporösen, kann die Qualität der quasistatischen Steifigkeitsbestimmung durch Auftreten lokaler Inelastizitäten stark beeinträchtigt werden. Im Gegensatz dazu erzeugen die sich in einem solchen Material fortpflanzenden Ultraschallwellen sehr kleine Spannungen und Verzerrungen (und auch Verzerrungsraten, die im quasistatischen Bereich liegen). Daher können die elastischen Eigenschaften solcher Materialien zuverlässig mittels Ultraschall bestimmt werden. Auf diese Weise charakterisierten wir die Mehrskalen-Elastizität poröser Biomaterialien (Publikation 3) und poröser Titanproben für biomedizinische Anwendungen (Publikation 4). Mittels Ultraschall bestimmte elastische Eigenschaften halfen uns schließlich, die Mikromechanik von Knochenersatzmaterial

aus bioresorbierbaren porösen CEL2 Glas-Keramiken zu verstehen (Publikation 5). Interessante Informationen zu verschiedenen Aspekten der Elastizitätsbestimmung mittels Ultraschall sind in den Anhängen A – H zusammengefasst.

Contents

Introduction

The term *ultrasound* denominates waves of certain frequency. The second part of the word refers to the type of waves. *Sound* waves propagate in solid, liquid and gaseous media. The word *ultra* refers to the frequency range of this sound waves. Human sensitivity of eyes and ears are used as reference for denominating certain ranges. Light waves with wavelength below and above the visible range of light are called *infra*red and *ultra*violet, respectively. Analog, sound waves below and above the hearable range of sound are called *infra*sonic (< 10 Hz) and *ultra*sonic (> 20 kHz), respectively. Ultrasound is classified according to its frequency as either (a) low frequency ultrasound: $0.02 - 0.5$ MHz, (b) conventional or industrial ultrasound: $0.5 - 100$ MHz, or (c) high frequency ultrasound: > 100 MHz. Ultrasonic frequencies applied in this work range from 50 kHz to 20 MHz.

Waves are an accumulation of 'particle' motions and these displacement of particles causes (very small) stresses in the propagation medium. Thus, sound waves are also called stress waves if they propagate in solid media. The stresses originated by an ultrasonic wave are so small that a linear relationship between the strains and stresses (linear material law) can be assumed. This implies that *elastic* waves are propagated.

As in the understanding of continuum micromechanics a 'particle' can be understood as a material volume, also called the representative volume element (RVE). In the case of elastic waves, the corresponding strain rate related to these material volumes is sufficiently low, as to be considered as quasi-static and the resulting stresses are small enough, such that linear elasticity is valid. Under these conditions, relationships between the velocity of ultrasonic waves (i.e. plane elastic stress waves) and the elastic stiffness of the material can be derived.

The wavelength, i.e. the distance of two particles at the same position or moving state, for elastic waves must be much larger than the atom or molecule distance. The frequency of a wave gives a value of how often a particle is in the same position within a second. The material sound velocity, wave velocity, or phase velocity is a measure of the velocity of a certain state (phase) of a particle. Elastic waves exhibit a wave velocity (order of magnitude [km/s]) that is much larger than the particle velocity (order of magnitude [mm/s]), as oppose to shock waves, where both are approximately equal.

Ultrasonic waves can freely propagate in solids and liquids and are reflected at boundaries of internal flaws or change of medium. Propagation distances in air or gases are very limited due to the high attenuation of ultrasound in such media. Ultrasound can be focused and is suitable for real-time processing. One of the most important properties of ultrasound is, that it is non-destructive to the propagation medium. Therefore, ultrasonic waves are harmless to the human body.

Usually, relationships between wave velocities and stiffnesses are derived for an *ideal* medium, i.e. an elastic, isotropic and single-phase material. The study of deformation of real media, i.e. an anelastic, anisotropic and multi-phase materials, under applied external stresses, e.g. waves, is called rheology. Here, we consider anisotropy of materials and two phase materials. Despite the fact that the theoretical knowledge of wave propagation in anisotropic media has

been developed for several decades, there are still uncertainties about the interpredation of measurements performed in such materials. Ultrasonic wave *pulses* in solids can be characterized by different velocities. Phase velocity, energy velocity, group velocity, and envelope velocity may all be different and may not point in propagation direction of the wave. In anisotropic elastic materials the wave propagation direction (wave vector; direction of phase velocity) and the direction of energy propagation (ray direction; direction of group velocity) do in general not coincide. Here, the focuses is on the difference of phase and group velocity vectors in anisotropic media.

This work deals with the measurement of velocities of ultrasound pulses and the experimental and theoretical considerations necessary for establishing these measurements as an experimental method for material characterization in engineering material science. Even though using ultrasonic waves for measuring elasticity tensor components is not a new method for quantitative material characterization, it was rarely used in structural engineering for this purpose. Mostly, ultrasonic waves were usually used for qualitative characterizations, such as position determination of faults in metals and welds or of knots in wood. Here, the focus is on the application of this method for determination of stiffness properties, in particular for materials with a lower symmetry class and heterogeneous microstructure. Development of ultrasonic stiffness measurements was pushed forward in crystal physics and for the investigation of composites. These have been also the main application areas of this method.

Ultrasonic contact pulse-transmission is a well-established method to determine elastic stiffness of materials and the broad application range has proven the effectiveness of determining elastic stiffness constants when quasi-static methods cannot be applied or do not yield the demanded accuracy of measurements. Problems related with conventional quasi-static mechanical tests may occur with small specimen sizes, with the need to determine several elastic constants of an anisotropic material, or when the applied forces induce mechanical damage in the samples. Application of ultrasound is especially of interest for porous materials, because mechanical testing may be strongly biased by inelastic deformations within the microstructure of such materials. The relative simple pulse methods (pulse-transmission method, pulse-echo method) are rough in the sense that the beginning and the end of the pulse are not well characterized, but with improvements (e.g. pulse-superposition method, sing around method) relative variations of 10^{-7} can be measured (Authier and Zarembowitch 2006). For usual accuracies generally accepted in the determination of elastic stiffnesses of engineering materials, the pulse-transmission provides very accurate and relatively easy realizable and deployable measurements. The limits of application ranges of ultrasonic contact pulse-transmission are not well quantified. Little work has been done on experimentally investigating transition of (pulse) wave propagation to certain theoretically well-known special cases (extensional wave). In transition regions of wave propagation modes, known relations between ultrasonic wave velocities and elastic stiffnesses for 'regular' wave propagation are not valid.

The growing use of (anisotropic) materials in complex structural applications, resulting in multiaxial straining of the material, increases the necessity for knowing the full elasticity tensor. Measuring the sound velocity of an induced ultrasonic waves and applying the physical laws for acoustic wave propagation in solids yields the components of the elastic stiffness tensor of this material as a function of its mass density. Depending on the polarization and propagation direction of the stress wave certain stiffness components are measured. A sufficient number of experiments with different polarization and propagation directions allows for the classification of the elastic material symmetry and for identification of all components of the stiffness tensor and, thus, of all independent engineering elastic constants. Even for materials with the lowest elastic symmetry, namely triclinc materials with 21 independent elastic constants, all elasticity stiffness components can be determined.

The ability to characterize also materials of low symmetry classes is among the most appealing

advantages of ultrasonic tests. Quasi-static (destructive) methods for material characterization at the macroscale, as well as nanoindentation for measurements of material properties at the nanoscale, allow only for determination of a limited number of elastic constants on a single specimen. Mostly, it is necessary to conduct experiments on several differently prepared specimen when using these methods, which are particularly suited for isotropic materials. However, for materials with lower elastic symmetry, e.g. orthotropic materials like bone or wood, with more than two independent elasticity constants, they may fail to measure the full set of elastic stiffness constants.

Furthermore, these methods are restricted to determination of material properties of a certain lengthscale. Ultrasonic tests, on the contrary, allow to determine material characteristics over a range of different lengthscales. By changing the frequency of the propagating wave the corresponding wavelength changes according to the quotient of the ultrasonic sound velocity and the frequency. Higher frequencies and smaller wavelength thus yield material properties at a lower material length scale. Thus, the ultrasonic method covers all length scales in a range starting from the centimeter down to the nanometer. Another benefit of the ultrasonic method is its nondestructive nature. The identification of temperature and moisture content dependency of mechanical properties can be accomplished with all the aforementioned methods. The ultrasonic method can be applied to solid, viscous, and fluid materials, e.g. wood, bone, plastics, composite materials, ice, and bitumen.

Preceding a short outline and the publications of this work, the mathematical framework for describing propagation of ultrasound in solids — space-independent oscillation of 'particles', and the propagation of this movements through space, i.e. waves — and the connection between ultrasonic waves and material stiffness is elucitaded in the following two sections.

Oscillation

Oscillation, the motion of a single particle in space, is characterized solely by a kinematic nature. Oscillation can be started by various means (force or displacement), but no matter how it is started, it always exhibits the same oscillation frequency (Hirose 2009). Waves always evolve from oscillation of particles (mechanical waves or sound waves) or charges (electromagnetic waves). This leads to mechanic considerations in terms of interaction of several particles with each other (see following Section on one-dimensional wave propagation).

Oscillation (of a single particle) can be modeled by an ideal, i.e. frictionless and lossless, mass-spring system (see Figure 1). Such a model comprises the basic components of mechanical oscillation (and thus mechanical waves), namely inertia (mass m [kg]) and elasticity (spring constant c [N/m]). Writing the equation of motion for a 'particle' or a 'material volume' of mass m yields

$$m\frac{dv}{dt} = -cu, \qquad \text{where} \qquad v = \frac{du}{dt} \tag{1}$$

is the velocity [m/s], $u(t)$ [m] is the displacement of the mass from the equilibrium position and t [s] is an arbitrary time. The right term of the first equation in (1) is the restoring force of the spring acting on the mass. Rewriting Eqs. (1) yields the oscillation differential equation

$$\frac{d^2u(t)}{dt^2} + \frac{c}{m}u(t) = 0 \qquad \text{or} \qquad \ddot{u}(t) + \omega^2 u(t) = 0 \tag{2}$$

with the oscillation angular frequency

$$\omega = \sqrt{\frac{c}{m}}, \tag{3}$$

$$[\omega] = \sqrt{\left[\frac{N/m}{kg}\right]} = \sqrt{\left[\frac{kg \cdot m/s^2}{kg \cdot m}\right]} = \sqrt{\left[\frac{1}{s^2}\right]} = \left[\frac{rad}{s}\right]. \tag{4}$$

The homogeneous second order differential equation (2) has the general oscillatory solution

$$u(t) = A \sin \omega t + B \cos \omega t. \tag{5}$$

From this solution one can see, that an oscillation must always be sinusoidal in nature (Hirose 2009), as plotting the displacement versus the time yields a sinus curve. This is only the case if the driving force is proportional to the displacement, i.e. for linear elastic deformations. Because the unit [rad] corresponds to 2π one can introduce the relationship

$$\omega = 2\pi f, \tag{6}$$

where the frequency of sinusoidal perturbation f has units of [Hz $= 1/\text{s}$], yielding again $[\omega] = [\text{rad/s}]$ (see Figure 1 for the sinusoidal oscillation curve and the graphical interpretation of the angular frequency ω).
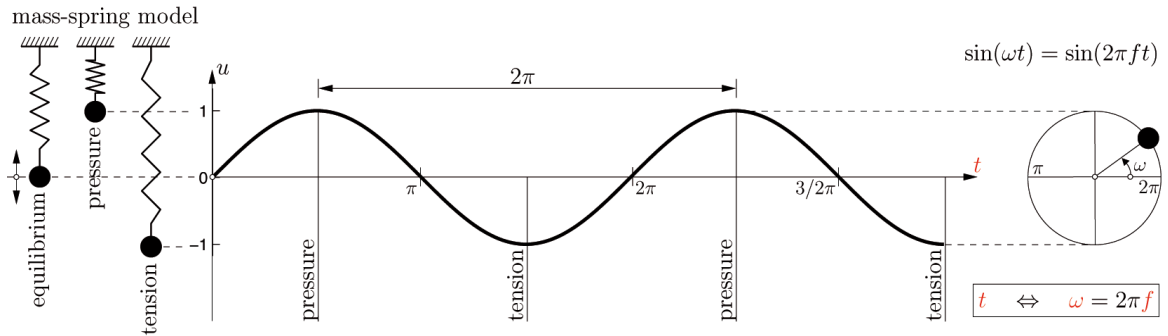
Figure 1: Oscillation of a single mass with respect to time t.

The oscillation differential equation (2) can also be derived from the condition of energy conservation, which states that the sum of the potential energy P and kinetic energy K, the total energy E [Nm $=$ J], must be constant, i.e.

$$E = P + K = \frac{1}{2}c\,u^2 + \frac{1}{2}m\,v^2 = const. \tag{7}$$

Differentiation of (7) with respect to time and using the definition of the velocity $(1)_2$ yields Eq. (2). The progression of the energy with respect to time can be elucidated by analyzing the oscillation due to an initial displacement $u(t = 0) = u_0$. The total energy E at $t = 0$ is the potential energy stored in the spring, i.e.

$$E_0 = \frac{1}{2}c\,u_0^2. \tag{8}$$

From (5) one finds $A = 0$ and $B = u_0$ and thus unique solutions for displacement and velocity are given as

$$u(t) = u_0 \cos \omega t \qquad \text{and} \qquad v(t) = \dot{u}(t) = -\omega u_0 \sin \omega t. \tag{9}$$

Hence the kinetic energy and potential energy with respect to time are

$$K = \frac{1}{2}mv(t)^2 = \frac{1}{2}cu_0^2 \sin^2 \omega t \qquad \text{and} \qquad P = \frac{1}{2}cu(t)^2 = \frac{1}{2}cu_0^2 \cos^2 \omega t, \tag{10}$$

respectively. The sum yields the (constant) total energy E, which is, as expected, equal to the initial energy (8). One can observe, that P is maximum, when K is zero, and vice versa, i.e. the kinetic and potential energy are' mutually exclusive.

Waves

A wave is a phenomenon whereby energy (or a displacement, a signal, or information), but not mass, is transferred through a medium. The source of a wave are the oscillations of particles of the medium in which the wave travels. Through radiation of waves, the oscillators lose energy to waves which carry this energy through space. What is moving in a wave is the state (or phase), e.g. the state of compaction and rarefaction in an elastic wave. The particles themselves remain at the same position and oscillate only about their equilibrium state (Krautkrämer and Krautkrämer 1986). In contrast to oscillations, which only depend on time, waves propagate in space. Thus spatial coordinates in addition to time enter as independent variables the mathematical formulation for wave motion.

A spatial sinusoidal wave (see Figure 2) can be written as

$$u(x) = A \sin\left(\frac{2\pi}{\lambda} x\right) = A \sin(k\,x), \tag{11}$$

where x [m] is the spatial coordinate, A [m] is the size of the transported deformation or wave amplitude and λ [m] the spatial period, the so-called wavelength. We will see later that the wavelength λ depends on the frequency f. The wavenumber k [rad/m] is related to the wavelength λ by

$$k = \frac{2\pi}{\lambda} \tag{12}$$

and is a measure for the number of waves per unit distance for a given wavelength. Note that this wave is only depending on the spatial coordinate x and not on time t (see also Figure 2). Evaluation of Eq. (11) for different values of the spatial coordinate $x = \{\lambda, \lambda/4, \lambda/2, 3/4\,\lambda\}$ yields the corresponding displacements $u = A\,\{0, 1, 0, -1\}$ (see also Figure 2).
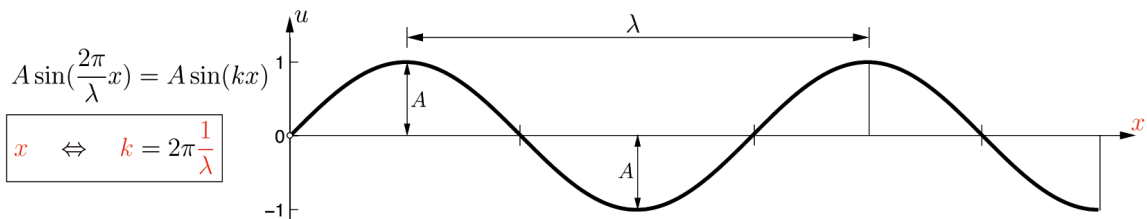
Figure 2: Spatial sinusoidal wave with respect to spatial coordinate x.

A (sinusoidal) wave is periodic in both time and spatial coordinate. Eq. (11) and Figure 2 can also be regarded as a snapshot of a sinusoidal wave at time $t = 0$. At another snapshot after t seconds in which the wave propagated to the right, it will have moved according to its propagation velocity v_p and thus will be shifted by a distance of $v_p\,t$. Infinite snapshots would create a moving wave motion as a function of time t. A snapshot can be understood as display of an oscilloscope that is used to observe the wave.

Parallel shift a of a function $f(x)$ to the right, i.e. wave motion in a positive x direction is obtained by $f(x - a)$, whereas a '+' sign yields motion in the negative x direction. Therefore

the mathematical form of a sinusoidal wave at an arbitrary time t is given by

$$u(x,t) = A \sin\left(\frac{2\pi}{\lambda}(x - v_p\,t)\right) = A\sin(k\,x - \omega\,t). \tag{13}$$

The coefficient of t must be equal to ω since time dependence is periodic with the frequency ω. This yields the relationship

$$v_p = \lambda \cdot f \qquad \text{or} \qquad v_p = \frac{\omega}{k}, \tag{14}$$

where v_p [m/s] is the rate of propagation of a point of constant phase, the so-called wave or phase velocity of the wave. The fact that the wavelength is inversely proportional to the frequency and their product is constant and equal to the wave velocity was first mentioned by Newton (1687) in his *Principia* (Carcione 2001). Eq. (14) relates Figure 1 and 2, and Eqs. (6) and (12).

The mathematical description of oscillation, $u(t)$ [see Eq. (5)], satisfied the oscillation differential equation (2) with derivatives only with respect to t, as this is the only independent variable. A similar equation must exist for the mathematical description of a wave, $u(x,t)$ [see Eq. (13)], with second order partial derivatives of t and x. Comparing

$$\frac{\partial^2 u(x,t)}{\partial x^2} = u''(x,t) = -k^2\,A\,\sin(k\,x - \omega\,t) \tag{15}$$

and

$$\frac{\partial^2 u(x,t)}{\partial t^2} = \ddot{u}(x,t) = -\omega^2\,A\,\sin(k\,x - \omega\,t) \tag{16}$$

and using (14), one can see that Eq. (13) satisfies the equation

$$\ddot{u}(x,t) = v_p^2\,u''(x,t). \tag{17}$$

This wave differential equation is satisfied for all arbitrary functional wave shapes in the form

$$u(x,t) = u(x \mp v_p\,t). \tag{18}$$

This becomes clear by substituting $X = x \mp v_p\,t$, with $X' = 1$ and $\dot{X} = \mp v_p$, which yields

$$u''(x,t) = \frac{d^2u(X)}{dX^2} \qquad \text{and} \qquad \ddot{u}(x,t) = v_p^2 \frac{d^2u(X)}{dX^2} \tag{19}$$

which again satisfy Eq. (17). Therefore in contrast to oscillations waves do not have to be sinusoidal or harmonic.

A single wave can not transmit a signal or information. To transfer a signal with a wave, it as to be turned on and off in some pattern, i.e. wave pulses have to be generated. Any arbitrary wave shape can be constructed by superposing several harmonic waves (Fourier analysis). Thus, also a (wave) pulse can be generated by several sinusoidal waves. Three examples for superposition of sinusoidal waves with equal amplitudes are given below. In all of them, use of the relationship

$$\sin x + \sin y = 2 \sin \frac{x+y}{2}\,\cos\frac{x-y}{2} \tag{20}$$

is made.

1. Two waves with equal wavelength, and therefore equal frequency, propagating in opposite

directions create a standing wave,

$$A/2 \left[\sin(k\,x - \omega\,t) + \sin(k\,x + \omega\,t)\right] = A \sin kx \, \cos \omega\,t\,. \qquad (21)$$

2. Superposition of two waves with equal wavelength but phase difference Φ [rad],

$$A \left[\sin(k\,x - \omega\,t) + \sin(k\,x - \omega\,t + \Phi)\right] = 2A \sin(k\,x - \omega\,t + \Phi/2) \, \cos(\Phi/2) \qquad (22)$$

can cause constructive (doubled amplitude) or destructive (zero amplitude) interference, if the phase difference is an even or odd factor of π, respectively.

3. Superposition of two waves with slightly different wavelengths (frequencies) when measured as a function of time only (observing position arbitrary, e.g. $x = 0$) yields

$$-A \left[\sin(\omega\,t) + \sin((\omega + \Delta\omega)\,t)\right] = -2A \sin[(\omega + \Delta\omega/2)\,t] \, \cos(\Delta\omega/2\,t)\,. \qquad (23)$$

For small $\Delta\omega$ this equation describes a harmonic wave $\sin(\omega\,t)$ confined between slowly varying envelopes $\pm 2A \cos(\Delta\omega t/2)$. $\Delta\omega$ is called the beat frequency, because the amplitude is modulated at this frequency.

Observing the last example, Eq. (23), in the time and space domain and considering that, for small frequency differences $\Delta k \ll k$ and $\Delta\omega \ll \omega$, one can reduced as follows

$$A \sin(k\,x - \omega\,t) + A \, \sin[(k + \Delta k)\,x - (\omega + \Delta\omega)\,t)]$$

$$= \quad 2A \sin[(k + \Delta k/2)\,x - (\omega + \Delta\omega/2)\,t] \, \cos(\Delta k/2\,x - \Delta\omega/2\,t) \qquad (24)$$

$$\approx \quad 2A \sin(kx - \omega t) \, \cos(\Delta k/2\,x - \Delta\omega/2\,t)\,.$$

This equation specify spatial and temporal beats. Again, the last function in (24) describes a rapidly oscillating sinusoidal function propagating at the phase velocity $v_p = \omega/k$. These wavelets are modulated by the envelopes $\pm \cos(\Delta k/2\,x - \Delta\omega/2\,t)$. The modulation pattern propagates at a speed such that the argument of the cosine function stays at a constant value, $\Delta k/2\,x - \Delta\omega/2\,t = const$. Differentiation with respect to the time yields the envelope speed

$$v_{env} = \frac{dx}{dt} = \frac{\Delta\omega}{\Delta k}. \qquad (25)$$

In the limit $\Delta k \to 0$, $\Delta\omega \to 0$, the envelope speed defines the group velocity

$$v_g = \frac{d\omega}{dk}. \qquad (26)$$

The group velocity is the speed of transmission of information and the speed of energy in a wave packet. Phase velocity [see Eq. (14)] and group velocity [see Eq. (26)] define an important property of waves:

- *Nondispersive waves* are characterized by $v_p = v_g$, i.e.

$$\frac{\omega}{k} = \frac{d\omega}{dk} = const. \qquad \Rightarrow \qquad \omega = v_p\,k = v_g\,k = v\,k. \qquad (27)$$

Such waves propagate without changing their wave form. The wave equation (17) is only valid for nondispersive waves.

- For *dispersive waves* the wave or phase velocity v_p depends on ω or k and thus $v_p \neq v_g$, i.e.

$$\frac{\omega}{k} \neq \frac{d\omega}{dk} \qquad \Rightarrow \qquad \omega = \omega(k). \tag{28}$$

The last equation in (28) is called the *dispersion relation*, which can be found for any given wave differential equation. Dispersive waves are deformed and become spatially spread (i.e. dispersed) as they propagate. A wave pulse or wave packet will hence not maintain its shape during propagation.

One-dimensional mechanical waves and their relation to the (elastic) material properties of the propagation media can be modeled by a mass-spring transmission line. Such a line consists of many mass-spring units connected in series. Only the mass motion along the transmission line is used in the following derivation. This coincides with the direction of wave propagation, i.e. with longitudinal waves. Nevertheless, the results are valid for all mechanical waves.

Each unit consists of a mass m [kg] and a spring with spring constant c [N/m] and an equilibrium length Δx [m]. A wave traveling through the transmission line will cause the masses to move from their equilibrium positions. These displacements $u(x,t)$ depend on the position x of the mass in the line, and on the time t at which the line is observed. To write the equation of motion for the mass at position x, the spring forces to the left F_l and to the right F_r have to be considered. From position changes of masses at x and $x \pm \Delta x$ the lengths of the springs and thus the forces follow to

$$F_r = c\,[u(x + \Delta x, t) - u(x,t)] \qquad \text{and} \qquad F_l = c\,[u(x,t) - u(x - \Delta x, t)]. \tag{29}$$

With the net force F acting on the mass at x, $F = F_r - F_l$, the equation of motion reads

$$m\frac{\partial u(x,t)}{\partial t} = c\,[u(x + \Delta x, t) + u(x - \Delta x, t) - 2\,u(x,t)]. \tag{30}$$

The discrete transmission line can be considered continuous if the distance between the masses Δx is small compared to the wavelength λ. Using the Taylor expansion for the displacements

$$u(x \pm \Delta x, t) = u(x,t) \pm \Delta x \frac{\partial u}{\partial x} + \frac{1}{2}(\Delta x)^2 \frac{\partial^2 u}{\partial x^2} + \dots, \tag{31}$$

Eq. (30) becomes the same form as wave equation (17)

$$m\,\ddot{u}(x,t) = c\,(\Delta x)^2\,u''(x,t) \qquad \text{if} \qquad \Delta x \ll \lambda. \tag{32}$$

Therefore, the wave velocity can be identified to

$$v_p^2 = \frac{c\,(\Delta x)^2}{m} = \frac{c\,\Delta x}{m/\Delta x} = \frac{C}{\rho_l}, \tag{33}$$

where C [N] is the elastic modulus of the spring (a material constant) and ρ_l [kg/m] is the linear mass density. The square root of the elastic modulus divided by the mass density is the general form of wave velocity of all mechanical waves. Therefore, a wave travels faster the greater the resistance of the medium to the deformation is.

The velocity of the mass can also be written as the differential of the displacement $v(x,t) = \partial u(x,t)/\partial t = \dot{u}$ and thus the kinetic energy of the mass can be computed to

$$K = \frac{1}{2}m\,\dot{u}^2. \tag{34}$$

Neglecting quadratic and higher order terms in the Taylor expansion of the displacement $u(x + \Delta x, t)$ [see Eq. (31)] the potential energy in the spring to the right of the mass is

$$P = \frac{1}{2} c \left[u(x + \Delta x, t) - u(x, t) \right]^2 \approx \frac{1}{2} c \, (\Delta x)^2 \, (u')^2. \tag{35}$$

By definition $u(x, t)$ describes a wave motion and thus can be an arbitrary function in the form $u(X) = u(x - v_p t)$. Using the first derivation equivalent of the Eqs. (19) the kinetic and potential energy follow to

$$K = \frac{1}{2} m \, v_p^2 \left(\frac{\partial u(X)}{\partial X} \right)^2 \qquad \text{and} \qquad P \approx \frac{1}{2} c \, (\Delta x)^2 \left(\frac{\partial u(X)}{\partial X} \right)^2, \tag{36}$$

respectively. Recalling Eq. (33) it becomes clear that — in contrast to oscillations — for mechanical waves with arbitrary wave shapes, the kinetic energy and the potential energy are identical everywhere, at anytime, i.e. they are in phase. This is not true for standing waves, which are more similar to oscillations as for both the kinetic and potential energy are mutually exclusive.

The total energy E [J] and the total energy density e [J/m] in a mass-spring unit thus follow from $E = 2K$ to

$$E = m \, v_p^2 \left(\frac{\partial u(X)}{\partial X} \right)^2 \qquad \text{and} \qquad e = \rho_l \, v_p^2 \left(\frac{\partial u(X)}{\partial X} \right)^2, \tag{37}$$

respectively. Substituting the linear mass density with the volume mass density ρ [kg/m^3] yields the intensity of a three-dimensional wave in [W/m^2].

Assuming a sinusoidal wave form according to Eq. (13) yields

$$e = \rho_l \, v_p^2 \, k^2 \, A^2 \, \cos^2(kx - \omega t). \tag{38}$$

The spatial average of the cos function at a snapshot at $t = 0$ is $1/2$. Using (14), the average energy density $\langle e \rangle$ [J/m] of the wave becomes

$$\langle e \rangle = \rho_l \, \omega^2 \, A^2. \tag{39}$$

Since in nondispersive waves ($v_p = v_g$) energy travels at the phase velocity, the energy carried by a wave per time, i.e. the rate of energy transfer (RMS power) follows to

$$\text{RMS} = \frac{1}{2} \rho_l \, v_p \, \omega^2 \, A^2. \tag{40}$$

Substituting again the linear with the volume mass density yields the rate of energy transfer per area [J/s/m^2 = W/m^2], i.e. the intensity.

Outline

Several different types of waves can propagate in solids (see Table 1). Here we focus on elastic wave propagation in (quasi-)infinite media and in bar-like media.

The theory applied to describe the relation between elastic wave propagation and material stiffness is based on the concept of a *plane* elastic wave propagating in an *infinite* medium (this wave is called bulk wave). While the assumption of a *plane* wave is justified for most experimental situations, this is not true for the assumption of an *infinite* medium, which does

Table 1: Different types of stress waves in solids related to material behavior and geometry.

	stress-strain function	type of wave
material	linear	elastic
	rate-dependent	visco-elastic
	concarve	plastic
	convex	shock
	infinte spacial dimensions	type of elastic wave
geometry	3	longitudinal, transversal
	2, 1 semi-infinite	longitudinal, transversal, surface
	2 (plate)	symmetrical, antisymmetrical plate
	1 (bar)	extensional, torsional, flexural

not hold for specimens of all sizes and forms. Determination of stiffness tensor components, i.e. measurement of ultrasonic velocities is usually performed on relatively small specimens, e.g. single crystals of solids and samples of biomaterials and biological materials. Due to the availability of only small samples, in combination with the need of using low frequencies (i.e. large wavelength compared to the sample size) for porous materials, the boundaries often have considerable effect on the characteristics of wave propagation. Ideally the side boundaries have no or little influence and the physics of propagation can be considered to be as in an unbounded infinite medium, where longitudinal and transversal waves propagate independenly.

Here, we want to answer the question: 'What are the necessary parameters (and their ranges for bulk wave propagation) to evaluate the type of wave propagation?'.

Voids or solid inclusions embedded in an homogeneous medium influence elastic wave propagation dependending on their size, geometry, and elastic stiffness properties. Scattering of ultrasonic waves, i.e. reflection and refraction of the wave at inclusion boundaries, is, in addition to attenuation due to direct absorbtion through internal friction by the material itself, the main source for energy loss and thus amplitude reduction. Moreover, wave propagation in an inhomogeneous medium leads to frequency dependency of attenuation and velocity, i.e. such heterogeneous materials are dispersive. In ultrasonic stiffness determination wave velocity measurements are of importance and thus influences on the amplitude (i.e. influence of attenuation) are only so far of interest as they reduce the signal to noise ratio and thus the confidence of the measured velocities.

In continuum (micro)mechanics details of a (macroscopically or statistically homogeneous) microstructure are not considered directly, as this would be specimen-specific, tantamount to extensive computational efforts (for complex microstructures), and it would be difficult to elicit general information from it (Drugan and Willis 1996). Instead, material volumes are defined, such that the respective material can be accurately considered homogeneous with spatially constant, 'average' or 'effective' (elastic) properties. Such a material volume (representative volume element, RVE) must be considerably larger than the inhomogeneities (inclusions) d inside the RVE, and the RVE must be subjected to homogeneous stress and strain states. Hence, the characteristic length of the RVE, ℓ_{RVE}, needs to be much smaller than the scale of the characteristic loading of the medium $\mathcal{L}$. In ultrasonic measurements the wavelength λ of the propagating wave, dependent on the frequency of the wave, defines the scale of the characteristic loading of the structure built up by the considered material, i.e. $\mathcal{L} = \lambda$, and thus $d \ll \ell_{RVE} \ll \lambda$. Hence, waves 'detect' materials at different length scales.

Here, we want to answer the question: 'What are the necessary parameters (and their ranges for effective wave propagation) to evaluate the material volume which is measured by a wave?'.

These two major problems — encountered when using ultrasonic pulse propagation for elastic stiffness determination — namely (a) the bulk wave propagation for finite geometries of specimens, including the transition to extensional wave propagation (see Figure 3) and (b) the principle of separation of scales for bulk wave propagation in multi-phase (porous) materials related to the wavelength and the definition of material properties (see Figure 4) will be covered in this work.
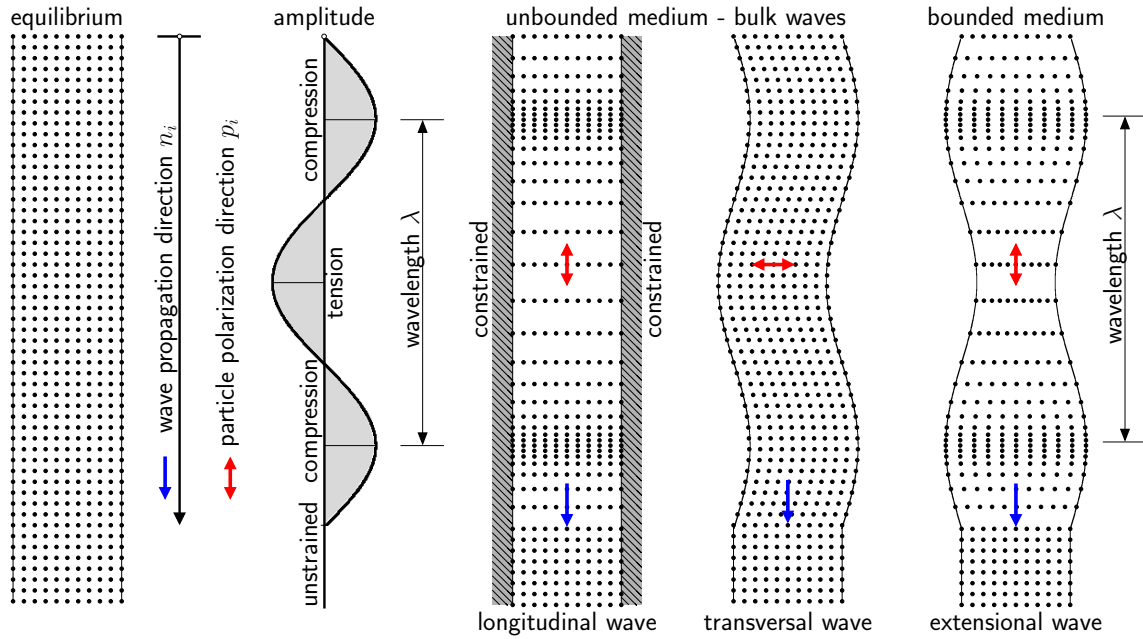
Figure 3: Wave propagation — bulk and extensional wave.
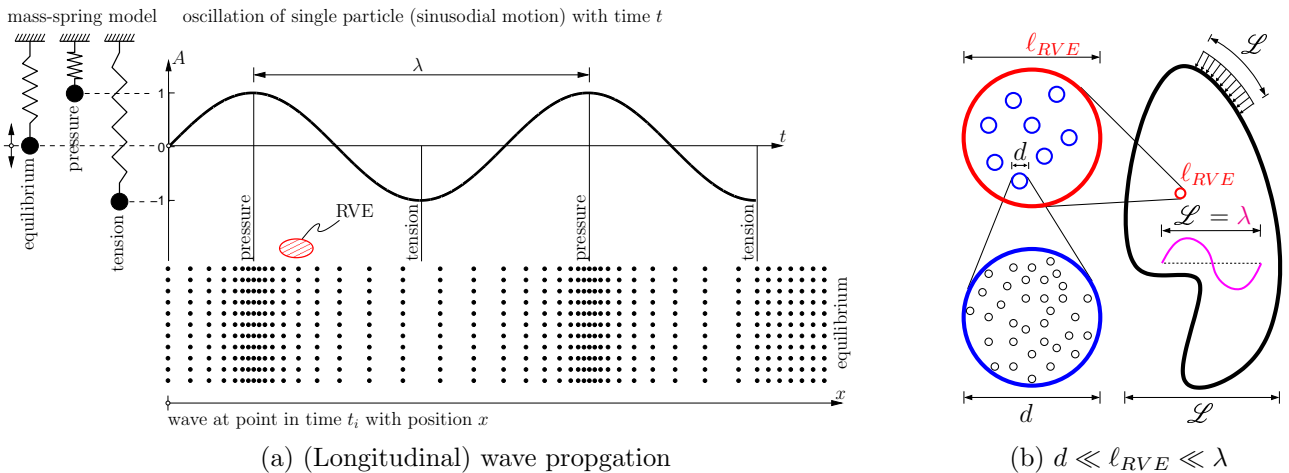
Figure 4: Wave propagation — separation of scales of inhomogeneity and wavelength.

This work consists of five publications in peer-reviewed journals and eight appendices covering unpublished results. The following five publications deal with (i) the ultrasonic contact pulse-transmission technique and its application range in terms of wavelength, specimen dimensions, and microstructure [Publication 1 — Kohlhauser and Hellmich (2009b)], (ii) with the determination of off-diagonal stiffness components (Poisson's ratios) of anisotropic materials

with a combined ultrasonic-mechanical technique [Publication 2 — Kohlhauser and Hellmich (2009a)], (iii) with the investigation of different porous materials across different ultrasonic frequencies [Publication 3 — Kohlhauser et al. (2008)], and with the application of the ultrasonic pulse-transmission technique in combination with micromechanical modelling to (iv) metallic [Publication 4 — Müllner et al. (2007)] and (v) bioresorbable glass ceramic [Publication 5 — Malasoma et al. (2008)] scaffolds for biomedical applications. Publications 1 and 2 were at the time of submission of this work in the review process. The publications are followed by eight appendices. A literature review on wave propagation in bars and on wave scattering in multi-phase media (Appendix A) is followed by a dimensional analysis of wave propagation in two-phase materials (Appendix B), a detailed solution of the Kelvin-Christoffel equation (Appendix C), the matrix noation of forth order elasticity tensors (Appendix D), and the single crystal and polycrystal material properties of aluminum (Appendix E). An alternative representation of sample-specific wave propagation results given in Publication 1 (Appendix F), graphical representation of Poisson's ratio ranges of different materials investigated in Publication 2 (Appendix G), and group velocities and energy deviation angles in different anisotropic materials (Appendix H) are covered in the last three appendices.

Ultrasonic contact pulse transmission for elastic wave velocity and stiffness determination: Influence of specimen geometry and porosity (Kohlhauser and Hellmich 2009b)

Authored by Christoph Kohlhauser and Christian Hellmich
Submitted to *Ultrasonics*

Isotropic solid and transversal isotropic porous aluminum specimens with shapes ranging from plates, via cubes, to bars, were transmitted by ultrasonic waves of frequencies between 50 kHz and 20 MHz. As for the solid specimens, the longitudinal wave propagation type depends the ratios 'cross-sectional-length-over-height' and the 'height-over-wavelength'. Bar-shaped specimens with a slenderness ratio larger than ten, excited by low-frequency signals, transmit (1D) extensional or bar waves, whereby the specimen needs to be the more slender the higher the signal frequency to be transmitted as extensional wave. Beyond a quite narrow extensional-bulk-wave transition regime, less slender bar-type specimens excited by higher frequency signals transmit (3D) bulk waves, whereby specimens need to be the less slender the lower the frequency to be transmitted as bulk waves. All non-slender bar-, cube-, and plate-shaped specimens are transmitted by bulk waves; however, thin plates exhibit large measurement errors. Transversal (or shear) wave propagation is not affected by specimen shape, except for measurement errors. As for porous non-slender specimens, the wave propagation type depends on the 'pore-diameter-over-wavelength' ratio and on the porosity. Cube-shaped porous specimens excited by low frequency signals transmit bulk waves relating to the effective porous medium (long-wavelength-limit), whereby the specimen needs to be the more porous, the higher the frequency to be transmitted as effective wave 'feeling' the porous medium. Beyond a long-to-short wavelength transition period, which is increasing with increasing porosity and with decreasing direction-dependent wave propagation velocity, cube-shaped porous specimens excited by higher frequencies transmit bulk waves relating to the solid aluminum matrix (short-

wavelength-limit). Thereby, specimens need to be the less porous, the lower the frequencies to be transmitted as waves 'feeling' the solid matrix. Long-limit wave velocities and stiffnesses in transversal isotropic porous media are well predicted by the Mori-Tanaka, Hashin-Rosen, and unit cell micromechanical methods.

1.1   Introduction

According to Kolsky (1964) *ultrasonics* relates to the wave propagation of high frequency pulses of sinusoidal oscillations with very small amplitudes. Generally, frequencies above the human audibility limit (≈ 20 kHz) are considered ultrasonic.

The ultrasonic (contact) pulse technique was developed during the second World War by Firestone and Frederick (1946) for the detection of flaws in metals (Lazarus 1949). Elasticity determination through ultrasonics has been applied to a wide range of materials, including single crystals (Huntington 1947; Lazarus 1949), polycrystalline materials (Hearmon 1946; Markham 1962), polymers (Ivey et al. 1949; Hartmann and Jarzynski 1974), metals and metal alloys (Markham 1957; Ledbetter et al. 1980), composite materials (Markham 1970; Dean and Turner 1973; Kriz and Stinchcomb 1979), geomaterials (Helbig 1994; Carcione 2001; Karki et al. 2001), biological materials such as bone (Ashman et al. 1984) and wood (Bucur and Archer 1984), as well as biomaterials such as porous titanium and glass-ceramic scaffolds (Kohlhauser et al. 2008).

Different types of waves can propagate in solid materials. If no energy is dissipated upon wave propagation, the corresponding wave is called elastic (Kolsky 1964). Such waves typically occur for small wave amplitudes (and correspondingly small strains in the material) and high frequencies. In contrast, larger amplitudes may lead to irrecoverable (plastic) strains in the material, the propagation of which is related to plastic waves — in this case, energy is dissipated upon wave propagation (Kolsky 1964). Another type of dissipative wave propagation relates to viscoelasticity, where stresses lead not only to instantaneous, but also to delayed strains (in a material said to have 'memory'). Viscoelastic waves typically occur at low frequencies when dissipative 'relaxation' processes within the material are allowed to result in an effectively lower stiffness behavior of the material (Carcione 2001). Finally, very large strains travel faster than small strains, and related waves are called shock waves (Kolsky 1964). However, the remainder of this paper will be devoted to small strain-related acoustic pulses at high (ultrasonic) frequencies, provoking the propagation of elastic waves. [More precisely, we will deal with elastic deformations ('small strains') where the atomic displacements are small with respect to the interatomic spacing. Hence, so-called higher-order elastic constants (Hiki 1981; Holt and Ford 1967; Thomas 1968), introduced for quantification of elastic wave propagation involving large strains — with atomic displacements being in the order of the atomic spacing — are beyond the scope of the manuscript.]

Ultrasonic wave propagation of elastic waves is associated with (small) temperature rises in the compressive regions and (small) temperature falls in the tensile regions of the excited solid. Given the short characteristic times of these stress fluctuations, related temperature differences cannot be equilibrated through heat conduction. Therefore, ultrasonic wave propagation is, strictly speaking, associated with adiabatic (also called entropic) elasticity. Accordingly, only at zero absolute temperature, adiabatic and isothermal properties (the latter measured under conditions where temperature differences are equilibrated) are identical. However (in particular in the small strain regime), the difference between adiabatic and isothermal elasticity is negligible, i.e. typically below 1% (Authier and Zarembowitch 2006). Therefore, in various situations, ultrasonic tests deliver practically the same results as quasi-static tests (Ledbetter

et al. 1980). However, the latter are often challenged by the occurrence of inelastic strains, so that ultrasonic tests are an expressedly suitable tool for arriving at elastic properties of solids.

Still, it is crucial to know the type of elastic wave travelling through the solid, when determining elastic properties ultrasonically. The following wave types are standardly distinguished:

- Bulk waves are travelling through infinite elastic media (Kolsky 1964). Thereby, displacements of material points and wave propagation velocities do generally not point into the same direction. In the special case where they do so, longitudinal (also called dilatational, irrotational, compressional, P- or L-) waves are encountered. In case the material point displacement is oriented perpendicular to the wave propagation velocity, transversal (also called distortional, equivoluminal, shear, S- or T-) waves are encountered (Love 1906; Kolsky 1953; Kino 1987; Auld 1990; Carcione 2001). In situations tending towards one or the other of the aforementioned special cases, quasi-longitudinal or quasi-transversal waves are encountered.

- Rayleigh surface waves may propagate along the free surface of a semi-infinite solid, or also through an infinite plate (if the wavelength is much smaller than the plate thickness).

- If the wavelength is much larger than the thickness, a symmetrical (longitudinal) and an antisymmetrical (flexural) Lamb wave can propagate in an infinite plate (Kolsky 1964).

- In cylindrical infinite bars extensional (bar), torsional and flexural (bending) waves may propagate in infinitely different modes with velocities depending on the wavelength (Thurston 1978).

- Guided waves appear in bounded media, i.e. bars and plates of finite dimensions, and resonate between the boundaries of their cross-section and propagate in the longitudinal direction (Redwood 1963).

Based on earlier work of Christoffel (1877b,a), Love (1906) was the first to mathematically capture the propagation of elastic waves in infinite three dimensional solids, be they isotropic or anisotropic, as will be shortly reviewed in Section 1.2. This theory of elastic ('bulk') wave propagation in infinite solids still holds for the pulse propagation of waves through finite bars — provided the wavelength is small compared to the characteristic cross-sectional length of the bar. On the other hand, for wavelengths which are very large as compared to the bar's cross-sectional length, appropriate wave velocities (of so-called 'extensional' or 'bar' waves, being always slower than the 'bulk' waves) follow from combining the constitutive theory of longitudinally deformed bars with Newton's second law (also reviewed in more detail in Section 1.2). The transition between these two limit cases have kept the scientific community busy for decades. Various experimental and theoretical studies were inspired by the analytical solutions of Pochhammer (1876) and Chree (1889) for (3D) wave propagation in (infinite) cylindrical rods, based on ansatz functions for harmonic waves fulfilling the (zero) stress boundary conditions at the rod surface. Pochhammer's solution predicts that decreasing wavelengths of such harmonic waves would lead to decreasing wave velocities, with the Rayleigh (surface) wave as the limit case for very small wavelenghts. Based on standing wave techniques (Morse 1948, 1950) the transition from extensional to Rayleigh waves could be experimentally reproduced. However, a certain portion of energy is always transported in form of a bulk ('precursor') wave emanating from a 'point' source (Northwood 1947; Kolsky 1964). Accordingly, this energy does not travel slower, but faster than the extensional wave, and reaching the bulk wave speed at very small wavelengths. While numerous studies (Hueter 1950; McSkimin 1956; Redwood 1959; Thurston 1978; Hayashi et al. 2003, 2006) were devoted to the dispersion (i.e. the frequency dependence) of waves fulfilling Pochhammer's boundary conditions, the frequency-dependent transition of

pulse ('precursor'-type) signals, from bulk wave propagation to extensional wave propagation
has been quite rarely studied (Tu et al. 1955; Ashman et al. 1984). However, this type of
signals lies at the very foundation for ultrasonic measurements of elasticity properties of solids
by means of the pulse-transmission(-through) technique — in this context, it needs to be known
whether the ultrasonic signal would travel through a specific sample as extensional or bulk wave.
Accordingly, the focus of the present paper is the identification of finite sample shapes which
would be related to one of the two limit cases interesting for ultrasonic elasticity determination:
The extensional wave propagation and the bulk wave propagation.

Both of the aforementioned wave types relate to the long-wavelength-limit, referring to wave-
lengths being considerably larger than the characteristic length of the material volumes [also
called representative volume elements (Zaoui 2002)] building up the medium through which the
waves travel. If the wavelength attains the size of the material volume, the wave starts to 'feel'
the material microstructure, e.g. they may be scattered at inhomogeneities (e.g. inclusions)
inside the material volume. The transition from the long-wavelength-limit to waves scattered
by microstructural elements has been the topic of various theoretical investigations, be it in the
framework of random homogenization theory (Mason and McSkimin 1948; Huntington 1950;
Berryman 1980; Sabina and Willis 1988; Stanke and Kino 1984; Yang and Mal 1994; Yang 2003;
Wei and Huang 2004) or of periodic homogenization technique (Foldy 1945; Lax 1952; Water-
man and Truell 1961; Bose and Mal 1973, 1974; Datta 1977; Varadan et al. 1978; Murakami
et al. 1979a,b; Willis 1980; Gubernatis and Domany 1984; Ledbetter and Datta 1986; Parnell
and Abrahams 2008). We here do not concentrate so much on this transition, but rather focus
on experimental revelation of two limit cases: The aformentioned long-wavelength-limit (how
large needs a wave to be in order to feel the 'homogenized medium' rather than microstructural
details?), and also the 'short-wavelength-limit' (how small needs a wave to be to 'feel' the mate-
rial components themselves, rather than their microstructural interaction?), which was beyond
the aforementioned theoretical investigations, relating to the question: How short needs a wave
to be in order to find an unscattered path between the microstructural inhomogeneities? Ob-
viously, the answers depend on the type of chosen microstructures. We here choose an extreme
case: Zero-stiffness, cylindrical pore inclusions.

Accordingly, the paper is organized as follows: After recalling some foundations of plane wave
propagation theory (Section 1.2), we present the ultrasonic measurement system used for the
present study (Section 1.3) and the investigated specimens (Section 1.4), together with a pre-
cision check of our measurement system (Section 1.5). On this basis, we study the transition
from bulk to extensional waves (Section 1.6), and from the long-wavelength-limit to the short-
wavelength-limit (Section 1.7), both from a dimensional analysis viewpoint. After discussing
the experimental results from a micromechanics viewpoint (Section 1.8), we conclude the paper
in Section 1.9.

1.2   Wave propagation in 3D and 1D linear elastic solids — theoretical basics

We focus on wave propagation in continua — where the basic property of a continuum solid is
that its deformations can be described at the basis of representative volume elements (RVEs)
'labelled' on the continuum and staying neighbours during deformation (Salençon 2001). The
characteristic lengths ℓ of such RVEs need to be smaller than those of the body made up of
the RVEs or than the excitation lengths of that body [such as wavelengths λ, see Eq. (1.9)] —
then use of differential calculus is admissible; and the RVE-length ℓ needs to be larger than
the microheterogeneities with characterisitc length d within the RVE (e.g. the void diameter

in Figure 1.4) — then material properties such as stiffness [see Eq. (1.5)] can be introduced. Mathematically, this is expressed by means of the separation-of-scales requirement (Zaoui 2002),

$$d \ll \ell \ll \lambda . \tag{1.1}$$

In the absence of body forces (Carcione 2001), the (local) conservation law of linear momentum in such a 3D continuum reads in each material point ('representative volume element' — RVE) as

$$\nabla \cdot \boldsymbol{\sigma} = \rho \, \mathbf{b} , \tag{1.2}$$

with the nabla operator ∇ reading, in a Cartesian base frame $\mathbf{e}_1$, $\mathbf{e}_2$, $\mathbf{e}_3$, as $\nabla = (\partial/\partial x_1 \, \mathbf{e}_1, \partial/\partial x_2 \, \mathbf{e}_2, \partial/\partial x_3 \, \mathbf{e}_3)$, with $\mathbf{x} = x_1 \, \mathbf{e}_1 + x_2 \, \mathbf{e}_2 + x_3 \, \mathbf{e}_3$ as the location vector, with the second-order symmetric stress tensor $\boldsymbol{\sigma}$, with the mass density ρ, and with the acceleration vector $\mathbf{b}$, measured in a Galilean (i.e. 'totally remote') frame (Salençon 2001). $\mathbf{b}$ equals to the twofold temporal derivative of the location-specific displacement vector $\mathbf{u}(\mathbf{x})$,

$$\mathbf{b} = \frac{\partial^2 \mathbf{u}}{\partial t^2} . \tag{1.3}$$

In a linear elastic body, the stresses evoke deformations in the form of linearized strains $\boldsymbol{\varepsilon}$ (being a symmetric tensor of second order),

$$\boldsymbol{\varepsilon} = \nabla^S \mathbf{u} = \frac{1}{2} \left(\nabla \mathbf{u} + \nabla^T \mathbf{u} \right) , \tag{1.4}$$

through the so-called generalized Hooke's law,

$$\boldsymbol{\sigma} = \mathbb{C} : \boldsymbol{\varepsilon} , \tag{1.5}$$

with the (symmetric) fourth-order elasticity tensor $\mathbb{C}$. Insertion of (1.3) to (1.5) into (1.2) results in the so-called wave equation,

$$\mathbb{C} : \nabla^2 \mathbf{u} = \rho \, \frac{\partial^2 \mathbf{u}}{\partial t^2} . \tag{1.6}$$

In the following, we shorty recall two solutions of (1.6): (i) a 3D solution in the form of a plane wave propagating through an infinite 3D elastic medium, (ii) a 1D solution relating to plane waves propapating through a bar, i.e. through a structure where one spatial dimension is orders of magnitude larger than the other two.

1.2.1 Bulk waves

One solution of the partial differential equation (1.6) is the equation of a plane wave in a 3D medium, given through

$$\mathbf{u}(\mathbf{x}, t) = \mathbf{u}_0 \, \exp[i \, (\mathbf{k} \cdot \mathbf{x} - \omega \, t)] , \tag{1.7}$$

with the amplitude $\mathbf{u}_0$, $i = \sqrt{-1}$, the wave vector $\mathbf{k} = k \, \mathbf{n}$ ($\mathbf{n}$ being the wave direction and k being the wave number), and the angular frequency $\omega = 2 \, \pi \, f$ (f being the frequency of sinusoidal pertubation). Insertion of (1.7) into (1.6) yields

$$(\mathbb{C} \cdot \mathbf{n} \cdot \mathbf{n} \, k^2 - \rho \, \omega^2 \, \mathbf{1}) \cdot \mathbf{p} = \mathbf{0} , \tag{1.8}$$

with the second-order unity tensor $\mathbf{1}$, having δ_{ij} (Kronecker delta — $\delta_{ij} = 1$ for $i = j$, and zero otherwise) as components, and with $\mathbf{p} = \mathbf{u}_0/|\mathbf{u}_0|$ as the normalized displacement or polarization

vector. Based on the definition of the phase velocity (Newton 1687; Carcione 2001)

$$v_p \equiv \frac{\omega}{k} = \lambda f \,, \tag{1.9}$$

with the wavelength λ, and of the acoustic tensor [also called 'Kelvin-Christoffel matrix' (Carcione 2001)]

$$\boldsymbol{\Gamma} = \mathbb{C} \cdot \mathbf{n} \cdot \mathbf{n} \,, \tag{1.10}$$

(1.8) can be recast in the form

$$(\boldsymbol{\Gamma} - \rho \, v_p^2 \, \mathbf{1}) \cdot \mathbf{p} = \mathbf{0} \,, \tag{1.11}$$

which constitutes an eigenproblem with eigenvalues $\rho \, v_p^2$ and eigenvectors $\mathbf{p}$. Due to the reality and symmetry of the acoustic tensor $\boldsymbol{\Gamma}$, the three eigenvalues are real and the three polarization vectors are orthogonal. While this holds for any stiffness tensor $\mathbb{C}$ (including general anisotropy with 21 independent tensor components), we here restrict ourselves to the cases of transversely isotropic and isotropic elasticity tensors. In addition, we are interested solely in wave propagation along the principal axes of a transversely isotropic material (coinciding then with wave propagation direction $\mathbf{n}$). For the respective solution of the eigenproblem (1.11), we adopt an orthogonal base frame coinciding with these principal directions, where $\mathbf{e}_1$ and $\mathbf{e}_2$ span the plane of isotropy, and $\mathbf{e}_3$ is oriented perpendicular to that plane. For wave propagation within the plane of isotropy (e.g. $\mathbf{n} = \mathbf{e}_1$), the three eigenvalues give access to the following phase velocities:

$$v_{1,1} = \sqrt{\frac{C_{1111}}{\rho}} \,, \quad v_{1,2} = \sqrt{\frac{C_{1212}}{\rho}} \,, \quad v_{1,3} = \sqrt{\frac{C_{1313}}{\rho}} \,. \tag{1.12}$$

The corresponding polarization (eigen)vectors are $\mathbf{e}_1$, $\mathbf{e}_2$, and $\mathbf{e}_3$, so that the first phase velocity in (1.12) is identified as longitudinal wave ($v_{1,1} = v_{L,iso}$, 'iso' refers to the isotropic plane), while the second and third one relate to transversal (or shear) waves ($v_{1,2} = v_{T,iso}$; $v_{1,3} = v_{T,aniso}$, 'aniso' indicates that either the polarization direction or the wave direction or both point out of the isotropic plane). Also $\mathbf{n} = \mathbf{e}_2$ relates to wave propagation within the plane of isotropy, so that

$$v_{2,2} = v_{1,1} = v_{L,iso} \,, \quad v_{2,1} = v_{1,2} = v_{T,iso} \,, \quad v_{2,3} = v_{1,3} = v_{T,aniso} \,. \tag{1.13}$$

For wave properties orthogonal to the plane of isotropy ($\mathbf{n} = \mathbf{e}_3$), the phase velocities read as

$$v_{3,1} = v_{T,aniso} = \sqrt{\frac{C_{1313}}{\rho}} \,, \quad v_{3,2} = v_{T,aniso} = \sqrt{\frac{C_{1313}}{\rho}} \,, \quad v_{3,3} = v_{L,aniso} = \sqrt{\frac{C_{3333}}{\rho}} \,. \tag{1.14}$$

In case of isotropy, wave propagation velocities are independent of the propagation direction, and in all directions, the wave velocities follow from specification of (1.12) and (1.14) for $C_{3333} = C_{1111}$ and $C_{1313} = C_{1212}$ so that we have

$$v_L = \sqrt{\frac{C_{1111}}{\rho}} \quad \text{and} \quad v_T = \sqrt{\frac{C_{1212}}{\rho}} \,, \tag{1.15}$$

with v_L and v_T as the longitudinal and transversal (shear) wave velocities in isotropic elastic media. Since isotropic solids are completely described by two elastic constant, e.g. C_{1111} and C_{1212} (shear modulus is equal to shear stiffness component, i.e. $G = C_{1212}$), the two velocities v_L and v_T can also be used to determine two engineering elastic constants, e.g. Young's modulus and Poisson's ratio, in the form

$$E = \rho \, \frac{v_T^2 \, (3 \, v_L^2 - 4 \, v_T^2)}{v_L^2 - v_T^2} \quad \text{and} \quad \nu = \frac{v_L^2/2 - v_T^2}{v_L^2 - v_T^2} \,. \tag{1.16}$$

1.2.2 Extensional waves or bar waves

Bars are characterized by a one-dimensional state of normal stress, $\boldsymbol{\sigma} = \sigma_{11}\,\mathbf{e}_1 \otimes \mathbf{e}_1$, $\mathbf{e}_1$ pointing into the direction of the bar axis, so that the wave equation (1.6) reduces to (Kolsky 1953)

$$E\nabla u_1 = \rho\,\frac{\partial^2 u_1}{\partial t^2}\,, \tag{1.17}$$

E being Young's modulus of the (isotropic or anisotropic) bar material in the bar axis direction. Accordingly, there is one (extensional or bar) wave propagating through the considered bar, with wave velocity

$$v_E = \sqrt{\frac{E}{\rho}}\,. \tag{1.18}$$

1.3 Ultrasonic measurement system

1.3.1 Equipment

The employed equipment consists of an ultrasonic pulser and a signal receiver built into a single unit [PR 5077, Panametrics Inc., Waltham, MA, USA; see Figure 1.5 (a)], a digital oscilloscope [WaveRunner 62Xi, Lecroy Corporation, Chestnut Ridge, NY, USA; see Figure 1.5 (a)], 17 pairs of ultrasonic, single-element, untuned contact transducers for longitudinal and transversal pulses (Panametrics Inc., Waltham, MA, USA; see Table 1.1 and Figure 1.1), an ultrasonic signal preamplifier (5676, Panametrics Inc., Waltham, MA, USA), a coupling medium, and an auxiliary testing device [see Figure 1.5 (a)].

Piezoelectric elements built into the ultrasonic transducers transform electrical signals into mechanical signals, or they transform mechanical signals into electrical signals, depending on whether the transducers are used as senders or receivers. The piezoelectric elements are tailored to the frequency and the polarization of the employed mechanical signal, e.g. the higher the frequency, the smaller the element and the smaller the corresponding transducer (see element diameter d_e of the transducers in columns four and eight of Table 1.1). Depending on the cut and orientation of the element, a longitudinal wave (X-cut) or a transversal wave [Y-cut or AT-cut, Firestone and Frederick (1946); Markham (1957); ANSI/IEEE-Std-176 (1987)] is emitted. Most of the used transducers (see labels with letter V in Table 1.1) are heavily damped, with a short signal typically stretching one and a half oscillation periods, with a broad frequency bandwidth and with a center frequency according to column one in Table 1.1. Some transducer (see labels with letter C in Table 1.1) are made of piezocomposite elements (i.e. the piezoelectric element is subdivided into a grid of small cuboidal pieces) that provide better sensitivity to signals passing highly attenuating materials, due to a high signal-to-noise ratio. Low frequency transducers (labeled with letter X in Table 1.1) are less heavily damped. Thus, they exhibit a pulse with a signal consisting of several oscillation periods. The polarization direction of transversal wave transducers is in line with the electricity cable connector. A wear plate protects the piezoelectric elements, and at the same time provides an acoustic impedance which matches approximately that of the material under investigation.

A coupling medium is necessary to provide energy transmission between the ultrasonic transducer and the specimen. Water or another suitable liquid may be used as coupling medium for longitudinal waves. Since the medium needs to be highly viscous for transversal wave transmission, we used honey for both longitudinal and transversal waves. Thereby, the influence of the type of honey on measurement results is very small. The higher the viscosity, the better

Table 1.1: Ultrasonic longitudinal and transversal transducers (frequency f, aluminum-related wavelength λ_i, element diameter d_e, system and transducer delay time t_d).

	longitudinal				transversal			
f	λ_L	label	d_e	t_d	λ_T	label	d_e	t_d
[MHz]	[mm]	[-]	[mm]	[μs]	[mm]	[-]	[mm]	[μs]
0.05	127	X1021	32	3.988	–	–	–	–
0.1	64	V1011	38	3.667	32	V1548	25	0.339
0.25	25	V1012	38	3.355	13	V150-RB	25	0.351
0.5	13	V101-RB	25	2.464	6.4	V151-RB	25	0.390
1.0	6.4	C602-RB	25	2.828	3.2	V152-RB	25	0.320
2.25	2.8	C604-RB	25	2.555	1.4	V154-RM	13	0.211
5.0	1.3	C109-RM	13	2.426	0.6	V155-RM	13	0.147
10	0.6	V112-RM	6	2.343	0.3	V221-BA-RM	6	6.939
20	0.3	V116-RM	3	2.346	0.16	V222-BA-RM	6	6.928

the transversal wave transmission, as less damping of the ultrasonic beam occurs. Avoidance of any air inclusions within the coupling layer had high priority, as to achieve a maximum of ultrasonic energy transfer.

The pulser unit of the ultrasonic pulser-receiver emits electrical (negative) square-pulses of 100, 200, 300 or 400 V pulse voltage and fixed pulse widths from 0.1 to 20 MHz (at −3 dB), with fine vernier tuning (± 25%). The pulse energy of a square-pulses is by up to 12 dB higher as compared to a spike excitation. The rise time of the pulse is typically below 10 ns (max. 20 ns) and its repetition rate is adjustable from 0.1 to 5 kHz. The receiver unit of the ultrasonic pulser-receiver has a bandwidth of 1 kHz to 35 MHz, a voltage gain of up to 59 dB and an attenuator range up to 49 dB. It amplifies and conditions the received electrical signal into a radio frequency output, which is to be processed by the oscilloscope. The receiver unit is able to filter frequencies below 1 MHz and/or above 10 MHz from the received signal, e.g. to decrease the signal noise.

Figure 1.1: Examples for used ultrasonic longitudinal (L) and transversal (T) transducers.

If the amplitude of the ultrasonic signal is too weak, an additional low noise preamplifier with a fixed voltage gain of 40 dB (bandwidth $0.05 - 20$ MHz) is used, which is interconnected between receiving transducer and the receiver.

The amplified signal is displayed on an digital oscilloscope with a bandwidth of 600 MHz and a sample rate of 10 GS/s (gigasamples per second).

1.3.2   Set-up

The most common ultrasonic (contact) measurement techniques are the pulse-transmission(-through) and the pulse-echo technique. With the first technique, two transducers are used, one sending a signal into the specimen and one receiving the sent signal at the opposite side of the specimen (Figure 1.2); with the second technique, only one ultrasonic transducer is used, sending the signal into the specimen, and also receiving the signal after having been reflected at the backside of the specimen.
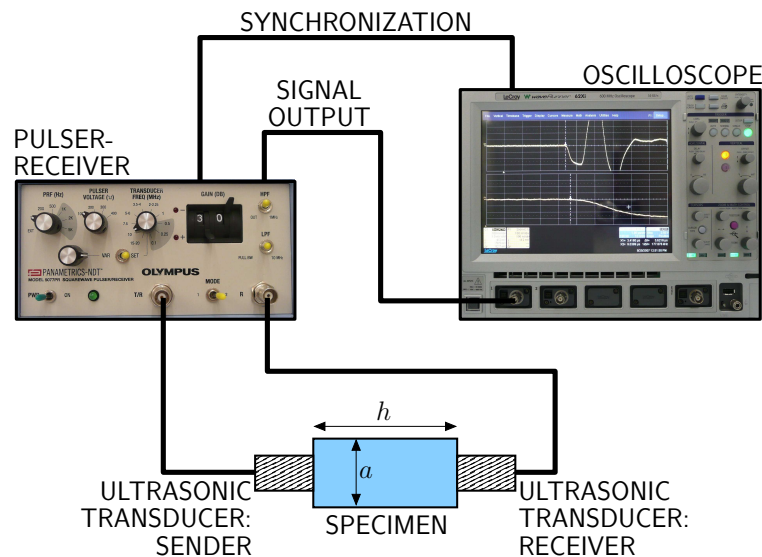
Figure 1.2: Set-up of ultrasonic equipment for pulse-transmission technique.

We here use the pulse-transmission technique, because of its major advantage over the pulse-echo technique, which is that the ultrasonic beam is only travelling once through the specimen and that no beam reflection is necessary. Thus, the influence of signal attenuation is minimized and problems emanating from reflection of waves, like beam divergence and mode conversion, are avoided. This is especially of interest when investigating porous materials (as dealt with in Section 1.7) or other highly attenuating materials like organic materials, e.g. plastics and rubber. Such materials attenuate the signal and/or scatter the signal at reflection, to a marginal amplitude that disappears within the signal noise. Reflections of the ultrasonic pulse from boundaries of the specimen are less likely to interfere with measurements in the pulse-transmission technique, as compared to the pulse-echo technique. Application of the pulse-echo technique is only possible in materials where a clear reflected signal is available, e.g. in metals. A potential drawback when using the pulse-transmission technique is that two transducers need to be coupled with the specimen, which may increase measurement errors related to wave velocity. An auxilliary testing device [see Figure 1.5 (a)] made of aluminum and steel was used to hold the two transducers in a parallel position and to apply a uniform pressure (with a micrometer screw). In this way, coupling was improved, and consistent test conditions were achieved.

The time of flight of the ultrasonic wave through the specimen, t_f, provides, together with the travel distance through the specimen, h, the phase velocity of the longitudinal (L) or transversal (T) wave, v_i $i = \{L, T\}$,

$$v_i = \frac{h}{t_f} \, . \tag{1.19}$$

t_f is determined by the difference of the total time of flight measured between the transducers, t_{tot}, and the wave transit time without the specimen, called system and transducer delay time t_d (see Table 1.1, columns five and nine). t_d includes the time delay caused by the transducers, by the coupling medium, by additional delay lines, and by the measurement system itself. The benchmark for the time of flight measurements is a reference signal sent by the ultrasonic pulser-receiver, on which the trigger of the oscilloscope is set. Since we are interested in the first arrival of the ultrasonic wave (even in case the pulse is strongly attenuated and consequently, the wave form is changed, i.e. broadened), we use the first apparent deviation of the received signal from constancy with time (i.e. the time instant when the signal rises beyond noise level) as the arrival time of the ultrasonic wave. This reference point is insensitive to wave attenuation, which is not the case for other, often automated reference points, such as the first or the highest crest of the signal (Nicholson and Strelitzki 1999). Transversal wave propagation is usually accompanied by a precursor longitudinal wave [see e.g. Papadakis et al. (1991); Rao and Prasanna Lakshmi (2003)]. In cases where the precursor longitudinal wave interferes with the first arrival of the transversal wave, the wave trough preceding the main transversal wave crest is used to determine the wave arrival time.

The time readings on the oscilloscope are performed manually. The deviation of the reveived pulse from the time constancy axis develops smoothly. Therefore, the signal amplitude and frequency (of both pulser-receiver and transducer), as well as the amplitude and time range chosen for display of the pulse on the oscilloscope, influence the time readings of signal arrival. In order to obtain comparable results, measurements were performed, as a rule, at fixed pulse voltage (100 V) and gain settings (30 dB) on the pulser-receiver, which was set to 100 Hz pulse repetition rate. Only in case a higher pulse energy was necessary to penetrate the specimen with a signal amplitude that allowed for precise time readings, a gain of 40 dB was used, together with a higher pulse voltage, namely 400 V for transducers with frequencies lower than 5 MHz, and 300 V for all other transducers (in order to protect the smaller piezolelectric crystals of the latter from overheating and depoling). In order to smoothen the wave signal at pulse frequencies below 5 MHz, the low pass filter was used, which inhibits frequencies higher than 10 Mhz.

Also the display settings on the oscilloscope were fixed, namely at a sample rate of 10 GS/s, at a time range of 5 μs, and at an amplitude range of ± 0.4 V. The bandwidth was limited to 20 MHz for transducers below 5 MHz, and to 200 MHz for higher frequency transducers, as to minimize signal noise. For the arrival time reading the first arrival part of the pulse was diplayed in an additional zoom window, covering 1 μs and ± 0.4 V in time and amplitude dimensions, respectively. The accuracy of cursor positioning was 0.1 ns, but reliable measurements were only possible up to an accuracy of 10 ns $= 0.01$ μs.

The exact identification of the signal arrival time is the major source of measurement inaccuracies. Especially for small thicknesses of the specimens and corresponding short times of flight and/or low transducer frequencies, this error may be essential. In order to minimize this error (as well as other sources of inaccuracies), delay lines have been used since the beginning of ultrasonic research (Arenberg 1948). Such delay lines may fulfill two purposes: (i) the near field of the transducer, located directly adjacent to the wear plate and characterized by an oscillating amplitude, is relocated out of the investigated specimen (Williams 1992); and (ii) the received pulse (arrival signal) is relocated out of the time range of receiver disturbances stemming from the electrical ignition of the pulser. The latter purpose is relevant here, since our present focus is on arrival times rather than on amplitude measurements. We used as delay

lines cylinders made of aluminum alloy 5083 with diameters 1.5 mm larger than the diameter of the transducers ($\approx d_e$ in Table 1.1), as to leave room for a notch that prevents the delay line from slipping between the transducer and the specimen. The heights of the delay lines were 15 mm and 20 mm, respectively, referring to a time delay of 2.35 μs and 3.14 μs, respectively. They were coupled to the sending transducers with honey (Figure 1.3). The longer time delay was used for the longitudinal transducers with the three lowest frequencies (f = 0.05, 0.1, 0.25 MHz), while the shorter time delay was used for the rest of the longitudinal transducers. Implementation of the delay lines led to higher accuracy over all frequencies when sending longi-
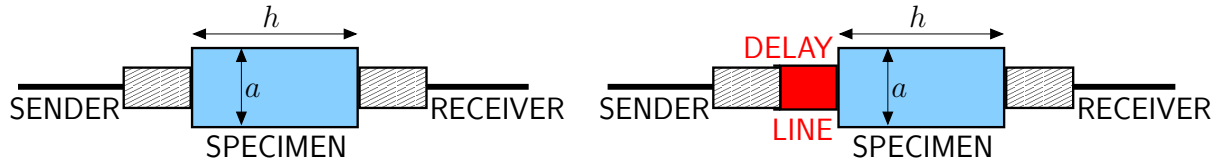
Figure 1.3: Measurement without and with delay line.

tudinal waves through thin specimens. Such a positive effect was not observed with transversal waves. On the contrary, delay lines even impaired the measurement results of low frequency transversal waves, due to the more complicated experimental setup (including a third coupling layer), which makes the discrimination of the correct wave crest more difficult. Thus, with transversal transducers no delay lines were used, except for the two transversal transducers with the highest frequencies, which have a built-in silica delay line (delay time ≈ 6.8 μs; see Table 1.1).

In order to minimize errors in time of flight measurements, we standardly employed two transducers of identical architecture and center frequency for the pulse-transmission measurements. As exception to that rule, the longitudinal and transversal transducers with center frequencies of 20 MHz were used in combination with the equivalent 10 MHz-transducers as receivers; the 0.05 MHz- and 0.1 MHz-longitudinal transducers were used in combination with a 0.1 MHz-longitudinal transducer (X1020, d_e = 16 mm) as receiver; and the 0.25 MHz-longitudinal transducer was used in combination with the 0.5 MHz-longitudinal transducer as receiver (see Table 1.1). These exceptions were allowed since shifting the center frequency of the receiving transducer did not remarkably change the test results on one and the same specimen.

When combining ultrasonic longitudinal and transversal velocity measurements, e.g. for the computation of engineering elastic constants [see Eq. (1.16)], only values related to comparable wavelengths should be used, referring to the same scale of mechanical investigation [see Eq. (1.1)]. The transversal wave velocity is approximately half of the longitudinal one, over most (isotropic) materials. From Eq. (1.9) it follows that, in order to achieve equal wavelengths $\lambda_L = \lambda_T$, a longitudinal frequency transducer should be combined with a transversal transducer exhibiting half the frequency of the longitudinal one, i.e. $f_T = f_L/2$ (see also Table 1.1, columns two and six).

Other sources of measurement errors include the flatness of the specimen surfaces where the transducers are applied, if these surfaces are not strictly parallel; and the character of the coupling layer. It is important to realize an evenly distributed coupling layer of constant thickness, without (air) inclusions. Measurements were performed near room temperature (i.e. ≈ 300 K $\approx 25°$C). According to Ledbetter (1980) a ten-degree-kelvin temperatur change alters (copper) ultrasonic velocities by only 0.05%, implying that the expected temperature variations in laboratories do not significantly affect corresponding results.

1.3.3   Error propagation

All spatial dimensions of specimens were determined from the average of five measurements with a micrometer gauge characterized by a precision of ± 10 μm. Masses were measured on a digital balance, with a precision of ± 1 mg. Then the apparent density ρ_{app} was determined, as the ratio of mass m and volume V

$$\rho_{app} = \frac{m}{V}\,, \tag{1.20}$$

whereby our cuboidal specimens (see Section 1.4 for more details) are characterized by height h and quadratic cross-section with edge length a, so that

$$V = h\,a^2\,. \tag{1.21}$$

In the sequel, we discuss how measurement errors in fundamental quantities, such as length (h, a), mass (m), and time of flight (t_f) affect errors in the following derived quantities (Rossi 2007): volume V [Eq. (1.21)], density ρ_{app} [Eq. (1.20)], velocity v_i [Eq. (1.19)], and stiffnesses C_{ijkl} or E [Eqs. (1.12), (1.14), (1.15), (1.18)]. Therefore, we recall the law of error propagation (Müller 1979)

$$s_y^2 \approx \sum_i \left(\frac{\partial \mathcal{F}}{\partial x_i} s_i \right)^2 + 2 \sum_{i<j} \frac{\partial \mathcal{F}}{\partial x_i} \frac{\partial \mathcal{F}}{\partial x_j} s_{ij} \qquad i\,,j = 1\,,2\,,\dots\,,n\,, \tag{1.22}$$

where s_y is the standard deviation of a random variable y, which is generated by evaluating a deterministic function $\mathcal{F}$ of n random variables x_i characterized by variances s_i^2 and covariances s_{ij}. Depending on the investigated quantity, $\mathcal{F}$ is chosen as V, ρ_{app}, v_i, C_{ijkl}, or E [according to Eqs. (1.21), (1.20), (1.19), (1.12), (1.14), (1.15), (1.18)], and the variables x_i are chosen as h, a, m, V, t_f, ρ_{app}, and/or v_i. If the variables x_i are uncorrelated, the last term in (1.22) vanishes. Approximation (1.22) is valid for small random alterations of the variables x_i, and implies that all errors are random, i.e. systematic errors are assumed to be zero. Thus, strictly speaking, we give precisions (reproducibility) rather than accuracies of measurements. The standard deviations s_i [also referred to as uncertainties or as errors (Müller 1979)] give access to the relative standard deviations (relative errors) δ_i, via

$$\delta_i = \frac{s_i}{x_i}\,. \tag{1.23}$$

Using this definition and the definition of the correlation coefficient $\delta_{ij} = s_{ij}/(s_i\,s_j)$, specifications of $\mathcal{F}$ according to (1.21), (1.20), (1.19), and (1.12) [or (1.14), (1.15), (1.18)] yields

$$\delta_V \;=\; \sqrt{\delta_h^2 + 2\,\delta_a^2}\,, \tag{1.24}$$

$$\delta_\rho \;=\; \sqrt{\delta_m^2 + \delta_V^2 - 2\,\delta_m\,\delta_V\,\delta_{mV}}\,, \tag{1.25}$$

$$\delta_v \;=\; \sqrt{\delta_h^2 + \delta_t^2 - 2\,\delta_h\,\delta_t\,\delta_{ht}}\,, \tag{1.26}$$

$$\delta_C \;=\; \sqrt{4\,\delta_v^2 + \delta_\rho^2 + 4\,\delta_\rho\,\delta_v\,\delta_{\rho v}}\,, \tag{1.27}$$

whereby δ_h is the relative error in h, and so forth. Based on (absolute) errors of $s_h = s_a = 0.01$ mm (precision of the micrometer gauge), Eqs. (1.23) and (1.24) give access to the relative errors in h, a, and V, see columns four to six in Table 1.2. Considering additionally $s_m = 0.001$ g (precision of the digital balance) and $\delta_{mV} = 1.00$ (as obtained from a statistical analysis of the measurements on all dense aluminum samples of Section 1.4, see Table 1.3, column three),

Eqs. (1.23) and (1.25) give access to the relative errors in m and ρ, see columns seven and eight of Table 1.2. The latter value was checked by computing δ_ρ directly from the measurements on all plate-type, cubic, and bar-type dense specimens, yielding 0.187%, which underlines the relevance of error propagation law (1.22) for our purposes (see Table 1.2, column eight, rows four to six).

Table 1.2: Geometrical dimensions of specimens, with corresponding relative errors δ_h, δ_a, δ_V, δ_m, and δ_ρ, and times of flight t_f related to longitudinal waves.

geometry	h	a	δ_h	δ_a	δ_V	δ_m	δ_ρ	t_f
	[mm]	[mm]	[%]	[%]	[%]	[%]	[%]	[μs]
thin plate	0.5	30	2.00	0.03	2.001	0.084	1.917	0.078
plate	5	30	0.20	0.03	0.205	0.008	0.197	0.785
cube	30	30	0.03	0.03	0.058	0.001	0.056	4.708
bar	30	1	0.03	1.00	1.415	1.255	0.160	4.708
long bar	100	1	0.01	1.00	1.414	0.376	1.038	15.69

Table 1.3: Standard deviations in the time of flight, s_t, as well as correlation coefficients δ_{mV}, δ_{ht}, and $\delta_{\rho v}$, given for different frequencies.

f	s_t	δ_{mV}	δ_{ht}	$\delta_{\rho v}$
[MHz]	[μs]	[-]	[-]	[-]
0.05, 0.1	0.10	1.000	0.995	0.249
0.25, 0.5, 1.0	0.05	1.000	0.996	0.029
2.25, 5	0.02	1.000	0.997	0.127
10, 20	0.01	1.000	0.998	0.122

The uncertainties in time of flight, s_t, are (conservatively) estimated, for each frequency, from the range of time instants in which the first deviation of the signal from the time constancy axis can be discerned (see Table 1.3, column two). This value for s_t gives access to the corresponding relative errors according to Eq. (1.23), $\delta_t = s_t/t$, based on the times of flight of longitudinal (bulk) waves, observed at different geometries (see Table 1.4, column three). Because of $v_T \approx v_L/2$, transversal waves exhibit double times of flight and half relative errors δ_t, when compared to those of longitudinal waves. Relative errors of velocity δ_v are determined via (1.26), with δ_h according to column four in Table 1.2, with δ_t according to column three in Table 1.4, and with the correlation coefficient of δ_{ht} according to column four in Table 1.3. Thereby, δ_{ht} is obtained from length and time of flight measurements on all (dense) specimens belonging to one of the frequency groups given in Table 1.3. Significant relative errors δ_v occur for low frequency measurements in thin specimens (see Table 1.4). The relative velocity errors for high frequencies are in accordance with Ledbetter (1980), who gives $\delta_v < 0.1\%$ for box-shaped copper specimens ($h = 19$ mm, $t \approx 4$ μs, $f = 3$–10 MHz). The relative error in stiffnesses, δ_C, (see column five in Table 1.4) is estimated through Eq. (1.27), with δ_ρ according to column eight in Table 1.2, δ_v according to column four in Table 1.4, and $\delta_{\rho v}$ according to column five in Table 1.3. Thereby, $\delta_{\rho v}$ is obtained from density and velocity measurements on all (dense) specimens belonging to one of the frequency groups of Table 1.3. In case $\delta_\rho \ll \delta_v$ (e.g. at lower

Table 1.4: Relative errors δ_i in time of flight, velocity and stiffnesses, given for different specimen geometries and different frequencies.

	f	δ_t	δ_v	δ_C
	[MHz]	[%]	[%]	[%]
thin plate	0.05, 0.1	127	126	251
	0.25, 0.5, 1.0	64	62	124
	2.25, 5	25	24	47
	10, 20	13	11	22
plate	0.05, 0.1	12.7	12.5	25.1
	0.25, 0.5, 1.0	6.4	6.2	12.4
	2.25, 5	2.5	2.3	4.7
	10, 20	1.3	1.1	2.2
cube	0.05, 0.1	2.12	2.09	4.20
	0.25, 0.5, 1.0	1.06	1.03	2.06
	2.25, 5	0.42	0.39	0.79
	10, 20	0.21	0.18	0.37
bar	0.05, 0.1	2.12	2.09	4.22
	0.25, 0.5, 1.0	1.06	1.03	2.07
	2.25, 5	0.42	0.39	0.82
	10, 20	0.21	0.18	0.41
long bar	0.05, 0.1	0.64	0.63	1.82
	0.25, 0.5, 1.0	0.32	0.31	1.22
	2.25, 5	0.13	0.12	1.09
	10, 20	0.06	0.05	1.06

frequencies, i.e. higher δ_v), or if ρ is a precisely known quantity, Eq. (1.27) reduces to

$$\delta_C = 2\,\delta_v\,, \tag{1.28}$$

i.e. the relative error doubles when deriving stiffness tensor components from measured ultrasonic velocities. This was approximately observed when computing relative errors δ_v and δ_C directly from (bulk) velocity measurements on dense specimens *A-5* to *A-12* (see following Section) and from the density measurements discussed below Eq. (1.27). We re-iterate that the errors given in Table 1.4 are due to measurement uncertainties and that they do not include other error sources, such as uneven surfaces. From the results in Table 1.4 it is evident that very high errors are only to be expected if very thin samples, characterized by short times of flight, are investigated at low frequencies. Conclusively, when considering all sources for inaccuracies, the ultrasonic contact pulse-transmission technique is in general satisfactorily exact.

1.4   Specimens for ultrasonic tests

All specimens were made of commercial aluminum alloy EN AW-5083-H111, produced according to the European standards EN-485-1 (2007) and EN-485-2 (2006), a material that is insensitive to temperature changes in the room temperature regime (Weston et al. 1975). The specimens

are subdivided into five sets. *Set A1, A2, B*, and *R* are used to investigate the effect of specimen geometry and size on ultrasonic wave propagation (see Table 1.5), and *set C* is used to investigate the effect of specimen microstructure (see Table 1.6). All specimens are box-shaped with characteristic cross-sectional dimension a (edge length of the two specimen surfaces having the shape of a square) and height h; except for specimens *R-2* and *R-3*, which are of cylinder-type; there, a equals the diameter.

In addition, an aluminum cube with an edge length of $a = h = 100$ mm (cut from a 100 mm thick plate) was used to obtain reference bulk wave velocitites (even for lower frequencies, as will be verified in Section 1.6).

Table 1.5: Aluminum specimen *set A1, A2, B*, and *R* — influence of geometry on wave propagation (dimensions in [mm]).

	set A1			set A2			set B	
#	a	h	#	a	h	#	a	h
1	1	30	1	3	30	1	30	0.5
2	2	30	2	3	40	2	30	1
3	3	30	3	3	60	3	30	2
4	5	30	4	3	70	4	30	3
5	10	30	5	3	90	5	30	4
6	15	30	6	3	110	6	30	5
7	20	30				7	30	7.3
8	30	30				8	30	10
9	40	30		set R		9	30	15
10	50	30	1	1	100	10	30	20
11	75	30	2	9	14	11	30	25
12	100	30	3	18	4	12	30	30
	A2-1 = A1-3						*B-12 = A1-8*	

The twelve specimens of *set A1* have a constant height $h = 30$ mm, but varying characteristic cross-sectional dimensions a ranging from 1 to 100 mm, therefore covering shapes ranging from bars, via cubes, to (thick) plates. *Set A2* consists of six specimens with a constant cross-sectional dimension of $a = 3$ mm, but with varying heights h from 30 to 110 mm, i.e. these specimens are bars of different slenderness. *Set B* consists of twelve specimens with constant $a = 30$ mm and h varying from 0.5 to 30 mm, i.e. covering shapes ranging from (thin) plates to cubes. *Set R* consists of a bar with the lowest ratio a/h, namely 0.01, and of two cylindcrical specimens.

Set C consists of four box-type aluminum specimens with cylindrical voids of different diameters d, in a hexagonal arrangement with different distances e between the cylinder axes, resulting in different porosities [see Figure 1.4 (a) (b) and columns four and five in Table 1.6]. Hexagonal symmetry is characterized by a six-fold axis, i.e. a rotation by $\pi/3$ about axis 3 [longitudinal cylinder direction, see Figure 1.4 (a)] does not change the elastic stiffness, which — in turn — implies invariance against rotation by *any* angle (Helbig 1994). Materials with one axis of complete rotational invariance are termed transversely isotropic. Four different drill bit diameters, namely $d = 1, 1.5, 2, 3.2$ mm were used to produce four specimens (termed *C-1*, *C-2, C-3*, and *C-4*), with 247, 161, 60, and 52 boreholes, respectively [see Figure 1.4 (b)], and with three different porosities (specimens *C-1* and *C-3* have approximately the same porosities,
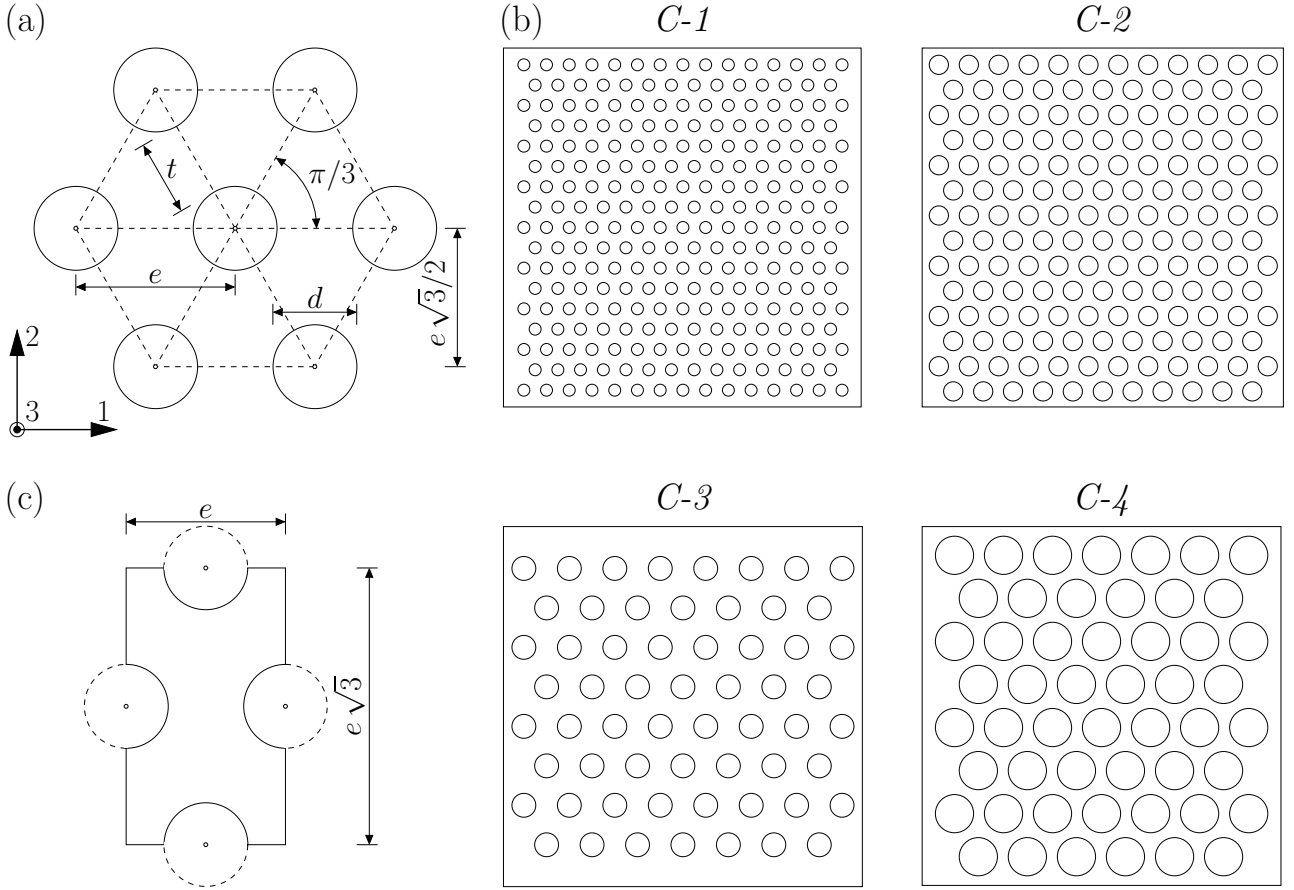
Figure 1.4: Specimens for investigation of microstructure (porosity) on wave propagation velocity: (a) Porous cylinders in hexagonal arrangement (and definition of principle material directions), (b) arrangements of voids in specimens of *set C*, (c) unit cell.

see column three in Table 1.6). Specimens *C-2*, *C-3*, and *C-4* are cubes with an edge length of $a = h = 30$ mm. The height of specimen *C-1* was reduced to $h = 20$ mm, in order to reduce problems in the deep drilling regime (characterized by drilling depth larger than ten times the drill bit diameter, i.e. 10 mm in case of the 1 mm boreholes). The wall thickness $t = e - d$ [see Figure 1.4 (a)], i.e. the thinnest part of solid matrix between the boreholes, is approximately 0.9 mm in specimens *C-1*, *C-2* and *C-4*, and 1.8 mm in specimen *C-3* [see Figure 1.4 (b)].

The geometrical properties of *set C* in Table 1.6 are determined by measuring the mass m and volume V for each specimen, and by computing the apparent density ρ_{app} according to (1.20). Knowing the apparent density ρ_{app} and the density of the solid, $\rho_s = 2.656$ g/cm^3 (see Table 1.7), the porosity φ [-] is given by

$$\varphi = \frac{\rho_s - \rho_{app}}{\rho_s} \, . \tag{1.29}$$

For an exactly (infinite) hexagonal arrangement of cylindrical voids, the porosity is propotional to the square of the ratio of the diameter of the voids d to their distance e,

$$\varphi = \frac{\pi}{2\sqrt{3}} \frac{d^2}{e^2} \, . \tag{1.30}$$

Knowing φ from measurements of the actual specimen (1.29) and d from the diameter of the drill bit, an average value for the actual size of e follows from (1.30) assuming an exact (infinite) hexagonal structure. The deviation of this actual (average) borehole distance e from its theoretical analogon related to an exact (finite) hexagonal structure according to Figure 1.4,

Table 1.6: Aluminum specimen *set C* — influence of microstructure on wave propagation.

#	ρ	φ	d	e	a	h
	[g/cm^3]	[%]	[mm]	[mm]	[mm]	[mm]
1	2.07	21.9	1.0	2.03	30	20
2	1.79	32.7	1.5	2.50	30	30
3	2.05	22.8	2.0	3.99	30	30
4	1.36	48.7	3.2	4.37	30	30

amounts to about 5% for all considered specimens. This is due to the inaccuracies in the borehole pattern, to the deviation of the borehole from the longitudinal direction, and to lack of boreholes in the borderarea (the realization of which was beyond the scope of this work, and would also have complicated the coupling of transducer and specimen). The actual porosity (see column three in Table 1.6) deviates from the infinite hexagonal structure porosity by around 10% for each specimen, so that our specimens can be regarded as decent approximation of quasi-infinite porous hexagonal patterns.

1.5 Bulk wave propagation: precision check

In order to check the precision of our ultrasonic measurement system, we compare bulk wave velocities measured on a cube of aluminum alloy 5083 with $a = h = 100$ mm [Figure 1.5 (a)], with wave velocities found in the literature, and with wave velocities back-calculated from quasi-static tests performed in our laboratory [Figure 1.5 (b)]. Corresponding results are collected into Table 1.7.

In our ultrasonic tests (see column two of Table 1.7), the wave velocity was measured with all nine longitudinal and eight transversal contact transducers, both with and without delay line. Each of these velocity values was determined from an average of at least three (actually three or four) independent time of flight measurements, i.e. a total of more than 100 data points were available. The longitudinal and transversal bulk wave velocities were determined from 18 and 16 average results, respectively. The extensional velocity and the elastic constants were determined from the 14 average results, each one corresponding to equal longitudinal and transversal wavelengths (see Table 1.7, column two).

When taking the average of eight values from four different literature sources (Weston et al. 1975; Naimon et al. 1975; Benck and Filbey 1976; Matweb 2009), we observe that the off-diagonal component C_{1122} shows by far the highest standard deviation of all, but that the average stiffness values agree very well with our own measurements (Table 1.7).

The mass density $\rho_s = 2.656$ g/cm^3 was determined on an aluminum cube with an edge length of 100 mm, according to Eq. (1.20) with $\rho_s = \rho_{app}$; this measurement was repeated twice.

Quasi-static load-controlled tensile tests were performed on a uniaxial electromechanical universal testing machine [LFM 150, Wille Geotechnik, Germany, see Figure 1.5 (b)]. Three dog bone-shaped specimens with constant rectangular cross-section of 30×10 mm over the measurement range of 150 mm (gradually broadened, over 10 mm, up to a cross-section of 50×10 mm in the clamping area) were made from the same aluminum alloy plate as was used for the production of the specimens for ultrasonic tests. The load was applied up to a stress σ_j of 75 MPa, with a stress rate of 0.17 MPa/s. The axial normal strains ε_j (those in direction of tensile

Table 1.7: Elastic stiffnesses and ultrasonic bulk velocities of aluminum alloy 5083, from literature (Weston et al. 1975; Naimon et al. 1975; Benck and Filbey 1976; Matweb 2009) (lit), and from our own quasi-static (qs) and ultrasonic (us) tests [average values ± standard deviation in percent of average; bold values measured or from literature, remaining derived from these via Eqs. (1.15), (1.16), and (1.18)].

quantity [unit]	ultrasonic (own experiment)	ultrasonic (literature)	quasi-static (own experiment)	deviation us lit	qs
n [-]	14	8	3	–	–
ρ [g/cm^3±%]	**2.656**	**2.663±0.1**	**2.656**	0.3	–
v_L [km/s±%]	**6.372±0.2**	6.349±2.6	6.301±1.5	−0.4	−1.1
v_T [km/s±%]	**3.205±0.7**	3.170±0.6	3.263±1.4	−1.1	1.8
v_E [km/s±%]	5.229±0.6	5.176±0.3	5.295±1.4	−1.0	1.3
C_{1111} [GPa±%]	107.86±0.3	107.47±5.2	105.49±3.0	−0.4	−2.2
C_{1212} [GPa±%]	27.29±1.4	**26.78±1.2**	28.29±2.9	−1.9	3.6
C_{1122} [GPa±%]	53.36±1.8	53.91±11.2	48.92±3.2	1.0	−8.3
E [GPa±%]	72.63±1.2	**71.40±0.7**	**74.49±2.9**	−1.7	2.6
ν [- ±%]	0.331±1.1	0.333±3.8	**0.317±0.3**	0.8	−4.2
C_{1111}/E [- ±%]	1.486±1.3	1.505±5.1	1.416±0.3	1.3	−4.7

force) and the lateral normal strains ε_i (those in direction perpendicular to tensile force) were measured by means of two separate Wheatstone bridge circuits of strain gauges (3/350XY13, Hottinger Baldwin Messtechnik GmbH, Germany) for compensation of any bending moment influences, yielding Young's modulus and Poisson's ratio according to

$$E_{qs} = \frac{\sigma_j}{\varepsilon_j} \qquad \text{and} \qquad \nu_{qs} = \frac{\varepsilon_i}{\varepsilon_j}, \tag{1.31}$$

respectively. The average of the results from the loading and the unloading path, respectively, was taken for each test (the corresponding differences amounted to less than 0.5%), and each of the three specimens was tested twice (the differences resulting from test repetition amounted to less than 0.5‰). For each set of E_{qs} and ν_{qs}, the other elastic constants and ultrasonic wave velocities were determined (average values and standard deviations in percent of average given

(a) ultrasonic velocity measurements   (b) quasi-static mechanical tests
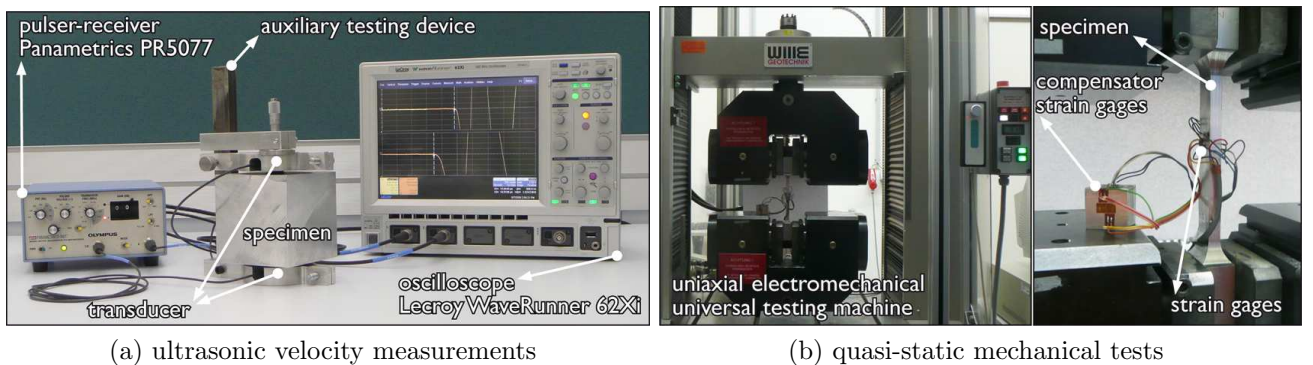
Figure 1.5: Determination of stiffness constants of aluminum alloy 5083.

in Table 1.7, column four).

The results from both measurement methods, quasi-static and ultrasonic, show good agreement with average literature values (compare Table 1.7, columns two to four). The ultrasonic stiffness measurements differ by at most 2% from literature values (see Table 1.7, column five). Ultrasonic wave velocities agree even better, with a deviation of only 1%. Excellent agreement is also found between the two different experimental setups, i.e. quasi-static and ultrasonic measurements (see Table 1.7, column six). Again the off-diagonal component exhibits the highest discrepancy between test methods (8%), for all other values, the difference is at most 4%.

1.6 Sample-specific wave propagation — bulk waves and extensional waves

According to the theory of elastic waves in infinite isotropic solids (built up by material volumes which are far smaller than the wavelengths λ), the longitudinal wave velocity is given through (Love 1906; Kolsky 1953; Auld 1990; Carcione 2001), see also $(1.15)_1$,

$$v_L = \sqrt{\frac{C_{1111}}{\rho}}, \tag{1.32}$$

with C_{1111} as the normal stiffness component of the material, and ρ as its mass density. For bounded solids, such as the box-type samples with square-shaped cross sections investigated in the present study, v_L additionally depends on sample height h, edge length a, and (longitudinal) wavelength λ_L,

$$v_{L,exp} = F(C_{1111}, \rho, a, h, \lambda_L). \tag{1.33}$$

Thanks to the dimensional independence of C_{1111}, ρ, and h, dimensional analysis (Buckingham 1914; Barenblatt 1996) allows for reducing the function F of four dimensional arguments [see (1.33)] to a (dimensionless) function of only two dimensionless arguments, reading as

$$\frac{v_{L,exp}}{\sqrt{C_{1111}/\rho}} = \mathcal{F}\left(\frac{a}{h}, \frac{h}{\lambda_L}\right), \tag{1.34}$$

which, according to Eq. (1.32), is equivalent to

$$\frac{v_{L,exp}}{v_L} = \mathcal{F}\left(\frac{a}{h}, \frac{h}{\lambda_L}\right). \tag{1.35}$$

In principal, Eq. (1.34) and (1.35) describe classes of similar problems defined through the same dimensionless quantities, being not restricted to a specific material, but valid for all materials with RVEs significantly smaller than the encountered wavelengths [compare Eq. (1.1)]. We are left with determination of $\mathcal{F}$ from our test series *A1*, *A2*, *B*, and *R* (performed on a specific material, aluminum alloy 5083):

Tests on sample *set A1* (solid aluminum boxes characterized by constant heights of 30 mm, and by square-shaped cross sections with edge lengths varying from 1 mm and 100 mm, passing all the shapes from plate-like, via cubic, to bar-like, see Table 1.5) reveal that longitudinal wave velocities increase with increasing cross section, unless they reach a constant value, which coincides with the bulk velocity of aluminum, $v_L = \sqrt{C_{1111}/\rho}$, see Figure 1.6 (a). The smallest cross sections are always related to the lowest wave velocities, but only at low frequencies, the extensional or bar velocity of aluminum, given through Eq. (1.18) as $v_E = \sqrt{E/\rho} = 0.821 \times v_L$, with E as the isotropic Young's modulus of the transmitted material (here aluminum), is reached,
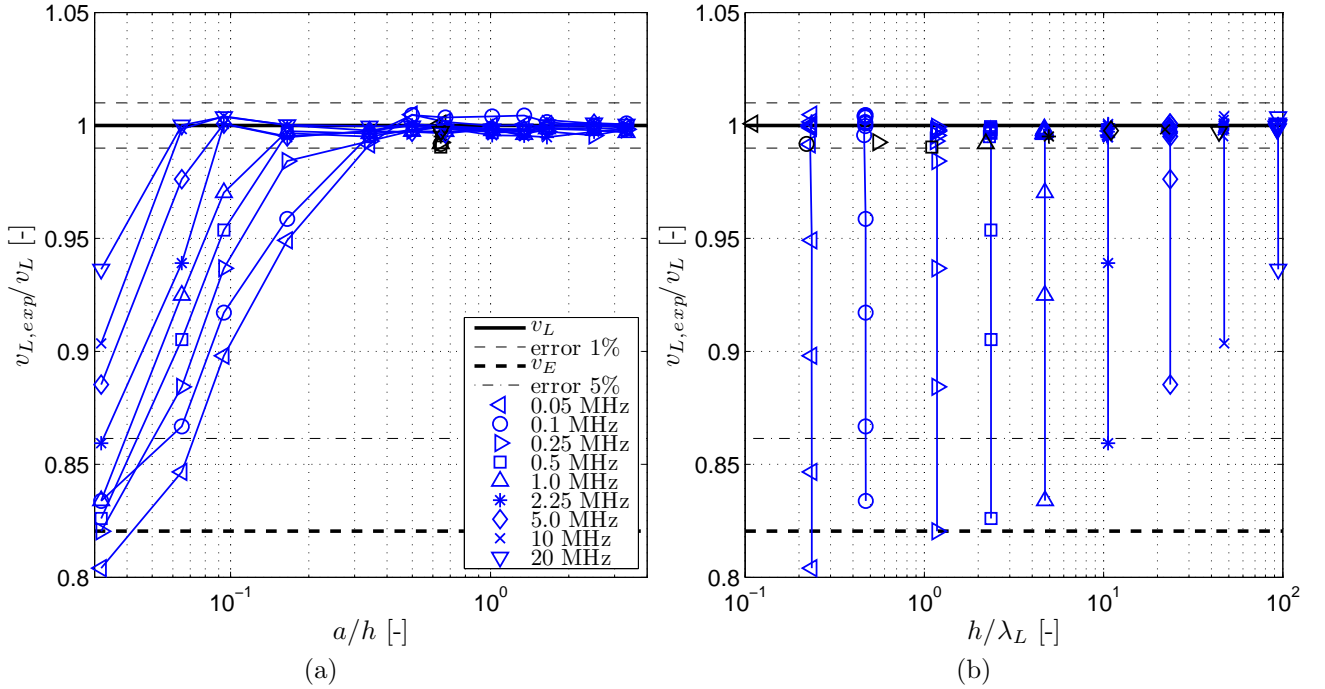
Figure 1.6: Specimen *set A1, R-2* (according to Table 1.5): Dependency of dimensionless longitudinal wave velocity ($v_{L,exp}/\sqrt{C_{1111}/\rho} = v_{L,exp}/v_L$), on (a) edge-length-over-height parameter (a/h), and on (b) height-over-wavelength parameter (h/λ_L); data points relating to the same h/λ_L-ratio are connected by solid lines.

see Figure 1.6 (a). The bulk velocity is reached the earlier, the higher the used frequency, i.e. the lower the wavelength of the pulses sent through the samples, see Figure 1.6 (b).

Tests on sample *set A2* (solid 'bar-like' aluminum boxes characterized by constant square-shaped cross sections with edge length of 3 mm, and by heights varying from 30 mm to 110 mm, see Table 1.5) reveal that longitudinal wave velocities increase with increasing frequency, unless they even reach, for $f = 10$ MHz and $f = 20$ MHz, the constant value of the bulk velocity of aluminum, $v_L = \sqrt{C_{1111}/\rho}$, see Figure 1.7. At frequencies below 10 MHz, the longitudinal wave velocities increase with decreasing height, i.e. with decreasing slenderness of the bar-like specimens. Only at the lower frequencies, the most slender samples are transmitted by extensional waves (also called bar waves), and only at the higher frequencies, the least slender samples are transmitted by bulk waves, see Figure 1.7 (a).

Tests on sample *set B* (solid 'plate-like' aluminum boxes characterized by constant square-shaped cross sections with edge length of 30 mm, and by heights/thicknesses varying from 0.5 mm to 30 mm, passing from plate-type to cubic shape, Table 1.5) reveal that propagation velocities are independent on height or thickness, being equal to the bulk velocity, and that they undergo large errors in case of small thicknesses in particular in combination with small frequencies (i.e. large wavelengths), see Figure 1.8. These errors are in perfect agreement with our estimation of Section 1.3.3; i.e. for small thicknesses, the precision of the ultrasonic measurement system is lost.

The aforementioned test results referring to samples *sets A1, A2, B*, and *R*, can be cast into a consistent whole, by considering the normalized longitudinal wave velocities as 'altitudes' related to locations in the plane spanned by the dimensionless variables 'edge-length-over-height (a/h)' and 'height-over-wavelength (h/λ_L)', see Figures 1.9 and 1.10. Figure 1.9 refers to a 3D representation of the function (1.35), covering a range of the dimensionless variables a/h
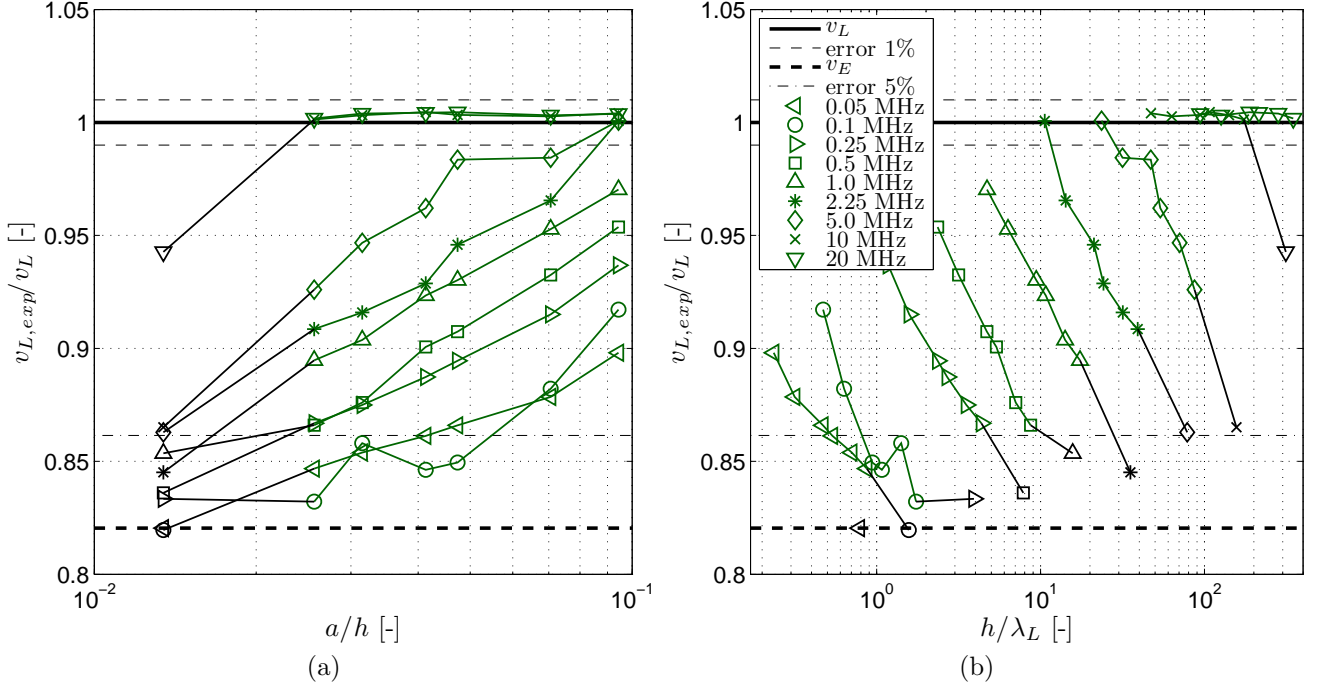
Figure 1.7: Specimen *set A2, R-1* (according to Table 1.5): Dependency of dimensionless longitudinal wave velocity ($v_{L,exp}/\sqrt{C_{1111}/\rho} = v_{L,exp}/v_L$), on (a) edge-length-over-height parameter (a/h), and on (b) height-over-wavelength parameter (h/λ_L); data points relating to the same a/λ_L-ratio are connected by solid lines — remarkably, these lines are nearly parallel, even if a changes.

and h/λ_L, over four orders of magnitude. The lowest longitudinal wave velocities, matching the extensional velocity, are reached for slender samples (small a/h) when excited through relatively long wavelengths (large h/λ_L). Shorter wavelenghts (smaller h/λ_L) seem to induce deformational constraints in the bar, being therefore transmitted by waves faster than the extensional wave. For less slender specimens (larger a/h) the bulk velocity is reached the earlier, the smaller the relative wavelengths h/λ_L, i.e. the more of the aforementioned deformational constraints are imposed onto the sample. The corresponding boundary of the 'high plateau' in Figure 1.9, related to bulk wave propagation, can be quantified by a linear relation in $\log(a/h)$ and $\log(h/\lambda_L)$, so that

$$\text{bulk wave propagation} \quad \forall \left(\frac{a}{h}\right), \left(\frac{h}{\lambda_L}\right) \quad \text{with} \quad A \log\left(\frac{a}{h}\right) + B \log\left(\frac{h}{\lambda_L}\right) \leq 1, \quad (1.36)$$

where $A = -1.426$ and $B = -0.530$ (see solid bold lines in Figures 1.9 and 1.10). The boundary for extensional wave propagation (with up to 5% error) is approximately parallel to this line (see dashed bold lines in Figures 1.9 and 1.10). Beyond that boundary when tending towards $h/\lambda_L \to 0$, $a/h \to 0$ (i.e. for bar-shaped specimens excited by low-frequency signals), the bar-shaped specimens are transmitted by extensional waves,

$$\text{extensional wave propagation} \quad \forall \left(\frac{a}{h}\right), \left(\frac{h}{\lambda_L}\right) \quad \text{with} \quad C \log\left(\frac{a}{h}\right) + D \log\left(\frac{h}{\lambda_L}\right) \geq 1,$$
$$(1.37)$$

with $C = -0.776$ and $D = -0.282$. However, it is interesting to note that bar-shaped specimens (see vertical line at $a/h \approx 0.015$ in Figure 1.10) may well be transmitted by bulk waves rather than by extensional waves. This is the case for wavelengths being smaller than the cross
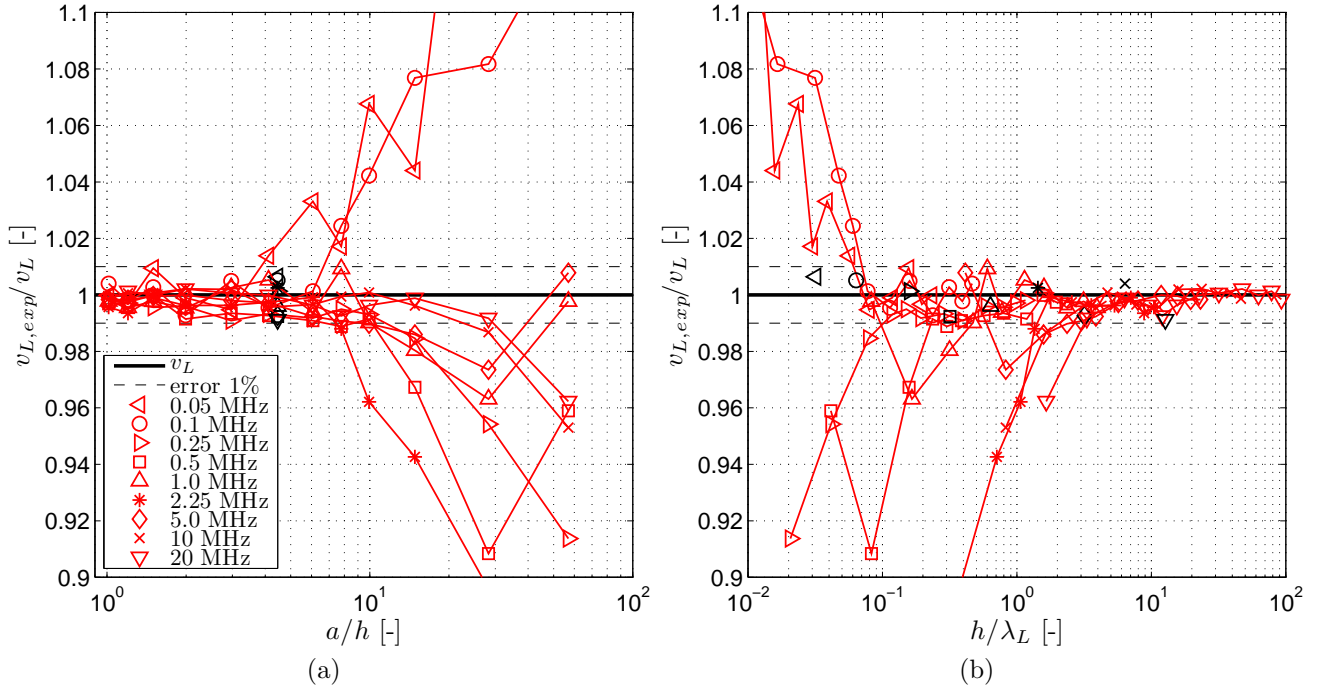
Figure 1.8: Specimen *set B, R-3* (according to Table 1.5): Dependency of dimensionless longitudinal wave velocity ($v_{L,exp}/\sqrt{C_{1111}/\rho} = v_{L,exp}/v_L$), on (a) edge-length-over-height parameter (a/h), and on (b) height-over-wavelength parameter (h/λ_L); data points relating to the same a/λ_L-ratio are connected by solid lines.

sectional length a (see $h/\lambda_L \approx 300$, $\lambda_L = 0.22\,a$, in Figure 1.10), i.e. for high frequency signals propagating through our bar-type specimens. Our finding is consistent with that of Kolsky (1964) who stated that the transition from extensional to bulk wave propagation through bar-type specimens starts at $\lambda_L \approx a$ ($h/\lambda_L \approx 100$, $a/h \approx 0.01$, in Figure 1.10). For $\lambda_L \leq a$, the stress distribution across the specimen cross section is not any more uniform. This uniformity, however, would be the prerequisite for the validity of beam theory, here in the sense of Eq. (1.18). On the other side of the 'bulk velocity plateau' in Figures 1.9 and 1.10, measurements of longitudinal waves through thin plates (large values of a/h) may become increasingly awkward and afflicted with errors, reflected by steep peaks and valleys adjacent to the 'high plateau' towards large edge-length-over-height ratios. Figures 1.9 and 1.10 also suggest cubes to be an appropriate specimen shape for bulk wave velocity determination, especially for high frequencies ($a/h = 1$, $h/\lambda_L \to \infty$, see dash-dotted line in Figures 1.9 and 1.10) when the wave is 'detecting' RVEs being much smaller than the specimen, while at low frequencies ($a/h = 1$, $h/\lambda_L \to 0$, see dash-dotted line in Figures 1.9 and 1.10) specimens and RVEs are not well separated by scale and the bulk wave plateau in Figure 1.9 becomes a little 'wavy'. The limit case $h/\lambda_L \to \infty$ is also preferable when aiming at bulk wave determination on platy specimens, see Figure 1.10 for $a/h \approx 10\text{--}100$, while, for $h/\lambda_L < 1$, measurements on platy specimens may be afflicted with large measurement errors (see Figure 1.10). This is consistent with the theoretical error propagation analysis in Section 1.3.3, Table 1.4.

The elastodynamic analogon to (1.32) for shear waves reads as

$$v_T = \sqrt{\frac{C_{1212}}{\rho}}, \tag{1.38}$$

with v_T as the ('bulk') shear wave velocity, and with C_{1212} as the shear stiffness component of
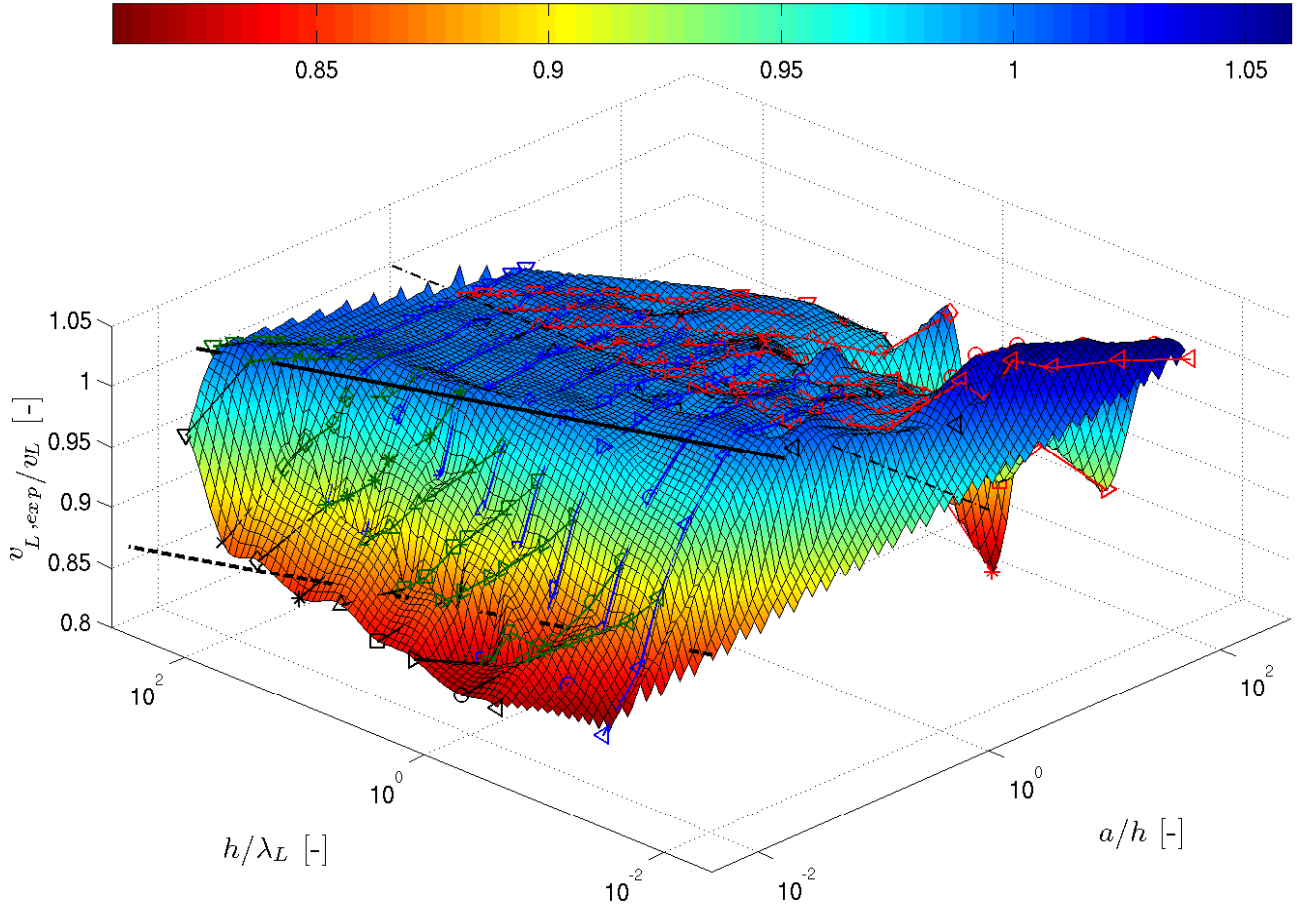
Figure 1.9: Specimen *sets A, B, R* (according to Table 1.5): Dependency of dimensionless longitudinal wave velocity ($v_{L,exp}/\sqrt{C_{1111}/\rho} = v_{L,exp}/v_L$), on specimen geometry (edge-length-over-height parameter a/h), and on wave frequency (in terms of height-over-wavelength parameter h/λ_L).

the elasticity tensor (being equal to the shear modulus G), compare $(1.15)_2$. Considerations analogous to $(1.33)-(1.35)$ yield the dimensionless shear wave velocity as

$$\frac{v_{T,exp}}{\sqrt{C_{1212}/\rho}} = \frac{v_{T,exp}}{v_T} = \mathcal{G}\left(\frac{a}{h}, \frac{h}{\lambda_T}\right) . \tag{1.39}$$

Function $\mathcal{G}$ is a 'high plateau' at altitude '1' (reflecting the fact that there do not exist 'bar-type' shear waves), and is only bounded by 'peaks' and 'valleys' related to the technical limitations of the employed measurement system (described in Section 1.3.2), see Figures 1.11 and 1.12.

1.7 Microstructure-specific wave propagation

While the last section was devoted to the case of the long-wavelength-limit, where the wavelengths are significantly larger than the material volumes [see right-hand side of Eq. (1.1)], we now discuss propagation velocities of waves spanning the entire range from wavelengths being much larger than the material volumes of porous media, via such being of the size of such porous material volumes or of the size of the microstructural entities (pores), to finally such being even smaller than the microstructural entities (pores). As described in Section 1.4, we study the microstructure 'cylindrical pores in solid (isotropic) aluminum matrix' [with hexagonal (and
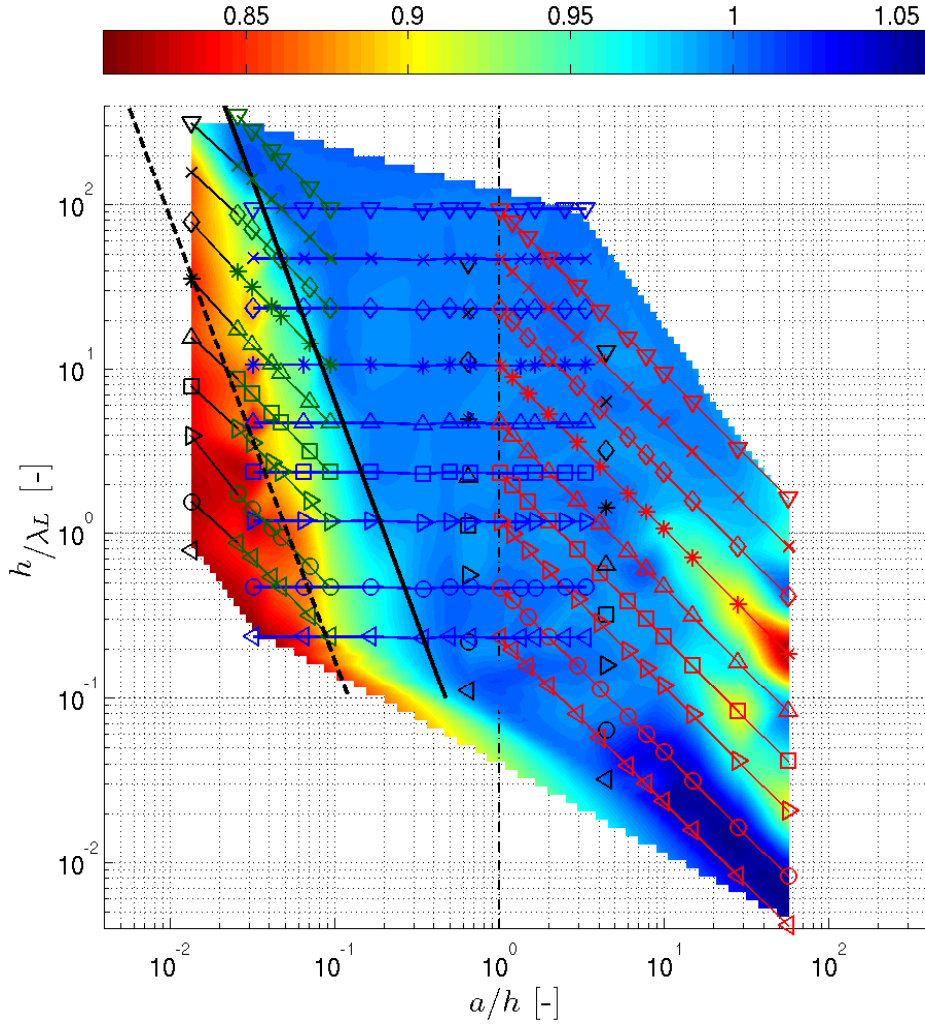
Figure 1.10: Specimen *sets A, B, R* (according to Table 1.5): Dependency of dimensionless longitudinal wave velocity $(v_{L,exp}/\sqrt{C_{1111}/\rho} = v_{L,exp}/v_L)$, on specimen geometry (edge-length-over-height parameter a/h), and on wave frequency (in terms of height-over-wavelength parameter h/λ_L) — top view.

hence transversely isotropic) instead of isotropic properties], which, according to Drugan and Willis (1996), is an extreme case where the microstructural entities start to have a discernable influence already at relatively large wavelengths. Accordingly, Eq. (1.35) now refers to very small waves traveling directly through the isotropic aluminum matrix, without interference with the cylindrical pores. However, the experimentally determined velocities are now functions of two additional arguments, pore diameter d and porosity φ, so that the dimensionless function (1.35) needs to be extended to the format

$$\frac{v_{L,exp}}{v_L} = \mathcal{H}\left(\frac{a}{\lambda_L},\ \frac{h}{\lambda_L},\ \frac{d}{\lambda_L},\ \varphi\right). \tag{1.40}$$

In order to keep the discussions in a tractable size, we now consider only ranges where our previous study on sample sizes did not suggest influences of a/h and h/λ_L on v_{exp}/v_L, i.e. we restrict ourselves to the 'high plateau'-regions of Figures 1.9 and 1.10. In other words, we study microstructure-specific wave propagation, independent of sample geometry-specific wave propagation. Accordingly, we consider the dimensionless functions

$$\frac{v_{L,exp}}{\sqrt{C_{1111}/\rho}} = \frac{v_{L,exp}}{v_L} = \mathcal{I}\left(\frac{d}{\lambda_L},\ \varphi\right) \quad \text{and} \quad \frac{v_{T,exp}}{\sqrt{C_{1212}/\rho}} = \frac{v_{T,exp}}{v_T} = \mathcal{J}\left(\frac{d}{\lambda_T},\ \varphi\right), \tag{1.41}$$
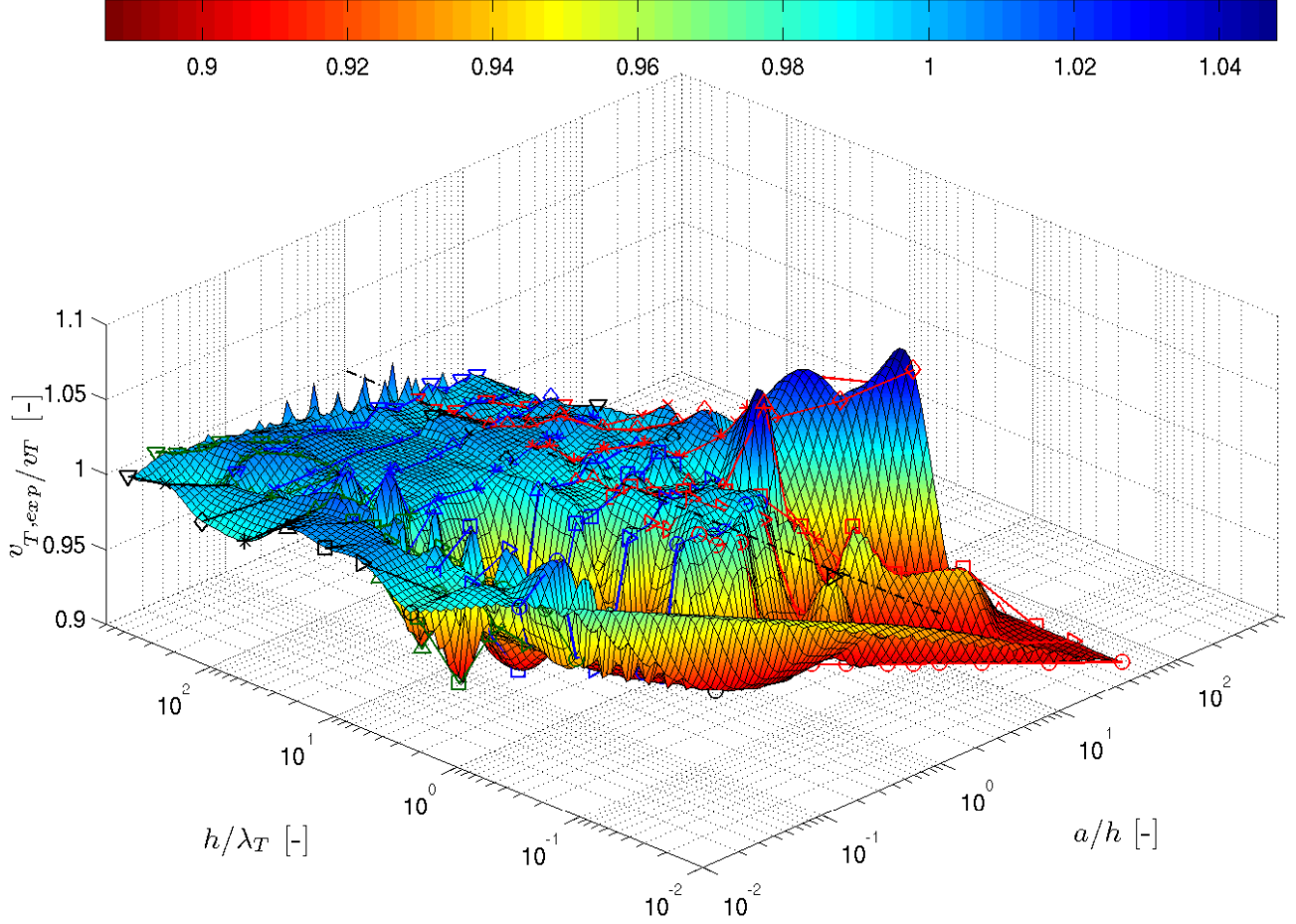
Figure 1.11: Specimen *sets A, B, R* (according to Table 1.5): Dependency of dimensionless transversal wave velocity ($v_{T,exp}/\sqrt{C_{1212}/\rho} = v_{T,exp}/v_T$), on specimen geometry (edge-length-over-height parameter a/h), and on wave frequency (in terms of height-over-wavelength parameter h/λ_T).

where $(1.41)_2$ relates to transversal waves through specimens which do not evoke measurement errors (see 'high plateau'-regions in Figures 1.11 and 1.12). In order to elucidate the features of $\mathcal{I}$ and $\mathcal{J}$, we evaluate the test results of sample *set C* (mainly cubic samples with cylindrical pores in different configurations, defined in Figure 1.4 (b) and Table 1.6). Because of the transversely isotropic nature of the specimen with the principle material directions 1, 2, and 3 (see Figure 1.4), functions $\mathcal{I}$ and $\mathcal{J}$ additionally depend on the propagation direction. Accordingly, we discuss in the following three functions $\mathcal{I}$, $\mathcal{I}_1$, $\mathcal{I}_2$, $\mathcal{I}_3$, related to longitudinal wave propagation velocities $v_{1,1,exp}$, $v_{2,2,exp}$, and $v_{3,3,exp}$, respectively (the repeated index indicates coincidence of the propagation and polarization directions in longitudinal waves), and six functions $\mathcal{J}$, $\mathcal{J}_{i,j}$, $i \neq j$, $i,j = 1, 2, 3$, related to transversal wave velocities $v_{i,j,exp}$ with propagation direction i and polarization direction j, $i \neq j$. 3D representations of functions $\mathcal{I}_1$ [see Figure 1.13 (a); velocity referring to longitudinal normal stiffness], average of $\mathcal{I}_2$ and $\mathcal{I}_3$ [see Figure 1.13 (b); velocities referring to (transverse) normal stiffness in isotropic plane], average of functions $\mathcal{J}_{1,3}$, $\mathcal{J}_{3,1}$, $\mathcal{J}_{2,3}$, and $\mathcal{J}_{3,2}$ [see Figure 1.14 (a); velocities referring to longitudinal shear stiffness], and average of functions $\mathcal{J}_{1,2}$, $\mathcal{J}_{2,1}$ [see Figure 1.14 (b); velocities referring to (transverse) shear stiffness in the isotropic plane] show the dependency of the bulk wave velocity on both the porosity φ and the pore-diameter-over-wavelength parameter d/λ_i.

Generally, longitudinal wave velocities increase with increasing pore diameter-over-wavelength ratio d/λ_L, with two limit cases:
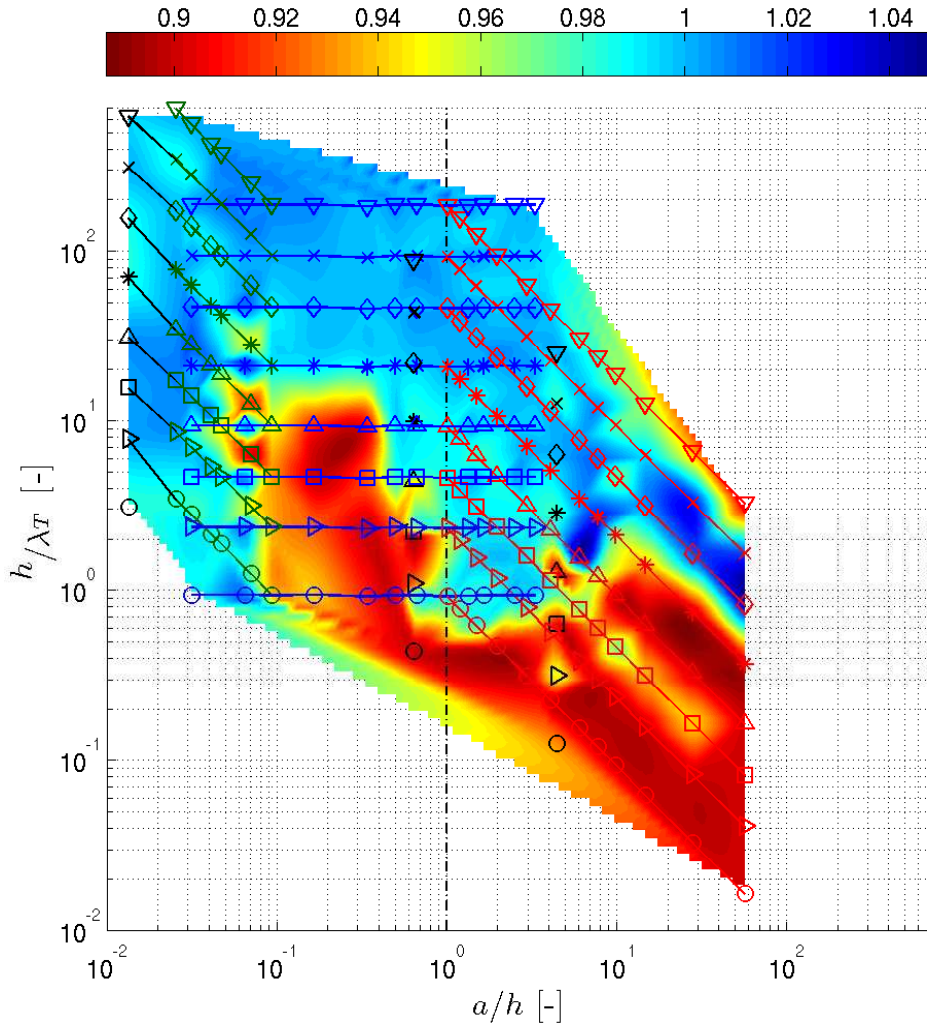
Figure 1.12: Specimen *sets A, B, R* (according to Table 1.5): Dependency of dimensionless transversal wave velocity ($v_{T,exp}/\sqrt{C_{1212}/\rho} = v_{T,exp}/v_T$), on specimen geometry (edge-length-over-height parameter a/h), and on wave frequency (in terms of height-over-wavelength parameter h/λ_T) — top view.

1. For large values of this ratio d/λ_L, the longitudinal waves travelling in the cylindrical pore direction reach the bulk velocity related to pure aluminium alloy [see Figure 1.15 (a)]; in other words, the waves [with wavelengths shorter than the pore diameters, i.e. for $d/\lambda_L \approx 2$ at higher porosities, but even for $d/\lambda_L \approx 0.04$ at low porosities] propagate through the solid aluminium matrix, while not interacting with the cylindrical pores [see Figure 1.15 (a)]. This is also true for the longitudinal waves travelling perpendicular to the cylindrical pore direction, within the specimens which exhibit the lower porosity [see lines labeled by circles and squares in Figures 1.15 (b) (c) (d)]. At higher porosities, the latter waves have to circumvent the pores, resulting in a more tortuous path through the solid aluminium matrix — this leads to longer times of flight and to a lower velocity measured along the shortest distance between the opposite faces of the considered specimen [see lines labeled by diamonds and triangles in Figures 1.15 (b) (c) (d)]. This tortuosity effect is more pronounced in the direction 2 (characterized by a zig-zag-type positioning of pores) than in the direction 1 [where straight (but only very thin) wall paths exist between the specimen faces, which, inspite of their straightness, cannot provide a tortuosity-free propagation of longitudinal waves, see Figure 1.4 (a) and compare Figures 1.15 (d) and (c)]. The tortuosity effect may be also enhanced by diffusive wave scattering and/or geometry-induced attenuation.
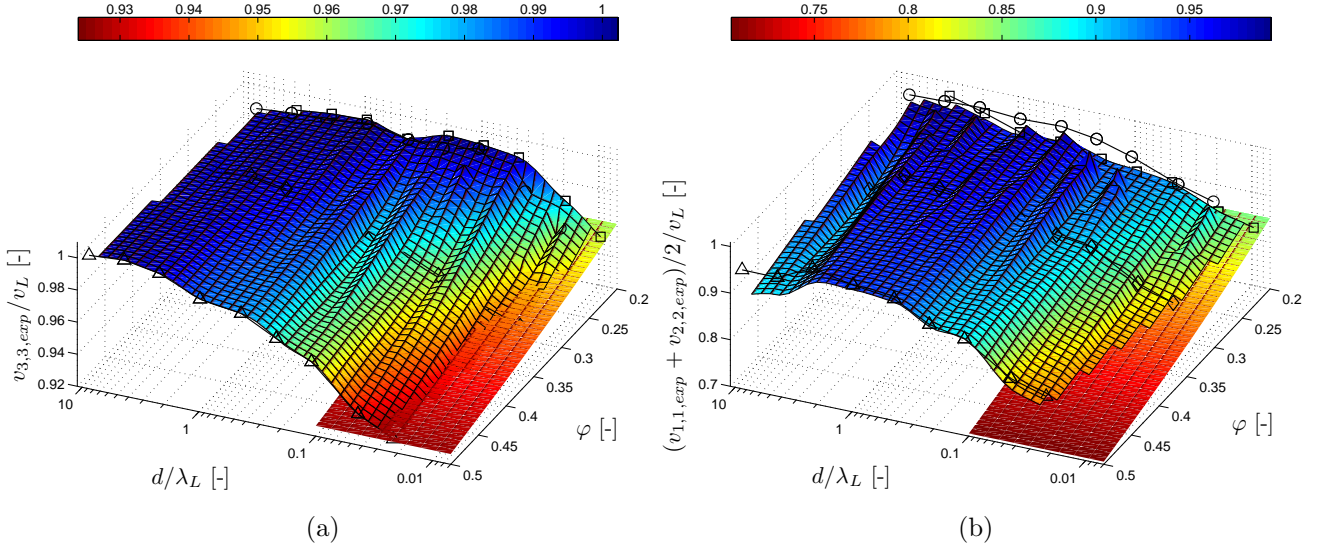
Figure 1.13: Dependency of normalized longitudinal ultrasonic velocities in transversal isotropic media in (a) longitudinal $[v_{1,1,exp}/v_L]$ and (b) transverse $[(v_{2,2,exp} + v_{3,3,exp})/2/v_L]$ direction on d/λ_L and φ [model predictions according to Hashin and Rosen (1964) and Hlavacek (1975), respectively, shown for reference in (a) and (b), respectively (surfaces without gridlines); for details see Section 1.8 and the Appendix].

2. For small values of d/λ_L, the waves reach the bulk velocity related to the porous media through which they travel. These bulk velocities can be reasonably predicted by random homogenization theory (continuum micromechanics), corresponding predictions are indicated in Figure 1.15 (while we refer to the next section for mathematical expressions related to different micromechanical models). This good predictability shows that the
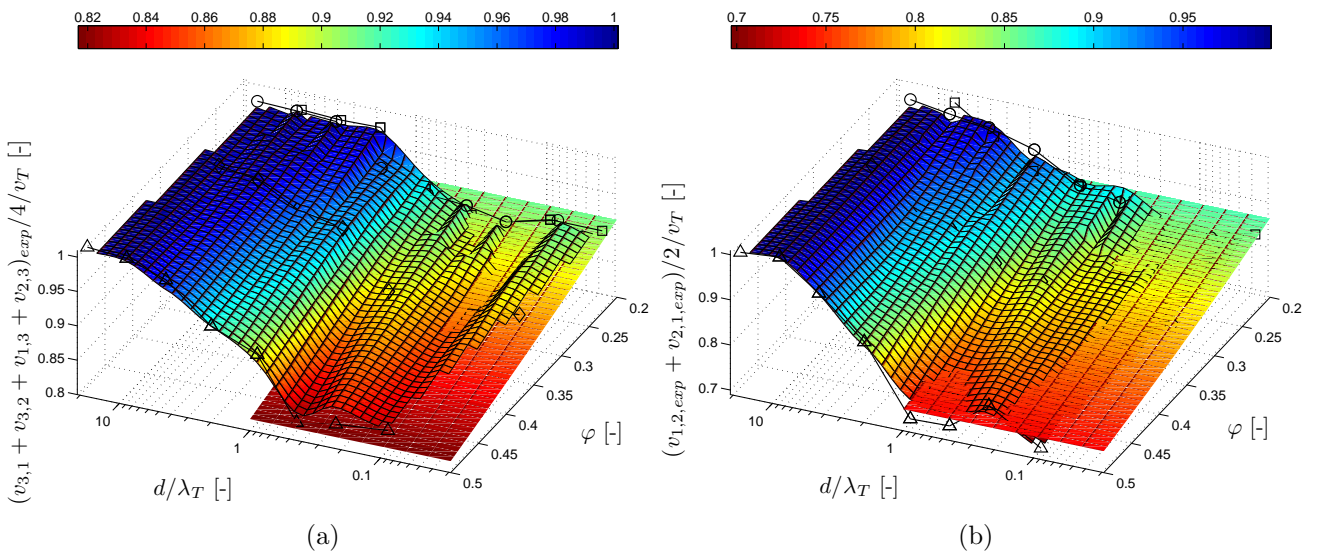
Figure 1.14: Dependency of normalized transversal ultrasonic velocities in transversal isotropic media in (a) longitudinal $[(v_{3,1,exp} + v_{3,2,exp} + v_{1,3,exp} + v_{2,3,exp})/4/v_T]$ and (b) transverse $[(v_{1,2,exp}+v_{2,1,exp})/2/v_T]$ direction on d/λ_T and φ [predictions of Mori-Tanaka-type model shown for reference (surfaces without gridlines); for details see Section 1.8 and the Appendix].

waves (with wavelengths being considerably larger than the pore diameter, i.e. tending towards the long-wavelength-limit) 'feel' the entire porous medium, consisting of both the solid aluminium matrix and the cylindrical air pores. In accordance with theoretical micromechanics, the bulk velocities through the considered specimens are the smaller the higher the porosity, and they are smaller in the transversely isotropic directions than in the anisotropic direction (that of the cylindrical pores). Still, it should be noted that for constant pore diameter d and constant frequency f, λ_L is smaller in the transverse directions (due to lower propagation velocities in these directions). At higher porosities, this smaller λ_L may not feel any more the porous medium in the sense of theoretical micromechanics, see Figure 1.15 (b) (c) (d), for $\varphi = 48.7\%$. Also, the implication of hexagonal microstructures exhibiting transversely isotropic material behaviour (Helbig 1994), i.e. $v_{2,2} = v_{3,3}$ in Figures 1.15 (c) (d), is experimentally reflected only at sufficiently large wavelengths. Otherwise, the continuous straight paths between the pores, oriented in direction 1 (see Figure 1.4), lead to overestimation of the effective porous medium-related longitudinal wave velocity.
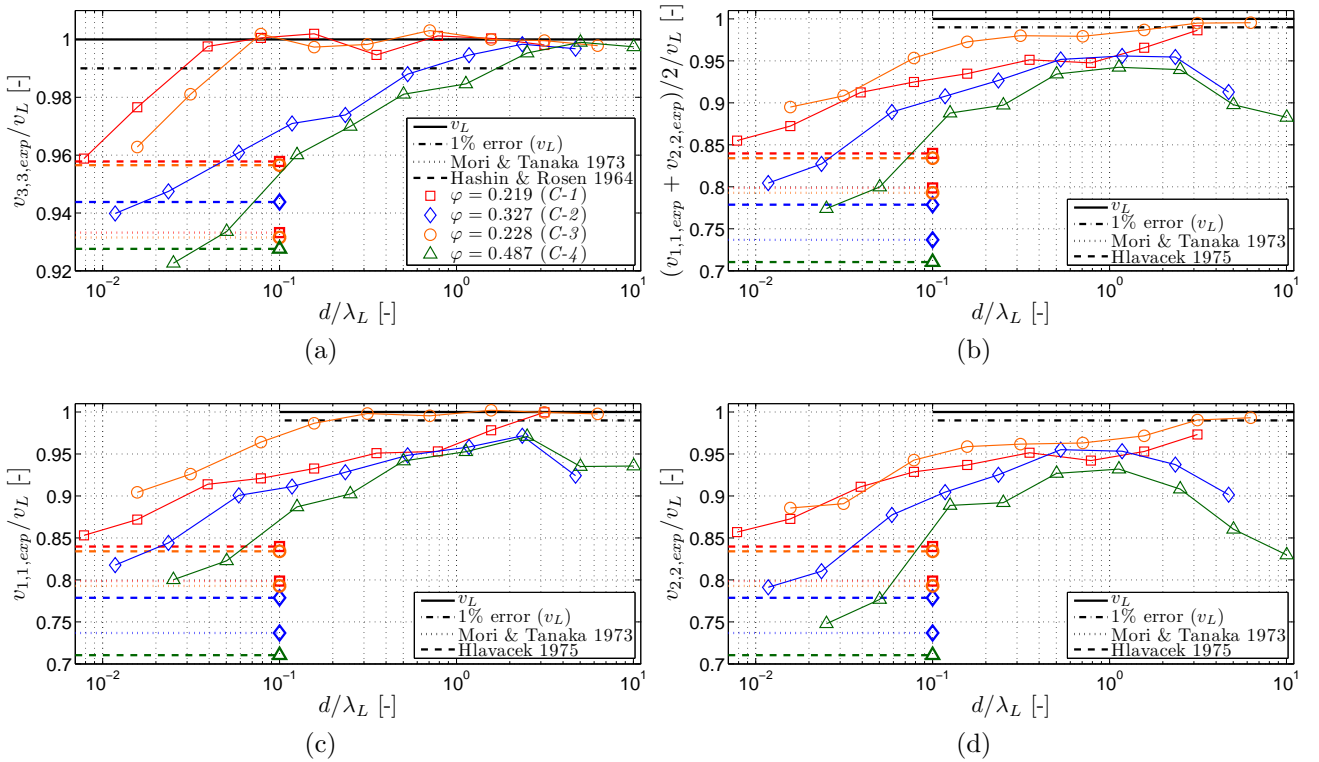
Figure 1.15: Specimen *set C* (transversely isotropic, porous specimens): Influence of pore diameter-over-wavelength ratio (d/λ_L), on longitudinal dimensionless wave velocities in (a) anisotropic direction 3 (orientation of cylindrical pores), $v_{3,3,exp}$, and in (b, c, d) directions within isotropic plane, $v_{1,1,exp}$, $v_{2,2,exp}$, $(v_{1,1,exp} + v_{2,2,exp})/2$ (for definition of directions 1 and 2, see Figure 1.4; micromechanical models are detailed in Section 1.8 and the Appendix).

Similar trends are observed for transversal waves travelling through the porous specimens of *set C* (see Figure 1.16). However, two major differences with respect to the longitudinal waves are noted: (i) the 'tortuosity effect' for short wavelengths is negligible, so that all waves reach, for large d/λ_T, the shear wave velocity related to the aluminum matrix (see Figure 1.16), (ii) for diminishing d/λ_T below 1, the effective (long-wavelength-limit-related) transversal velocities related to the porous medium are reached significantly faster than it is the case for longitudinal waves. This effect is particulary characteristic for transversal velocities in the cylindrical pore direction, $v_{3,1}$ and $v_{1,3}$ [see Figure 1.16 (a) (b)]. For small d/λ_T, when the separation-of-scales
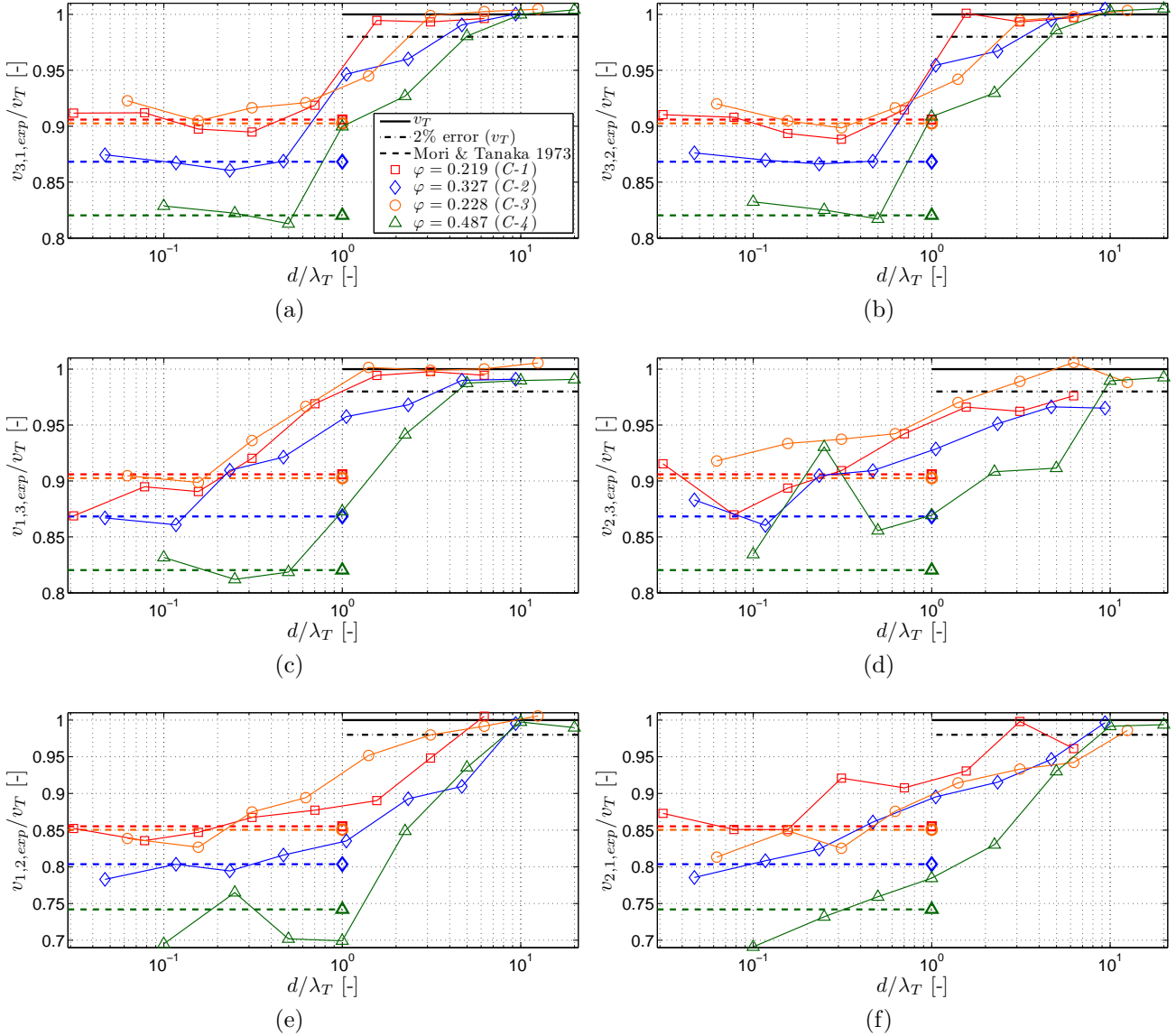
Figure 1.16: Specimen *set C* (transversely isotropic, porous specimens): Influence of pore diameter-over-wavelength ratio (d/λ_T), on transversal dimensionless wave velocities in (a, b) anisotropic direction 3 (orientation of cylindrical pores), $v_{3,1,exp}$ and $v_{3,2,exp}$, in propagation directions within the isotropic plane with (c, d) polarization directions perpendicular to this plane, $v_{1,3,exp}$ and $v_{2,3,exp}$, and with (e, f) polarization directions within this plane, $v_{1,2,exp}$ and $v_{2,1,exp}$, (for definition of directions 1 and 2, see Figure 1.4; micromechanical models are detailed in Section 1.8 and the Appendix).

requirement (1.1) is fulfilled, the experimental measurements show the theoretically expected symmetries $v_{1,3} = v_{3,1} = v_{2,3} = v_{3,2}$ and $v_{1,2} = v_{2,1}$ (Figure 1.16). When leaving this limit, wave propagation is less influenced by a change of polarization direction only [compare Figures 1.16 (a) and (b)], as compared to a change in both polarization and propagation directions [compare Figures 1.16 (a) and (c) as well as Figures 1.16 (b) and (d)].

1.8 Waves characterizing representative material volumes — comparison to theoretical micromechanics

For small d/λ, the separation-of-scales requirement (1.1) is fulfilled and the ultrasonic waves characterize a representative volume element of the transversely isotropic porous aluminum material of specimen *set C*. It is instructive to compare these experimental results (Figures 1.13 to 1.16) to mathematical models from the micromechanics field, as to elucidate the relevance of both the employed experimental technique and the theories developed over half a century. For this purpose we have evaluated the theoretical predictions of four different mathematical models relating pore morphology and volume fraction to elastic stiffness tensors of the investigated porous materials (which are related, via (1.12), (1.13), and (1.14), to the long-wavelength-limit-related propagation velocities $v_{i,j}$, i, $j = 1, 2, 3$): (i) Hashin & Rosen's 1964 variational method for effective elastic properties of a (isotropic) solid matrix perforated by randomly distributed cylindrical pores (Hashin and Rosen 1964), (ii) Hlavacek's 1975 Hamilton's principle-based method for effective elastic properties of a (isotropic) solid matrix perforated by hexagonally arranged pores (Hlavacek 1975), (iii) Eshelby (1957) problem-based, Mori-Tanaka-type estimation of effective elastic properties of a solid matrix with randomly distributed pores, in the context or random homogenization theory (mean field homogenization) or continuum micromechanics (Mori and Tanaka 1973; Benveniste 1987; Zaoui 2002), and (iv) the unit cell method for effective elastic properties of periodic media (Suquet 1987; Böhm 2004; Li 2000), applied to an array of periodically arranged cylindrical pores in a solid matrix. Details on these micromechanical models can be found in Appendix 1.10. For discussion of these models with
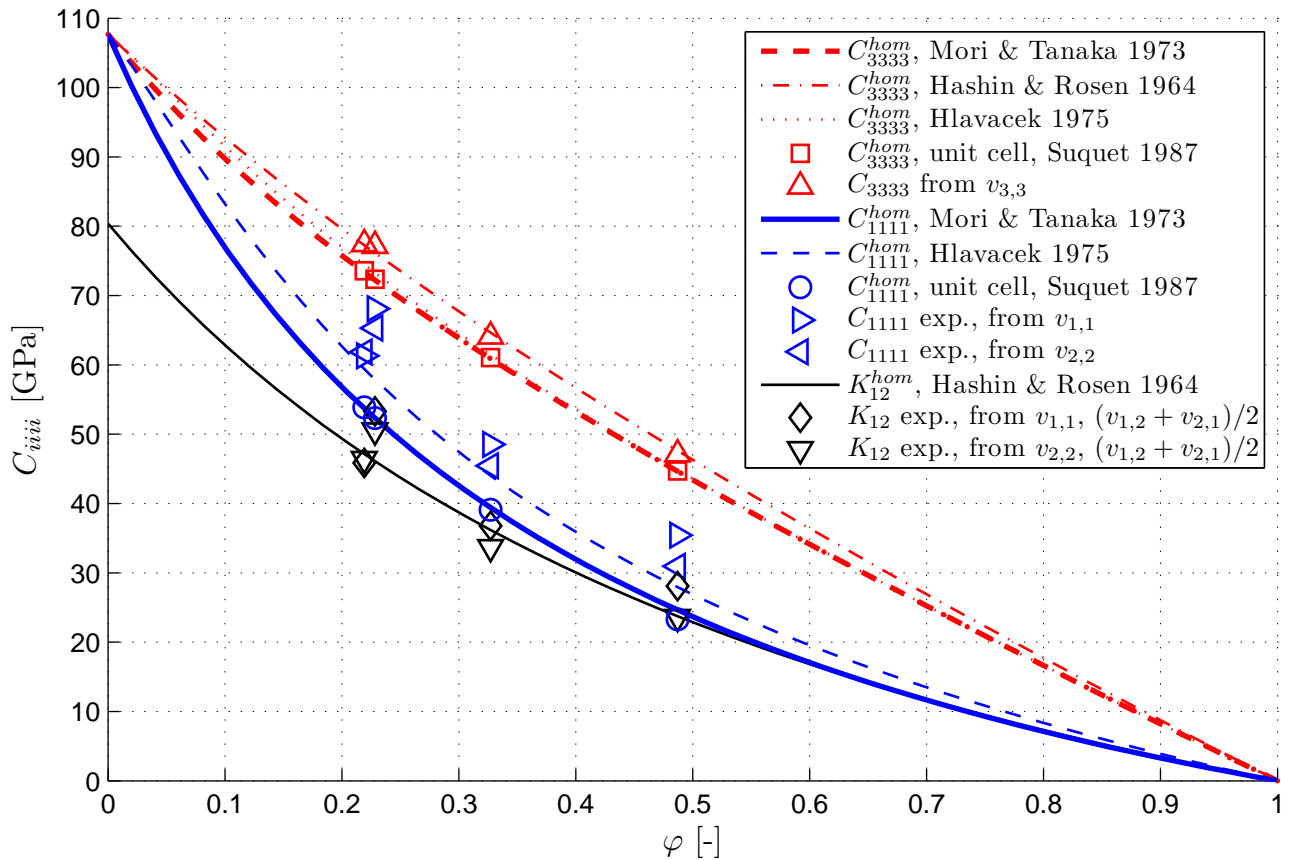
Figure 1.17: Normal stiffness tensor components (C_{3333}, $C_{1111} = C_{2222}$) as function of volume fraction of pores φ — comparison of ultrasonic measurements ($f = 50$ kHz) with hexagonal array models [Hlavacek (1975) and unit cell according to Figure 1.4 (c)] and random array models (Hashin and Rosen 1964; Mori and Tanaka 1973).

respect to our experiments, we employ the following error measures

$$\delta = \frac{1}{k}\sum_{n=1}^{k} \frac{C_{ijij}^{hom}(n) - C_{ijij}^{exp}(n)}{C_{ijij}^{exp}(n)} = \frac{1}{k}\sum_{n=1}^{k} \delta_n \quad \text{and} \quad s = \sqrt{\frac{1}{k-1}\sum_{n=1}^{k}(\delta_n - \delta)^2} \qquad (1.42)$$

where $k = 4$ for C_{3333} and C_{1212}, $k = 8$ for C_{1111} and C_{1313}, δ_n is the relative error of each model stiffness prediction, and δ and s are the mean and standard deviations of these errors, respectively.
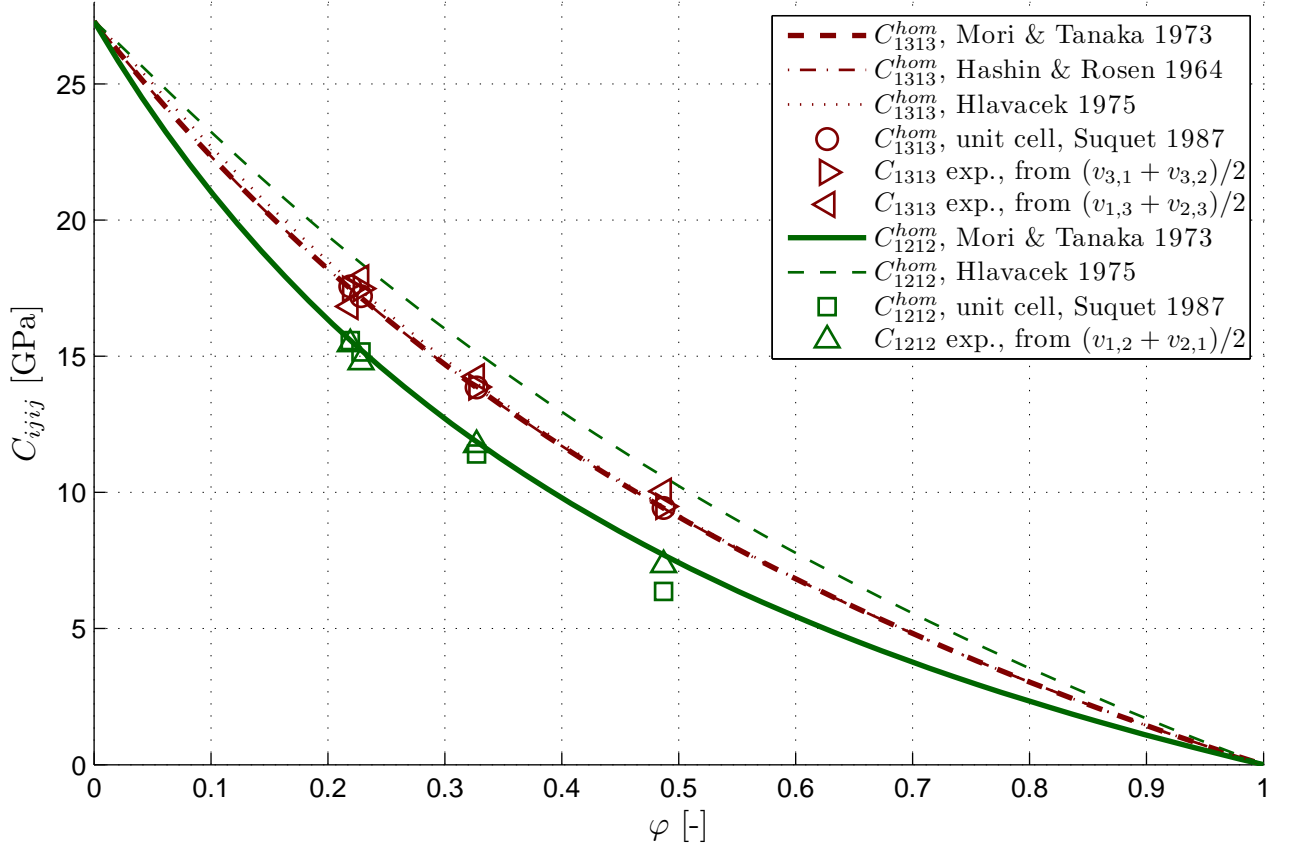
Figure 1.18: Shear stiffness tensor components ($C_{1313} = C_{2323}$, C_{1212}) as function of volume fraction of pores φ — comparison of ultrasonic measurements (average of results from $f = 100$, 250, and 500 kHz were used) with hexagonal array models [Hlavacek (1975) and unit cell according to Figure 1.4 (c)] and random array models (Hashin and Rosen 1964; Mori and Tanaka 1973).

As regards normal stiffnesses (Figure 1.17), the experimental values for the longitudinal stiffness component C_{3333} agrees almost perfectly with Hashin and Rosen's micromechanical estimates (relative error of $0.1 \pm 1.1\%$, see thin dash-dotted line and upright triangular marker in Figure 1.17), while these values lie slightly above the micromechanical predictions of the Hlavacek model, the Mori-Tanaka-type random homogenization result, and our unit cell approach (relative errors of $-4.5 \pm 0.6\%$, $-5.5 \pm 0.6\%$, and $-5.3 \pm 0.7\%$, respectively; see thin dotted and thick dashed lines, as well as square and upright triangular markers in Figure 1.17), and they are larger for the tests in specimen *C-3* (with $\varphi = 22.8\%$ and larger pores) than for *C-1* (with $\varphi = 21.9\%$ and smaller pores). The latter observation reflects the effectively larger RVE of *C-3*, when compared to that of *C-1*. The experimental values for the transverse normal stiffness component C_{1111} lie slightly above the predictions of the Hlavacek model (relative error of $-9.6 \pm 6.3\%$, see thin dashed line and horizontal triangles in Figure 1.17), and are even more distant from the Mori-Tanaka-type and unit cell predictions (relative errors of $-18.9 \pm 6.1\%$

and $-20.0 \pm 7.4\%$, respectively; see thick solid line, as well as circular and horizontal triangular markers in Figure 1.17). The aforementioned deviations between experimental values and micromechanical model predictions are the more pronounced the higher the porosity of the investigated specimens. The experimental values for the plane strain bulk modulus in the isotropic transverse plane, $K_{12} = C_{1111} - C_{1212}$, almost perfectly agree with Hashin and Rosen's micromechanical estimates (relative error of $-3.4 \pm 8.2\%$, see thin solid line and diamond as well as upside-down triangle markers in Figure 1.17).

As regards shear stiffnesses (Figure 1.18), the experimental values for the longitudinal shear stiffness component C_{1313} agree almost perfectly with the Mori-Tanaka-type micromechanical estimates (relative error of $-1.5 \pm 3.0\%$, see thick dashed line and horizontal triangular markers in Figure 1.18), as well as with those of our unit cell models (relative error $-1.3 \pm 3.1\%$, see circular and horizontal triangular markers in Figure 1.18), with those of Hlavacek's 1975 model (relative error of $-0.2 \pm 3.3\%$, see thin dotted line and horizontal triangular markers in Figure 1.18), and with those of Hashin and Rosen's 1964 model (relative error of $-1.5 \pm 3.0\%$, see thin dash-dotted line and horizontal triangular markers in Figure 1.18). The experimental values for the transverse inplane shear stiffness C_{1212} agree almost perfectly with the Mori-Tanaka-type stiffness estimate (relative error of $2.5 \pm 2.0\%$, see thick solid line and upright triangular markers in Figure 1.18), and almost as well with the predictions from our unit cell approach (relative error of $-3.2 \pm 7.1\%$, see square and upright triangular markers in Figure 1.18), while Hlavacek's 1975 model grossly overestimates the experimentally determined shear stiffnesses (relative error of $29.7 \pm 10.1\%$, see thin dashed line and upright triangular markers in Figure 1.18).

1.9   Discussion and conclusion

Our experimental and theoretical results allow for a number of conclusions:

– concerning measurement errors: Ultrasonic measurements are a very precise means to determine diagonal (normal and shear) stiffness components, while they give (by a factor of two) less precise values for off-diagonal (Poisson-effect-related) stiffness components (Section 1.5). Ultrasonic measurements are satisfactorily precise on bar-type, cubic and thick plate-type specimens, while they may exhibit large measurement erros on thin plates, especially at low frequencies (Section 1.5 and 1.6).

– concerning specimen shape (extensional-bulk-wave transition): Bar-shaped specimens with slenderness ratio larger than ten excited by low-frequency signals transmit (1D) extensional or bar waves, whereby the specimen needs to be the more slender the higher the signal frequency to be transmitted as extensional wave. Beyond a quite narrow extensional-bulk-wave transition regime, less slender bar-type specimens excited by higher frequency signals transmit (3D) bulk waves whereby specimens need to be the less slender the lower the frequency to be transmitted as bulk waves. All non-slender bar-, cube-, and plate-shaped specimens are transmitted by bulk waves. Transversal wave propagation is not affected by specimen shape, except for measurement errors (Section 1.6).

– concerning porosity: For porous non-slender specimens, the wave propagation type depends on the 'pore-diameter-over-wavelength' ratio and on the porosity. Cube-shaped porous specimens excited by low frequency signals transmit bulk waves relating to the effective porous medium (long-wavelength-limit), whereby the specimen needs to be the more porous, the higher the frequency to be transmitted as effective wave 'feeling' the porous medium. Beyond a long-to-short wavelength transition period, the size of which

is comparable to transition regions in other (two-phase) materials (Mason and McSkimin 1948; Kinra and Anand 1982; Stanke and Kino 1984; Gubernatis and Domany 1984) and which is increasing with increasing porosity and with decreasing direction-dependent wave propagation velocity, cube-shaped porous specimens excited by higher frequencies transmit bulk waves relating to the solid aluminum matrix (short-wavelength-limit). Thereby, specimens need to be the less porous, the lower the frequencies to be transmitted as waves 'feeling' the solid matrix (Section 1.7).

– concerning micromechanic predictions: Long-limit wave velocities and stiffnesses in transversal isotropic porous media are well predicited by the Mori-Tanaka, Hashin-Rosen, and unit cell micromechanical methods. This is particularly true for shear stiffnesses, for normal stiffnesses in cylindrical pore direction, and for plain strain bulk moduli. While experimentally determined normal stiffnesses perpendicular to the cylindrical pore direction are better predicted by Hlavacek's micromechanical model (Section 1.8).

Acknowledgments

1.10   Appendix: Micromechanics models — background

1.10.1   Variational method for effective elastic properties of a solid matrix perforated by randomly distributed parallel cylindrical pores — Hashin and Rosen (1964)

Hashin and Rosen (1964) aim at estimating the elastic behaviour of a porous material consisting of a solid matrix perforated by parallel, randomly distributed, coated cylindrical pores — which we here specialize for non-coated pores. Therefore, a representative volume element of such a porous material is considered, and subjected to homogeneous boundary conditions, be it in terms of macroscopic stresses or strains. In order to estimate the elastic response of such an RVE to these boundary conditions, single cylinders ('composite cylinders') consisting of a cylindrical pore and surrounding material are subjected to homogeneous stress boundary conditions [this leads to a lower bound for the effective (homogenized) stiffness], and to homogeneous strain boundary conditions [this leads to an upper bound for the effective (homogenized) stiffness]. In case of a random arrangement of pores, the entire material space is filled up with the composite cylinders, so that the upper and the lower bounds coincide. Then, the effective (homogenized) Young's modulus E_3^{hom} and the plain strain bulk modulus in the isotropic transverse plane $K_{12}^{hom} = C_{1111}^{hom} - C_{1212}^{hom}$ are given as

$$E_3^{hom} = E\,(1 - \varphi) \quad \text{and} \quad K_{12}^{hom} = (C_{1111} - C_{1212})\frac{2\,\nu\,(1 - \varphi)}{2\,\nu + \varphi}, \tag{1.43}$$

respectively, where E, ν, C_{1111}, and C_{1212} are the elastic constants of the isotropic matrix (in our case aluminum alloy, see Table 1.7), and φ denotes the porosity (see Table 1.6). The corresponding longitudinal (normal and shear) stiffness components, C_{3333}^{hom} and $C_{1313}^{hom} = C_{2323}^{hom}$ read as

$$C_{3333}^{hom} = E_3^{hom} + 4\,\nu^2\,K_{12}^{hom} \quad \text{and} \quad C_{1313}^{hom} = C_{1212}\,\frac{1-\varphi}{1+\varphi}. \tag{1.44}$$

1.10.2 Hamilton's principle-based method for effective elastic properties of a solid matrix perforated by hexagonally arranged, parallel cylindrical pores — Hlavacek (1975)

Hlavacek (1975) developed an effective stiffness theory for a hexagonal array of (isotropic) cylindrical inclusions embedded in a (isotropic) matrix (which we here specialize for pore inclusions), by assuming specific (continous) displacement distributions within the composite, and by relating them to some 'gross-displacements', which, via Hamilton's principle in combination with the elastic and mass properties of the solid matrix and with the porosity, gives access to phase velocities of waves propagating in the lowest mode through the porous medium. Comparing these expressions for the phase velocities with those obtained from elastodynamics of the homogenized medium, yields the effective (homogenized) elastic properties of the porous medium as

$$C_{1111}^{hom} = \Big(q + p\,(3\,q + 1)$$

$$- p^2\,\frac{2\,p\,q\,(3\,q+1)\,(q+1) - \varphi\,(3\,q+1)\,(q-1) - \varphi\,q\,(q+1)^2}{[p\,(q+1) - \varphi]\,[2\,p\,q - \varphi\,(q-1)]} \Big)\,C_{1212}, \tag{1.45}$$

$$C_{3333}^{hom} = \Big(q\,(1-\varphi) - \frac{\varphi^2\,r^2}{2\,p\,q - \varphi\,(q-1)} \Big)\,C_{1212}, \tag{1.46}$$

$$C_{1212}^{hom} = \Big(1 + p\,(q+1) - \frac{p^2\,(q+1)^2}{p\,(q+1) - \varphi} \Big)\,C_{1212}, \tag{1.47}$$

$$C_{1313}^{hom} = \Big(\frac{4\,p - \varphi\,(4\,p+1)}{4\,p - \varphi} \Big)\,C_{1212}, \tag{1.48}$$

with the abbreviations p, q, and r being defined as

$$p = -\frac{\varphi\,\log(\varphi)}{8\,(1-\sqrt{\varphi})^2}, \qquad q = 2\,\frac{1-\nu}{1-2\,\nu}, \quad \text{and} \quad r = 2\,\frac{\nu}{1-2\,\nu}. \tag{1.49}$$

1.10.3 Mean-field homogenization method (Mori-Tanaka estimate) for effective elastic properties of a solid matrix perforated by randomly distributed, parallel cylindrical pores — Eshelby (1957); Mori and Tanaka (1973); Benveniste (1987)

A representative volume element (RVE) of the above mentioned porous material is considered, and subjected to homogeneous boundary conditions, be it in terms of macroscopic stresses or strains. These boundary conditions imply that the spatial average of the equilibrated microstresses within the RVE are equal to the homogeneous (macroscopic) strains (strain average rule), and the spatial average of the kinematically admissible microstrains within the RVE are equal to the homogeneous (macroscopic) stresses (stress average rule). Then, the strain

average rule is combined with Eshelby's 1957 matrix inclusion problem relating the strains in a cylindrical pore to those subjected to the remote boundary of an infinite matrix surrounding this pore, yielding relations between the remote auxiliary strains and the macroscopic, RVE-related strains. The resulting concentration relations between RVE-related homogeneous strains and pore and matrix strains, together with the stress average rule, give finally access to the homogenized elastic properties, in the form (Zaoui 2002)

$$\mathbb{C}^{hom} = (1 - \varphi)\, \mathbb{C} : \left[(1 - \varphi)\, \mathbb{I} + \varphi\, \left[\mathbb{I} - \mathbb{P}_{cyl} : \mathbb{C} \right]^{-1} \right]^{-1} , \qquad (1.50)$$

where $\mathbb{I}$, $I_{ijkl} = (\delta_{ik}\,\delta_{jl} + \delta_{il}\delta_{jk})$, is the fourth-order unity tensor, and where $\mathbb{P}_{cyl}$ is a fourth-order (symmetric) tensor depending on the shape of cylindrical inclusions and on the stiffness tensor $\mathbb{C}$ of the (herein isotropic) matrix (components see Table 1.7, column two). The non-zero tensor components of $\mathbb{P}_{cyl}$ read as [see e.g. Hellmich et al. (2004)]

$$\begin{aligned} P_{1111} = P_{2222} &= P\,(5\,C_{1111} - 3\,C_{1122}), & P_{1122} &= -P\,(C_{1111} + C_{1122}), \\ P_{1313} = P_{2323} &= 2\,P\,C_{1111}, & \text{and}\quad P_{1212} &= P\,(3\,C_{1111} - C_{1122}), \end{aligned} \qquad (1.51)$$

with $P = 1/(8\,C_{1111}\,(C_{1111} - C_{1122}))$.

1.10.4 Unit cell method for effective elastic properties of a solid matrix perforated by hexagonally arranged, parallel cylindrical pores

The unit cell is subjected to periodic (symmetric or antisymmetric) boundary conditions for the displacements (Böhm 2004), such that the spatial averages of the corresponding strains are equal to the macroscopic strains related to the porous material. Linking these macroscopic strains to the spatial average of the periodic microstresses they provoke, i.e. to the macroscopic stresses, yields the homogenized effective stiffness of the porous material. In detail, four independent displacement configurations are imposed on the boundary of the unit cell to provoke unit values of macroscopic strain components. More specifically, the spatial averages of the corresponding periodic (normal and shear) microstresses are equal to the components of the homogenized stiffness tensor of the porous material.

Four finite element models of unit cells (consisting of 6550, 8690, 13104, and 19750 eight-node linear brick elements, respectively) were built in ABAQUS according to Figure 1.4 (c) [see Table 1.6 and Eq. (1.30) for pore-diameter-over-pore-distance ratios d/e related to different porosities], in order to represent the microstructure of the specimens making up *set C*. No significant changes in elastic stiffnesses were observed when (almost 200000) elements half the size of the aforementioned elements were used for representation of specimen *C-4*, so that the numerical results indicated by circles and squares in Figures 1.17 and 1.18 can be considered as converged in the sense of a sufficiently fine Finite Element discretization (Zienkiewicz and Taylor 2000).

Publication 2

Determination of Poisson's ratios in isotropic, transversely isotropic, and orthotropic materials by means of combined ultrasonic-mechanical testing of normal stiffnesses: Application to metals and wood (Kohlhauser and Hellmich 2009a)

Authored by Christoph Kohlhauser and Christian Hellmich
Submitted to *European Journal of Mechanics — A/Solids*

Poisson's ratios (and thus off-diagonal stiffnesses) of materials exhibiting different symmetries can be directly determined by means of mechanical tests. However, this is sometimes not possible or too complex, due to low material symmetries or awkward specimen preparation. An alternative approach, using ultrasonic wave propagation, is very sensitive to errors in the determination of off-diagonal stiffness tensor components. As a remedy, we here propose to obtain Poisson's ratios from the normal (diagonal) elasticity tensor components and the Young's moduli. Thereby, Young's moduli are determined from quasi-static mechanical tests, and normal stiffness tensor components are determined from ultrasonic tests with the pulse transmission technique. In this context, we review the notions of energy, group, and phase velocity.

Poisson's ratios of isotropic, transversely isotropic, and orthotropic non-axially auxetic materials are expressed as functions of normal elastic stiffnesses, considering the positive definiteness of the stiffness and compliance tensors. The relevance of our method is shown by comparing Poisson's ratios computed from normal elastic stiffnesses given in the literature, to experimentally given Poisson's ratios, for a range of materials including (isotropic) aluminum, (transversely isotropic) aluminum matrix-fiber composite and (orthotropic) stainless-steel weld metal. Finally, the method is applied to (orthotropic) wood (namely spruce), by measuring four normal

stiffnesses, and relying on a spruce-specific universal constant involving longitudinal Poisson's ratios and on reasonable estimates for the radial Young's modulus. Resulting ranges of Poisson's ratios agree well with ranges of Poisson's ratios obtained from direct mechanical measurements on spruce.

2.1   Introduction

In a linear elastic solid, Poisson's ratio for one pair of orthogonal directions is the ratio of the lateral (or transverse) contraction in one of these directions, to the axial extension in the other direction, due to a uniaxial tension applied along this (axial) direction (Ting and Barnett 2005). Knowledge of Poisson's ratios (defining the off-diagonal components of the compliance tensor) or of the off-diagonal components of the elasticity tensor is necessary for the complete description of the elastic behavior of materials, e.g. for use in finite element simulations or other spatial modeling approaches. Especially for anisotropic materials, where all Poisson's ratios cannot be anymore computed from the Young's and shear moduli (as it is the case for isotropic materials), their exact experimental determination is necessary. Besides stiffness and strength of a material, the complexity of experimental determination of Poisson's ratios strongly depends on material anisotropy. Symmetry properties of anisotropic materials are usually described by symmetry classes used to characterize crystal symmetry (the lowest symmetry to be considered in this work is the orthorhombic one). Materials with orthorhombic symmetry imply three mutually perpendicular two-fold symmetry axes, i.e. three orthogonal symmetry planes [for a classification of orthotropic materials based on normal stiffnesses, see (Musgrave 1981)].

While Poisson's ratio of isotropic materials is bounded by -1 and 0.5 (stemming from the necessary positive definiteness of the strain energy density), Poisson's ratios of anisotropic materials do not exhibit any bounds (Ting and Chen 2005). Materials with at least one negative Poisson's ratio for a pair of orthogonal directions are called auxetic; and if all Poisson's ratios are positive, the material is nonauxetic. Materials are axially auxetic or axially nonauxetic, depending on whether or not a negative Poisson's ratio arises for principal material directions (Baughman et al. 1998). Negative Poisson's ratios have been observed experimentally for isotropic materials (Lakes 1987) and cubic materials (Baughman et al. 1998), and negative Poisson's ratios have been predicted numerically for orthotropic, physical reasonable materials (Boulanger and Hayes 1998; Rovati 2003). Still, negative Poisson's ratios are not common in the principle directions of most materials. Ting and Barnett (2005) gave simple necessary conditions for compliance tensor components of general anisotropic materials (and sufficient conditions for isotropic, cubic, and hexagonal symmetry), as to identify if the material is nonauxetic (or completely auxetic). In this paper, we shall restrict ourself to the most common case of axially nonauxetic materials.

Determination of Poisson's ratios is, in most cases, either performed using standard mechanical (tensile) tests or via inversion of the elasticity tensor measured in ultrasonic tests. While in the former methods Poisson's ratios are determined directly from strain measurements, the latter methods use wave propagation in different directions to obtain the elastic stiffness tensor components. In order to obtain orthotropic elasticity tensor components in the principle material directions, wave propagation in symmetry planes, more precisely in all principle and three non-principle directions, is necessary. Ultrasonic measurements in non-principle directions (for off-diagonal stiffnesses) are very sensitive to errors in velocity measurements. Errors of 0.1% in velocity can yield errors in off-diagonal stiffness components of 35% (Kriz and Stinchcomb 1979), and errors higher than 25% were expected by several researchers (Papadakis et al. 1991; Every and Sachse 1992). Measurements (in particular such involving off-diagonal elasticity

tensor components) are also extremely sensitive to the angle of incidence with respect to the principle material directions. Wooh and Daniel (1991) showed (for a fiber composite) that a change of 20° can yield values for Poisson's ratios that are ten times larger than the correct values, and Turner and Cowin (1988) showed that a 5° off-axis angle in bone yields 10% errors in Poisson's ratios. Ultrasound may even suggest negative Poisson's ratios in materials not showing such behavior, like composites or wood (Mouchtachi et al. 2004; Kazemi-Najafi et al. 2005). All these errors might not be obvious when comparing ultrasonic-derived Young's moduli to results from mechanical tests, where deviations may be attributed to the difference in experimental methods, or may be simply considered non-relevant.

Our approach to overcome these problems is to measure (normal) stiffnesses rather than Poisson's ratios, and determine the latter analytically from the former. In this context, Kim (1994) gave analytical expressions for off-diagonal elastic stiffnesses of orthotropic materials in terms of diagonal normal stiffness. Lei et al. (1994) used the product of the stiffness and compliance tensors to numerically solve for off-diagonal stiffness tensor components. Thereby, ultrasonic wave propagation was employed as to obtain normal stiffnesses, and a resonance method was used to obtain Young's moduli. Application on a weakly orthotropic composite of boron fibers in an aluminum matrix showed good agreement between measured and computed shear and off-diagonal elasticity tensors. In the sequel, we give analytical expressions for Poisson's ratios of orthotropic, transversely isotropic, and isotropic materials, in terms of (diagonal) normal stiffnesses. The expressions are applied to three metallic materials (isotropic aluminum alloy, transversely isotropic aluminum matrix-silica fiber composite, and orthotropic stainless-steel weld metal) and to the biological orthotropic material wood (softwood spruce). Thereby, we take normal stiffnesses from literature or from our own experiments (for spruce) and compare the obtained Poisson's ratios with results from direct mechanical measurements and/or ultrasonic measurements in non-principal directions of anisotropic materials.

The paper is organized as follows: First, the direct measurement of Poisson's ratios in mechanical tests is described (Section 2.2), followed by their determination from ultrasonic tests (Section 2.3). Section 2.4 gives the analytical relationships between Poisson's ratios and normal elastic stiffnesses. In Section 2.5, Poisson's ratios of three different materials (aluminum, aluminum matrix-silica fiber composite, stainless-steel weld metal) are determined from normal stiffnesses, and compared to literature values. In Section 2.6 the combined ultrasonic-mechanical method is applied to softwood spruce, before the paper is concluded in Section 2.7.

2.2   Poisson's ratios from uniaxial mechanical tests: measurement of axial and lateral strain

Mechanical testing is performed by applying stresses (tensile, pressure, bending) to the material, and by measuring the resulting deformation in terms of displacements and strains. The most common mechanical test is the uniaxial tensile test, in which a tensile stress $\boldsymbol{\sigma} = \sigma_{jj}\,\mathbf{e}_j \otimes \mathbf{e}_j$, $\sigma_{jj} > 0$, is applied in axial direction $\mathbf{e}_j$; and the resulting strain state $\boldsymbol{\varepsilon} = \varepsilon_{jj}\,\mathbf{e}_j \otimes \mathbf{e}_j + 2\,\varepsilon_{ii}\,\mathbf{e}_i \otimes \mathbf{e}_i$ is measured, in terms of the axial (active) normal strain ε_{jj} in direction of the tensile force, and the normal strain ε_{ii} perpendicular to this direction, i.e. the transverse (passive) or lateral strain. This is done with extensometers or non-contact full-field measurement methods. Young's modulus E_j in the direction of the applied tensile stress is given by

$$E_j = \frac{\sigma_{jj}}{\varepsilon_{jj}}\,. \tag{2.1}$$

Poisson's ratios (see also Section 2.1) are defined according to

$$\nu_{ij} = -\frac{\varepsilon_{ii}}{\varepsilon_{jj}} \, . \tag{2.2}$$

It is seen from (2.2) that Poisson's ratios are determined from directly measured quantities. Eqs. (2.1) and (2.2) are valid in any direction in an anisotropic material. In this context, we refer to Zhang et al. (2008) for general expressions for orthotropic symmetry for Young's modulus and Poisson's ratios in terms of E_j and ν_{ij} (with principle axes i, $j = \{1, 2, 3\}$).

2.3   Poisson's ratios from ultrasonic tests: measurement of (quasi-)longitudinal and (quasi-)transversal wave velocities

Our developments focus on the ultrasonic pulse transmission(-through) technique where a transmitter sends an acoustic signal of a specific frequency f through a sample, and a receiver records the arrival of the signal at the opposite side of the sample. In this case, the distance ℓ_p between the interfaces between the sample and the transmitter, and between the sample and the receiver, together with the time of flight of the signal through this distance, t_f, gives access to the phase velocity v_p of the traveling wave, via

$$v_p = \frac{\ell_p}{t_f} \, , \tag{2.3}$$

see Appendix 2.8 for more general deliberations on ultrasonic wave velocity measurements with emphasis on the differences between phase velocity and group or energy velocity.

Combination of the conservation law of linear momentum in a 3D continuum, the generalized Hooke's law, the linearised strain tensor, and the general plane wave solution for the displacements inside an infinite solid medium

$$\mathbf{u}(\mathbf{x}, \, t) = \mathbf{u}_0 \, \exp[i \, (\mathbf{k} \cdot \mathbf{x} - \omega \, t)] \, , \tag{2.4}$$

with the amplitude $\mathbf{u}_0$, the wave vector $\mathbf{k} = k \, \mathbf{n}$ ($\mathbf{n}$ being the wave direction and k being the wave number), and the angular frequency $\omega = 2 \, \pi \, f$ (f being the frequency of sinusoidal pertubation) yields the so-called Kelvin-Christoffel equations

$$(\mathbf{\Gamma} - \rho \, v_p^2 \, \mathbf{1}) \cdot \mathbf{p} = \mathbf{0} \, , \tag{2.5}$$

with the acoustic tensor [also called 'Kelvin-Christoffel matrix' (Carcione 2001)],

$$\mathbf{\Gamma} = \mathbb{C} \cdot \mathbf{n} \cdot \mathbf{n} \, , \tag{2.6}$$

the phase velocity v_p (also often referred to as wave or material sound velocity) of this so-called bulk wave, defined as (Newton 1687; Carcione 2001)

$$v_p \equiv \frac{\omega}{k} = \lambda \, f \, , \tag{2.7}$$

the wavelength λ, the (apparent) mass density ρ, the (symmetric) fourth-order elasticity tensor $\mathbb{C}$ [of a material defined on a representative volume element being much smaller than the wavelength λ, Zaoui (2002), see also Section 2.6] and the second-order unity tensor $\mathbf{1}$, having

δ_{ij} (Kronecker delta — $\delta_{ij} = 1$ for $i = j$, and zero otherwise) as components. $\mathbf{p} = u_0/|u_0|$ is the normalized displacement or polarization vector, which defines the motion direction of a material point ('representative volume element') and thus defines the mode of the wave. Pure longitudinal ($\mathbf{n} \cdot \mathbf{p} = 1$) and pure transversal ($\mathbf{n} \cdot \mathbf{p} = 0$) modes travel in isotropic materials and along principle material directions of anisotropic materials, while in all other cases, mixed modes ($0 < \mathbf{n} \cdot \mathbf{p} < 1$) occur (Ledbetter and Kriz 1982). If the larger component of $\mathbf{p}$ is along $\mathbf{n}$, one speaks of quasi-longitudinal waves; if the larger component is along a direction normal to $\mathbf{n}$ one speaks of quasi-transversal waves.

By restricting ourselves to materials of orthorhombic or higher symmetries and to wave propagation within the symmetry plane $1 - 2$, more precisely in *any* direction within this plane, $\mathbf{n}_{1-2} = \{n_1, n_2, 0\}^T$, the three eigenvalues $v_{p,1-2}^{(i)}$ of (2.5), $i = \{1, 2, 3\}$, give access to the following (frequency-independent, i.e. non-dispersive) phase velocities

$$
v_{p,1-2}^{(1,2)} = \sqrt{\frac{C_{1111}\, n_1^2 + C_{2222}\, n_2^2 + C_{1212} \pm c}{2\,\rho}} \quad \text{with}
$$

$$
c = \sqrt{\left[(C_{2222} - C_{1212})\, n_2^2 - (C_{1111} - C_{1212})\, n_1^2\right]^2 + 4\left[(C_{1122} + C_{1212})\, n_1\, n_2\right]^2} \quad (2.8)
$$

and

$$
v_{p,1-2}^{(3)} = \sqrt{\frac{C_{1313}\, n_1^2 + C_{2323}\, n_2^2}{\rho}} \,. \tag{2.9}
$$

The plus sign in the solutions $v_{p,1-2}^{(1,2)}$ [Eq. (2.8)] corresponds to the (quasi-)longitudinal velocity $v_{p,1-2}^{(1)}$, and the minus sign corresponds to the (quasi-)transversal solution $v_{p,1-2}^{(2)}$. $v_{p,1-2}^{(3)}$ given in (2.9), is a pure out-of-plane transversal mode, i.e. the polarization vector is oriented perpendicular on the propagation plane $1 - 2$. Analogous solutions of the eigenvalue problem (2.5) for waves propagating in the symmetry planes $1 - 3$ ($\mathbf{n}_{1-3} = \{n_1, 0, n_3\}^T$) and $2 - 3$ ($\mathbf{n}_{2-3} = \{0, n_2, n_3\}^T$) yield $v_{p,1-3}^{(i)}$ and $v_{p,2-3}^{(i)}$, respectively. Specializing these nine solutions for wave propagation in the principle material directions ($\mathbf{n}_1 = \{1, 0, 0\}^T$, $\mathbf{n}_2 = \{0, 1, 0\}^T$, $\mathbf{n}_3 = \{0, 0, 1\}^T$), yields 18 solutions for ultrasonic phase velocities (each solution is obtained twice). These solutions, in turn, define the six (diagonal) normal and shear stiffness components,

$$
\begin{array}{llllll}
C_{1111} &=& \rho\, v_{1,1}^2\,, & C_{2222} &=& \rho\, v_{2,2}^2\,, \\
C_{2323} &=& \rho\, v_{2,3}^2 = \rho\, v_{3,2}^2\,, & C_{1313} &=& \rho\, v_{1,3}^2 = \rho\, v_{3,1}^2\,,
\end{array}
\qquad
\begin{array}{lll}
C_{3333} &=& \rho\, v_{3,3}^2\,, \\
C_{1212} &=& \rho\, v_{1,2}^2 = \rho\, v_{2,1}^2\,,
\end{array}
\tag{2.10}
$$

where the first index i of the velocities $v_{i,j}$ designates the wave propagation direction, and the second index j designates the direction of the particle motion induced by the wave, i.e. the polarization direction ($i = j$ for a longitudinal wave; $i \neq j$ for a transversal wave). The condition

$$
v_{i,j} = v_{j,i} \tag{2.11}
$$

implies *perfect* orthorhombic symmetry of the material. Thus, the diagonal components of the elasticity tensor follow from phase velocities measured in principal directions (two-fold symmetry axes) of a material with orthotropic or higher symmetry. More precisely, normal stiffnesses are related to purely longitudinal phase velocities, and shear stiffnesses are related to purely transversal phase velocities.

For the determination of off-diagonal terms C_{iijj}, the propagation of ultrasonic waves along non-principal directions in symmetry planes is necessary. When specializing solutions $v_{p,1-2}^{(1,2)}$

[Eq. (2.8)], and analogous solutions for other symmetry planes, namely $v^{(1,2)}_{p,1-3}$ and $v^{(1,2)}_{p,2-3}$, for propagation directions in symmetry planes inclined by 45° to the principle material directions (i.e. $\mathbf{n} = \{1/\sqrt{2}, 1/\sqrt{2}, 0\}^T$ in symmetry plane $1-2$, $\mathbf{n} = \{1/\sqrt{2}, 0, 1/\sqrt{2}\}^T$ in symmetry plane $1-3$, and $\mathbf{n} = \{0, 1/\sqrt{2}, 1/\sqrt{2}\}^T$ in symmetry plane $2-3$), the off-diagonal terms turn out to be

$$
C_{1122} = \sqrt{\left(C_{1111} + C_{1212} - 2\rho \left(v^{qL,qT}_{12,12} \right)^2 \right) \left(C_{1212} + C_{2222} - 2\rho \left(v^{qL,qT}_{12,12} \right)^2 \right)}
$$
$$
- C_{1212}, \tag{2.12}
$$

$$
C_{1133} = \sqrt{\left(C_{1111} + C_{1313} - 2\rho \left(v^{qL,qT}_{13,13} \right)^2 \right) \left(C_{1313} + C_{3333} - 2\rho \left(v^{qL,qT}_{13,13} \right)^2 \right)}
$$
$$
- C_{1313}, \quad \text{and} \tag{2.13}
$$

$$
C_{2233} = \sqrt{\left(C_{2222} + C_{2323} - 2\rho \left(v^{qL,qT}_{23,23} \right)^2 \right) \left(C_{2323} + C_{3333} - 2\rho \left(v^{qL,qT}_{23,23} \right)^2 \right)}
$$
$$
- C_{2323}, \tag{2.14}
$$

where $v^{qL,qT}_{ij,ij}$ are wave velocities corresponding to both, one quasi-longitudinal wave $v^{qL}_{ij,ij}$ and one quasi-transversal wave $v^{qT}_{ij,ij}$, propagating in the direction in the $i - j$ plane enclosing an angle of 45° with both the i-th and j-th symmetry axis, with particle motion in the $i - j$ plane. Hence, the off-diagonal elasticity components C_{iijj} of (2.12), (2.13), or (2.14) can be determined from wave velocity $v^{qL}_{ij,ij}$, and this result can be checked by inserting the measurements for $v^{qT}_{ij,ij}$ into (2.12), (2.13), or (2.14), or vice versa — always provided the normal and shear elasticity components, C_{iiii} and C_{ijij}, were experimentally accessed through (2.10). The out-of-plane purely transversal waves propagating in the same plane as $v^{qL}_{ij,ij}$ and $v^{qT}_{ij,ij}$ do $[v^T_{ij,k} = v^{(3)}_{p,i-j}$, see Eq. (2.9)], can be used to cross-check the shear components of the last of Eqs. (2.10), according to

$$
C_{1313} + C_{2323} = 2\rho \left(v^T_{12,3} \right)^2,
$$
$$
C_{1212} + C_{2323} = 2\rho \left(v^T_{13,2} \right)^2, \quad \text{and} \tag{2.15}
$$
$$
C_{1212} + C_{1313} = 2\rho \left(v^T_{23,1} \right)^2.
$$

Inversion of the elasticity tensor $\mathbb{C}$ delivers the compliance tensor $\mathbb{D} = \mathbb{C}^{-1}$, which reads for an orthotropic material in Kelvin- or Mandel-notation as (Cowin and Mehrabadi 1992; Helnwein 2001; Cowin 2003)

$$
\{D_{ijkl}\} = \begin{bmatrix}
1/E_1 & -\nu_{12}/E_2 & -\nu_{13}/E_3 & 0 & 0 & 0 \\
-\nu_{21}/E_1 & 1/E_2 & -\nu_{23}/E_3 & 0 & 0 & 0 \\
-\nu_{31}/E_1 & -\nu_{32}/E_2 & 1/E_3 & 0 & 0 & 0 \\
0 & 0 & 0 & 2/G_{23} & 0 & 0 \\
0 & 0 & 0 & 0 & 2/G_{13} & 0 \\
0 & 0 & 0 & 0 & 0 & 2/G_{12}
\end{bmatrix}, \tag{2.16}
$$

with three Young's moduli E_i ($i = 1, 2, 3$) referring to the principle material directions, three shear moduli $G_{ij} = G_{ji}$ ($i \neq j = 1, 2, 3$) referring to principal material (symmetry) planes, and six Poisson's ratios ν_{ij} ($i \neq j = 1, 2, 3$) [according to (2.2), the first index of Poisson's ratio

refs to the (passive) strain and the second index refers to the stress direction]. In this way, the compliance tensor (2.16) gives access to six Poisson's ratios, as part of twelve engineering constants E_1, E_2, E_3, G_{12}, G_{13}, G_{23}, ν_{12}, ν_{13}, ν_{23}, ν_{21}, ν_{31}, ν_{32}, nine of which are independent (see also Section 2.4).

In case of transversal isotropy, the elasticity tensor components follow from specification of (2.10), (2.12), (2.13), and (2.14) for $v_{3,3} = v_{2,2}$, $v_{3,1} = v_{2,1}$, $v_{1,3} = v_{1,2}$, and $v_{13,13} = v_{12,12}$, yielding $C_{3333} = C_{2222}$, $C_{1313} = C_{1212}$, and $C_{1133} = C_{1122}$. This reduces the number of independent elasticity components to five. As stated before, the compliance tensor gives access to seven engineering constants [two Young's moduli E_1, E_2; two shear moduli $G_{12}(= G_{21})$, $G_{23} = G_{13}(= G_{32} = G_{31})$; and three Poisson's ratios $\nu_{32} = \nu_{23}$, $\nu_{21} = \nu_{31}$, $\nu_{12} = \nu_{13}$], five of which are independent (see also Section 2.4).

In case of isotropy, wave propagation velocities are independent of the propagation direction. In all directions, the wave velocities follow from specification of (2.8) for $C_{3333} = C_{2222} = C_{1111}$, and $C_{2323} = C_{1313} = C_{1212}$ so that we have one longitudinal wave velocity $v_L = \sqrt{C_{1111}/\rho}$ and two transversal wave velocities of equal magnitude $v_T = \sqrt{C_{1212}/\rho}$, from which the elasticity tensor components can easily be computed [C_{1111} and C_{1212} in (2.10) yield the isotropic off-diagonal component $C_{1122} = C_{1111} - 2\,C_{1212} = C_{2233} = C_{1133}$]. Isotropic solids are completely described by two elastic constant, e.g. C_{1111} and C_{1212}, therefore also engineering elastic constants can be given as a function of the two velocities, e.g. Young's modulus and shear modulus,

$$E = \rho\frac{v_T^2\,(3\,v_L^2 - 4\,v_T^2)}{v_L^2 - v_T^2} \qquad \text{and} \qquad G = C_{1212} = \rho\,v_T^2\,, \tag{2.17}$$

respectively. Also Poisson's ratio can be given as a closed-form function of the wave velocities in an isotropic material,

$$\nu = \frac{v_L^2/2 - v_T^2}{v_L^2 - v_T^2}\,. \tag{2.18}$$

2.4 Poisson's ratios from combined ultrasonic and mechanical tests: Measurement of axial strain and longitudinal wave velocities

Since the lateral (passive) strain measurements in uniaxial mechanical tests are often complicated to perform (see Section 2.2) and since the off-(principle-)axis wave velocities in ultrasonic tests (see Section 2.3) are frequently characterized by significant measurement errors, we here present a combined ultrasonic-mechanical method, doing without the aforementioned measurements, but relying solely on quasi-static uniaxial stress measurements in the (orthotropic) principle material directions (yielding, together with strain measurements in the same direction, orthotropic Young's moduli E_i) and longitudinal wave velocities (yielding normal stiffness components C_{iiii}). In order to get access to Poisson's ratios, a few mathematical transformations are due: The symmetry requirement of the orthotropic compliance tensor (2.16) implies a relationship between the Poisson's ratios, reading as

$$\nu_{ij} = \nu_{ji}\frac{E_j}{E_i} \quad (i \neq j,\ i,j = 1\,,2\,,3)\,, \tag{2.19}$$

involving nine independent engineering material constants. Inversion of the positive definite compliance tensor (2.16) and comparing the resulting diagonal components to the diagonal components of the stiffness tensor, yields (omit Einstein summation, i.e. do not sum over equal

indices) (Itskov and Aksel 2002)

$$C_{iiii} = E_i \frac{1 - \nu_{jk}\,\nu_{kj}}{\Delta}, \quad \text{and} \tag{2.20}$$

$$C_{iijj} = C_{jjii} = E_i \frac{\nu_{ij} + \nu_{kj}\,\nu_{ik}}{\Delta}, \quad (i \neq j \neq k, \; i,\,j,\,k = 1,\,2,\,3), \tag{2.21}$$

where

$$\Delta = 1 - \nu_{23}\,\nu_{32} - \nu_{13}\,\nu_{31} - \nu_{12}\,\nu_{21} - 2\,\nu_{32}\,\nu_{13}\,\nu_{21}. \tag{2.22}$$

Insertion of (2.19) into (2.20), and solving the resulting equation for ν_{21}, ν_{31}, and ν_{32}, yields

$$\begin{aligned}
\nu_{21} &= \frac{1}{2\,\sqrt{2}\,E_2\,E_3} \sqrt{\frac{n_{21}}{C_{1111}\,C_{2222}}}, \\[2mm]
\nu_{31} &= \frac{1}{2\,\sqrt{2}\,E_2\,E_3} \sqrt{\frac{n_{31}}{C_{1111}\,C_{3333}}}, \\[2mm]
\nu_{32} &= \frac{n_{32}}{f\,g_{12}\,g_{32}} \sqrt{n_{21}\,n_{31}\,\frac{C_{2222}}{C_{3333}}},
\end{aligned} \tag{2.23}$$

where

$$\begin{aligned}
n_{21} &= n_{12} - h, \\
n_{31} &= c_3^2 - 2\,E_3\,c_3\,d_{31} + E_3^2\,e_{31} - h, \\
n_{32} &= c_3^2 - 2\,E_3\,c_3\,d_{32} + E_3^2\,e_{32} + h,
\end{aligned} \tag{2.24}$$

and

$$\begin{aligned}
f &= -16\,c_1\,c_2\,E_3^2, \\
g_{12} &= c_3 - E_3\,d_{12}, \\
g_{32} &= c_3 - E_3\,d_{32}, \\
n_{12} &= c_3^2 - 2\,E_3\,c_3\,d_{21} + E_3^2\,e_{21}, \\
h &= \sqrt{f\,g_{12}^2 + n_{12}^2},
\end{aligned} \tag{2.25}$$

with

$$\begin{aligned}
e_{21} &= c_2^2 - 2\,E_2\,c_2\,b_2 + E_2^2\,a_2^2, \\
e_{31} &= c_2^2 - 2\,E_2\,c_2\,a_1 + E_2^2\,a_2^2, \\
e_{32} &= c_2^2 - 2\,E_2\,c_2\,a_2 + E_2^2\,a_2\,b_1,
\end{aligned} \tag{2.26}$$

$$\begin{aligned}
d_{12} &= c_2 - E_2\,a_2, \\
d_{21} &= c_2 + E_2\,a_1, \\
d_{31} &= c_2 + E_1\,E_2 - 3\,c_1, \\
d_{32} &= c_2 + E_1\,E_2 - c_1,
\end{aligned} \tag{2.27}$$

$$c_1 = C_{1111} \, E_2 \,, \qquad c_2 = C_{2222} \, E_1 \,, \qquad c_3 = C_{3333} \, E_1 \, E_2 \,, \tag{2.28}$$

$$a_1 = E_1 + C_{1111} \,, \quad a_2 = E_1 - C_{1111} \,, \quad b_1 = E_1 + 3 \, C_{1111} \,, \quad b_2 = E_1 - 3 \, C_{1111} \,. \tag{2.29}$$

(2.23)–(2.29) constitute one of eight solutions for ν_{21}, ν_{31}, and ν_{32}, namely the only solution that gives exclusively positive Poisson's ratios, i.e. that relates to axially nonauxetic materials. The remaining three Poisson's ratios are then determined from Eq. (2.19).

Specialization of Eqs. (2.23)–(2.29) for the transversely isotropic symmetry class, i.e. for $E_3 = E_2$ and $C_{3333} = C_{2222}$ (see Section 2.3), yields

$$\nu_{32} = \nu_{23} = \frac{a_2 \, E_2}{4 \, c_2} + \sqrt{1 - \frac{a_1 \, E_2}{2 \, c_2} + \left(\frac{a_2 \, E_2}{4 \, c_2}\right)^2} \,,$$

$$\nu_{21} = \nu_{31} = \sqrt{\frac{a_2^2}{c_{12}} - \frac{a_2 \, E_1}{2 \, c_1} - \sqrt{\left(\frac{a_2 \, E_1}{2 \, c_1}\right)^2 - \frac{a_1 \, a_2^2 \, E_1}{c_1 \, c_{12}} + \left(\frac{a_2^2}{c_{12}}\right)^2}} \,, \tag{2.30}$$

$$\nu_{12} = \nu_{13} = \nu_{21} \frac{E_2}{E_1} \,,$$

with a_1, a_2, c_1, and c_2 according to (2.28) and (2.29), and with $c_{12} = 8 \, C_{1111} \, C_{2222}$. For the plane of isotropy $2 - 3$, we have

$$G_{23} = C_{2323} = \frac{1}{2} \, (C_{2222} - C_{2233}) = \frac{E_2}{2 \, (1 + \nu_{23})} \,, \tag{2.31}$$

so that the shear modulus in the isotropic plane can be determined from normal stiffnesses, once Poisson's ratios are known.

Specialization of (2.30) for isotropic materials, i.e. for $E_2 = E_1 = E$ and $C_{2222} = C_{1111}$ (see Section 2.3), yields

$$\nu = \frac{1}{4} \left(\sqrt{9 - 10 \frac{E}{C_{1111}} + \frac{E^2}{C_{1111}^2}} + \frac{E}{C_{1111}} - 1 \right) \,, \tag{2.32}$$

i.e. Poisson's ratio for an isotropic material is a function of only one argument, the ratio C_{1111}/E,

$$\nu = \mathcal{F}_{iso} \left(\frac{C_{1111}}{E} \right) \tag{2.33}$$

(see Figure 2.1). For $C_{1111}/E \to \infty$, Poisson's ratio tends to the upper bound for ν in isotropic materials, i.e. to $\nu = 0.5$ (related to a so-called incompressible material). Already at $C_{1111}/E = 10$, ν deviates by only 3.5% from the aforementioned bound. Eq. (2.32) can also be obtained from the well-known relationship between the isotropic normal stiffness tensor $\mathbb{C}$ component and the isotropic engineering constants E and ν, reading as

$$\frac{C_{1111}}{E} = \frac{1 - \nu}{(1 + \nu)(1 - 2 \, \nu)} \,. \tag{2.34}$$
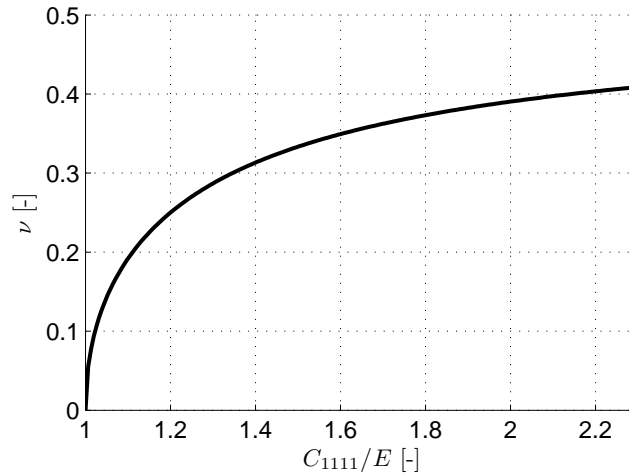
Figure 2.1: Poisson's ratio for isotropic materials, as a function of C_{1111}/E (normal stiffness tensor component over Young's modulus).

2.5   Validity check of combined mechanical-ultrasonic method: Application to metals

2.5.1   Isotropic aluminum alloy

First, we check the reliability of the combined ultrasonic-mechanical method for a well-known, homogeneous and isotropic material, namely the aluminum alloy EN AW-5083-H111. Therefore, the elastic constants were determined by means of both uniaxial mechanical tests and ultrasonic tests. The mechanical tests were performed with an LFM 150 uniaxial testing machine of Wille Geotechnik (Germany) and 3/350XY13 strain gauges of Hottinger Baldwin Messtechnik (Germany), on three dog-bone shaped specimens with 30×10 mm rectangular cross-section in the strain measurement region. The results according to Eqs. (2.1) and (2.2) are shown in the third line of Table 2.1.

Table 2.1: Elastic constants of isotropic aluminum from mechanical (me), ultrasonic (us) and combined (co) tests (bold values from direct measurements).

aluminum alloy 5083	C_{1111} [GPa]	C_{1122} [GPa]	E [GPa]	G [GPa]	C_{1111}/E [-]	ν [-]
mechanical	105.5	48.99	**74.49**	28.28	1.42	**0.317**
ultrasonic	**107.9**	53.36	72.63	**27.29**	1.49	0.331
combined	**107.9**	51.58	**74.49**	28.14	1.45	0.323
deviation us/me [%]	2.2	8.9	−2.5	−3.5	4.9	4.3
deviation co/me [%]	2.2	5.3	0.0	−0.5	2.2	2.0
deviation co/us [%]	0.0	−3.3	2.6	3.1	−2.5	−2.2

The ultrasonic pulse transmission tests were performed by a pulser-receiver unit of Panametrics Inc. (USA), a digital oscilloscope of Lecroy (USA), and 17 transducers of Panametrics Inc., with frequencies ranging from 0.05 to 20 MHz, on a cube with an edge length of 100 mm [for more equipment details, see Kohlhauser and Hellmich (2009b)]. The results according to Eqs. (2.10)

specialized for C_{1111} and $C_{1212} = G$, are shown in the fourth line of Table 2.1. In order to compare the purely mechanical and purely ultrasonic methods with the combined method of Section 2.4, Poisson's ratio is calculated according to Eq. (2.32) from normal stiffness C_{1111} and Young's modulus E, see fifth line of Table 2.1. It lies well between the Poisson's ratios determined purely ultrasonically and purely mechanically (see last column of Table 2.1), which underlines the significance of Eq. (2.32) for reliable determination of Poisson's ratio.

More generally, one observes that deviations between purely ultrasonic and purely mechanical test results (see row six of Table 2.1) are higher than those between the results from the combined ultrasonic-mechanical method and from purely mechanical or purely ultrasonic tests (see rows seven and eight in Table 2.1). As a rule, the highest deviations in values from different methods concern the off-diagonal stiffness C_{1122} and Poisson's ratio ν (columns three and seven of Table 2.1).

2.5.2 Transversely isotropic aluminum-silica fiber composite

Next, we apply the combined ultrasonic-mechanical method to the experiments of Mouchtachi et al. (2004), on transversely isotropic fiber composites, consisting of aluminum-silica (Al_2O_3-SiO_2) fibers embedded into a matrix made of aluminum alloy AS7G0.3; characterized by a fiber diameter $d_F = 15 \ \mu$m and by a fiber volume fracion $f_F = 0.35$. Elasticity tensor components related to normal strains and stresses (see row three of Table 2.2) and to shear strains and stresses (see row eight, columns five to seven, in Table 2.2) were measured on plate-like specimens, by means of an automated, computer-assisted immersion device, based on longitudinal and transversal waves propagating in the principle material directions as well as in several different angles to these directions.

Longitudinal and transversal Young's moduli, E_1 and $E_2 = E_3$, were determined by means of mechanical tension tests (see row seven of Table 2.2). While the inversion of the ultrasonically determined stiffness tensor components C_{ijkl} yields, according to (2.16), a longitudinal Young's modulus E_1, which differs by only 3% from that obtained from mechanical tests, the aforementioned inversion suggests negative Poisson's ratios ν_{21} and ν_{12} (see row 16 in Table 2.2). This results most probably from errors in determining the off-diagonal terms of the stiffness tensor, i.e. from measurement errors in the velocities of waves propagating off the principle material directions.

In order to overcome this problem, we employ the combined ultrasonic-mechanical method of Section 2.4, Eqs. (2.30), together with (2.29) and (2.28), to the experimentally determined values for the normal stiffnesses E_1, E_2, C_{1111}, and C_{2222} (the latter was determined as the average of the normal stiffnesses C_{2222} and C_{3333}, which differ by only 2%): This procedure, which does not depend on the unreliable measurements of wave velocities off the principle material directions, yields positive Poisson's ratios (see row 17 of Table 2.2). This underlines the relevance of the combined ultrasonic-mechanical testing method.

2.5.3 Orthotropic stainless-steel weld metal

The last validity test of the normal stiffness-based, combined ultrasonic-mechanical method for determination of Poisson's ratios, relates to an austenitic 308 stainless steel electroslag weld, tested both mechanically and ultrasonically by Dewey et al. (1977). Solidification processes in welds cause local preferred crystallographic orientation, resulting in orthotropic material behavior (Dewey et al. 1977). Tensile tests were performed on cylindrical dog-bone shaped specimens with a measurement length of 25 mm and a diameter of 3.2 mm, six of these specimens were cut along the principle material directions, while another 15 specimen were cut in orientations off

Table 2.2: Elastic constants of (approximately transversely isotropic) fiber composite Al-Al$_2$O$_3$ from mechanical, ultrasonic and combined tests [bold values from direct measurements; $L = (C_{1111}/C_{2222})/(E_1/E_2) = (C_{1111}/E_1)/(C_{2222}/E_2)$, $T = (C_{2222}/C_{3333})/(E_2/E_3) = (C_{2222}/E_2)/(C_{3333}/E_3)$].

elastic stiffness tensor constants	C_{1111} [GPa]	C_{2222} [GPa]	C_{3333} [GPa]	C_{1122} [GPa]	C_{1133} [GPa]	C_{2233} [GPa]
ultrasonic	**135.30**	**128.90**	**126.20**	**15.50**	**51.80**	**58.30**
combined	**135.30**	**127.55**	**127.55**	45.62	45.62	37.00

engineering elastic constants	E_1 [GPa]	E_2 [GPa]	E_3 [GPa]	G_{23} [GPa]	G_{13} [GPa]	G_{12} [GPa]
mechanical	**110.00**	**108.00**	**108.00**	–	–	–
ultrasonic	113.34	101.34	84.80	**32.10**	**33.40**	**57.00**
combined	**110.00**	**108.00**	**108.00**	45.28	–	–

normal stiffness ratios & fraction	f_F [-]	L [-]	T [-]	C_{1111}/E_1 [-]	C_{1111}/C_{2222} [-]	C_{2222}/C_{3333} [-]
ultrasonic	0.35	0.94	0.85	1.19	1.05	1.02
combined	–	1.04	1.00	1.23	1.06	1.00

Poisson's ratios	ν_{32} [-]	ν_{31} [-]	ν_{21} [-]	ν_{23} [-]	ν_{13} [-]	ν_{12} [-]
ultrasonic	0.492	0.449	−0.083	0.412	0.336	−0.074
combined	0.193	0.277	0.277	0.193	0.272	0.272

the principle material directions. Longitudinal and transversal strains were measured by means of extensometers. Ultrasonic measurements were performed at frequencies of 2.25 and 5 MHz, on a single, initially box-shaped specimen (with dimensions $50 \times 38 \times 38$ mm), which underwent progressive cuts, in order to allow for measurements in non-principal directions. These tests allowed for determination of three Young's moduli, three shear moduli, and six Poisson's ratios (see Table 2.3, rows three, four, eight, nine, 18, and 19).

When evaluating stiffness components and Poisson's ratios, respectively, from mechanical and ultrasonic/combined tests, respectively, the propagating relative measurement errors may be augmented by a factor of two or three, respectively, see Table 2.4. This would indicate a fairly similar performance of all three methods. However, off-axis velocity measurements exhibit large errors as compared to quasi-static measurements, so that Poisson's ratios derived from ultrasonic measurements deviate considerably from directly measured Poisson's ratios (by up to 80%, Table 2.3, row 21). By comparison, the combined method, Eqs. (2.23) to (2.29), delivers Poisson's ratios much closer to the directly determined ones (see Table 2.3, row 22) — this underlines the method's potential in case direct measurements are complicated to be performed, as is often the case for wood, dealt with next.

Table 2.3: Elastic constants of stainless-steel weld metal from mechanical (me), ultrasonic (us) and combined (co) tests [bold values from direct measurements; $L = (C_{1111}/C_{2222})/(E_1/E_2) = (C_{1111}/E_1)/(C_{2222}/E_2)$, $T = (C_{2222}/C_{3333})/(E_2/E_3) = (C_{2222}/E_2)/(C_{3333}/E_3)$].

elastic stiffness tensor constants	C_{1111} [GPa]	C_{2222} [GPa]	C_{3333} [GPa]	C_{1122} [GPa]	C_{1133} [GPa]	C_{2233} [GPa]
mechanical	264.47	263.50	235.14	148.36	155.68	163.30
ultrasonic	**278.00**	**242.00**	**223.00**	**127.00**	**170.00**	**135.00**
combined	**278.00**	**242.00**	**223.00**	146.13	159.50	141.32
engineering elastic constants	E_1 [GPa]	E_2 [GPa]	E_3 [GPa]	G_{23} [GPa]	G_{13} [GPa]	G_{12} [GPa]
mechanical	**150.60**	**140.06**	**111.48**	**94.34**	**107.64**	**52.63**
ultrasonic	144.78	156.36	101.17	**87.00**	**77.00**	**57.00**
combined	**150.60**	**140.06**	**111.48**	–	–	–
normal stiffness ratios		L [-]	T [-]	C_{1111}/E_1 [-]	C_{1111}/C_{2222} [-]	C_{2222}/C_{3333} [-]
mechanical		0.93	0.89	1.76	1.00	1.12
ultrasonic		1.24	0.70	1.92	1.15	1.09
combined		1.07	0.86	1.85	1.15	1.09
Poisson's ratios	ν_{32} [-]	ν_{31} [-]	ν_{21} [-]	ν_{23} [-]	ν_{13} [-]	ν_{12} [-]
mechanical	**0.529**	**0.476**	**0.268**	**0.421**	**0.352**	**0.249**
ultrasonic	0.482	0.671	0.150	0.312	0.469	0.162
combined	0.437	0.528	0.296	0.348	0.391	0.275
deviation us/me [%]	9.9	−29.1	78.4	35.2	−24.9	53.6
deviation co/me [%]	−17.4	10.9	10.2	−17.4	10.9	10.2
deviation co/us [%]	−9.2	−21.4	96.7	11.7	−16.7	69.3

2.6 Application of combined ultrasonic-mechanical method: Determination of Poisson's ratios in a biological orthotropic material — spruce wood

According to Section 2.4, Eqs. (2.23)–(2.29), three uniaxial quasi-static tests and three ultrasonic tests, performed in the three principle material directions of an orthotropic material, respectively, can be employed to get access to the six Poisson's ratios of an orthotropic material. The application of this method to wood [which, in contrast to the materials of Section 2.5, is highly porous, with a porosity of about 67%, see e.g. Hofstetter et al. (2005)] is challenged by the fact that quasi-static tests in the radial (2) and circumferential (3) directions are difficult to be performed — while uniaxial tests in the longitudinal (stem) direction (1) are common, and also ultrasonic tests involving longitudinal waves in all principal material directions are easy to perform. Consequently, based on only four (instead of six) tests (three ultrasonic and one quasi-static one) on the investigated specimens, Poisson's ratios of that specimen cannot be directly computed from (2.23)–(2.29) — which would require given values for C_{1111}, C_{2222}, C_{3333}, E_1, E_2, and E_3 —, but these equations need to be seen as functions of two variables L

Table 2.4: Errors [%] induced in Poisson's ratios or normal and off-diagonal stiffness tensor components of orthotropic stainless-steel weld metal (see Section 2.5.3) considering 1% deviation of a measured property for three different methods to determine Poisson's ratios.

	1% error in ν_{ij}	C_{1111}	C_{2222}	C_{3333}	C_{1122}	C_{1133}	C_{2233}
	ref. [GPa]	278.0	242.0	223.0	146.1	159.5	141.3
mechanical	ν_{32} or ν_{23}	0.5	0.9	0.9	1.3	1.1	1.7
	ν_{31} or ν_{13}	1.1	0.6	1.1	1.5	1.9	1.4
	ν_{21} or ν_{12}	0.6	0.6	0.4	1.2	0.8	0.8
	1% error in C_{iijj}	ν_{32}	ν_{31}	ν_{21}	ν_{23}	ν_{13}	ν_{12}
	ref. [-]	0.437	0.528	0.296	0.348	0.391	0.275
ultrasonic	C_{1111}	0.7	0.0	0.0	1.0	−1.4	−1.7
	C_{2222}	0.0	0.6	−1.6	−1.4	0.7	0.0
	C_{3333}	−1.7	−1.6	1.6	0.0	0.0	1.5
	C_{1122}	−1.5	−1.2	3.2	−0.5	−0.2	3.2
	C_{1133}	−0.1	2.2	−2.2	−1.5	2.2	−0.9
	C_{2233}	2.5	0.0	−1.1	2.5	−1.2	−2.2
	1% error in C_{iiii}, E_i	ν_{32}	ν_{31}	ν_{21}	ν_{23}	ν_{13}	ν_{12}
	ref. [-]	0.437	0.528	0.296	0.348	0.391	0.275
combined	C_{1111}	−1.8	0.7	2.0	−1.8	0.7	2.0
	C_{2222}	0.9	−1.3	1.8	0.9	−1.3	1.8
	C_{3333}	1.3	0.9	−3.0	1.3	0.9	−3.0
	E_1	1.8	−0.2	−1.5	1.8	−1.2	−2.5
	E_2	−0.4	1.3	−2.3	−1.4	1.3	−1.3
	E_3	−1.8	−1.4	2.9	−0.8	−0.4	2.9

and T,

$$\nu_{ij} = \mathcal{F}_{ortho,ij}\left(L, T\right)_{C_{1111}, C_{2222}, C_{3333}, E_1 \text{ fixed}} \tag{2.35}$$

with

$$L = \frac{C_{1111}/E_1}{C_{2222}/E_2} = \frac{C_{1111}/C_{2222}}{E_1/E_2} \quad \text{and} \quad T = \frac{C_{2222}/E_2}{C_{3333}/E_3} = \frac{C_{2222}/C_{3333}}{E_2/E_3}, \tag{2.36}$$

i.e. L being the longitudinal-to-radial ratio of normal stiffnesses to Young's modulus ratios, and T being the respective radial-to-circumferential ratio.

In the sequel, we will discuss the nature of the functions (2.35) by example of ultrasonic and quasi-static tests on spruce samples, as detailed hereafter.

2.6.1 Uniaxial, quasi-static tests on spruce samples

We consider three different samples tested mechanically by Teischinger and Patzelt (2005). These samples originate from three different trees with bottom diameters of around 60 cm, grown in the north-east of Austria, at altitudes of 550, 800, and 940m, see Table 2.5.

Specimens for mechanical, micromechanical, and density tests were extracted from a $20 \times 6 \times 6$ cm^3 region consisting of adult wood, located within the tree around one meter above ground. The considered specimens were fairly similar in terms of moisture content and mass density, see

Table 2.5: Properties of spruce specimens for mechanical (uniaxial, quasi-static) tests (Teischinger and Patzelt 2005), and for ultrasonic tests (this work).

tree		uniaxial, quasi-static tests (Teischinger and Patzelt 2005)							ultrasonic tests (this work)	
#	radial position	age	moisture content	density	ring width	latewood proportion	spiral grain	MFA	density	ring width
[-]	[cm]	[years]	[%]	[g/cm^3]	[mm]	[%]	[°]	[°]	[g/cm^3]	[mm]
1	16	37	12.0	0.487	2.12	21.7	4.9	-	0.497	2.05
2	24	120	12.6	0.476	1.00	30.2	0.8	9.8	0.486	0.95
3	20	61	12.8	0.459	2.37	28.4	0.3	11.7	0.444	1.97

Table 2.5. None of them contained compression wood (i.e. the micro fibril angle (MFA) was below 30°, see Table 2.5 and lignin content was below 35%), so that their chemical compositions can be regarded as fairly similar. The fiber length of wood cells was approximately 5 mm, both in earlywood and latewood. The diameter of the wood cells, i.e. the lumen diameter, was 34 μm on average, and the cell wall thickness was 3 μm on average. The average lignin content was measured to be $28.4 \pm 0.2\%$ (Teischinger and Patzelt 2005).

The three samples for uniaxial quasi-static testing were characterized by a total length of 100 mm, by a measurement length of 40 mm, and by a rectangular cross-section spanning, in the measurement region, 7.8 mm in radial and 1.25 mm in circumfential direction. In the clamping region (which was reinforced by pine veneer), the rectangular cross-section widened up to 12 mm. Given the typical growth ring dimensions of Table 2.5, a specimen contained four to eight growth rings along the larger dimension of the rectangular cross-section. Measurements were performed on a uniaxial tensile testing machine (Z100/SW5A, Zwick/Roell, Germany), at stress levels ranging from 10% to 40% of the tensile strength f_t ($f_t = 201$, 154, and 116 MPa for specimens 1 to 3), and at a displacement rate of 1 mm/min (Teischinger and Patzelt 2005). Longitudinal strains were determined by means of an extensometer with a measurement length of 25 mm. Test results in terms of the longitudinal Young's modulus E_1 are given in Table 2.8, column two, lines $9-13$.

2.6.2 Ultrasonic tests on spruce samples

Ultrasonic testing in wood has a long tradition, starting with Lee (1958) and Hearmon (1965), followed by many others, including Paschalis (1978); Bucur and Archer (1984); Kamioka (1988); Ouis (2002); Payton (2003); Koponen et al. (2005). We here report tests on twelve samples, four each having been harvested at a $20 \times 6 \times 6$ cm^3 region at the same longitudinal and radial positions where the three specimens for the aforementioned quasi-static, uniaxial tests were harvested, but 10 cm off the latter in the circumferential direction. In this way, it was guaranteed that the samples for ultrasonic tests had density and ring width characteristics similar to those of the samples for mechanical tests. The twelve samples for ultrasonic testing were of cubical shape with 20 mm edge length. Densities used for stiffness determination from ultrasonic tests were specimen-specific (tree-specific density values are given in Table 2.5, column ten). All six surfaces of *one* out of four tree-specific samples were parallel to the principle material directions, and only two surfaces of the other three (out of four) samples were parallel to one material symmetry plane, while the corresponding four other surfaces were

inclined by an angle of 45° with respect to the principle material directions. All samples were kept at approximately the same moisture content as the samples used for mechanical testing, and the samples were insonified by longitudinal ultrasonic waves of frequencies $f = 50$, 100, 250, 500 kHz, and by transversal waves of frequency $f = 250$ kHz, according to the pulse transmission method (Markham 1957; Kohlhauser and Hellmich 2009b). A cellophane film was used to prevent the coupling medium honey from infiltrating the wood mircostructure and thus influencing its stiffness properties, while not reducing the accuracy of the wave velocity measurements, as shown by Kamioka (1988) for thin (55 micron) plastic foil (which changed the velocity measurements by only $1-2\%$). Accuracy was also maintained through application of a constant pressure onto the ultrasonic transducers, ensuring the reception of a constant pulse amplitude, as done by Kamioka (1988).

Table 2.6: Wavelengths of longitudinal waves transmitting spruce wood at different ultrasonic frequencies, and characteristic length of the wood inhomogenities 'lumen' and 'growth ring'.

	velocity: $v_{i,i}$			wavelength: $\lambda_{L,i}$ [see Eq. (2.7)]			lumen: $d \approx 0.03$ mm		growth ring: $d \approx 2.00$ mm	
f	$v_{1,1}$	$v_{2,2}$	$v_{3,3}$	$\lambda_{L,1}$	$\lambda_{L,2}$	$\lambda_{L,3}$	d/λ_1	$d/\lambda_{2\approx3}$	d/λ_1	d/λ_3
[MHz]	[km/s]	[km/s]	[km/s]	[mm]	[mm]	[mm]	10^{-3}	10^{-3}	10^{-1}	10^{-1}
0.05	6.05	2.25	2.01	120	45	40	0.3	0.8	0.2	0.5
0.10	5.97	2.25	2.02	60	23	20	0.5	1.5	0.3	1.0
0.25	6.37	2.26	2.09	25	9.0	8.3	1.2	3.5	0.8	2.5
0.50	6.45	2.27	2.09	13	4.5	4.2	2.3	7.0	1.5	4.5

Longitudinal wave velocities $v_{i,i}$ and transversal wave velocities $v_{i,j}$ [according to Eq. (2.10)] were measured in the three principle material directions (given the aforementioned cut of the samples, this was done on two tree-specific samples per material direction), yielding normal and shear stiffnesses (see Table 2.8, columns two to seven, lines three to five for tree-related normal and Possion-type stiffness components, and line six for corresponding average values; as well as columns five to seven, lines nine to eleven for shear stiffness components, and line twelve for corresponding average values). In this context, average values for the transversal or shear wave velocities were used, since $v_{i,j} \neq v_{j,i}$ for the non-perfect orthotropic structure of wood. While the ultrasonically determined values of (longitudinal) wave velocities documented in Table 2.6 are physically reasonable, quasi-longitudinal velocities $v_{ij,ij}$ (the index-pair relates to plane of propagation and polarization) yielded complex solutions for off-diagonal stiffnesses, and quasi-transversal wave velocities $v_{ij,ij}$ yielded positive off-diagonal stiffnesses, but unrealistic (including negative) Poisson's ratios. Such physically questionable results [due to sensitivity of off-diagonal stiffness components to measurement errors in $v_{ij,ij}$] were also obtained by Bucur and Archer (1984), whose ultrasonically determined Poisson's ratios differ by relative errors as huge as 237%, 383%, −35%, 27%, 68%, and −38%, respectively, from the averages over a wide collection of literature values from mechanical tests (see Table 2.7). More generally, the authors are not aware of a single published ultrasonic measurement result for Poisson's ratios that compare well with a corresponding mechanical measurement. Thus, ultrasonic-based values for Poisson's ratios are not considered as reference in this work.

Our ultrasonically determined shear stiffnesses compare well with ultrasonic measurements by the other authors, see e.g. Bucur and Archer (1984); Kohlhauser et al. (2008), but they deviate from a large number of quasi-statically determined shear stiffnesses, by up to 50% in longitudinal

planes [compare $G_{12} = 0.62 \pm 0.08$ and $G_{13} = 0.70 \pm 0.12$, $n = 10$ (Jenkin 1920; Carrington 1923; Hörig 1935; Stamer 1935; Doyle and McBurney 1946; Hearmon 1948; Kollmann and Côté 1968; Neuhaus 1981; Niemz and Caduff 2008)], and by up to 100% in radial-circumferential planes (compare $G_{23} = 0.033 \pm 0.007$, $n = 10$). However, these discrepancies are probably due to difficulties in mechanical testing of pure shear, which is known to underestimate shear stiffness. However, good agreement between ultrasonic and mechanical shear testing has been obtained by Soule and Nezbeda (1968) on graphite; and very recent mechanical tests of the transverse (radial-circumferential) shear modulus of spruce (Hassel et al. 2009), based on full field strain measurements on a single cube apparatus, delivered values of $G_{23} = 68.0 \pm 22.2$ MPa ($n = 9$), which agree well (i.e. within 10% relative error) with our ultrasonic measurements (see Table 2.8, column five, row nine to twelve).
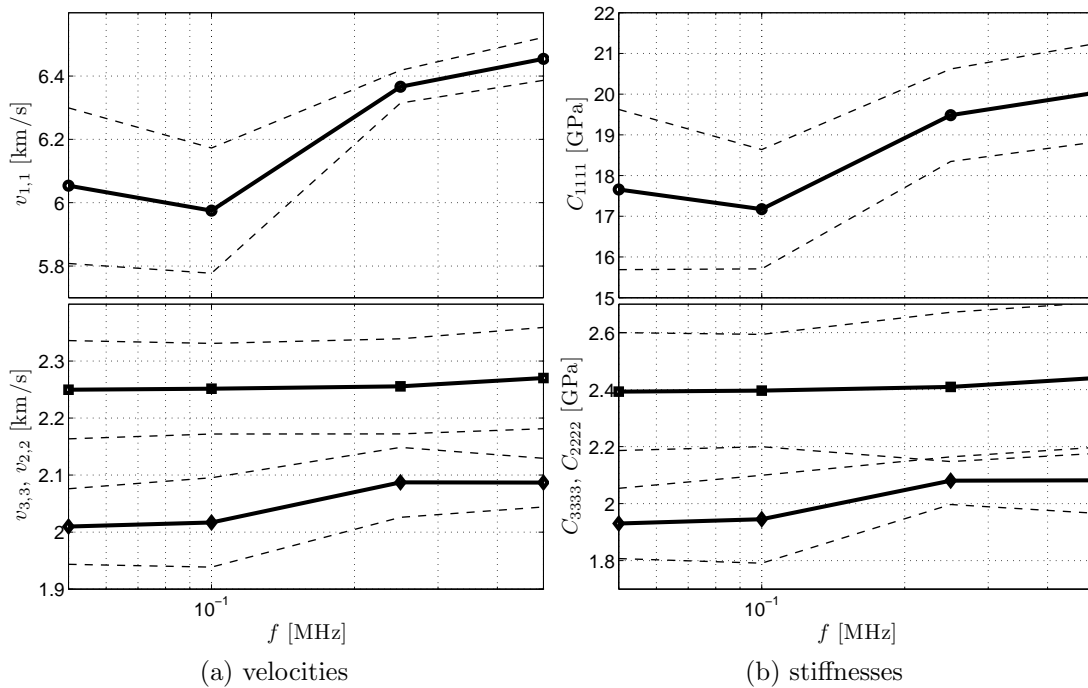
Figure 2.2: Influence of wave frequency on measured longitudinal wave velocities and stiffnesses in spruce [solid lines show averages over six values (two per tree), dashed lines show standard deviations of these values] — frequencies below or equal 100 kHz characterize the microheterogeneous material 'spruce wood'.

According to the fundamentals of continuum mechanics (Salençon 2001; Zaoui 2002), ultrasonically determined stiffnesses relate to representative volume elements (RVE) of a material being much smaller than the wavelength of the wave exciting the samples ($\ell_{RVE} \ll \lambda$), and the length of the RVE needs to be much larger than the inhomogeneities d within the RVE, so that material properties can be measured on the RVE ($\ell_{RVE} \gg d$). While RVEs of softwood or hardwoods with lumen inhomogeneities are clearly far smaller than the employed wavelengths, RVEs of (spruce) wood containing several growth rings are only 'felt' by waves with exciting frequencies of 50 and 100 kHz (see Table 2.6). This becomes evident from the ratios between d and λ_L reported in Table 2.6 and from the independence of wave velocities from frequency in Figure 2.2. Therefore, only measurements based on these two frequencies are reported in Table 2.8. Notably, when choosing $f = 250$ kHz instead of 100 kHz, the longitudinal and circumferential wave velocities $v_{1,1}$ and $v_{3,3}$ increase by 6.5 and 5%, respectively (see circles and diamond markers in Figure 2.2). These velocities (with wavelengths separated by less than factor ten from inhomogeneity size d, see Table 2.6, column ten and eleven) do not any more refer to the material 'spruce wood', but the effect of single growth rings in latewood transporting the

ultrasonic signals at a faster pace, becomes remarkable. This is not the case in the radial direction where no contiguous path of latewood rings between ultrasonic transmitter and receiver exists (see square markers in Figure 2.2). As compared to longitudinal waves, transversal waves are less sensitive to material inhomogeneities, and typically reveal the 'homogenized' behavior of a microheterogeneous material ($\ell_{RVE} \gg d$), already at d/λ_T-ratios as high as $d/\lambda_T = 0.1 - 1$ (Kohlhauser and Hellmich 2009b). This is the case for the transversal waves employed in the present study.

2.6.3 Poisson's ratios at known normal stiffnesses and longitudinal Young's modulus — functional representation

For a set of normal stiffnesses C_{1111}, C_{2222}, C_{3333}, and E_1, function $\mathcal{F}_{ortho,ij}(L, T)$ according to (2.35) exhibits both real and complex values depending on the set of argument pairs (L, T). For an axially nonauxetic material such as spruce wood, only positive real values of $\mathcal{F}_{ortho,ij}$ make physical sense. This, together with the relations

$$L = \frac{1 - \nu_{23}\,\nu_{32}}{1 - \nu_{13}\,\nu_{31}} \quad \text{and} \quad T = \frac{1 - \nu_{13}\,\nu_{31}}{1 - \nu_{12}\,\nu_{21}}, \tag{2.37}$$

which result from definition (2.36) and from Eq. (2.20), yields admissible values for Poisson's ratios, once C_{1111}, C_{2222}, C_{3333}, and E_1 are given, coinciding with the real values depicted as surfaces in Figure 2.3 (depicted as top view in Figure 2.4). In these figures, values represented through surfaces are computed from the average normal stiffnesses given in Table 2.8, rows 6, 12, and 18. Regions in the (L, T)-plane related to admissible Poisson's ratios are bounded by three curved lines which contact each other at non-smooth edges A, B, C, with coordinates $A(L = 0, T = 1)$, $B(L = 1, T = C_{1111}/E_1)$, and $C(L = C_{1111}/E_1, T = E_1/C_{1111})$. At all these three edge points, domains of real positive, real negative, and complex values of $\mathcal{F}_{ortho,ij}$ 'meet'. Accordingly, a large ratio C_{1111}/E_1 yields a wide range of T-values related to admissible Poisson's ratios. Nevertheless, this range of T-values depends on the values for L (see Figures 2.4). Hence, it is of interest to narrow the relevant ranges for T and L, as to further minimize the domain of admissible ν_{ij}'s. Therefore, we continue with discussing a wide range of mechanical tests revealing a typical value for T, as well as for the radial Young's modulus E_2.

2.6.4 Data collection on mechanical test-derived orthotropic Poisson's ratios on spruce's universal value for $T = (1 - \nu_{13}\,\nu_{31})/(1 - \nu_{12}\,\nu_{21})$

A collection of Poisson's ratios determined from different mechanical testing campaigns at different laboratories (see Table 2.7) reveals that the radial-to-circumferential ratio of normal stiffnesses of spruce, T, is always very close to 1, in fact, the scattering (in percent) around this value is two to even three orders of magnitude lower than the scattering related to the longitudinal-to-radial normal stiffness ratio L, as well as to each of the Poisson's ratios (see Table 2.7). Adapting this value $T = 1$ as relevant for any spruce wood sample, including those tested by the combined ultrasonic-mechanical method in Table 2.8, bold values in lines three to eleven and columns two to four, further contracts the domains of admissible Poisson's ratios, from 2D surfaces in Figure 2.3, to 1D lines in Figure 2.5 (a). This results in already narrow admissible ranges (around $0.4 - 0.5$) for ν_{31} and ν_{21}, irrespective of the actual value of L. Still, L has a major influence on all other Poisson's ratios, see Figure 2.5. In our present setting,

L depends on the transverse Young's modulus E_2, and a reliable spruce-related range of this quantity should finally give us characteristic values for all Poisson's ratios.
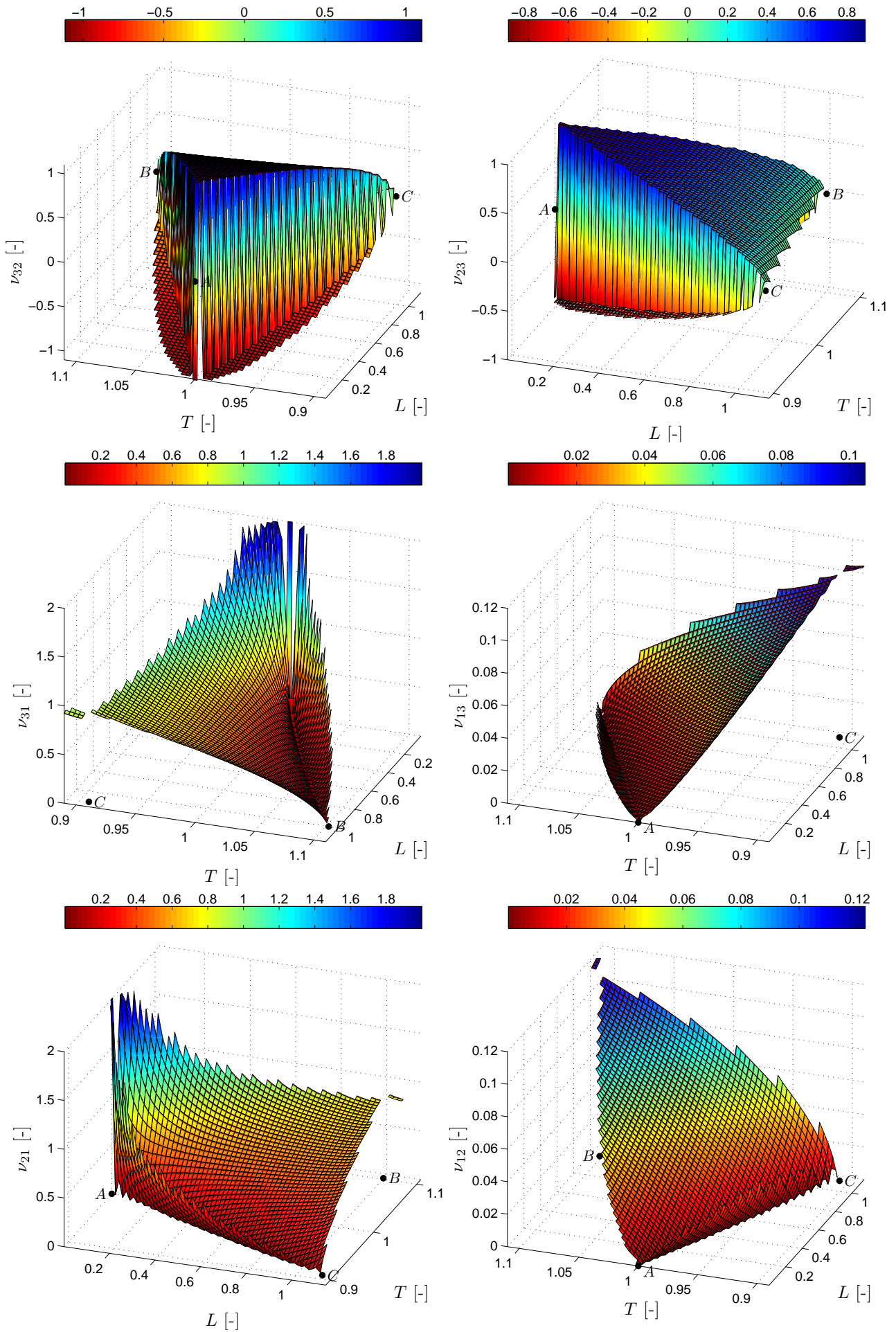
Figure 2.3: Poisson's ratios of spruce as function of ratios L and T from average stiffnesses in Table 2.8.
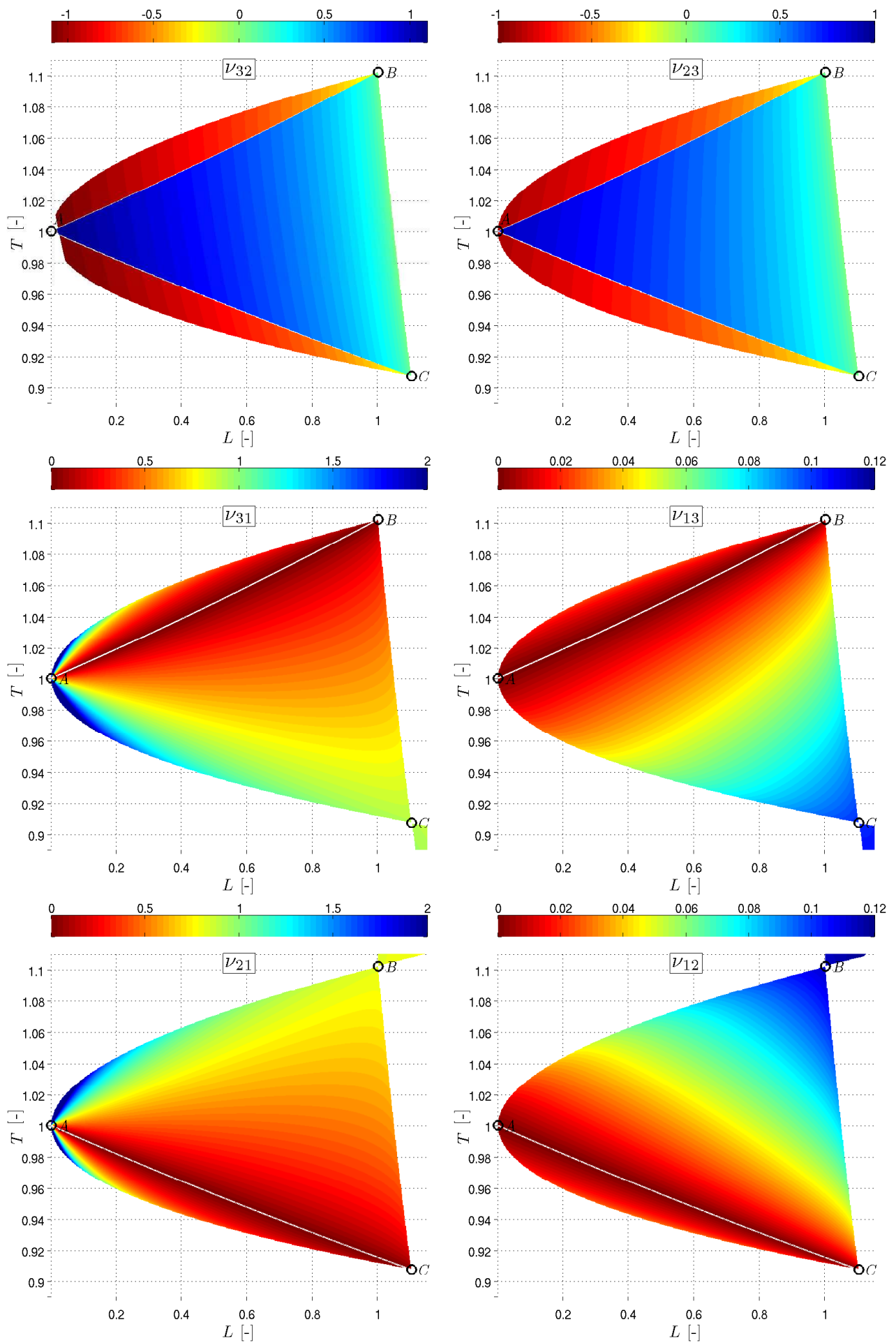
Figure 2.4: Poisson's ratios of spruce as function of ratios L and T from average stiffnesses in Table 2.8 — top view.

Table 2.7: Poisson's ratios ν_{ij} [-], ratios L [-] and T [-], and densities ρ [g/cm^3] for spruce compared with values from different literature sources: 1. . . Hearmon (1948) [collected data from Jenkin (1920); Carrington (1923); Hörig (1935); Stamer (1935); Doyle and McBurney (1946)], 2. . . Kollmann and Côté (1968), 3. . . Neuhaus (1981), 4. . . Niemz and Caduff (2008), 5. . . Bodig and Jayne (1993), 6. . . USDA (1999), 7. . . Dahl and Malo (2008), 8. . . Eberhardsteiner (2002).

literature	ρ	ν_{32}	ν_{31}	ν_{21}	ν_{23}	ν_{13}	ν_{12}	L	T
1	0.390	0.430	0.470	0.370	0.250	0.020	0.029	0.901	1.001
1	0.370	0.570	0.560	0.440	0.290	0.013	0.031	0.841	1.006
1	0.500	0.430	0.520	0.360	0.330	0.023	0.018	0.868	0.994
1	0.390	0.510	0.510	0.380	0.310	0.025	0.030	0.853	0.999
1	0.390	0.640	0.490	0.390	0.320	0.019	0.029	0.803	1.002
1	0.430	0.560	0.540	0.450	0.300	–	–	–	–
1	0.440	0.470	0.380	0.440	0.250	0.013	0.028	0.887	1.007
2	–	0.420	0.530	0.279	0.329	0.028	0.019	0.875	0.990
3	–	0.600	0.550	0.410	0.310	0.035	0.056	0.830	1.004
4	0.445	0.640	0.420	0.376	0.335	0.015	0.022	0.791	1.002
5	–	0.470	0.420	0.370	0.350	0.033	0.041	0.847	1.001
6	–	0.435	0.467	0.372	0.245	0.025	0.040	0.904	1.003
6	–	0.530	0.462	0.422	0.255	0.058	0.083	0.889	1.009
7	–	–	0.575	0.451	–	–	–	–	–
8	–	–	–	0.450	–	–	–	–	–
average	0.419	0.516	0.486	0.394	0.298	0.026	0.036	0.857	1.002
st. dev.	0.043	0.080	0.056	0.046	0.037	0.012	0.018	0.037	0.005
st. dev. [%]	10.2	15.6	11.5	11.8	12.3	48.7	51.5	4.3	0.5
50% fractile		0.510	0.489	0.394	0.296	0.023	0.032	0.857	1.002
5% fractile		0.316	0.337	0.271	0.200	0.006	0.008	0.746	0.985
95% fractile		0.823	0.709	0.574	0.438	0.094	0.130	0.984	1.018
5% fractile [%]		-38	-31	-31	-32	-75	-75	-13	-1.6
95% fractile [%]		61	45	46	48	303	305	15	1.7

this work	ν_{32}	ν_{31}	ν_{21}	ν_{23}	ν_{13}	ν_{12}	L	T
50% fractile	0.567	0.518	0.466	0.459	0.044	0.048	0.756	1.000
5% fractile	0.607	0.512	0.461	0.491	0.041	0.045	0.716	1.000
95% fractile	0.522	0.525	0.472	0.422	0.047	0.052	0.798	1.000

deviation	ν_{32}	ν_{31}	ν_{21}	ν_{23}	ν_{13}	ν_{12}	L	T
from avg.	0.052	0.032	0.072	0.161	0.018	0.013	-0.102	-0.002
from avg. [%]	10.0	6.6	18.4	54.0	70.4	36.6	-11.9	-0.2

2.6.5   Radial Young's modulus of spruce

Measuring reliable values for the radial Young's modulus of spruce is challenged by the correct measurement of strains. When estimating average strains from displacement measurements on macroscopic samples, local strain concentrations occuring together with strain softening ('strain localization') may artificially augment the average strain value estimated from such displacement measurements, yielding finally probably too low values for the radial Young's

(a) cross-section at $T = 1.00$ (b) cross-section at $L = 0.76$
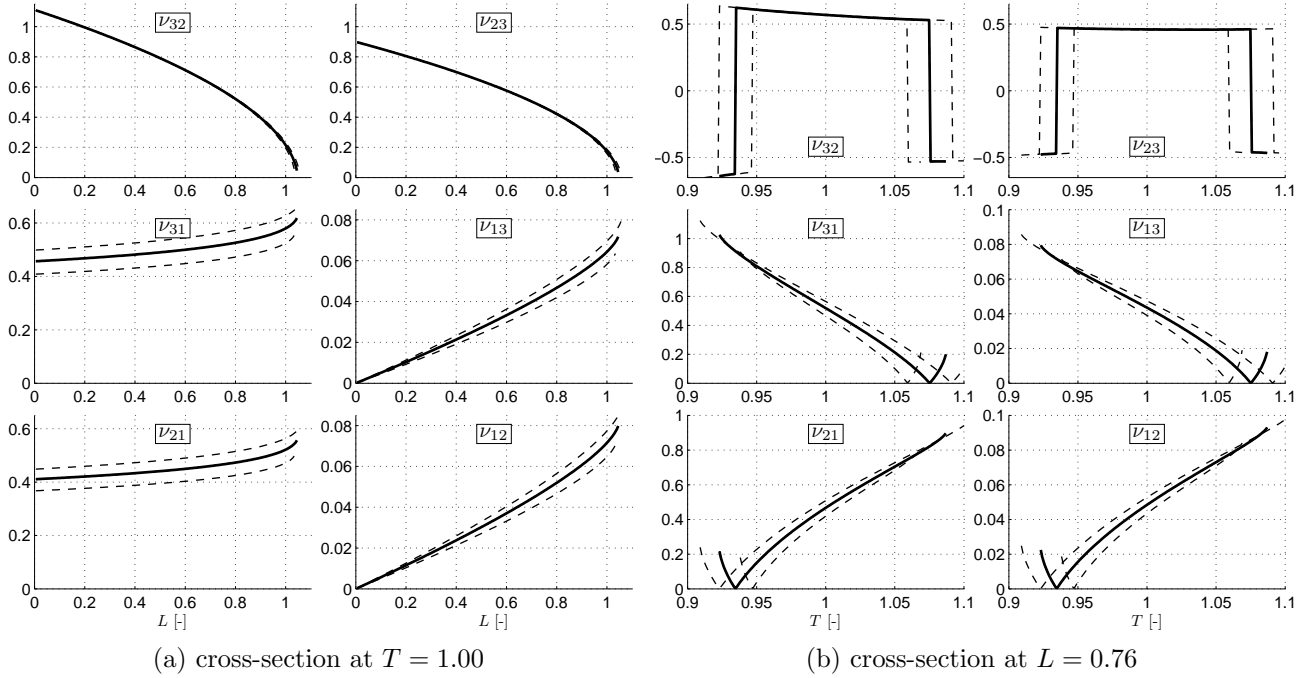
Figure 2.5: Poisson's ratio ranges: cross-sections through Figures 2.3 and 2.4 at relevant values of L and T for orthotropic softwood spruce (see Table 2.8; dashed lines indicate new ranges for deviations of C_{1111}/E_1 of $\pm 2\%$).

modulus of spruce (Miyauchi and Murata 2007). The inferiority of such values, amounting to $E_2 = 0.82 \pm 0.13$ GPa (Jenkin 1920; Carrington 1923; Hörig 1935; Stamer 1935; Doyle and McBurney 1946; Hearmon 1948; Kollmann and Côté 1968; Neuhaus 1981; Niemz and Caduff 2008) is underlined by their incompatibility, in the sense of Eqs. (2.23)–(2.29), with the fairly consistent set of Poisson's ratios in Table 2.7. Hence, a finer resolution of strains as that provided by extensometers is due, such as the digital speckle photography of Modén and Berglund (2008) who measured the radial Young's modulus on specimens with a length covering the complete radial range from pith to bark (≈ 20 cm) and a cross-section of 5×2 mm (longitudinal $\times$ circumferential directions), at a resolution of 50 μm, i.e. at the scale of a few wood cells. Focusing, in Figure 5 of Modén and Berglund (2008), on (micro-)densities between $0.45 - 0.50$ g/cm³ (coinciding with the macroscopic apparent density investigated in the present study in Table 2.8), suggests $E_2 = 1.41$ GPa. Given, however, the macroscopic apparent density of Moden and Berglund's specimens, amounting to ≈ 0.3 g/cm³, to be far smaller than that investigated at Table 2.8 of the present study, the aforementioned value is probably still lower than the one relevant for our case. Therefore, we evaluate the 50 μm-resolution digital speckle photographs of Jernkvist and Thuvander (2001), of a growth ring of 2.44 mm width (similar to widths given in Table 2.5) subjected to radial uniaxial tension, see Figures 4 (a) and 5 (a) of Jernkvist and Thuvander (2001). For each circumferential position [row position in Figure 2.6 (a)], we average the radial (micro-)strains ε_2^{micro} over the entire growth ring, as to obtain the 'macroscopic' radial strain ε_2

$$\varepsilon_2 = \frac{1}{\ell_{ring}} \int_{\ell_{ring}} \varepsilon_2^{micro} \, dr \,, \tag{2.38}$$

characteristic for the investigated sample of spruce wood. Given the uniaxial nature of the mechanical test of Jernkvist and Thuvander (2001), this radial strain, together with the known (*prescribed* uniaxial) radial stress σ_2, gives access to values for the radial Young's modulus $E_2 = \sigma_2/\varepsilon_2$, for each of the 476 rows of Figure 2.6 (a), representing the experimental scattering
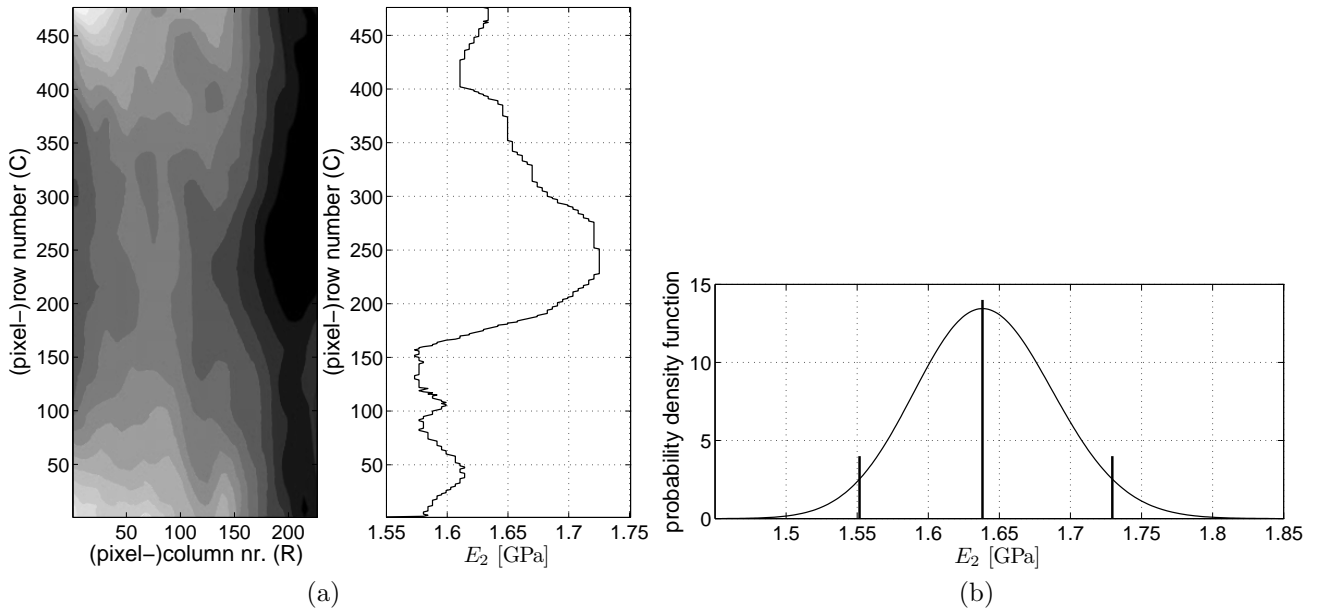
Figure 2.6: (a) Strain field in a growth ring of 2.44 mm width in radial direction and 5.40 mm in circumferential direction [black: $\varepsilon_2^{micro} = 0.7306 \cdot 10^{-3}$, white: $\varepsilon_2^{micro} = 3.8292 \cdot 10^{-3}$; from Jernkvist and Thuvander (2001)] and scattering of Young's modulus in radial direction, E_2, over circumferential direction and (b) log-normal distribution of E_2 with 5, 50 and 95%-fractiles.

of E_2 over the circumferential direction Figure 2.6 (b). These values for E_2 are characterized by a mean value of $E_2 = 1.64$ GPa, as well as by 5% and 95%-fractiles of 1.55 GPa (-5.3%) and 1.73 GPa ($+5.6\%$), respectively [see Figure 2.6 (b)].

2.6.6   Poisson's ratios of spruce — results
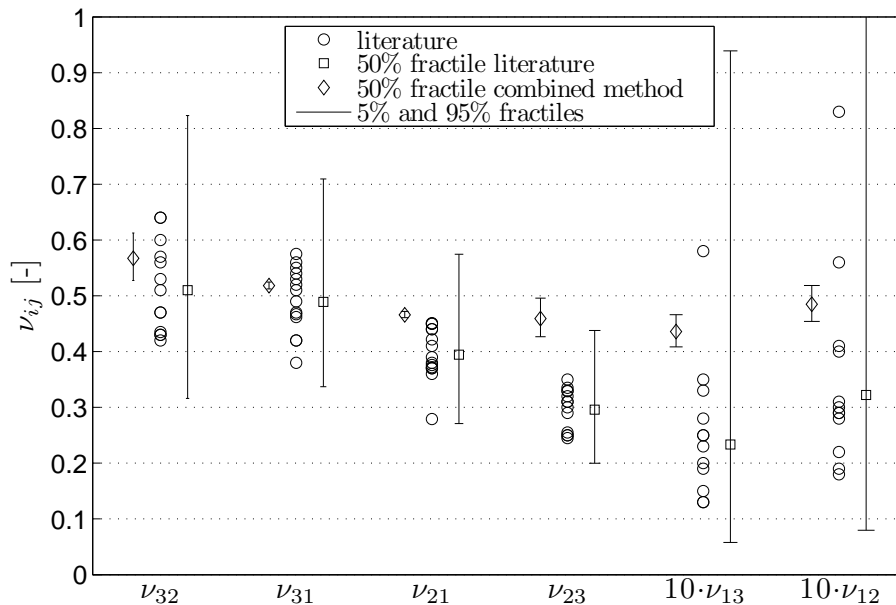
Figure 2.7: Poisson's ratios of spruce. Comparison of results with literature (given in Table 2.7).

Specification of admissible (positive) regions of Figures 2.3 and 2.4, for $T = 1$ and $E_2 = 1.64$ GPa (or for $E_{2,5\%} = 1.55$ GPa and $E_{2,95\%} = 1.73$ GPa) yields the sought expected values of Poisson's ratios for the samples of Table 2.5 (or of the 5% and 95%-fractiles, see Figure 2.7).

Table 2.8: Elastic constants of spruce (specimens from three different trees) from combined ultrasonic-mechanical tests (bold values from direct measurements; densities are average values from quasi-static and ultrasonic test specimens, see Table 2.5, columns five and ten).

elastic stiffness tensor constants	C_{1111} [GPa]	C_{2222} [GPa]	C_{3333} [GPa]	C_{1122} [GPa]	C_{1133} [GPa]	C_{2233} [GPa]
tree 1	**18.09**	**2.54**	**2.07**	1.78	1.61	1.34
tree 2	**17.80**	**2.25**	**1.84**	1.61	1.46	1.03
tree 3	**16.36**	**2.39**	**1.91**	1.78	1.59	1.16
average	17.42	2.39	1.94	1.72	1.55	1.18

engineering elastic constants	E_1 [GPa]	E_2 [GPa]	E_3 [GPa]	G_{23} [GPa]	G_{13} [GPa]	G_{12} [GPa]
tree 1	**16.52**	1.64	1.34	**0.077**	**0.95**	**1.05**
tree 2	**16.27**	1.64	1.34	**0.061**	**0.87**	**0.87**
tree 3	**14.65**	1.64	1.31	**0.085**	**0.92**	**0.91**
average	15.81	1.64	1.33	0.074	0.91	0.94

normal stiffness ratios & densities	ρ [g/cm^3]	L [-]	T [-]	C_{1111}/E_1 [-]	C_{1111}/C_{2222} [-]	C_{2222}/C_{3333} [-]
tree 1	**0.492**	0.706	1.000	1.10	7.12	1.23
tree 2	**0.481**	0.795	1.000	1.09	7.90	1.23
tree 3	**0.451**	0.765	1.000	1.12	6.84	1.25
average	0.475	0.756	1.000	1.10	7.29	1.24

Poisson's ratios	ν_{32} [-]	ν_{31} [-]	ν_{21} [-]	ν_{23} [-]	ν_{13} [-]	ν_{12} [-]
tree 1	0.614	0.489	0.442	0.500	0.040	0.044
tree 2	0.522	0.526	0.475	0.426	0.043	0.048
tree 3	0.566	0.539	0.481	0.451	0.048	0.054
average	0.567	0.518	0.466	0.459	0.044	0.048

Except for ν_{23}, they lie well within the ranges suggested by the collected literature data of Table 2.7, see Figure 2.7. Notably, the agreement for ν_{31} and ν_{21}, where the mechanical tests (with the uniaxial stress applied in the longitudinal direction) are most reliable as indicated by the lowest standard deviation in rows 20, 24, 25, columns four and five of Table 2.7, is very satisfactory. This underlines the relevance of the proposed method. This is far more so if one considers that the bars in Figure 2.7 relate to scattering among laboratory-specific *mean* values, while the scattering within the values from one and the same laboratory might be far larger [see e.g. Eberhardsteiner (2002), page 77 and Figure 4.6]. Also, the combined method for determination of Poisson's ratios is by far superior to the purely ultrasonic one [although relative measurement errors might propagate to the same extent in both the former (for $T = 1$) and the latter (see Table 2.9)], because the off-axis velocity measurement errors are enormous, as already mentioned in Section 2.1 and 2.6.2. On the other hand, in the case of spruce wood with $C_{1111}/E_1 = 1.10$, the additional information of $T = 1$ is important to restrict relative error enlargement during propagation (compare rows $16-21$ with rows $22-25$ in Table 2.9), while the relative errors do not significantly increase through propagation if $C_{1111}/E_1 > 1.20$ (as is the case for steel weld, see Table 2.4).

Table 2.9: Errors [%] induced in Poisson's ratios or normal and off-diagonal stiffness tensor components of orthotropic softwood spruce (see Section 2.6) considering 1% deviation of a measured property for three different methods to determine Poisson's ratios.

		C_{1111}	C_{2222}	C_{3333}	C_{1122}	C_{1133}	C_{2233}
mechanical	1% error in ν_{ij}						
	ref. [GPa]	17.42	2.39	1.94	1.72	1.55	1.18
	ν_{32} or ν_{23}	0.1	0.8	0.8	1.2	1.2	1.8
	ν_{31} or ν_{13}	0.1	0.1	0.1	0.4	0.8	0.1
	ν_{21} or ν_{12}	0.1	0.1	0.1	0.8	0.4	0.1
		ν_{32}	ν_{31}	ν_{21}	ν_{23}	ν_{13}	ν_{12}
ultrasonic	1% error in C_{iijj}						
	ref. [-]	0.569	0.517	0.465	0.461	0.043	0.048
	C_{1111}	0.1	0.0	0.0	0.1	−1.1	−1.1
	C_{2222}	0.0	0.8	−1.4	−1.1	1.1	0.0
	C_{3333}	−1.1	−1.4	0.8	0.0	0.0	1.1
	C_{1122}	−0.1	−1.2	2.2	0.0	−1.1	2.2
	C_{1133}	0.0	2.2	−1.2	−0.1	2.2	−1.1
	C_{2233}	1.1	−0.4	−0.4	1.1	−1.2	−1.2
		ν_{32}	ν_{31}	ν_{21}	ν_{23}	ν_{13}	ν_{12}
combined	1% error in C_{iiii}, E_i						
	ref. [-]	0.569	0.517	0.465	0.461	0.043	0.048
	C_{1111}	−1.1	5.4	5.3	−1.1	5.4	5.3
	C_{2222}	0.7	−11.5	10.3	0.7	−11.5	10.3
	C_{3333}	0.7	10.3	−11.5	0.7	10.3	−11.5
	E_1	1.0	−5.1	−5.1	1.0	−6.1	−6.1
	E_2	−0.2	11.0	−11.1	−1.1	11.0	−10.2
	E_3	−1.1	−11.1	11.0	−0.2	−10.2	11.0
$T = 1$	C_{2222} & C_{3333}	1.3	−0.7	−0.7	1.3	−0.7	-0.7
	E_2 & E_3	−1.4	0.2	0.2	−1.4	1.2	1.2
	C_{2222} & E_2	0.5	0.0	−0.5	−0.5	0.0	0.5
	C_{3333} & E_3	−0.5	−0.5	0.0	0.5	0.5	0.0

2.7 Conclusion

Poisson's ratios of isotropic, transversely isotropic, and orthotropic non-axially auxetic materials were expressed as functions of normal elastic stiffnesses, considering the positive definiteness of the stiffness and compliance tensors. Insertion of measured normal elastic stiffness values documented in the literature for (isotropic) aluminum, (transversal isotropic) aluminum matrix-fiber composite and (orthotropic) stainless-steel weld metal into the aforementioned functions yielded estimates for Poisson's ratios which agree very well with directly measured values. This confirmed the relevance of the proposed combined ultrasonic-mechanical method. Finally, the method was applied to (orthotropic) wood (namely spruce), by measuring four normal stiffnesses, and relying on a spruce-specific universal constant involving longitudinal Poisson's ratios, namely $T = (1 - \nu_{13}\nu_{31})/(1 - \nu_{12}\nu_{21}) = 1$, and on reasonable estimates for the radial Young's modulus. Resulting ranges of Poisson's ratios agree well with ranges of Poisson's ratios obtained from direct mechanical measurements on spruce. This is particularly the case for mechanical tests where the specimens are pulled in the longitudinal directions and strains are

measured in one of the transverse directions, which exhibit the highest experimental precision.

Acknowledgments

2.8 Appendix: Phase versus group velocities in ultrasonic tests

In *anisotropic* media (such as the ones investigated in Sections 2.5.2, 2.5.3, and 2.6), ultrasonic techniques may not detect phase velocities [as defined through Eq. (2.7)], but also so-called group velocities related to wave packets of more than one frequency [which is practically always the case (i.e. in wave pulse techniques), except for the continuous wave transmission techniques (Lynnworth et al. 1981)]. On the other hand, group and phase velocities are identical within *isotropic* media. Therefore, it seems appropriate to shortly recall the difference between group and phase velocity, and to show that the evaluation of our tests as described throughout the paper indeed always delivers phase velocities (which, *a priori*, is not so straight forward). The group velocity $\mathbf{v}_g$, defined as (Lighthill 1965; Auld 1990; Carcione 2001)

$$\mathbf{v}_g = \frac{\partial \omega}{\partial \mathbf{k}} \,, \tag{2.39}$$

can be shown to be identical to the energy velocity $\mathbf{v}_e$, which is defined as the time-averaged power flow vector $\langle \mathbf{p} \rangle = \langle \boldsymbol{\sigma} \cdot \mathbf{v}^\star \rangle$ ($\mathbf{v}^\star$ being a velocity vector along which work per time is done, $\langle . \rangle$ being the time average of quantity '.') over the time-averaged total (i.e. potential and kinetic) energy density $\langle E \rangle$ [(Carcione 2001), pages $16-19$]

$$\mathbf{v}_e = \frac{\langle \mathbf{p} \rangle}{\langle E \rangle} \,. \tag{2.40}$$

Definition (2.40) implies (Fedorov 1968; Auld 1990; Wolfe 1998; Carcione 2001)

$$\mathbf{v}_e \cdot \mathbf{n} = v_p = \mathbf{v}_g \cdot \mathbf{n} \,, \tag{2.41}$$

which results from extension of the momentum balance used in Section 2.3, to a power form [through multiplication with velocity vector $\mathbf{v}^\star$, (Carcione 2001), page 17]. It follows from (2.41) that

$$\mathbf{v}_g = \frac{\partial v_p}{\partial \mathbf{n}} = \mathbf{v}_{env} \,, \tag{2.42}$$

which is the defintion of the so-called envelope velocity $\mathbf{v}_{env}$ (Shercliff 1970; Carcione 2001), being identical to the group and energy velocities in elastic media [but not necessarily in attenuating media, (Carcione 2001), page 20]. According to (2.41), the wave group or energy travels faster than or as fast as the wave phase, and the group velocity direction deviates (Musgrave 1970), by an angle of $\alpha = \arccos\left(\mathbf{v}_e \cdot \mathbf{n}\right)/|\mathbf{v}_e|$, from the phase velocity (which is directed towards $\mathbf{n}$, i.e. $\mathbf{v}_p = v_p \mathbf{n}$). In test set-ups like the ones dealt with in this paper, where transducers of sizes comparable to that of the tested specimen are put onto opposite surfaces of the latter [see Figure 2.8 (a); and where the transducer is large as compared to

(a) plane-wave source   (b) point source
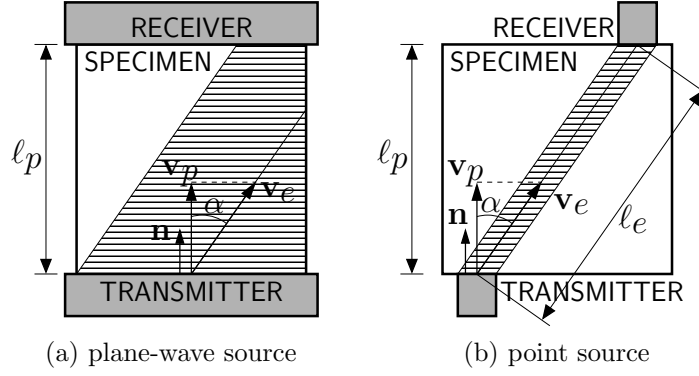
Figure 2.8: Measuring (a) phase and (b) group/energy velocities, in ultrasonic measurement systems with (a) plane-wave sources and (b) point sources — all experiments dealt with in this paper refer to case (a).

the wavelength, so that a plane wave is generated (Musgrave 1954)], the time of flight, t_f, can only be related to the normal distance ℓ_p between transmitter and receiver, and both t_f and ℓ_p indeed give access to v_p [see Eq. (2.3)], irrespective of the energy flux direction, see Figure 2.8 (a) as well as the discussions of Musgrave (1954); Sahay et al. (1992); Every (1980, 1994); Wolfe and Hauser (1995); Wolfe (1998); Carcione (2001). As a further comment on the ultrasonic tests dealt with in this paper, α in Figure 2.8 (a) is *only* non-zero for the off-diagonal quasi-longitudinal and quasi-transversal wave velocity measurements [this might induce the frequently encountered measurement errors in these directions (Kriz and Stinchcomb 1979)], and zero in all other cases, i.e. for waves traveling in principle material directions, group and phase velocities coincide. Also oblique pulse transmission techniques, e.g. immersion techniques (Rokhlin and Wang 1989, 1992), allow for phase velocity measurements [for details see (Every 1994)]. However, when using pulse transmission techniques where the transducers are much smaller than the specimens [see Figure 2.8 (b)], the receiver must be placed correctly (Sahay et al. 1992) as to receive any signal (which follows the energy flux direction), while in (pulse) echo techniques the acoustic echo returns to the source even for strongly oblique energy flux directions (Wolfe 1998). In these cases, the total distance ℓ_e between the transducers, when combined with t_f, gives access to the energy velocity, through

$$v_e = \frac{\ell_e}{t_f}, \tag{2.43}$$

where $\ell_e \cos \alpha = \ell_p$, which reflects a specific case of the general relation (2.41) (Wolfe 1998; Carcione 2001). Point sources and group velocity measurements can be suitably realized with laser-generated ultrasound (Castagende et al. 1991). In these cases, determination of elastic constants needs to be approached indirectly, as there does not exist any simple relation analogous to (2.5), that would relate group velocities to elastic constants (Every and Sachse 1990; Kim 1994; Kim et al. 1997; Degtyar and Rokhlin 1997).

Publication 3

Ultrasonic characterisation of porous biomaterials across different frequencies (Kohlhauser et al. 2008)

Authored by Christoph Kohlhauser, Christian Hellmich, Chiara Vitale-Brovarone,
Aldo R. Boccaccini, Astrid Rota and Josef Eberhardsteiner
Published in *Strain*, Volume 45, pages 34–44

Mechanical testing is the most common experimental technique to determine elastic stiffness of materials. In case of porous materials, especially such with very high porosity, the determination of material stiffness may be strongly biased by inelastic deformations occurring in the material samples, especially in the vicinity of the load transfer devices, such as loading platens. In contrast, ultrasonic waves propagating through a material generate very small stresses and strains (and also strain rates lying in the quasistatic regime). Thus, they enable the direct determination of the components of elastic stiffness tensors of materials, and also of those with a very high porosity. We shortly revisit from the theoretical basis of continuum (micro)mechanics that, depending on the frequency of the employed acoustical signals, the investigated materials are characterised at different observation scales, e.g. the elasticity of the overall porous medium, or that of the solid matrix inside the material are determined. We here report the elastic properties of biomaterials and biological materials at different length scales, by using ultrasound frequencies ranging from 100 kHz to 20 MHz. We tested isotropic scaffolds for biomedical engineering, made up of porous titanium and two different bioactive glassceramics, and we also determined the direction-dependent normal and shear stiffness components of the anisotropic natural composite spruce wood.

3.1   Introduction

The elastic stiffness of materials is often determined by means of mechanical testing, by referring the force exerted on the samples to the nominal crosssection of the latter (to define stress) and by dividing this stress by the corresponding strain, approximated as the relative displacement of the

load platens over the sample height. However, because of nonhomogeneous strain distributions within the sample (often reflected by the absence of any linearity in corresponding stressstrain curves), it is sometimes very difficult or even impossible to extract the elastic modulus of the material from the stressstrain curve obtained in a mechanical test. This is particularly the case for very porous materials. If the latter are comprised of open cell-type microstructures, corresponding stressstrain curves are not even monotonic, but rather of the zigzag type (see, e.g. Figure 6 of Chen et al. (2006) as regards mechanical testing of Bioglass®-derived highly porous glassceramic scaffolds), because of local collapse of the struts and plates building up the cellular foams.

These problems can be circumvented by ultrasonic measurement techniques, as they imply the application of only very small stresses to the material, avoiding any inelastic phenomena in the tested samples. Ultrasonic techniques are based on the measurement of wave propagation velocities, so that it is relatively easy to determine all components of the (isotropic or anisotropic) elasticity tensors (or related technical constants such as Youngs moduli and Poissons ratios) from one sample, reducing the expenditure needed for specimen preparation.

Elasticity determination through ultrasonics has been applied to a wide range of materials, including single-crystal and polycrystalline materials since the 1940s (Hearmon 1946; Huntington 1947), geomaterials and composite materials since the 1970s (Helbig 1994; Markham 1970), and biological materials such as bone and wood since the 1980s (Ashman et al. 1984; Bucur and Archer 1984). To the knowledge of the authors, they have at most very rarely been applied to biomaterials for biomedical engineering (Thelen et al. 2004). Hence, we here describe ultrasonic testing of biomaterials for which experimental data have never been gained so far. To gain additional confidence in our measurement device, we also conducted experiments on a biological composite, spruce wood, and compared the results with those published (Bucur and Archer 1984).

This paper is divided into four main parts. First, the processing and the microstructure of the aforementioned materials are described, followed by a formulation of the methods used for determination of density, porosity, ultrasonic wave velocity and elastic stiffness. Determination of the elastic stiffness is based on classical continuum elastodynamics, while considering the proper micromechanical definition of material volumes and a structure built up thereof. Experimental results for spruce wood, porous titanium, porous Bioglass®-ceramic foams, and porous CEL2 glassceramic scaffolds are followed by a short summary and conclusion.

3.2   Materials

At Vienna University of Technology, Laboratory for Micro and Nanomechanics of Biological and Biomimetic Materials, four different types of porous materials were tested ultrasonically. In order to reproduce well-accepted results of the literature as a baseline for our investigations, the first material tested was spruce wood (Figure 1), the material properties of which are characterised by orthorhombic symmetry. The remaining three material types were man-made biomaterials, namely porous titanium, produced at the Fraunhofer Institute for Manufacturing Technology and Applied Materials Research (Bremen), Bioglass®-based open scaffolds, produced at Imperial College London, and CEL2 glassceramic, produced at Politecnico di Torino, Italy. These biomaterials, all isotropic, were provided in the form of dense and porous specimens, of different shapes and sizes (see Figures 3.2–3.6).

3.2.1 Spruce wood

Wood has a cellular structure. The wood cells (prosenchymatous cells called tracheids) are hollow tubes oriented in the direction of the stem (i.e. longitudinal direction). In softwood, such as spruce, the cells are 1-3 mm long (Kollmann 1982; Wagenführ 1989), and they exhibit a diameter which ranges typically from 20 to 40 μm (see Figure 3.1, in particular the image of the right-side panel, for the microstructure of wood in a transverse cross-section, i.e. in a plane perpendicular to the longitudinal direction). Smaller cell diameters and thicker cell walls are found in latewood, while larger diameters and thinner walls are found in earlywood. The average cell wall thickness in earlywood is 4 μm, and that in latewood is 9 μm (Fengel and Wegener 2003). Two adjacent, concentric layers of earlywood (with lower mass density) and latewood (with higher mass density) form an annual ring with a thickness of 1 to 2 mm (see left and right panel images of Figure 3.1 for the entire width of a growth ring and for an annual ring border, respectively). This cellular structure is the cause for the orthotropic elastic properties of spruce, with the three orthogonal symmetry planes being the longitudinal, radial and tangential planes, defined by the natural growing directions of a tree, i.e. the stem direction, the direction orthogonal to the growth rings, and the circumferential direction orthogonal to the two aforementioned directions.

3.2.2 Porous titanium

Porous titanium is produced by compaction of a mixture of (i) metal powder, (ii) paraformaldehyde spheres of 500 μm characteristic size, which function as space holders for spherical pores, and (iii) process aids that are dissolved in water to ensure bonding of the constituents. Subsequently, the space holder material is removed from the mixture by means of chemical (catalytic) processes. Then, the material is sintered for 2 h at 1300°C in an argon atmosphere, at atmospheric pressure. In this way, cylindrically shaped specimens (Figure 3.2) with and without polymer sphere-induced pores, i.e. dense and porous specimens, were produced (see Figures 3.3 and 3.4 for the microstructure of these materials).
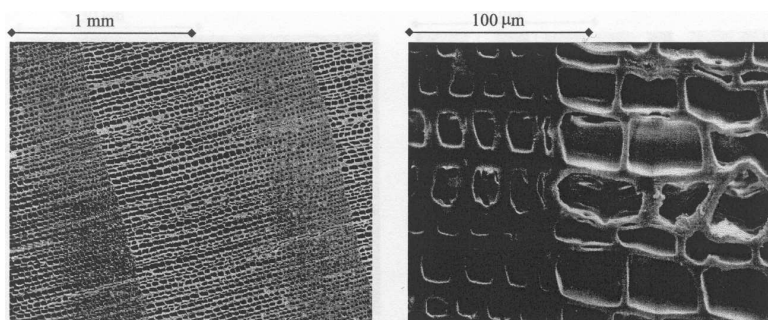
Figure 3.1: SEM micrograph images, showing spruce wood anatomy in transversal direction (reproduced from Lichtenegger (1999) with permission from H. Lichtenegger)

Figure 3.2: Titanium samples (left porous, right dense)

3.2.3 Bioglass®-derived glass-ceramic scaffolds

Bioglass® is a bioactive and biodegradable material with a molar composition of 46.1% SiO_2, 24.4% Na_2O, 26.9% CaO and 2.6% P_2O_5 (Chen et al. 2006). Scaffolds with slightly different porosities, as well as dense specimens (Figure 3.5) were manufactured. A fully reticulated
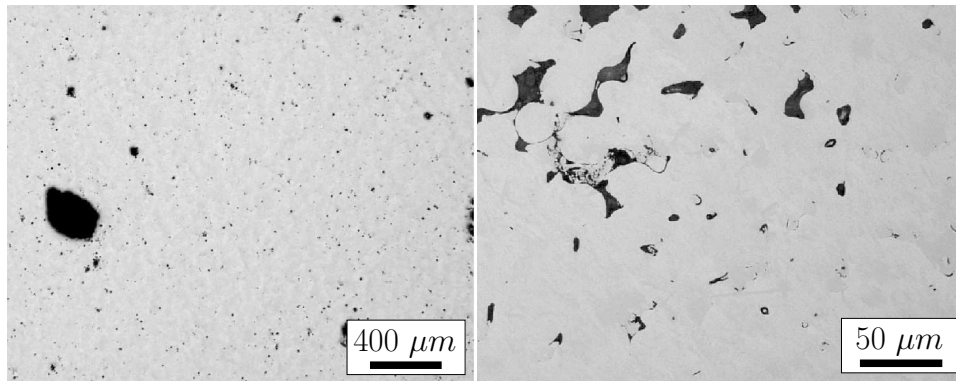
Figure 3.3: Two micrographs of dense titanium

white polyester-based polyurethane foam with a pore size in the range of 1080-1580 μm, used as template for a skeletal structure, was impregnated with a slurry made of melt-derived 45S5 Bioglass® powder with a particle size smaller than 5 μm, of poly-D,L-lactic acid (PDLLA) and of dimethylcarbonate (DMC). After drying of this material, the resulting green bodies were heat-treated at 1050°C for 3 h. During this period, the organic phases PDLLA, DMC and the polyurethane foam burned out, and the Bioglass® phase sintered. As a result, hollow struts formed by smoothly shaped particles form a foamtype microstructure with approximately 800 μm characteristic pore size (Figure 3.7), inside cuboidshaped specimens (Figure 3.5).

3.2.4   CEL2-derived glass-ceramic scaffolds

Highly bioactive glass (CEL2) with a molar composition of 45% SiO_2, 26% CaO, 15% Na_2O, 7% MgO, 4% K_2O and 3% P_2O_5 was synthesised by melting the raw products at 1400°C for 1 h, followed by quenching in cold water, grounding and sieving to a grain size of <30 μm (Vitale-Brovarone et al. 2007). The manufacturing of the CEL2 glass–ceramic scaffolds is similar to the aforementioned procedure described for the Bioglass®-based scaffolds. A polymeric template exhibiting a porous microstructure was impregnated with a suitable water-based powder suspension containing the aforementioned glass powder, together with 6 wt.% polyactic acid as binder, Figure 3.8. Then, thermal treatment above the crystallisation temperature of the used glass (around 800°C) burned out the organic phase, sintered the inorganic phases, led to a partial crystallisation of the glass, and delivered cuboidshaped samples (Figure 3.6) of CEL2 glassceramic scaffolds with approximately 500 μm characteristic pore size (Figure 3.8).
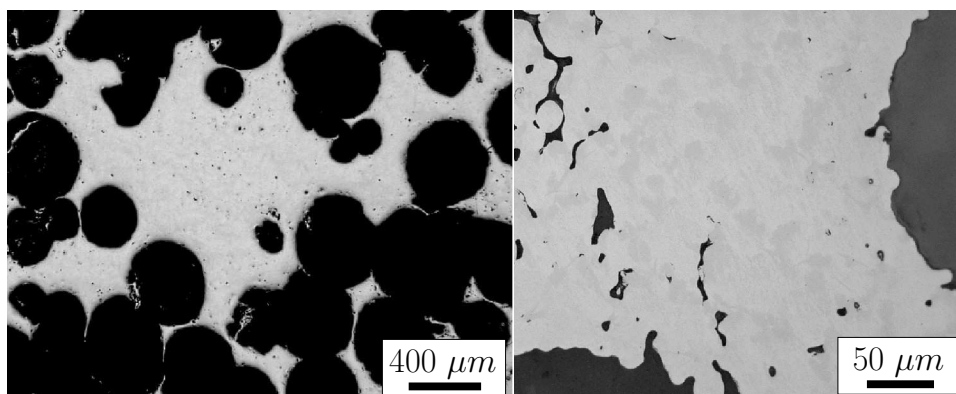
Figure 3.4: Two micrographs of porous titanium

Figure 3.5: Bioglass®-ceramic samples (left dense, right porous)

Figure 3.6: CEL2 glassceramic samples (left dense, right porous)

3.3 Methods

3.3.1 Density and porosity

All governing geometrical quantities of the cylindrical or cuboid-shaped specimens, such as height H, diameter D, or edge length A and B, were measured five times at different positions, and the corresponding average values were used for computation of the volume and the density of the samples. The apparent mass density ρ_{app} (g cm^{-3}) of specimens was determined by dividing the mass M (g) of each specimen by its volume V (cm^3), i.e.

$$\rho_{app} = \frac{M}{V} \tag{3.1}$$

Additional measurement or knowledge of the mass density of the solid phase ρ_s (g cm^{-3}) in the samples (see *Results* section for numbers) yields the sample-specific porosity ϕ (%) as

$$\phi = \frac{\rho_{app} - \rho_s}{\rho_s} \times 100 \,. \tag{3.2}$$

The number of specimens of each material, their masses, dimensions, densities and porosities are given in Tables 3.1, 3.3, 3.5 and 3.9.
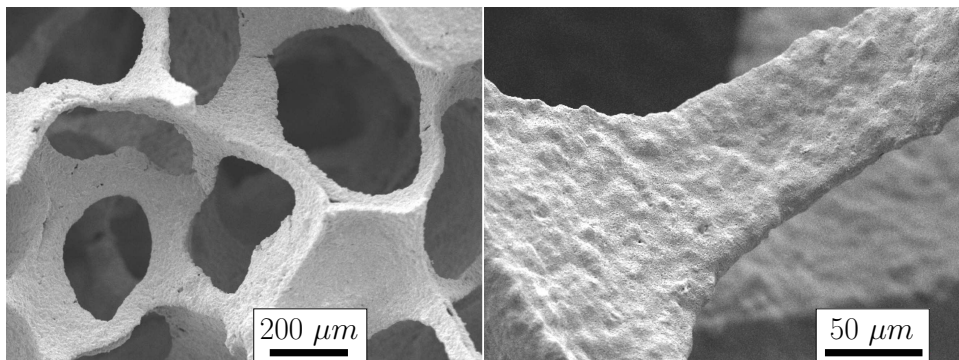
Figure 3.7: Bioglass®-ceramic scaffold and magnified strut
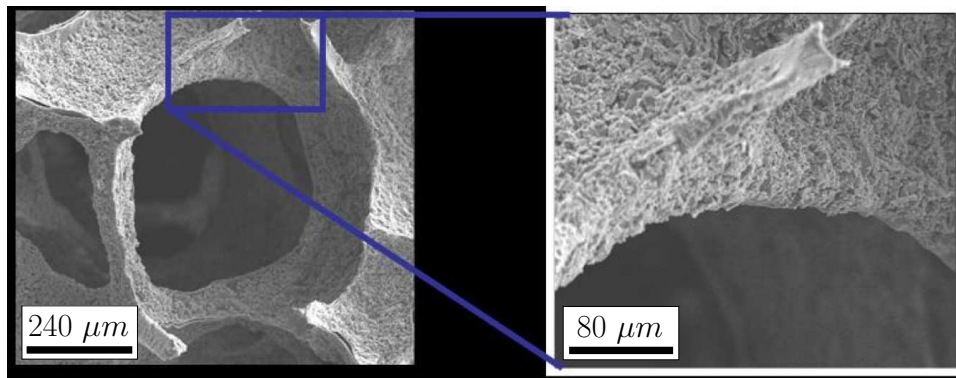
Figure 3.8: Polymeric sponge covered with CEL2-glass slurry – subsequent sintering leads to CEL2-derived glass-ceramic scaffolds

3.3.2 Ultrasonic wave velocity — equipment and experiment

The equipment for performing ultrasonic measurements consists of a pulser receiver PR 5077 (Panametrics Inc., Waltham, MA USA; see Figure 3.9), an oscilloscope and several ultrasonic transducers (see Figure 3.10). Seven different pairs of Panametrics Inc. transducers were used: X1020 and V1011 (0.1 MHz), two C602 (1.0 MHz), two V112 (10 MHz), V112 and V116 (20 MHz), two V151 (0.5 MHz, transversal), two V155 (5 MHz, transversal) and two V221 (10 MHz, transversal).

Figure 3.9: Pulser receiver

Figure 3.10: Ultrasonic transducers

The pulser unit emits an electrical square-pulse of up to 400 V pulse voltage, with frequencies from 0.1 to 20 MHz. The piezoelectric elements inside the ultrasonic transducers transform such electrical signals into mechanical signals (when operating in the sending mode, transferring, via a coupling medium, the mechanical signals to one side of the specimen under investigation), or they transform mechanical signals back to electrical signals (when receiving mechanical signals having travelled through the specimen under investigation). The coupling medium for longitudinal waves can be water or another suitable liquid. In order to transmit shear forces into the medium, the coupling medium for transversal waves must be a highly viscous material, e.g. honey. We used honey as the coupling medium for both longitudinal and transversal waves. The influence of the type of honey is very small, as it only provides a connection for the ultrasound to be transmitted from the transmitter to the sample. The higher the viscosity, the better the shear wave transmission, as less damping of the ultrasonic beam occurs. The use of any standard viscous honey is possible. To our knowledge, there are no restrictions concerning the quality of the honey. The piezoelectric elements are tailored to the frequency of the employed mechanical signal: the higher the frequency, the smaller the element and the corresponding transducer

(see Figure 3.10). Depending on the cut and orientation of the element, a longitudinal or a transversal wave is emitted. The receiver unit of the pulser receiver has a bandwidth of 0.1–35 MHz and a voltage gain of up to 59 dB. The amplified signal is displayed on an oscilloscope WaveRunner 62Xi (Lecroy Corporation, Chestnut Ridge, NY, USA) with a bandwidth of 600 MHz and a sample rate of 10 GS s^{-1} (gigasamples per second). The oscilloscope gives access to the time of flight of the ultrasonic wave through the specimen, t_s (μs), which provides, together with the travel distance through the specimen, ℓ_s (mm), the phase velocity (km s^{-1}) of the longitudinal (compressional) or transversal (shear) wave, v_L or v_T, reading as

$$v_i = \frac{\ell_s}{t_s} \, . \tag{3.3}$$

We used two transducers here, one sending a signal into the specimen and one receiving the sent signal at the opposite side of the specimen (transmission through technique, see Figure 3.11). As the pulse travels only once through the specimen, the influence of signal attenuation is minimised, and problems emanating from reflection of waves are avoided. However, in contrast to the pulse echo technique where a single transducer acts as both signal sender and receiver, both transducers need to be coupled with the specimen, which may increase measurement errors related to wave velocity. Moreover, the exact identification of the arrival time of the received signal (first apparent deviation from time axis) is a source of measurement inaccuracies, especially for small thicknesses of the specimens and corresponding short times of flight. Still, ultrasonic techniques are in general satisfactorily exact, as the wave velocity related to the time of flight via Equation (3.3), is directly related to the material stiffness, as described next.
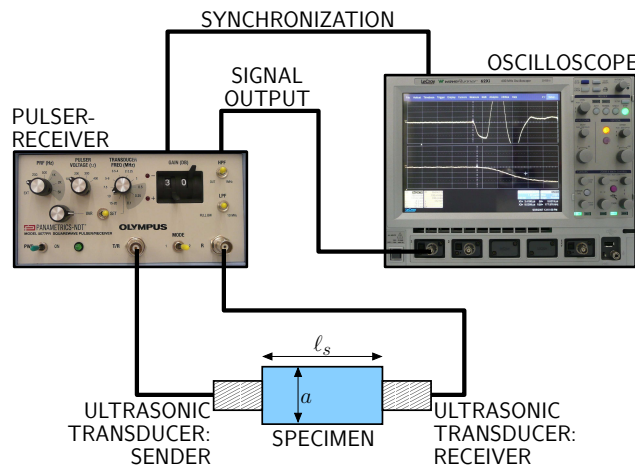
Figure 3.11: Transmission through technique

3.3.3 Elastic stiffness — theory of ultrasonic wave propagation

Frequency f (MHz) and wave velocity v (km s^{-1}) of an ultrasonic wave give access to the wavelength λ (mm), through (Newton 1687; Carcione 2001),

$$\lambda = \frac{v}{f} \, . \tag{3.4}$$

If the wavelength is considerably smaller than the characteristic length a (mm) of the sample surface where the transducer is applied (see Figure 3.11, either diameter D or edge length A, B), a (compressional) bulk wave, i.e. a laterally constrained wave, propagates in a quasi-infinite medium. On the other hand, if the wavelength is larger than the characteristic length a of the

side of the specimen where the transducer is applied, a bar wave propagates, i.e. the specimen acts as one-dimensional bar without lateral constraints (Ashman et al. 1984; Kolsky 1953). Mathematically,

$$\frac{a}{\lambda} \gg 1 \dots \text{bulk wave} \qquad \text{and} \qquad \frac{a}{\lambda} < 1 \dots \text{bar wave.} \tag{3.5}$$

In contrast, shear waves propagate identically in quasi-infinite media and bar-like structures (Ashman et al. 1987).

As regards bulk waves, combination of the conservation law of linear momentum, the generalised Hookes law, the linearised strain tensor and the general plane wave solution for the displacements inside an infinite solid medium yields the elasticity tensor components as functions of the material mass density and the wave propagation velocity (Carcione 2001), reading for isotropic materials as

$$C_{1111} = \rho\, v_L^2 \qquad \text{and} \qquad C_{1212} = G = \rho\, v_T^2\,, \tag{3.6}$$

where C_{1111} and $C_{1212} = G$ (GPa) are the elastic stiffness tensor components related to normal and shear deformation, the second equation of Equation (3.6) being valid for both quasi-infinite spatial structures and bar-type structures.

Combination of Equation (3.6) with the definitions of the engineering constants Youngs modulus E (GPa) and Poissons ratio ν (−), yields the latter as functions of the wave velocities, in the form

$$E = \rho\frac{v_T^2\,(3\,v_L^2 - 4\,v_T^2)}{v_L^2 - v_T^2} \qquad \text{and} \qquad \nu = \frac{v_L^2/2 - v_T^2}{v_L^2 - v_T^2}\,, \tag{3.7}$$

respectively. Orthotropic materials have nine independent elastic stiffness tensor components and thus nine engineering constants. In order to determine all of them, at least nine wave velocities in different propagation directions must be known. We will focus on determination of diagonal (normal and shear) stiffness tensor components according to

$$\begin{array}{llllll}
C_{\ell\ell\ell\ell} & = & \rho\, v_{L|\ell}^2\,, & C_{rrrr} & = & \rho\, v_{L|r}^2\,, \\
C_{tttt} & = & \rho\, v_{L|t}^2, & & & \\
C_{rtrt} & = & \rho\, v_{T|r,t}^2\,, & C_{\ell t\ell t} & = & \rho\, v_{T|\ell,t}^2\,, \\
\text{and} \quad C_{\ell r\ell r} & = & \rho\, v_{T|\ell,r}^2\,, & & &
\end{array} \tag{3.8}$$

where ℓ, r and t indicate the principal material directions of wood, i.e. different planes of symmetry of the orthotropic material in which the wave is propagating. For both longitudinal $v_{L|i}$ and transversal $v_{T|i,j}$ velocities, the second index stands for the propagation direction of the wave, whereas for a transversal wave, indicated by three indices, the third index defines the polarisation direction.

In the case of bar wave propagation, we have (Kolsky 1953)

$$E = \rho\, v_{bar}^2\,, \tag{3.9}$$

where v_{bar} is the velocity of a bar wave.

In continuum (micro)mechanics (Zaoui 2002), the elastic properties [Equations (3.6)–(3.9)] are related to a material volume (representative volume element RVE), with a characteristic length ℓ_{RVE} (mm) being considerably larger than the inhomogeneities d (mm) inside the RVE, and the RVE being subjected to homogeneous stress and strain states. Hence, the characteristic length of the RVE, ℓ_{RVE}, needs to be much smaller than the scale of the characteristic loading of the medium, here the wavelength λ. Mathematically,

$$d \ll \ell_{RVE} \ll \lambda\,. \tag{3.10}$$

Therefore, ultrasonic tests at different frequencies 'detect', inside a sample, materials at different

observation scales, such as the macroscopic porous material or the solid phase of the material, as described for bone in Hellmich (2005); Fritsch and Hellmich (2007). In this way, the elastic properties of spruce wood, porous titanium, Bioglass®-ceramic scaffolds and CEL2-derived glass-ceramic scaffolds were characterised at different observation scales.

3.4   Results

3.4.1   Spruce wood

Three cuboid-shaped specimens were cut so that each of them allowed a measurement in one of the three symmetry planes through a distance H of approximately 20 mm. The densities of the three samples are close to the value of $\rho_{app} = 0.430$ g cm^{-3}, commonly given in the literature for spruce wood (Wagenführ 1989). The porosity is estimated according to Equation (3.2), with $\rho_s = 1.4$ g cm^{-3} (see Table 5 in Hofstetter et al. (2005)) as the mass density of the cell wall material. This results in $\phi \approx 70\%$ (see Table 3.1).

Table 3.1: Spruce wood specimens: geometry, mass and porosity

	No.	H	A	B	V	M	ρ_{app}	ρ_s	ϕ
	[-]	[mm]	[mm]	[mm]	[mm^3]	[g]	[g/cm^3]	[g/cm^3]	[%]
Equation							(3.1)		(3.2)
Longitudinal	1	21.12	47.04	40.33	40073	16.890	0.421	1.4	69.9
Radial	1	19.81	40.70	40.58	32715	13.982	0.427	1.4	69.5
Transverse	1	20.75	40.67	41.12	34698	14.391	0.415	1.4	70.4

Table 3.2: Elasticity of spruce wood samples, determined from propagation velocity of bulk waves

	Polarisation	f	$v_{L|i}, v_{T|i,j}$	d	ℓ_{RVE}	λ	a/λ	C_{iiii}, C_{ijij}
	[-]	[MHz]	[km/s]	[mm]	[mm]	[mm]	[-]	[GPa]
Equation			(3.3)		(3.10)	(3.4)	(3.1)	(3.8)
ℓ	Longitudinal	1.0	6.38	0.03	≥ 0.15	6.4	3.6	17.2
r			2.26			2.3	9.3	2.19
t			2.03			2.0	11	1.71
ℓr	Transversal	0.5	1.47	0.03	≥ 0.15	2.9	15	0.760
$r\ell$			1.19			2.4	17	
ℓt			1.50			3.0	15	0.885
$t\ell$			1.41			2.8	14	
rt			0.35			0.7	58	0.076
tr			0.49			1.0	42	

Longitudinal waves at ultrasonic frequencies f of 1 MHz and transversal waves of 0.5 MHz were employed to characterise three cuboidal spruce wood samples. The waves travelled along the

height H of each sample. A cellophane sheet was inserted between the coupling medium honey and the sample, as to keep the wood microstructure free from honey. The latter might change the properties of the wood cell wall material.

The inhomogeneities within an RVE of 'spruce softwood' are the wood cells with an average diameter of $d = 30$ μm. Thus, the ultrasonic waves with frequencies of 0.5 and 1.0 MHz and velocities of typically $\approx$ 1.5–2 km s^{-1} (see Table 3.2), implying [according to Equation (3.4)] wavelengths of typically $\approx$ 2–3 mm, characterise [according to Equation (3.10)] an RVE of 'spruce softwood' with $\ell_{RVE} \geq 0.15$ mm. Bulk wave propagation is ensured by a high ratio of the lateral dimension to the wavelength [see Equation (3.5)]. Notably, the transversal (shear) velocities $v_{T|i,j}$ are not equal to $v_{T|j,i}$, which shows that wood is not perfectly orthotropic. We use the average of $v_{T|i,j}$ and $v_{T|j,i}$ for estimation of the corresponding shear stiffness (shear modulus) $C_{ijij} = G_{ij} = \rho \left(v_{i,j} + v_{j,i} \right)^2 / 4$ (see Table 3.2). Axial and shear stiffness tensor components of all orthotropic symmetry directions (see Table 3.2) agree quite well with earlier measurements performed on spruce wood (Bucur and Archer 1984).

3.4.2 Porous titanium

The (macro-)porosities of the titanium samples (cylinders with height H and diameter D, see Table 3.3) were determined according to Equation (3.2), using the mass density of pure titanium $\rho_s = 4.5$ g cm^{-3} (Thelen et al. 2004). The specimens without space holder-induced spherical pores (dense titanium) still exhibited a porosity of approximately 15%, related to approximately 10-μm-sized pores visible in Figure 3.3, while the porous titanium had a porosity of approximately 60% (Table 3.3). Longitudinal waves at ultrasonic frequencies f of 0.1 and 10 MHz, and transversal waves at $f = 5$ MHz were employed to characterise the cylindrical samples. The waves travelled along the height H of the specimens.

Table 3.3: Titanium specimens: geometry, mass, and porosity (mean value $\pm$ standard deviation)

	Nr. [-]	H [mm]	D [mm]	V [mm^3]	M [g]	ρ_{app} [g/cm^3]	ρ_s [g/cm^3]	ϕ [%]
Equation						(3.1)		(3.2)
Dense cylinder	4	13.43 ± 1.02	9.28 ± 0.06	908 ± 60	3.48 ± 0.27	3.83 ± 0.05	4.50	14.9 ± 1.2
Porous cylinder	4	13.54 ± 0.31	9.34 ± 0.02	927 ± 25	1.57 ± 0.07	1.69 ± 0.09	4.50	62.4 ± 2.1

Table 3.4: Elasticity of dense and porous titanium samples, determined from propagation velocity of bar waves

	Polarisation [-]	f [MHz]	v_{bar} [km/s]	d [mm]	ℓ_{RVE} [mm]	λ [mm]	a/λ [-]	E [GPa]
Equation			(3.3)		(3.10)	(3.4)		(3.9)
Dense cylinder	Longitudinal	0.1	5.06 ± 0.09	0.02	≥ 0.10	50.6 ± 0.9	0.18	98.1 ± 4.4
Porous cylinder	Longitudinal	0.1	3.39 ± 0.05	0.50	≥ 2.50	33.9 ± 0.5	0.28	19.5 ± 1.7

The employed frequencies and the measured wave velocities (see Tables 3.8 and 3.4) implied, according to Equation (3.4), wavelengths characterising the RVEs 'porous titanium'

($\ell_{RVE} \geq 2.50$ mm), 'dense titanium' ($\ell_{RVE} \geq 0.10$ mm) and 'dense phase of the porous titanium' ($\ell_{RVE} \geq 0.10$ mm) (see Tables 3.8 and 3.4). Depending on the wavelength, measured velocities correspond to bulk waves (Table 3.8) or to bar waves (Table 3.4). Remarkably, two independent test series at different frequencies, providing Young's modulus of dense titanium either directly through bar wave propagation at $f = 0.1$ MHz [see Equation (3.9)], or via C_{1111} and C_{1212} at $f = 5$ and $f = 10$ MHz [see Equations (3.6) and (3.7)], differ by only 4% (see underlined values in Tables 3.8 and 3.4). Poisson's ratio of dense titanium (see Table 3.8) was found to be slightly smaller than that for pure titanium. This finding can be supported by Mori-Tanaka's micromechanical model (Zaoui 2002; Mori and Tanaka 1973) when considering spherical pores embedded in a titanium matrix.

Bulk waves, i.e. waves of higher frequency, sent through the porous samples, were attenuated too much, and therefore did not yield any useful results. Preparation of thinner porous samples might allow for measurement of bulk waves.

3.4.3 Bioglass®-derived glass-ceramic scaffolds

The (macro-)porosity of the Bioglass®-derived glass-ceramic scaffolds, with pore sizes of typically 800 μm (see Figure 3.7), was in a range from $\approx 80\%$ to $\approx 90\%$, with a mean value of 85.7% (see Table 3.5). The dense disc-shaped specimen (height H and diameter D, see Figure 3.5) exhibited a density of $\rho_s = 2.54$ g cm^{-3}, which reached almost that of pure Bioglass® [2.70 g cm^{-3} (Chen et al. 2006)] and had a characteristic pore size of less than a few microns. The density of the dense specimens was used to compute the porosities of the porous samples (see Table 3.5), according to Equation (3.2).

Table 3.5: Bioglass®-derived glass-ceramic specimens: geometry, mass, and porosity (mean value $\pm$ standard deviation)

	Nr. [-]	H [mm]	D, A [mm]	V [mm^3]	M [g]	ρ_{app} [g/cm^3]	ρ_s [g/cm^3]	ϕ [%]
Equation						(3.1)		(3.2)
Dense disc	2	2.29 ± 0.02	8.83 ± 0.06	140 ± 3	0.356 ± 0.003	2.54 ± 0.03	2.54	≈ 0
Porous cuboid	7	12.00 ± 2.09	8.00 ± 0.33	818 ± 199	0.271 ± 0.091	0.36 ± 0.10	2.54	85.7 ± 3.8

Table 3.6: Elasticity of dense Bioglass®-derived glass-ceramic samples, determined from propagation velocity of bulk waves

	Polarisation [-]	f [MHz]	v_L [km/s]	d [mm]	ℓ_{RVE} [mm]	λ [mm]	a/λ [-]	C_{1111} [GPa]
Equation			(3.3)		(3.10)	(3.4)		(3.6)$_1$
Dense disc	Longitudinal	20	5.82 ± 0.05	$\ll 0.01$	≥ 0.01	0.29 ± 0.00	30	86.0 ± 0.3

Longitudinal waves at ultrasonic frequencies f of 0.1 and 20 MHz were employed to characterise the dense, disc-shaped samples and the porous, cuboidal samples (height H, edge length A and B). The porous material has a quite low material strength. Small pieces of the scaffold broke off easily during handling, especially when applying honey to the specimen surface. Because of the small and irregular specimen geometry and a little loss of mass during testing, dimensions,

Table 3.7: Elasticity of porous Bioglass®-derived glass-ceramic samples, determined from propagation velocity of bar waves

	Polarisation [-]	f [MHz]	v_{bar} [km/s]	d [mm]	ℓ_{RVE} [mm]	λ [mm]	a/λ [-]	E [GPa]
Equation			(3.3)		(3.10)	(3.4)		(3.9)
Porous cuboid	Longitudinal	0.1	2.10 ± 0.13	0.80	≥ 4.00	21.0 ± 1.4	0.38	1.57 ± 0.30

mass density, and porosity of the porous samples could not be determined as accurately as for the other materials.

The employed frequencies and measured wave velocities (see Tables 3.6 and 3.7) implied, according to Equation (3.4), wavelengths characterising the RVEs 'porous Bioglass®-ceramic scaffolds' ($\ell_{RVE} \geq 4.00$ mm), and 'dense Bioglass®-ceramic' ($\ell_{RVE} \geq 0.01$ mm). The 20-MHz pulse had an average velocity of 5.82 km s^{-1} and a wavelength of 0.29 mm, implying bulk wave propagation [see Equation (3.5)] and an average normal stiffness component of $C_{1111} = 86.0$ GPa of dense Bioglass®-ceramic (see Table 3.6). The 0.1-MHz wave had an average velocity of 2.10 km s^{-1} corresponding, via Equation (3.4), to a wavelength of 21.0 mm, implying bar wave propagation according to Equation (3.5) (see Table 3.7). Hence, Equation (3.9) allows for computation of Youngs modulus, with mean and standard deviation of 1.57 ± 0.30 GPa. The relatively high value of the standard deviation is due to the difficulties in determining the mass density as accurately as for stronger materials. Nevertheless, the specific values for Young's modulus of the seven scaffolds show a decrease with increasing porosity (see Figure 3.12), as expected from a micromechanical point of view.
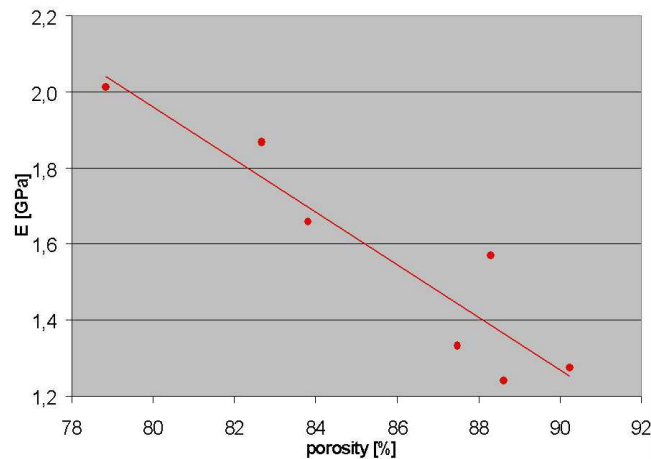
Figure 3.12: Youngs modulus over porosity for Bioglass®-ceramic scaffolds: square of correlation coefficient amounts to $R^2 = 0.87$

Bulk waves, i.e. waves of higher frequency, sent through the porous samples, were attenuated too much, and therefore did not yield any useful results. The limited height of the disc-shaped, dense specimens did not allow for realisation of bar wave propagation through these specimens.

3.4.4 CEL2-derived glass-ceramic scaffolds

Dense and porous cuboidal CEL2-derived glass-ceramic specimens (height H, edge length A and B, see Figure 3.6) with porosities of approximately 0% and 65%, respectively, were tested.

The density of the dense specimens was used to compute the porosities of the porous samples (see Table 3.9) according to Equation (3.2).

Longitudinal waves at ultrasonic frequencies f of 0.1 and 20 MHz, and transversal waves at $f = 10$ MHz were employed to characterise two dense and two porous cuboidal samples. The waves travelled along the dimensions H and A of the porous specimens, and along dimensions H, A and B of the dense specimens, allowing for a greater number of measurements, and thus for a higher reliability of the corresponding mean values. The porous scaffolds had to be grinded before testing, in order to obtain two parallel and plane surfaces.

The employed frequencies and measured wave velocities (see Tables 3.10 and 3.11) implied, according to Equation (3.4), wavelengths characterising the RVEs 'porous CEL2-derived glass-ceramic' ($\ell_{RVE} \geq 2.50$ mm) and 'dense CEL2-derived glass-ceramic' ($\ell_{RVE} \geq 0.01$ mm). Depending on the wavelength, measured velocities correspond to bulk waves (Table 3.10) or bar waves (Table 3.11). We note that two independent test series at different frequencies, providing Young's modulus of dense CEL2-derived glass-ceramic either directly through bar wave propagation ($f = 0.1$ MHz), or via C_{1111} and C_{1212} ($f = 10; 20$ MHz), result in fairly consistent values for Youngs modulus (see underlined values in Tables 3.10 and 3.11).

Bulk waves sent through the porous samples, were attenuated too much and therefore did not yield any useful results.

Table 3.8: Elasticity of dense titanium samples, determined from propagation velocity of bulk waves

	Polarisation	f	v_L, v_T	d	ℓ_{RVE}	λ	a/λ	C_{1111}, C_{1212}	E, G	ν
	[-]	[MHz]	[km/s]	[mm]	[mm]	[mm]	[-]	[GPa]	[GPa]	[-]
Equation			(3.3)		(3.10)	(3.4)		(3.6)	$(3.7)_1, (3.6)_2$	$(3.7)_2$
Dense cylinder	Longitudinal	10	5.59 ± 0.02	0.02	≥ 0.10	0.56 ± 0.00	17	119.7 ± 2.3	$\underline{94.3 \pm 4.0}$	0.28 ± 0.03
Porous cylinder	Transversal	5	3.11 ± 0.12	0.02	≥ 0.10	0.62 ± 0.02	15	37.0 ± 2.3	37.0 ± 2.3	

Table 3.9: CEL2-derived glass-ceramic specimens: geometry, mass, and porosity (mean value ± standard deviation)

	Nr.	H	A	B	V	M	ρ_{app}	ρ_s	ϕ
	[-]	[mm]	[mm]	[mm]	[mm^3]	[g]	[g/cm^3]	[g/cm^3]	[%]
Equation							(3.1)		(3.2)
Dense cuboid	2	49.46 ± 0.01	9.82 ± 0.06	5.96 ± 0.14	2894 ± 50	7.403 ± 0.214	2.56 ± 0.03	2.56	≈ 0
Porous cuboid	2	35.67 ± 3.87	9.45 ± 0.33	10.68 ± 0.59	3622 ± 714	3.219 ± 0.613	0.89 ± 0.01	2.56	65.2 ± 0.2

Table 3.10: Elasticity of dense CEL2-derived glass-ceramic samples, determined from propagation velocity of bulk waves

	Polarisation	f	v_L, v_T	d	ℓ_{RVE}	λ	a/λ	C_{1111}, C_{1212}	E	ν
	[-]	[MHz]	[km/s]	[mm]	[mm]	[mm]	[-]	[GPa]	[GPa]	[-]
Equation			(3.3)		(3.10)	(3.4)		(3.6)	$(3.7)_1$	$(3.7)_2$
Dense cuboid	Longitudinal	20	6.38 ± 0.20	$\ll 0.01$	≥ 0.01	0.32 ± 0.01	69 ± 35	104.1 ± 6.4	$\underline{85.3 \pm 5.0}$	0.25 ± 0.02
Dense cuboid	Transversal	10	3.65 ± 0.11	$\ll 0.01$	≥ 0.01	0.36 ± 0.01	68 ± 25	34.1 ± 2.2		

Table 3.11: Elasticity of dense and porous CEL2-derived glass-ceramic samples, determined from propagation velocity of bar waves

	Polarisation	f	v_{bar}	d	ℓ_{RVE}	λ	a/λ	E
	[-]	[MHz]	[km/s]	[mm]	[mm]	[mm]	[-]	[GPa]
Equation			(3.3)		(3.10)	(3.4)		(3.9)
Dense cuboid	Longitudinal	0.1	6.19 ± 0.21	$\ll 0.01$	≥ 0.01	61.9 ± 2.1	0.36 ± 0.18	$\underline{98.1 \pm 6.9}$
Porous cuboid	Longitudinal	0.1	4.24 ± 0.08	0.50	≥ 2.50	42.4 ± 0.8	0.39 ± 0.19	16.0 ± 0.6

3.5 Summary and Conclusion

It was shown in this study that ultrasonic phase velocity measurements comprise an interesting possibility to measure the elastic stiffness of wood and of very porous biomaterials. Our measurement results on wood agree quite well with data given in the literature. This gives confidence in the experimental devices used. The frequencies employed allowed transmission of bar waves, leading to direct determination of Young's modulus of highly porous bone replacement materials. Stiffness tensor component C_{1111} of dense glass-ceramic and titanium samples were determined from longitudinal bulk wave velocities. In addition, the velocities of transversal waves gave access to shear stiffnesses C_{1212}, and thus, both Young's modulus and Poisson's ratio of dense CEL2-derived glass-ceramics and dense titanium. The ratio of longitudinal to shear wave velocity in these materials amounted to 0.56 and 0.57, respectively, and is consistent with typical values for this ratio in well-known materials, such as titanium (0.52), steel (0.55), iron (0.56) and quartz (0.58) [see Table 6.3 in Briggs (1992)]. Even though our wood specimens had a much lower density (≈ 0.42 g cm^{-3}) than our porous titanium specimens (≈ 1.69 g cm^{-3}), the longitudinal elastic modulus of wood was the same as the isotropic elastic modulus of porous titanium (15.4 and 19.5 GPa, respectively), while the specimens also exhibited nearly equal porosities ($\approx 70\%$ and $\approx 62\%$, respectively). Hence, besides mass density, microstructural morphology is a key factor for the elastic stiffness of porous biomaterials.

Acknowledgements

Publication **4**

Acoustical and poromechanical characterization of titanium scaffolds for biomedical applications (Müllner et al. 2007)

Authored by Herbert W. Müllner, Andreas Fritsch, Christoph Kohlhauser,
Roland Reihsner, Christian Hellmich, Dirk Godlinski,
Astrid Rota, Robert Slesinski and Josef Eberhardsteiner

Biocompatible materials are designed so as to mimic biological materials such as bone as closely as possible. As regards the mechanical aspect of bone replacement materials, a certain stiffness and strength are mandatory to effectively carry the loads imposed on the skeleton. In this paper, porous titanium with different porosities, produced on the basis of metal powder and space holder components, is investigated as bone replacement material. For the determination of mechanical properties, i.e. strength of dense and porous titanium samples, two kinds of experiments were performed - uniaxial and triaxial tests. The triaxial tests were of poromechanical nature, i.e. oil was employed to induce the same pressure both at the lateral surfaces of the cylindrical samples and inside the pores. The stiffness properties were revealed by acoustic (ultrasonic) tests. Different frequencies give access to different stiffness components (stiffness tensor components related to high-frequency-induced bulk waves versus Young's moduli related to low-frequency-induced bar waves), at different observation scales; namely, the observation scale the dense titanium with around 100 μm characteristic length (characterized through the high frequencies) versus that of the porous material with a few millimetres of characteristic length (characterized through the low frequencies). Finally, the experimental results were used to develop and validate a poro-micromechanical model for porous titanium, which quantifies material stiffness and strength from its porosity and (in the case of the aforementioned triaxial tests) its pore pressurisation state.

Notation

a	radius of cylindrical specimen
$\mathbb{C}_{hom}$	Homogenized stiffness of porous medium
$\mathbb{C}_S$	Elasticity tensor of pure titanium
C_{1111}	Normal component of isotropic elasticity tensor
C_{1212}	Shear component of isotropic elasticity tensor
d	Characteristic size of inhomogeneities within material volume (RVE)
div	divergence of a vector field
$\boldsymbol{e}_{1,2,3}$	Base vectors
$\boldsymbol{E}$	Macroscopic strain tensor
E	Young's modulus of porous titanium
E_S	Young's modulus of pure titanium
$\mathfrak{F}$	Homogenized, macroscopic yield criterion
f	Frequency
f_y	Yield stress
G	Shear modulus of porous titanium
i	Index denoting tensor components
$\mathbb{I}$	Fourth-order identity tensor
j	Index denoting tensor components
$\mathbb{J}$	Volumetric part of fourth-order identity tensor
J_0	Bessel function of first kind and order 0
J_1	Bessel function of first kind and order 1
$\mathbb{K}$	Deviatoric part of fourth-order identity tensor
k_f	Compressibility of porous medium
k_S	Bulk modulus of pure titanium
ℓ_{RVE}	Characteristic length of the RVE
l_S	Travel distance through the specimen
p	Pore pressure in porous titanium
p_0	Lateral pressure built up in pressure cell
m	Fluid mass per unit volume of porous medium
r	Radial polar coordinate
RVE	Representative volume element
$\mathbb{S}$	Eshelby tensor
t	Time
tr	trace of tensor
t_S	Travel time through the specimen
v	Phase velocity of acoustic wave
v_L	Bulk velocity of longitudinal (or compressional) wave
v_{bar}	Bar velocity of bar wave
v_T	Velocity of transversal (or shear) wave
$\boldsymbol{v}$	Fluid velocity
V_{solid}	Solid volume inside the RVE of porous medium
$\boldsymbol{w}$	Mass flow vector
$\boldsymbol{x}$	Location vector in the RVE
$\boldsymbol{1}$	Second-order identity tensor
α_n	Roots of J_0, $J_0(\alpha_n) = 0$
β	Inverse characteristic time of surface pressue built-up

δ_{ij}	Kronecker delta
Δ	Laplace operator
$\boldsymbol{\varepsilon}$	Microscopic strain tensor
$\boldsymbol{\varepsilon}_d$	Equivalent (micro-) shear strains
$\varepsilon_{eff,d}$	Effective equivalent deviatoric microstrains
η_f	Viscosity of fluid
κ	Intrinsic permeability of porous medium
λ	Wavelength
μ_S	Shear modulus of pure titanium
ν	Poisson's ratio of porous titanium
ν_S	Poisson's ratio of pure titanium
ρ	Mass density of specimen
ρ_f	Mass density of fluid
$\boldsymbol{\Sigma}$	Macroscopic stress tensor
Σ_d	Equivalent deviatoric macroscopic stress
Σ_m	Mean macroscopic stress
φ	Porosity of porous medium
:	Second-order tensor contraction
$\otimes$	Dyadic product of tensors

4.1 Introduction

Many bone replacement materials, based on a multitude of different chemical compositions, are available nowadays. All these materials are designed so as to mimic bone as closely as possible. In other words, the bone biomaterials are required to be biocompatible (Jones 2005), i.e. they should smoothly fit into the biological, chemical, and mechanical environment inside the body of the patient. As regards the mechanical aspect, a certain stiffness and strength are mandatory to effectively carry the loads imposed onto the skeleton. In addition, the biomaterial should match the mechanical properties of the original bone as precisely as possible, in order to preserve the standard physiological stress fields around the implant. These stress fields are required to guarantee effective functioning of the biological cells resorbing the bone and forming new bone.

In this study,we aimed at contributing to the latter aspect. Precise determination of the stress fields around an implant requires profound knowledge of the material properties of both the bone material and the bone replacement material under multiaxial stress states, as found in the living body (Kobayashi et al. 2001). In addition to multiaxial stress fields, the pore pressure inside the bone is often believed to play a mandatory role, as regards both mechanical integrity (Hellmich and Ulm 2005a,b; Ochoa et al. 1991; Lim and Hong 2000) and biological function (Mizuno et al. 2004; Weinbaum et al. 1994). However, related experimental data are extremely scarce in the open literature. Therefore, we have started a campaign of triaxial test series on bone and bone biomaterials, giving access to the strength properties of the tested materials. Moreover, to determine the stiffness of such materials, our test campaign included ultrasonic measurements as well. Here we describe processing as well as its mechanical and acoustic characterization of titanium biomaterials. Finally, the experimental results are used to develop and validate a first poro-micromechanical model for porous titanium, which quantifies material stiffness and strength from its porosity and (in the case of the aforementioned triaxial tests) its pore pressurization state.

4.2   Materials

Porous titanium samples with open cell structures were produced by using metal powder (pure titanium particles with $<45\mu$m characteristic length) and spherical space holder components (para-formaldehyde with a mean diameter of 500 μm), at Fraunhofer IFAM (Bremen, Germany). The manufacturing process included four steps.

1. *Powder mixture preparation:* Titanium and para-formaldehyde (as space holder) were mixed with paraffin (as a pressing agent), and with additional process aids dissolved in water or organic solvent, to ensure a good bonding of the metal powder and the space holder particles.

2. *Pressing:* The mixture was densified, by means of axial pressing in a powder press.

3. *Debinding:* After compaction, the space holder and bonding agent phases was removed from the samples, in a catalytic process.

4. *Sintering:* After complete space holder removal, the samples were sintered in a high vacuum atmosphere, at a temperature of 1200°C.

The above-described process ensures crack-free and homogeneous titanium samples, with two different porosities (Figure 4.1).
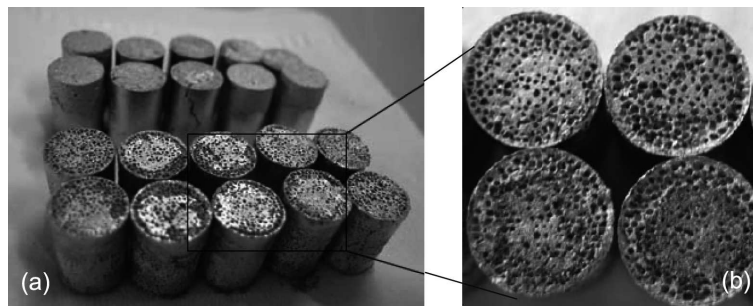
Figure 4.1: (a) Titanium samples (porous in foreground, dense in background); (b) higher magnification of porous titanium samples
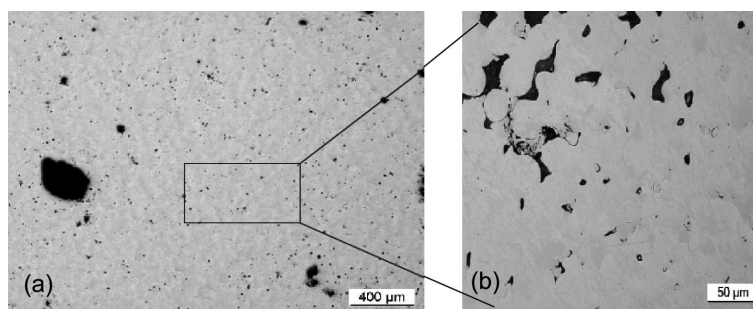
Figure 4.2: (a) Micrograph of the center of a dense titanium sample; (b) higher magnification of the denser part of the same sample

1. *Dense titanium* [Figure 4.1(a), background] was processed without space holders. However, the formation of some microns-sized pores inside the material (Figure 4.2) results in a mass density of 3.80 g/cm^3, remarkably lower than the mass density of pure titanium, which is 4.50 g/cm^3 (Thelen et al. 2004).

2. *Porous titanium* [Figure 4.1(a), foreground; and Figure 4.1(b)] was produced by use of spaceholders as described before. The solid matrix between the hundreds-of-microns-sized pores is similar to the material depicted in Figure 4.2. The overall porous material exhibits a mass density of 1.64 g/cm^3.

4.3   Mechanical testing

All tests were conducted at room temperature. The average height and diameter of the samples were 10.0 and 5.0 mm, respectively. In uniaxial testing mode, the samples were subjected to axial compressive loads by means of a 150 kN uniaxial electromechanical machine [LFM 150; Wille Geotechnik, Germany, with displacement control, Figure 4.3(a)], at a displacement rate of 0.01 mm/s. Extension of uniaxial testing mode to triaxial loading was realized through a high-pressure triaxial testing cell [LT 63500-2/50-T; Wille Geotechnik, Germany, Figure 4.3(b)], filled with mineral oil. In order to stabilize the sample during the filling process, it was attached to the lower die by means of plasticine [Figure 4.3(d)].

An outlet valve on the top of the cell eliminated air bubbles within the testing chamber. This valve was locked once the chamber was properly filled with oil. Then, the oil was pressurized by means of an electromechanical pressure control [DV 350-150/10; Wille Geotechnik, Figure 4.3(c)], up to a pressure of 14.5 MPa. Pressures of this order of magnitude occur if the bone is deformed under undrained conditions (Lim and Hong 2000). A vertical compressive force was applied simultaneously by the electromechanical uniaxial testing machine. The specimens were loaded in a state of axisymmetric triaxial compressive stress until the vertical displacement of the upper die [Figure 4.3(d)], driven by the electromechanical machine, reached 30% of the specimen height.
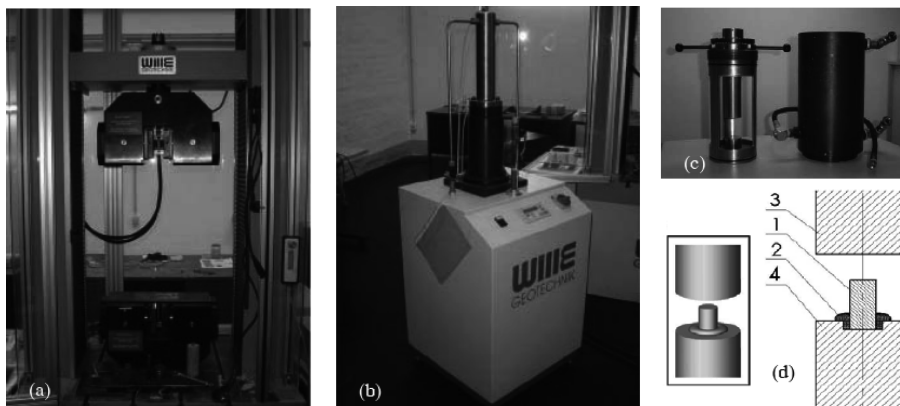
Figure 4.3: Experimental setup for uniaxial and triaxial tests: (a) 150 kN uniaxial testing machine; (b) pressure control; (c) 150 bar triaxial cell; (d) fixing of specimen: (1) specimen, (2) plasticine, (3) upper die, (4) lower die

4.3.1   Identification of triaxial tests as poromechanical tests

Here, we show that the pore pressure build-up within the porous titanium samples is very much faster than the uniaxial load application through the electromechanical machine, so that the uniaxial macroscopic deformation is increased, while a constant pore pressure is prescribed in the pores. In order to estimate corresponding characteristic times, we study the transport of oil through an undeformed (incompressible) porous medium (metal foam).

The fluid mass conservation law for this case reads as

$$\frac{\mathrm{d}m}{\mathrm{d}t} + \mathrm{div}\,\boldsymbol{w} = 0, \tag{4.1}$$

where m is the fluid mass per unit volume of porous medium, $\mathrm{d}(.)/\mathrm{d}t$ denotes the temporal derivation of quantity $(.)$, div denotes the divergence of a vector field, and $\boldsymbol{w}$ is the mass fluid vector. The latter is related to the fluid velocity $\boldsymbol{v}$ through

$$\boldsymbol{w} = \varphi \rho_f \boldsymbol{v}, \tag{4.2}$$

where φ is the porosity and ρ_f the mass density of the fluid. The fluid mass change is related to the fluid pressure change $\mathrm{d}p/\mathrm{d}t$ through the state equation of the fluid (Coussy 2004)

$$\frac{\mathrm{d}m}{\mathrm{d}t} = \varphi \frac{\mathrm{d}\rho_f}{\mathrm{d}t} = \varphi \, \rho_f \frac{1}{k_f} \frac{\mathrm{d}p}{\mathrm{d}t}, \tag{4.3}$$

where $k_f = 1.5$ GPa (Rydberg 2001) is the compressibility or bulk modulus of the (oil) fluid. The fluid velocity $\boldsymbol{v}$ results from a pressure gradient, as expressed in Darcy's fluid conduction law

$$\boldsymbol{v} = -\frac{\kappa}{\eta_f} \mathrm{grad}\, p, \tag{4.4}$$

where η_f is the fluid viscosity ($\eta_f = 450$ mPas for oil (Grimm and Williams 1997)), and κ the intrinsic permeability of the porous medium ($\kappa = 3.1$ x 10^{-8} m^2 for an open metal foam of comparable porosity (Leong and Jin 2006)). Use of Equations (4.2)-(4.4) in (4.1) yields an analogon to the so-called diffusion equation (Crank 1975), reading for space-invariant material properties k_f, η_f and κ, as

$$\frac{\mathrm{d}p}{\mathrm{d}t} = \frac{k_f \kappa}{\eta_f} \Delta p, \tag{4.5}$$

with Δ as the Laplace operator.

Solutions of this partial differential equation are widely documented, see e.g. (Crank 1975). Specifically, the pore pressure development $p(r,t)$ inside a cylindrical porous sample due to rapid pressure build-up around the sample,

$$p = p_0(1 - \exp(-\beta t)) \quad \text{with } \beta \to \infty \tag{4.6}$$

can be given in the form (Crank 1975):

$$\frac{p}{p_0} = 1 - \frac{J_0(\sqrt{\beta r^2 \eta_f / k_f \kappa})}{J_0(\sqrt{\beta a^2 \eta_f / k_f \kappa})} \exp(-\beta t) + \frac{2\beta \eta_f}{ak_f \kappa} \sum_{n=1}^{\infty} \frac{J_0(r\alpha_n)}{\alpha_n J_1(a\alpha_n)} \frac{\exp(-k_f \kappa \alpha_n^2 t / \eta_f)}{\alpha_n^2 - (\beta \eta_f / k_f \kappa)} \tag{4.7}$$

where r is the radial polar coordinate, t denotes the time elapsed since the initiation of pressure build-up, J_0 and J_1 are the Bessel functions of the first kind and of order 0 and 1, respectively,

and α_n are the roots of J_0, $J_0(\alpha_n) = 0$: $\alpha_1 = 2.4048$, $\alpha_2 = 5.5201$, $\alpha_3 = 8.6537$, ...

Evaluation of Eq. (4.7) for the intrinsic permeability values of metal foams (Table 4.1), and the compressibility and viscosity of mineral oil, $k_f = 1.5$ GPa (Rydberg 2001) and $\eta_f = 450$ mPas (McNeil and Stuart 2004), respectively, clearly shows that the pore pressure inside the tested titanium samples is built up within a small fraction of 1 s. This holds even for the intrinsic permeability values of bone (Table 4.1) which are lower than the one for metal foams. Hence, during the mechanical experiments, lasting typically 10 min, the pore pressure is always quasi-identical to the oil pressure built up in the pressure cell. Therefore, the triaxial tests performed here may be regarded as poromechanical tests, where the pore pressure *inside* the samples is prescribed.

Table 4.1: Intrinsic permeabilities κ of metal foams and bone

Source	Material	κ [m^2]
Leong and Jin (2006)	Metal foam	3.1 x 10^{-8}
Grimm and Williams (1997)	Trabecular bone	8.5 x 10^{-9}
Li et al. (1987)	Cortical bone	2.5 x 10^{-13}

4.3.2 Determination of strength properties

Load-displacement curves obtained for uniaxial and triaxial tests (Figure 4.4) are characterized by a considerable decrease of the slope of the load-displacement curve at a certain load level. This refers to ductile material behavior, which is also evident from the deformed shape of the samples after mechanical testing, as shown in the photographs of Figure 4.5. Bilinear approximation of the load-displacement curves gives access to the yield load (Figure 4.4). Dividing the latter by the sectional area of the specimen gives access to the yield stress of the material (see Table 4.2 for corresponding experimental results). The results of the uniaxial and triaxial tests are not markedly different. This is probably due to the fact that the lateral pressure of 14.5 MPa is by far smaller than the uniaxial yield stress of the samples. More profound investigations into the poromechanical behavior of the titanium materials considered herein would call for a pressure cell apt for extremely high pressures.

The remarkably high ductility of the titanium materials does not necessarily match the mechanical characteristics of natural bone, often showing a more brittle behavior in compression (Morgan et al. 2005). This underlines the fact that, in addition to the anisotropy of natural bone (Lees et al. 1979), which is not mimicked by the tested biomaterial, the inelastic constitutive behavior of man-made biomaterials still needs to be improved as to match more precisely the one of natural bone.

The load-displacement curves presented in Figure 4.4 do not show any linear regime, which indicates that inelastic phenomena are at action right from the initial testing phase, when they are restricted to the regions of the samples close to the load platens. Hence, elastic properties cannot be derived from the load-displacement curves; therefore, the mechanical tests were used for determination of strength properties, only; and the materials' elasticity was revealed through ultrasonics measurements (shown below).
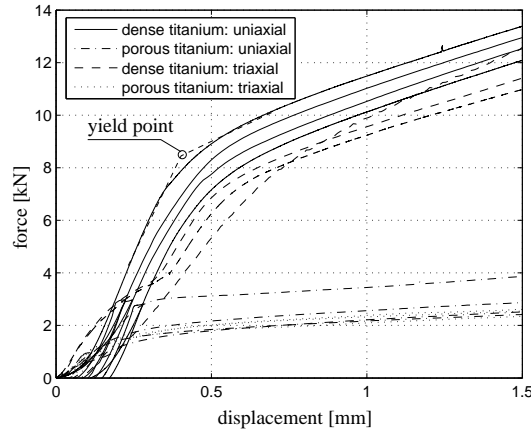
Figure 4.4: Load-displacement curves for dense and for porous titanium samples

4.4   Acoustical Testing

4.4.1   Equipment for transmission through technique

The used ultrasonic device consists of a pulser-receiver PR 5077 [Panametrics Inc., Waltham, MA, Figure 4.6(a)], an oscilloscope, and several ultrasonic transducers [Figure 4.6(b)]. The pulser unit emits an electrical square-pulse of up to 400 V, with frequencies from 0.1 MHz to 20 MHz. The piezoelectric elements inside the ultrasonic transducers transform such electrical signals into mechanical signals [when operating in the sending mode, transferring, via a coupling medium (here honey), the mechanical signals to one side of the specimen under investigation], or they transform mechanical signals back to electrical signals (when receiving mechanical signals from the opposite side of the specimen under investigation). The piezoelectric elements are tailored for the frequency of the employed mechanical signal: The higher the frequency, the smaller the element and the corresponding transducer. Depending on the cut and orientation of the element, a longitudinal or a transversal wave is emitted.

The receiver unit of the pulser-receiver has a bandwidth of 0.1 to 35 MHz and a voltage gain of up to 59 dB. The amplified signal is displayed on an oscilloscope Lecroy WaveRunner 62Xi (Lecroy Corporoation, Chestnut Ridge, NY) width a bandwidth of 600 MHz and a sample rate of 10 gigasamples per second. The oscilloscope gives access to the time of flight of the ultrasonic wave through the specimen, t_S, which provides, together with the travel distance through the specimen, l_S, the phase velocity of the wave as

$$v = \frac{l_S}{t_S} \tag{4.8}$$

Table 4.2: Mean values and standard deviations of yield stresses in [MPa] (p...oil pressure, n ...number of tests)

	Titanium dense	Titanium porous
Uniaxial test ($p = 0$ MPa)	400 ± 26 (n=4)	103 ± 32 (n=4)
Triaxial test ($p = 15$ MPa)	353 ± 70 (n=4)	88 ± 15 (n=4)
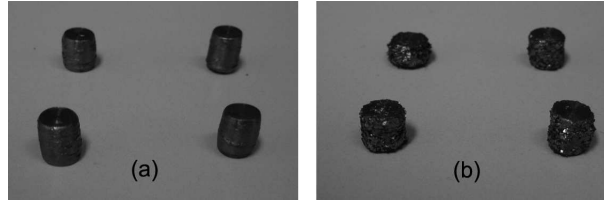
Figure 4.5: Photographs of tested samples: (a) dense titanium; (b) porous titanium

see Table 4.3 for typical velocities of longitudinal or compressional waves (v_L), where the particle displacement points into the wave propagation direction, and transverse or shear waves (v_T), where the particle displacement is perpendicular to the wave propagation direction.

Table 4.3: Ultrasonic measurement results for titanium (Ti) samples (mean values ± standard deviations)

	ρ [g/cm^3]	f [MHz]	v [km/s]	λ [mm]	ℓ_{RVE} [mm]	C_{1111}/C_{1212} [GPa]	E/G [GPa]	ν
Dense Ti samples	3.83±0.05	10.0	$v_L=$ 5.59±0.02	0.56±0.00	≥0.10	$C_{1111}=$ 119.7±2.3	$E=$ 94.3±4.0	0.28±0.03
Dense Ti samples	3.83±0.05	5.0	$v_T=$ 3.11±0.12	0.62±0.02	≥0.10	$C_{1212}=$ 37.0±2.3	$G=$ 37.0±2.3	
Dense Ti samples	3.83±0.05	0.1	$v_{bar}=$ 5.06±0.09	50.6±0.9	≥0.10		$E=$ 98.1±4.4	
Porous Ti samples	1.69±0.09	0.1	$v_{bar}=$ 3.39±0.05	33.9±0.5	≥2.50		$E=$ 19.5±1.7	

4.4.2 Theoretical basis of ultrasonic measurements

Frequency f and wave velocity v give access to the wavelength λ, through

$$\lambda = \frac{v}{f} \tag{4.9}$$

If the wavelength is considerably smaller than the diameter of the specimen, a (compressional) 'bulk wave', i.e. a laterally constrained wave, propagates with velocity v_L in a quasi-infinite medium. On the other hand, if the wavelength is considerably larger than the diameter of the specimen, a 'bar wave' propagates with velocity v_{bar}, i.e. the specimen acts as one-dimensional
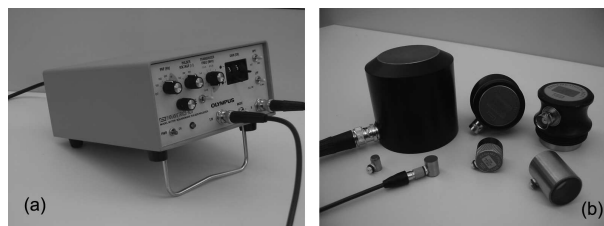
Figure 4.6: Equipment for acoustical testing: (a) pulser-receiver; (b) ultrasonic transducers

bar without lateral constraints (Ashman et al. 1984). In contrast, shear waves' propagation is identical in quasi-infinite media and bar-like structures (Ashman et al. 1987).

As regards bulk waves, a combination of the conservation law of linear momentum, the generalized Hooke's law, the linearized strain tensor, and the general plane wave solution for the displacements inside an infinite solid medium yields the elasticity tensor components C_{1111} and C_{1212} of isotropic materials as functions of the material mass density ρ and the bulk wave propagation velocities v_L and v_T (Carcione 2001),

$$C_{1111} = \rho v_L^2 \quad \text{and} \quad C_{1212} = G = \rho v_T^2 \tag{4.10}$$

with G as the shear modulus.

Combination of (4.10) with the definitions of the engineering constants Young's modulus E and Poisson's ratio ν, yields the latter as functions of the wave velocities, in the form

$$E = \rho \frac{v_T^2 (3v_L^2 - 4v_T^2)}{v_L^2 - v_T^2} \tag{4.11}$$

and

$$\nu = \frac{E}{2G} - 1 = \frac{v_L^2/2 - v_T^2}{v_L^2 - v_T^2} \tag{4.12}$$

respectively.

In the case of bar wave propagation (Kolsky 1953), the measured bar wave velocity v_{bar} gives direct access to the Young's modulus,

$$E = \rho v_{bar}^2 \tag{4.13}$$

In continuum (micro)mechanics (Zaoui 1997, 2002), elastic properties are related to a material volume [representative volume element (RVE)], with a characteristic length ℓ_{RVE} being considerably larger than the inhomogeneities d inside the RVE, and the RVE being subjected to homogeneous stress and strain states (Figures 4.7 and 4.8). Hence, the characteristic length of the RVE, ℓ_{RVE}, needs to be much smaller than the scale of the characteristic loading of the medium, here the wavelength λ (Figure 4.7). Mathematically,

$$d \ll \ell_{RVE} \ll \lambda \tag{4.14}$$

Therefore, ultrasonic tests at different frequencies 'detect', inside a sample, materials at different observation scales (Fritsch and Hellmich 2007), such as the macroscopic porous material or the solid phase of the material. In the following, this is detailed for the titanium samples.

4.4.3 Determination of elastic properties

Longitudinal waves at ultrasonic frequencies of 0.1 and 10 MHz, and transversal waves at 5 MHz were employed to characterize four dense and four porous cylindrical samples. The waves traveled along the height of the specimen.

The employed frequencies implied wavelengths of around half a millimeter and half a decimeter, respectively (Table 4.3), characterizing the RVEs of dense and porous titanium samples, with at least 0.1 and 2.5 mm characteristic length, respectively (Table 4.3). Depending on the wavelength, measured velocities correspond to bulk waves (rows 1 and 2 of Table 4.3) or to bar waves (rows 3 and 4 of Table 4.3). Remarkably, two independent test series at different
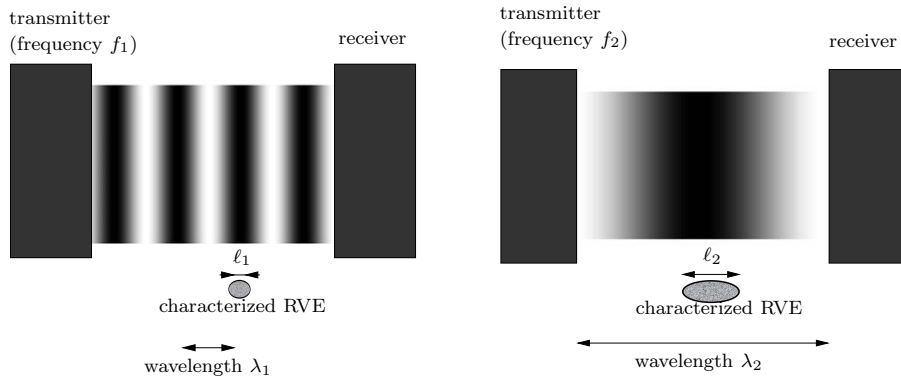
Figure 4.7: Schematic, grey-scale based illustration of stress magnitude in specimens tested ultrasonically with different frequencies ($f_1 > f_2$) (Fritsch and Hellmich 2007)

frequencies, providing Young's modulus of dense titanium either directly ($f = 0.1$ MHz) or via C_{1111} and C_{1212} ($f = 5$ and $f = 10$ MHz), differ by only 3% (rows 3 and 1 in Table 4.3).

4.5 Prediction of mechanical properties by means of poro-micromechanics — microstructure-property relationships

In this section, we aim at explaining the above-collected stiffness and strength properties from the internal structure and composition of the tested materials. Therefore, we consider the basic morphological feature of the pores inside the samples, which is its spherical shape, and the volume occupied by these pores normalized by the volume of the entire material volume, i.e. the porosity of the samples. In a first micromechanical approximation of the material's microstructure, we do not distinguish between the typically 10-μm-sized pores discernable in Figure 4.2 and the typically 500-μm-sized pores discernible in Figure 4.1; but we consider the sum of both porosities as overall porosity. Accordingly, the measured mass density of each specimen and the mass density of pure titanium, equal to 4.50 g/cm3, give access to the aforementioned overall porosity of each sample (see coordinates on abscissa of experimental data points in Figures 4.9 and 4.10, as well as Table 4.4 for mean values and standard deviations).

We consider an RVE of porous titanium (Figure 4.8, see also Section 4.4 and Figure 4.7), with
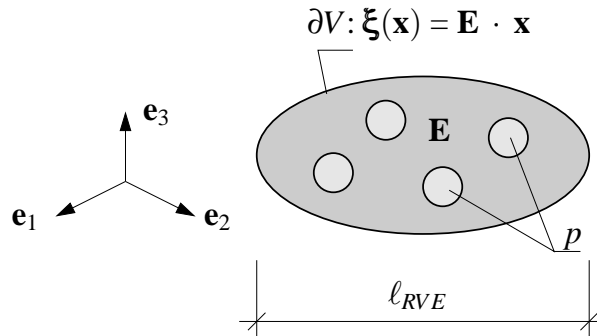
Figure 4.8: Micromechanical representation of porous medium (Dormieux 2005; Dormieux et al. 2002, 2006): a representative volume element (RVE) is loaded by displacements related to homogeneous (macroscopic) strains $\boldsymbol{E}$, and by a pore pressure p

characteristic length $\ell_{RVE} = 2 \ldots 5$ mm. Therein, we distinguish two quasi-homogeneous sub-domains (also called material phases): (i) the pores of characteristic size $d = 10 \ldots 500$ microns $\ll \ell_{RVE}$, with a volume fraction equal to the porosity φ and with a prescribed hydrostatic stress state equal to the pore pressure; and (ii) the solid titanium matrix with volume fraction $(1 - \varphi)$ and with mechanical properties of pure (non-porous) titanium. The elastic properties of the latter are typically given by a Young's modulus $E_S = 120$ GPa and a Poissons ratio $\nu_S = 0.32$, i.e. by a bulk modulus $k_S = 111$ GPa and a shear modulus $\mu_S = 45.5$ GPa (Matweb 2007), see also the stiffnesses in Figure 4.9 at $\varphi = 0$, and the uniaxial strength of pure titanium typically amounts to 450 MPa (Matweb 2007). These quantities are the basis for determination of the 'homogenized' mechanical behavior of the overall material, i.e. the relation between homogeneous ('macroscopic') deformations $\boldsymbol{E}$ acting on the boundary of the RVE (being identical to the average of the ('micro'-) strains inside the RVE) and resulting average ('micro'-) stresses (being identical to the 'macroscopic' stresses $\boldsymbol{\Sigma}$), as well as the macroscopic stress states related to material failure ('homogenized strength'). The homogenized or effective material behavior of the porous titanium samples is estimated from the mechanical behavior of the aforementioned homogeneous phases, representing the inhomogeneities within the RVE, their dosages within the RVE, their characteristic shapes, and their interactions, as described next.
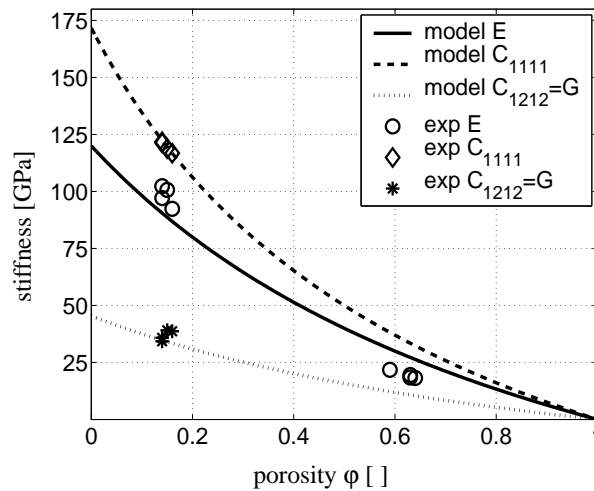
Figure 4.9: Prediction of stiffness properties of titanium samples, by means of poro-micromechanical model, Equations (4.15)–(4.18); experimental values according to Sections 4.3 and 4.4

Table 4.4: Porosities of samples (mean values ± standard deviations)

	φ (%)
Dense titanium samples	14.9 ± 1.2
Porous titanium samples	62.4 ± 2.1

4.5.1   Stiffness

For predicting the effective stiffness properties of the (empty) porous titanium samples, we consider - on average - the interaction of spherical pores inside a pure titanium matrix, by
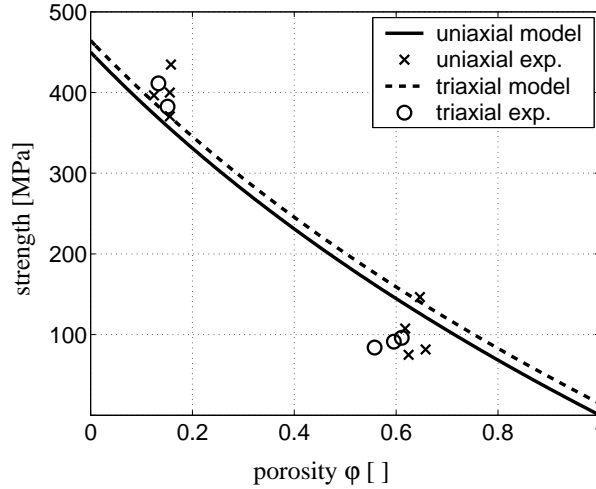
Figure 4.10: Prediction of strength properties of titanium samples, by means of poro-micromechanical model, Equations (4.19)-(4.20); experimental values according to Sections 4.3 and 4.4

means of a Mori-Tanaka homogenization scheme (mean-field homogenization) (Zaoui 2002; Dormieux 2005; Dormieux et al. 2002; Mori and Tanaka 1973; Benveniste 1987), delivering the following estimate $\mathbb{C}_{hom}$ for the 'homogenized' stiffness of the composite material 'porous titanium'

$$\mathbb{C}_{hom} = \mathbb{C}_S : (\mathbb{I} - \varphi[\mathbb{I} - (\mathbf{1} - \varphi)\mathbb{S}]^{-1}), \tag{4.15}$$

relating macroscopic stresses $\boldsymbol{\Sigma}$ to macroscopic strain $\boldsymbol{E}$. In (4.15), $\mathbb{C}_S$ is the elasticity tensor of pure titanium, $\mathbb{C}_S = 3k_S\mathbb{J} + 2\mu_S\mathbb{K}$ with

$$\mathbb{J} = \frac{1}{3}\mathbf{1} \otimes \mathbf{1} \quad \text{and} \quad \mathbb{K} = \mathbb{I} - \mathbb{J} \tag{4.16}$$

as the volumetric and the deviatoric part of the fourth-order identity tensor,

$$\mathbb{I} = I_{ijkl} = \frac{1}{2}(\delta_{ik}\delta_{jl} + \delta_{il}\delta_{kj}) \tag{4.17}$$

and δ_{ij} (Kronecker delta) are the components of the second-order identity tensor $\mathbf{1}$, $\delta_{ij}=1$ for $i=j$ and 0 otherwise.

The Eshelby tensor $\mathbb{S}$ for spherical inclusions accounts for the inclusion shape and is of the form (Eshelby 1957)

$$\mathbb{S} = \frac{3k_S}{3k_S + 4\mu_S}\mathbb{J} + \frac{6(k_S + 2\mu_S)}{5(3k_S + 4\mu_S)}\mathbb{K} \tag{4.18}$$

The predictions of the micromechanical model (4.15)-(4.18) compare well with corresponding experimentally determined stiffnesses (Figure 4.9).

4.5.2 Strength

In contrast to the homogenized elastic properties, which can be derived from averages of microstrains and microstresses over the material phases, homogenization of strength properties

calls for additional information on the heterogeneity of these micro-quantities, i.e. the strain or stress peaks inside the microstructure (possibly cancelled out through averaging) need to be appropriately considered.

It has recently been shown (Dormieux et al. 2002; Kreher 1990), that this heterogeneity can reasonably be considered through the so-called effective microstrains, such as the square root of the average over the solid material phase, of the squares of the equivalent deviatoric (micro-)strains $\boldsymbol{\varepsilon}_d(\boldsymbol{x})$,

$$\varepsilon_{eff,d} = \sqrt{\int_{V_{solid}} \boldsymbol{\varepsilon}_d(\boldsymbol{x}) : \boldsymbol{\varepsilon}_d(\boldsymbol{x}) \mathrm{d}V} \tag{4.19}$$

with

$$\boldsymbol{\varepsilon}_d(\boldsymbol{x}) = \boldsymbol{\varepsilon}(\boldsymbol{x}) - \frac{1}{3}\mathrm{tr}\boldsymbol{\varepsilon}(\boldsymbol{x})\mathbf{1} \tag{4.20}$$

where V_{solid} is the volume inside the RVE, which is occupied by the solid matrix, $\boldsymbol{x}$ the location vector indicating positions inside the RVE (Figure 4.8), and tr denotes the trace of a tensor. By non-linear homogenization theory (Dormieux 2005; Dormieux et al. 2002; Suquet 1997), the limit case of large effective microstrains, being related to microstresses fulfilling a failure criterion (such as the ideally plastic von Mises criterion calibrated by the uniaxial strength of pure titanium herein), can be assigned to corresponding macroscopic stress states, defining a 'macroscopic', homogenized (ideally plastic) yield criterion of the following, elliptical form:

$$\mathfrak{F}(\Sigma_m, \Sigma_d, p) = \frac{3\varphi}{4(1-\varphi)^2}(\Sigma_m + p)^2 + \frac{1 + (2/3)\varphi}{(1-\varphi)^2}\Sigma_d^2 - \frac{f_y^2}{3} = 0 \tag{4.21}$$

with Σ_m and Σ_d as the mean and the equivalent macroscopic stress, reading as

$$\Sigma_m = \frac{1}{3}\mathrm{tr}\boldsymbol{\Sigma} \tag{4.22}$$

and

$$\Sigma_d = \sqrt{\frac{1}{2}\boldsymbol{\Sigma}_d : \boldsymbol{\Sigma}_d}, \quad \boldsymbol{\Sigma}_d = \boldsymbol{\Sigma} - \frac{1}{3}\mathrm{tr}\boldsymbol{\Sigma}\,\mathbf{1} \tag{4.23}$$

and p as the pressure acting inside the pores. It is important to note that p is a state variable independent of $\boldsymbol{\Sigma}$. In particular, p is not equal to hydrostatic part of the macroscopic stress, $1/3\,\mathrm{tr}\,\boldsymbol{\Sigma}$, as it is sometimes used in the open literature.

For validation of the micromechanics model through our experimental data, we consider a Cartesian base frame with base vectors $\boldsymbol{e}_1$, $\boldsymbol{e}_2$ and $\boldsymbol{e}_3$, where the third axis coincides with the long axis of the cylindrical samples. We consider model predictions for the yield stress in:

1. uniaxial compression without internal pore pressure:

$$\boldsymbol{\Sigma} = \Sigma_{33}\boldsymbol{e}_3 \otimes \boldsymbol{e}_3,$$

$$p = 0,$$

and in

2. triaxial (not hydrostatic) compression with internal pore pressure:

$$\boldsymbol{\Sigma} = -p_0 \boldsymbol{e}_1 \otimes \boldsymbol{e}_1 - p_0 \boldsymbol{e}_2 \otimes \boldsymbol{e}_2 + \Sigma_{33} \boldsymbol{e}_3 \otimes \boldsymbol{e}_3,$$

$$p = p_0, \ p_0 = 14.5 \, \text{MPa},$$

where Σ_{33} is the normal stress related to the axial compression load imposed by the electromechanical machine onto the specimen, irrespective of the pore pressure p_0.

The aforementioned model predictions compare quite well to corresponding, experimentally obtained values (Figure 4.10). Consideration of two differently sized porosities in a multistep-homogenization procedure, instead of only one as done herein, might improve the model predictions.

4.6   Conclusions

Triaxial mechanical tests and ultrasound experiments were performed on porous titanium samples of different porosity, in order to determine their Young's moduli and Poisson's ratios, as well as their plastic behavior and yield stresses. The investigations indicate that porous titanium material has a hardening plasticity behavior as seen in load-displacement curves (Figure 4.4). Experiments show that yield stress and Young's modulus decrease at increasing porosity (see data points in Figures 4.9 and 4.10). The experimental results were consistent with poro-micromechanical model predictions based on the stiffness and strength properties of pure titanium, as well as on the sample specific porosity. In addition, the corresponding Mori-Tanaka model for upscaling of elasticity shows that the overall Young's modulus of the porous titanium samples depend nonlinearly and convexly on the porosity (Figure 4.9); while a nonlinear homogenization scheme based on effective microstrains in the solid material matrix, shows that the uniaxial yield stress depends more linearly on the porosity and that internal oil pressure increases the yield stress (Figure 4.10). However, as the employed oil pressure is by far smaller than the uniaxial yield stress, the aforementioned increase is very small in the present case. This is probably the reason why it could not be clearly confirmed by the experiments. This leads the way to our next step in the described research project, devoted to application of the same oil pressure to materials characterized by a higher porosity, and to application of by far higher oil pressures to materials such as the ones described herein. In addition, we plan an extension of the experimental program towards cyclic loading. This loading condition is highly relevant for the day-to-day use of implants (Hosoda et al. 2006), and also plays an important mechanobiological role (Mizuno et al. 2004).

Acknowledgements

Publication 5

Micromechanics of bioresorbable porous CEL2 glass ceramic scaffolds for bone tissue engineering (Malasoma et al. 2008)

Authored by Andrea Malasoma, Andreas Fritsch, Christoph Kohlhauser,
Tomasz Brynk, Chiara Vitale-Brovarone, Zbigniew Pakiela,
Josef Eberhardsteiner, and Christian Hellmich

Owing to their stimulating effects on bone cells, ceramics are identified as expressly promising materials for fabrication of tissue engineering (TE) scaffolds. To ensure the mechanical competence of TE scaffolds, it is of central importance to understand the impact of pore shape and volume on the mechanical behaviour of the scaffolds, also under complex loading states. Therefore, the theory of continuum micromechanics is used as basis for a material model predicting relationships between porosity and elastic/strength properties. The model, which mathematically expresses the mechanical behaviour of a ceramic matrix (based on a glass system of the type SiO_2-P_2O_5-CaO-MgO-Na_2O-K_2O; called CEL2) in which interconnected pores are embedded, is carefully validated through a wealth of independent experimental data. The remarkably good agreement between porosity based model predictions for the elastic and strength properties of CEL2-based porous scaffolds and corresponding experimentally determined mechanical properties underlines the great potential of micromechanical modelling for speeding up the biomaterial and tissue engineering scaffold development process — by delivering reasonable estimates for thematerial behaviour, also beyond experimentally observed situations.

Notation

$\mathbb{A}_r$	fourth order strain concentration tensor of phase r
$\mathbb{A}_S$	fourth order strain concentration tensor of solid phase (dense CEL2 glass ceramic)
$\mathbb{A}_{por}$	fourth order strain concentration tensor of pores
a	typical cross-sectional dimension of a CEL2-based porous biomaterial sample
$\mathbb{C}_{hom}$	fourth order homogenised stiffness tensor
C_{ijkl}	components of fourth order homogenised stiffness tensor
$\mathbb{C}_{por}$	fourth order stiffness tensor of pores
$\mathbb{C}_S$	fourth order stiffness tensor of solid phase (dense CEL2 glass ceramic)
d	characteristic length of inhomogeneity within an RVE
$\boldsymbol{E}$	second order 'macroscopic' strain tensor
$\boldsymbol{E}_d$	deviatoric part of macroscopic strain tensor
E_S	Young's modulus of solid phase (dense CEL2 glass ceramic)
E_{exp}	experimentally determined Young's modulus of porous CEL2-based biomaterial
$\bar{E}_{exp}$	mean over all experimentally determined Young's moduli of porous CEL2-based biomaterial
E_{hom}	homogenised Young's modulus of porous CEL2-based biomaterial
$\bar{e}$	mean of relative error between predictions and experiments
e_S	standard deviation of relative error between predictions and experiments
$\underline{e}_1$	unit base vector of Cartesian reference base frame
f	ultrasonic excitation frequency
$\mathfrak{f}(\boldsymbol{\sigma}) = 0$	boundary of elastic domain of solid material phase, in space of microstresses
$\mathfrak{F}(\boldsymbol{\Sigma}) = 0$	boundary of elastic domain of porous CEL2-based biomaterial, in space of macrostresses
g_1, g_2	functions for determination of homogenised elastic constants k_{hom} and μ_{hom} [see Eq. (5.18)]
$\mathbb{I}$	fourth-order identity tensor
$\mathbb{J}$	volumetric part of fourth-order identity tensor $\mathbb{I}$
$\mathbb{K}$	deviatoric part of fourth-order identity tensor $\mathbb{I}$
k_{DS}^{j}, k_{DS}^{j+1}	homogenised bulk moduli of step j and $j + 1$ in a Differential Scheme
k_S	Bulk modulus of solid phase (dense CEL2 glass ceramic)
k_{hom}	homogenised bulk modulus of porous CEL2-based biomaterial
L	characteristic length of a structure containing an RVE
ℓ_{RVE}	characteristic length of RVE of porous CEL2-based biomaterial
l	length of ultrasonic path
M	mass of a porous CEL2-based biomaterial sample
RVE	representative volume element
r	index for phases
$\mathbb{S}_{sph}$	fourth order Eshelby tensor for spherical inclusion embedded in isotropic matrix with stiffness $\mathbb{C}_S$
t	transition time of an ultrasonic wave through a CEL2-based biomaterial sample
tr	trace of a second order tensor

V	volume of a porous CEL2-based biomaterial sample
V_{por}	volume of pores within an RVE of porous CEL2-based biomaterial
V_S	volume of the solid phase (dense CEL2 glass ceramic) within an RVE of porous CEL2-based biomaterial
V_{RVE}	volume of an RVE of porous CEL2-based biomaterial
v	propagation velocity of ultrasonic wave within a CEL2-based biomaterial sample
$\underline{x}$	position vector within an RVE
$\Delta\varphi$	pore increment in a Differential Scheme
Δx	very small volume fraction of homogenised material in a Differential Scheme, to be replaced by pores
δ_{ij}	Kronecker delta
$\boldsymbol{\varepsilon}$	second order microscopic strain tensor
$\boldsymbol{\varepsilon}_d$	deviatoric part of microscopic strain tensor
ε_d	equivalent deviatoric microscopic strain
ε_d^{eff}	effective deviatoric microscopic strain
$\boldsymbol{\varepsilon}_{por}$	average microscopic strain in pore phase
$\boldsymbol{\varepsilon}_r$	average microscopic strain in phase r
$\boldsymbol{\varepsilon}_S$	average microscopic strain in solid phase (dense CEL2 glass ceramic)
λ	ultrasonic wave length
$\mu_{DS}^j, \mu_{DS}^{j+1}$	homogenised shear moduli of step j and $j+1$ in a Differential Scheme
μ_{hom}	homogenised shear modulus of porous CEL2-based biomaterial sample
ν_S	Poisson's ratio of solid phase (dense CEL2 glass ceramic)
ν_{hom}	homogenised Poisson's ratio of porous CEL2-based biomaterial sample
$\underline{\xi}$	displacements within an RVE and at its boundary
ρ	material mass density of porous CEL2-based biomaterial sample
ρ_S	material mass density of solid phase (dense CEL2 glass ceramic)
$\boldsymbol{\Sigma}$	second order 'macroscopic' stress tensor
$\boldsymbol{\Sigma}_d$	deviatoric part of macroscopic stress tensor
$\Sigma_{pred}^{ult,c}$	model predicted uniaxial compressive strength of porous CEL2-based biomaterial
$\Sigma_{exp}^{ult,c}$	experimentally determined uniaxial compressive strength of porous CEL2-based biomaterial
$\boldsymbol{\sigma}$	second order 'microscopic' stress tensor
$\boldsymbol{\sigma}_d$	deviatoric part of microscopic stress tensor
σ_d	equivalent deviatoric microscopic stress
σ_d^{eff}	effective deviatoric microscopic stress
$\boldsymbol{\sigma}_S$	average microscopic stress in solid phase (dense CEL2 glass ceramic)
τ_S^{ult}	shear strength of dense CEL2 glass ceramic
τ^{ult}	shear strength
φ	volume fraction of pores within an RVE of porous CEL2-based biomaterial
∂V	boundary of an RVE
$\mathbf{1}$	second order identity tensor
$\langle(.)\rangle_V = 1/V \int_V (.)\mathrm{d}V$	average of quantity (.) over volume V
$\cdot$	first order tensor contraction
$:$	second order tensor contraction
$\otimes$	dyadic product of tensors

5.1   Introduction

Bone replacements are needed for many orthopaedic, maxillofacial and craniofacial surgeries. The latter may be required due to e.g. trauma or bone neoplasia. Hence, bone regeneration is an increasingly important clinical need. Autografts, allografts and xenografts can be used as bone substitutes; autografts are still considered as the best choice, because of their ability to support osteoinduction and osteogenesis, but considerable drawbacks are associated with the need for further surgery and with donor site morbidity. Allografts and xenografts represent a promising alternative, but they show worse bone induction properties, lower integration rates and non-negligible risks of viral contamination. For these reasons, artificial grafts (also called scaffolds) are interesting candidates to stimulate bone regeneration.

The term scaffold refers to a structure, realised with natural or synthesised materials, which is able to promote cellular regeneration and to guide bone regeneration. Therefore, synthetic scaffolds may be seeded with carefully chosen biological cells and/or growth factors: this is referred to as tissue engineering (Langer and Vacanti 1993). Within this concept, the main role of a scaffold is to assure a mechanical support to the growing tissue, to guide this growth and to induce correct development of the bony organ. Due to their stimulating effects on bone cells, ceramics (such as hydroxyapatite (Akao et al. 1981; Verma et al. 2006), β-tricalcium phosphate (Charrière et al. 2001), bioactive glasses (Hench and Jones 2005; Boccaccini et al. 2005), or glass ceramics (Vitale-Brovarone et al. 2007)) are identified as expressly promising materials for fabrication of tissue engineering scaffolds.

However, the design of such scaffolds is still a great challenge since (at least) two competing requirements must be fulfilled:

(i) on the one hand, the scaffold must exhibit a sufficient mechanical competence, i.e. stiffness and strength comparable to natural bones;

(ii) on the other hand, once the scaffold would be implanted into the living organism, it should be continuously resorbed and replaced by natural bones. This typically requires a sufficient pore space (pore size in the range of hundred micrometres and porosity of more than 50-60% (Cancedda et al. 2007)), which discriminates the aforementioned mechanical properties, and therefore competes with the first requirement.

For finding a good balance between these competing requirements, it is of central importance to understand the impact of pore shape and volume on the mechanical behaviour of the scaffolds, also under complex loading states. In order to contribute to this understanding, the authors started a multidisciplinary activity driven forward by physicists, chemists, material scientists, and engineering mechanicians. While the authors' endeavours comprised state of the art processing and characterisation techniques, ranging all the way from microscopy to mechanical and acoustical testing, the focus of the present contribution is on an engineering science based synthesis tool for consistent explanation of the experimental data: in more detail, the theory of continuum micromechanics (Suquet 1997; Zaoui 2002) provides the authors with the basis for a material model predicting relationships between porosity and elastic/strength properties. The model, which mathematically expresses the mechanical behaviour of a ceramic matrix in which interconnected pores are embedded (see Section 5.3), is carefully validated through a wealth of independent experimental data (see Section 5.4). The latter are gained from geometrical and weighing measurements and from mechanical tests on CEL2 biomaterials (see Section 5.4). These biomaterials are based on a glass system of the type SiO_2-P_2O_5-CaO-MgO-Na_2O-K_2O, the production and microstructural morphology of which will be given in Section 5.2. The remarkably good agreement between porosity based model predictions for elastic and strength

properties of CEL2-based porous scaffolds and corresponding experimentally determined mechanical properties (see Section 5.4) underlines the great potential of micromechanical modelling for speeding up the biomaterial and tissue engineering scaffold development process – by delivering reasonable estimates for the material behaviour, also beyond experimentally observed situations. A related discussion concludes the present paper (see Section 5.5).

5.2 Processing and microstructural characterisation of CEL2 biomaterials before and after bioactivity treatment

The production of glass ceramic tissue engineering scaffolds with different porosities was based on a glass called CEL2 (Vitale-Brovarone et al. 2007). This glass belongs to the system SiO_2-P_2O_5-CaO-MgO-Na_2O-K_2O, with the following molar composition: 45% SiO_2, 3% P_2O_5, 26% CaO, 7% MgO, 15% Na_2O, 4% K_2O. CEL2 was prepared by melting the raw products in a platinum crucible at $1400^{o}C$ for 1 h and by quenching the melt in cold water to obtain a frit that was finally ground and sieved. This resulted in a final grain size of less than 30 μm.

The porous scaffolds were produced by means of two different methods:

(i) the replication technique based on a polymeric sponge

(ii) the burning-out method based on a mixture of glass and organic powders.

In the latter method, different quantities of an (polyethylene) organic powder with grain sizes of 100-600 μm are mixed with the aforementioned CEL2 powder, leading to different porosities of the end product. Subsequently, the mixture is pressed, then it passes through a heat treatment where the polymer burns, leaving pores on the substrate; finally, the powders are sintered. As an alternative production technique, the replication method involves the impregnation of a polymeric template with a suitable powder suspension (slurry). The chosen template possesses a porous microstructure and, after the impregnation phase, the template undergoes a thermal treatment that burns out the organic phase and sinters the inorganic one.

To check the bioactivity requirement given in Section 5.1, some of the replication technique based 3D scaffolds were treated in simulated body fluid (SBF) for one week (sample 'B' in Tables 5.2 and 5.3) and for four weeks (sample 'D' in Tables 5.2 and 5.3) respectively, in order to study the formation of hydroxyapatite crystals on the sintered struts (Figure 5.2). In addition, 3D scaffolds were also soaked in a buffered medium, trishydroxymethylaminomethane (standardly abbreviated as tris), again for one week (sample 'C' in Tables 5.2 and 5.3) and four weeks (sample 'D' in Tables 5.2 and 5.3) respectively, so as to assess the scaffolds bioresorption with time.

The microstructural morphology of the scaffolds was studied by means of scanning electron microscopy (SEM). The replication technique allows for realisation of strut like morphologies inspired by trabecular bone architecture [Figure 5.1(a)-(b)], while the powder mixture technique results in porous matrix type morphologies [Figure 5.1(c)-(d)]. In both cases, the pore sizes related to the tailored (macro) porosity range between 100 and 500 μm. Moreover, the sintering process induces a microporosity (with characteristic length of 15 μm) important for adhesion of proteins and cells. After soaking in SBF or tris at $37^{o}C$, a new phase formed on the pore surfaces (Figure 5.2), showing the remarkable bioactivity of the material. In SBF, the chemical composition of this new phase was confirmed to be close to hydroxyapatite, by means of X-ray diffraction (XRD) and energy dispersion spectrometry (EDS). The pH variations in the pores
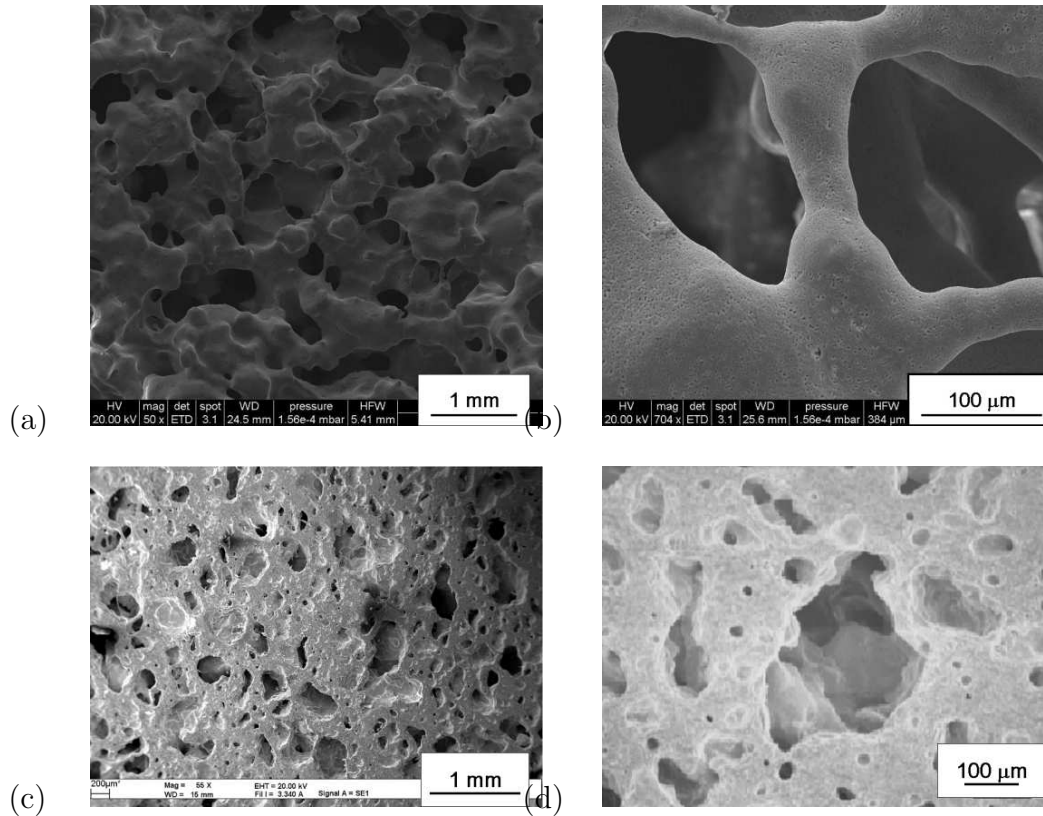
Figure 5.1: Scanning electron micrographs of CEL2 glass ceramic scaffolds at different resolutions, produced by replication method (a)-(b), and by burning-out method (c)-(d)

during the soaking of the scaffolds were also monitored: ranging between 7.4 and 8, they fall into the moderately alkaline conditions preferred by the osteoblasts, the biological cells building up an extracellular bone matrix.

Next, the microstructural information contained in Figures 5.1 and 5.2 is reduced to the features which are essential to capture the mechanical behaviour of the scaffolds. Therefore, the authors will not distinguish between the solid glass ceramic substance and the new phase initiated through treatment in SBF or tris. The relevance of this simplification will be underlined in the section devoted to model validation. The model itself will be cast in the framework of continuum micromechanics, as is detailed next.

5.3   Micromechanical model

5.3.1   Fundamentals of continuum micromechanics — representative volume element

In continuum micromechanics (Suquet 1997; Zaoui 2002; Hill 1963) a material is understood as a macrohomogeneous, but microheterogeneous body filling a representative volume element (RVE) with characteristic length ℓ_{RVE}, $\ell_{RVE} \gg d$, d standing for the characteristic length of inhomogeneities within the RVE, and $\ell_{RVE} \ll L$, L standing for the characteristic lengths of the geometry or loading of a structure built up by the material defined on the RVE. In general, the microstructure within each RVE is so complicated that it cannot be described in complete detail. Therefore, quasihomogeneous subdomains with known physical quantities (such as volume fractions, elastic or strength properties) are reasonably chosen. They are
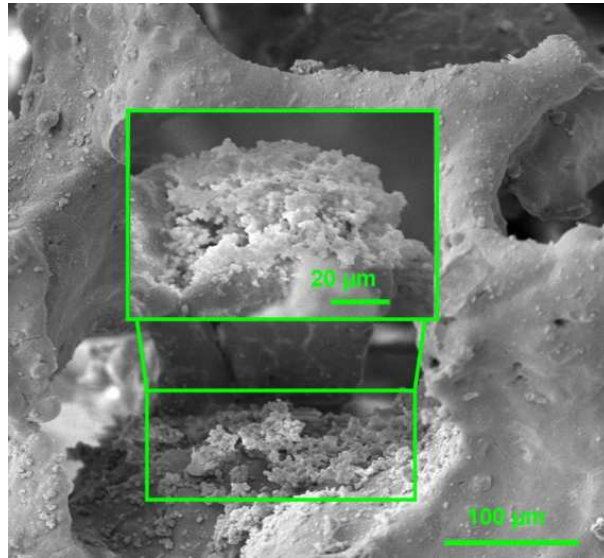
Figure 5.2: Scanning electron micrograph of CEL2 glass ceramic scaffold after one week of soaking in SBF

called material phases. The 'homogenised' mechanical behaviour of the overall material, i.e. the relation between homogeneous deformations acting on the boundary of the RVE and resulting (average) stresses, or the ultimate stresses sustainable by the RVE, can then be estimated from the mechanical behaviour of the aforementioned homogeneous phases (representing the inhomogeneities within the RVE), their dosages within the RVE, their characteristic shapes, and their interactions.

5.3.2 Micromechanical representation of CEL2-based biomaterial

An RVE of CEL2-based biomaterial is considered, with characteristic length ℓ_{RVE}=55 mm and with volume V_{RVE}, hosting spherical, empty pores with characteristic size d=100-500 μm $\ll \ell_{RVE}$, with volume V_{por} and volume fraction φ ($=V_{por}/V_{RVE}$). These pores are embedded in a solid matrix with volume V_S and volume fraction (1-φ) (see Figure 5.3).

Homogeneous ('macroscopic') strains $\boldsymbol{E}$ are imposed onto the RVE, in terms of displacements $\underline{\xi}$ at its boundary ∂V

$$\forall \underline{x} \in \partial V : \quad \underline{\xi}(\underline{x}) = \boldsymbol{E} \cdot \underline{x} \tag{5.1}$$

with $\underline{x}$ as the position vector within the RVE. As a consequence, the resulting kinematically compatible microstrains $\boldsymbol{\varepsilon}(\underline{x})$ throughout the RVE with volume V_{RVE} fulfil the average condition
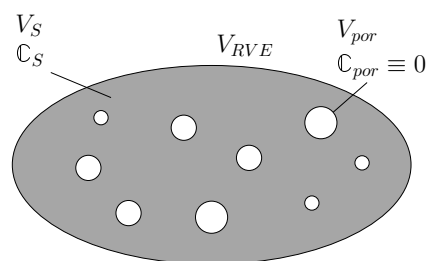
Figure 5.3: Micromechanical representation of CEL2-based biomaterial: macropores of porosity φ are embedded and interconnected within dense (microporous) solid glass substance with elasticity tensor $\mathbb{C}_S$

(Hashin 1983)

$$\boldsymbol{E} = \langle \boldsymbol{\varepsilon} \rangle = \frac{1}{V_{RVE}} \int\limits_{V_{RVE}} \boldsymbol{\varepsilon}(\underline{x}) \, \mathrm{d}V = (1 - \varphi) \, \boldsymbol{\varepsilon}_S + \varphi \, \boldsymbol{\varepsilon}_{por} \tag{5.2}$$

with

$$\boldsymbol{\varepsilon}_S = \frac{1}{V_S} \int\limits_{V_S} \boldsymbol{\varepsilon}(\underline{x}) \, \mathrm{d}V, \quad \boldsymbol{\varepsilon}_{por} = \frac{1}{V_{por}} \int\limits_{V_{por}} \boldsymbol{\varepsilon}(\underline{x}) \, \mathrm{d}V, \quad V_S + V_{por} = V_{RVE} \tag{5.3}$$

Equation (5.2) provides a link between 'micro' and 'macro' strains. Thereby, $\boldsymbol{\varepsilon}_S$ and $\boldsymbol{\varepsilon}_{por}$ are the averages of the (micro)strain tensor fields, over the solid and the porous phase respectively [see equation (5.3)]. Analogously, homogenised ('macroscopic') stresses $\boldsymbol{\Sigma}$ are defined as the spatial average over the RVE of the microstresses $\boldsymbol{\sigma}(\underline{x})$

$$\boldsymbol{\Sigma} = \langle \boldsymbol{\sigma} \rangle = \frac{1}{V_{RVE}} \int\limits_{V_{RVE}} \boldsymbol{\sigma} \, \mathrm{d}V = (1 - \varphi) \, \boldsymbol{\sigma}_S \tag{5.4}$$

with $\boldsymbol{\sigma}_S$ as the average of the (micro)stress tensor field over the solid phase.

5.3.3 Constitutive behaviour of CEL2 and pores

The solid phase (consisting of dense CEL2 glass ceramic, and in case of samples tested for biocompatibility, also of tris or SBF-derived substances) inside the RVE V_{RVE} behaves linear elastically

$$\boldsymbol{\sigma} = \mathbb{C}_S : \boldsymbol{\varepsilon}_S \tag{5.5}$$

with $\mathbb{C}_S = 3k_S \mathbb{J} + 2\mu_S \mathbb{K}$ as the isotropic elastic stiffness of the solid phase; with bulk modulus k_S and shear modulus μ_S. $\mathbb{J} = 1/3\mathbf{1} : \mathbf{1}$ and $\mathbb{K} = \mathbb{I} - \mathbb{J}$ are the volumetric and the deviatoric part of the fourth order identity tensor $\mathbb{I}$, with components $I_{ijkl} = 1/2(\delta_{ik}\delta_{jl} + \delta_{il}\delta_{kj})$; the components of the second order unit tensor $\mathbf{1}$, δ_{ij} (Kronecker delta), read as $\delta_{ij} = 1$ for $i = j$ and $\delta_{ij} = 0$ for $i \neq j$. The pores are empty, therefore $\mathbb{C}_{por} = \mathcal{V}$. The load bearing capacity of the solid phase is bounded according to a von Mises-type failure criterion, reading as

$$\mathfrak{f}(\boldsymbol{\sigma}(\underline{x})) = \sigma_d(\underline{x}) - \tau^{ult} = 0 \tag{5.6}$$

where τ^{ult} is the shear strength of the solid phase, and σ_d is the equivalent deviatoric microscopic stress, reading as

$$\sigma_d(\underline{x}) = \sqrt{\frac{1}{2} \boldsymbol{\sigma}_d(\underline{x}) : \boldsymbol{\sigma}_d(\underline{x})} \tag{5.7}$$

with

$$\boldsymbol{\sigma}_d(\underline{x}) = \boldsymbol{\sigma}(\underline{x}) - \frac{1}{3} \operatorname{tr} \boldsymbol{\sigma}(\underline{x})\mathbf{1} \tag{5.8}$$

as the deviatoric part of the microscopic stress tensor $\boldsymbol{\sigma}$.

5.3.4 Homogenisation of elastic properties

Homogenised ('macroscopic') stresses and strains, $\boldsymbol{\Sigma}$ and $\boldsymbol{E}$, are related by the homogenised ('macroscopic') stiffness tensor $\mathbb{C}_{hom}$

$$\boldsymbol{\Sigma} = \mathbb{C}_{hom} : \boldsymbol{E} \tag{5.9}$$

which needs to be linked to the solid stiffness $\mathbb{C}_S$, as well as to the shape, and to the spatial arrangement of the phases (solid glass ceramic substance and pores). This link is based on the linear relation between the homogenised ('macroscopic') strain $\boldsymbol{E}$ and the average ('microscopic') strain $\boldsymbol{\varepsilon}_r$, resulting from the superposition principle valid for linear elasticity [equation (5.5)] (Hill 1963). This relation is expressed in terms of the fourth order concentration tensors $\mathbb{A}_r$ of each of the phases r ($r=S$ or por)

$$\boldsymbol{\varepsilon}_r = \mathbb{A}_r : \boldsymbol{E} \tag{5.10}$$

which implies, together with equation (5.2), that

$$(1 - \varphi)\,\mathbb{A}_S + \varphi\,\mathbb{A}_{por} = \mathbb{I} \tag{5.11}$$

Insertion of equation (5.10) into equation (5.5) and averaging over all phases according to equation (5.4) leads to

$$\boldsymbol{\Sigma} = (1 - \varphi)\,\mathbb{C}_S : \mathbb{A}_S : \boldsymbol{E} \tag{5.12}$$

From equations (5.12) and (5.9), the sought relation between the phase stiffness tensor $\mathbb{C}_S$ and the overall homogenised stiffness $\mathbb{C}_{hom}$ of the RVE can be identified

$$\mathbb{C}_{hom} = (1 - \varphi) : \mathbb{C}_S : \mathbb{A}_S = \mathbb{C}_S : (\mathbb{I} - \varphi\,\mathbb{A}_{por}) \tag{5.13}$$

If the porosity is very small, $\varphi \ll 1$ (dilute dispersion of pores), the mechanical interactions between the pores can be neglected. In this case, the macroscopic strains $\boldsymbol{E}$ acting on the RVE of Figure 5.3 can be set equal to those acting on the remote boundary of an infinite matrix made up by the solid phase, a matrix which hosts one pore like inclusion. Under this condition, the homogeneous (microscopic) strains $\boldsymbol{\varepsilon}_{por}$ within a spherical empty pore follows from Eshelby's 1957 problem (Eshelby 1957), and read as

$$\boldsymbol{\varepsilon}_{por} = \underbrace{[\mathbb{I} - \mathbb{S}_{sph}]^{-1}}_{\mathbb{A}_{por}} : \boldsymbol{E} \tag{5.14}$$

whereby $\mathbb{A}_{por}$ follows from equation (5.10). The fourth order Eshelby tensor $\mathbb{S}_{sph}$ accounts for the morphology of the inclusion. For spheres, it reads as

$$\mathbb{S}_{sph} = \frac{3k_S}{3k_S + 4\mu_S}\mathbb{J} + \frac{6(k_S + 2\mu_S)}{5(3k_S + 4\mu_S)}\mathbb{K} \tag{5.15}$$

Use of equations (5.14) and (5.15) in equation (5.13) yields the so called 'dilute estimate' for the stiffness of a porous material with spherical pores. In the present situation, however, this estimate needs to be extended to the case of higher porosities made up by interconnected pores (see Figures 5.1 and 5.2). Therefore, the so called Differential Scheme is used (Boucher 1976; McLaughlin 1977; Molinari and El Mouden 1996; Dormieux and Lemarchand 2001). Initially, a very small volume fraction of pores $\Delta\varphi$ is introduced into the solid matrix and the material is homogenised via equations (5.14), (5.15) and (5.13). The following steps consist in (i) removing

a very small portion $\Delta x \ll 1$ of the previously homogenised material (containing already some porosity), in (ii) replacing it by the same volume fraction of pores (see Figure 5.4), and in (iii) homogenisation of the slightly more porous material. Thereby, the overall porosity increases by the increment $\Delta \varphi$.
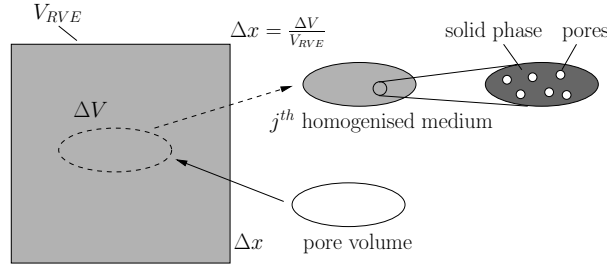
Figure 5.4: Schematical representation of Differential Scheme, in the line of (Dormieux and Lemarchand 2001)

$$\Delta \varphi = -\varphi \Delta x + \Delta x = (1 - \varphi)\Delta x, \quad \Delta x \ll 1 \tag{5.16}$$

Repeating this removal and introduction of small volume fractions, followed by subsequent homogenisation, leads to an iteration scheme of the form (Dormieux et al. 2006)

$$
\begin{aligned}
k_{DS}^{j+1} &= k_{DS}^{j} \left[1 - \left(1 + \frac{3k_{DS}^{j}}{4\mu_{DS}^{j}} \right) \Delta x \right] \\
\mu_{DS}^{j+1} &= \mu_{DS}^{j} \left[1 - \left(5\frac{3k_{DS}^{j} + 4\mu_{DS}^{j}}{9k_{DS}^{j} + 8\mu_{DS}^{j}} \right) \Delta x \right]
\end{aligned}
\tag{5.17}
$$

with k_{DS}^{j} and μ_{DS}^{j} as the homogenised moduli after the jth homogenisation step. Realising scheme (5.17) for the limit case $\Delta \varphi \to 0$, as long as the actual porosity is reached, $\sum_{j} \varphi_j = \varphi$, yields the differential estimate (Dormieux et al. 2006)

$$
\begin{aligned}
g1 &= \frac{(1 + 4\mu_S/3k_S)(\mu_{hom}/\mu_S)^3}{2 - (1 - 4\mu_S/3k_S)(\mu_{hom}/\mu_S)^{3/5}} - (1 - \varphi)^6 = 0 \\
g2 &= \frac{\mu_{hom}}{\mu_S} - \frac{(1 - 4/3\,\mu_{hom}/k_{hom})^{5/3}}{(1 - 4/3\,\mu_S/k_S)^{5/3}} = 0
\end{aligned}
\tag{5.18}
$$

with k_{hom} and μ_{hom} as the bulk and the shear modulus of the homogenised stiffness tensor $\mathbb{C}_{hom}$, $\mathbb{C}_{hom} = 3k_{hom}\mathbb{J} + 2\mu_{hom}\mathbb{K}$. Equation (5.18) is valid as long as Poisson's ratio $\nu_S = (3k_S - 2\mu_S)/(6k_S + 2\mu_S)$ is larger than 0.2 (see (Dormieux et al. 2006)). Finally, standard isotropic elasticity relates k_{hom} and μ_{hom} to the Young's modulus E_{hom}

$$E_{hom} = \frac{9k_{hom}\mu_{hom}}{3k_{hom} + \mu_{hom}} \tag{5.19}$$

5.3.5 Upscaling of failure properties

In order to determine the effective failure properties resulting from local failure characteristics [equation (5.17)], we are left with relating the local strains and stresses to corresponding macroscopic quantities. In contrast to the homogenised elastic properties, which can be derived from (first order) averages of microstrains and microstresses over the material phases [see $\boldsymbol{\varepsilon}_S$ and $\boldsymbol{\varepsilon}_{por}$

in equation (5.3)], homogenisation of strength properties calls for additional information on the heterogeneity of these microquantities, i.e. the strain or stress peaks inside the microstructure (possibly cancelled out through averaging) need to be appropriately considered. This heterogeneity can reasonably be considered through so called effective microstrains ε_d^{eff} (Kreher 1990; Dormieux et al. 2002; Barthélémy and Dormieux 2003, 2004) (see (Fritsch et al. 2007a,b, 2009) for application to hydroxyapatite ceramics), such as the square root of the average over the solid material phase, of the squares of the equivalent deviatoric (micro) strains $\varepsilon_d(\underline{x})$,

$$\varepsilon_d^{eff} = \sqrt{\frac{1}{V_S} \int_{V_S} \varepsilon_d^2(\underline{x}) \mathrm{d}V} \tag{5.20}$$

with

$$\varepsilon_d(\underline{x}) = \sqrt{\frac{1}{2} \boldsymbol{\varepsilon}_d(\underline{x}) : \boldsymbol{\varepsilon}_d(\underline{x})} \tag{5.21}$$

with the deviatoric microstrain tensor

$$\boldsymbol{\varepsilon}_d(\underline{x}) = \boldsymbol{\varepsilon}(\underline{x}) - \frac{1}{3} \operatorname{tr} \boldsymbol{\varepsilon}(\underline{x}) \, \mathbf{1} \tag{5.22}$$

and with tr $\boldsymbol{\varepsilon}$ as the trace of the microscopic strain tensor. Energy considerations (Dormieux et al. 2002) allow for determination of the effective deviatoric strain ε_d^{eff} from the macroscopic strains $\boldsymbol{E}$, according to

$$\varepsilon_d^{eff,2} = \frac{1}{2(1-\varphi)} \left[\frac{1}{2} \frac{\partial k_{hom}}{\partial \mu_S} (\operatorname{tr} \boldsymbol{E})^2 + \frac{\partial \mu_{hom}}{\partial \mu_S} \boldsymbol{E}_d : \boldsymbol{E}_d \right] \tag{5.23}$$

with tr $\boldsymbol{E}$ and $\boldsymbol{E}_d$ as the trace and the deviatoric part of the macroscopic strain tensor $\boldsymbol{E}$. The definition of $\boldsymbol{E}_d$ is analogous to equation (5.22). The derivations of k_{hom} and μ_{hom} with respect to μ_S are obtained via implicit differentiation of equation (5.18), leading to

$$\frac{\partial \mu_{hom}}{\partial \mu_S} = \frac{-\frac{\partial g_1}{\partial \mu_S}}{\frac{\partial g_1}{\partial \mu_{hom}}}, \quad \frac{\partial k_{hom}}{\partial \mu_S} = \frac{-\left(\frac{\partial g_2}{\partial \mu_{hom}} \frac{\partial \mu_{hom}}{\partial \mu_S} + \frac{\partial g_2}{\partial \mu_S} \right)}{\frac{\partial g_2}{\partial k_{hom}}} \tag{5.24}$$

whereby

$$\frac{\partial g_1}{\partial \mu_S} = -\frac{6\mu_{hom}^3(9k_S + 8\mu_S)\left(4\mu_{hom}\mu_S + 5\mu_S\left(\frac{\mu_{hom}}{\mu_S}\right)^{2/5}k_S - 2\mu_{hom}k_S\right)}{\mu_S\,\mathcal{N}},$$

$$\frac{\partial g_1}{\partial \mu_{hom}} = \frac{6\mu_{hom}^2(3k_S + 4\mu_S)\left(8\mu_{hom}\mu_S + 15\mu_S\left(\frac{\mu_{hom}}{\mu_S}\right)^{2/5}k_S - 6\mu_{hom}k_S\right)}{\mathcal{N}},$$

$$\mathcal{N} = 5\mu_S^4\left(6k_S - 3\left(\frac{\mu_{hom}}{\mu_S}\right)^{3/5}k_S + 4\left(\frac{\mu_{hom}}{\mu_S}\right)^{3/5}\mu_S\right)^2\left(\frac{\mu_{hom}}{\mu_S}\right)^{2/5},$$

$$\frac{\partial g_2}{\partial \mu_S} = -\frac{\mu_{hom}}{\mu_S^2} - \frac{20\left(1 - \frac{4\mu_{hom}}{3k_{hom}}\right)^{5/3}}{9k_S\left(1 - \frac{4\mu_S}{3k_S}\right)^{8/3}}, \quad \frac{\partial g_2}{\partial \mu_{hom}} = \frac{1}{\mu_S} + \frac{20\left(1 - \frac{4\mu_{hom}}{3k_{hom}}\right)^{2/3}}{9k_{hom}\left(1 - \frac{4\mu_S}{3k_S}\right)^{5/3}},$$

$$\frac{\partial g_2}{\partial k_{hom}} = \frac{20\mu_{hom}\left(1 - \frac{4\mu_{hom}}{3k_{hom}}\right)^{2/3}}{9k_{hom}^2\left(1 - \frac{4\mu_S}{3k_S}\right)^{5/3}} \tag{5.25}$$

The macroscopic strains $\boldsymbol{E}$ and $\boldsymbol{E}_d$ in equation (5.23) are related to the corresponding macroscopic stress states via the homogenised stiffness tensor $\mathbb{C}_{hom}$ [see equation (5.9)]. In equation (5.6), stress peaks of $\sigma_d(\underline{x})$ are left to be estimated by the effective microstress σ_d^{eff}. The latter reads as

$$\sigma_d^{eff} = 2\mu_S\,\varepsilon_d^{eff} \tag{5.26}$$

Insertion of equation (5.26), together with equations (5.18)-(5.25) and (5.9), into the microscopic failure criterion (5.6) with $\sigma_d(\underline{x}) \approx \sigma_d^{eff}$, delivers an elastic limit criterion for macroscopic stress states (representing ultimate strength in the case of brittle materials), as function of the porosity φ

$$\mathfrak{F}(\boldsymbol{\Sigma}) = \frac{2\mu_S}{\sqrt{2(1-\varphi)}}\left[\frac{1}{2}\frac{\partial k_{hom}}{\partial \mu_S}\left(\frac{\mathrm{tr}\,\boldsymbol{\Sigma}}{3k_{hom}}\right)^2 + \frac{\partial \mu_{hom}}{\partial \mu_S}\frac{\boldsymbol{\Sigma}_d : \boldsymbol{\Sigma}_d}{2\mu_{hom}^2}\right]^{1/2} - \tau^{ult} = 0 \tag{5.27}$$

with $\mathrm{tr}\,\boldsymbol{\Sigma}$ and $\boldsymbol{\Sigma}_d$ as the trace and the deviatoric part of the macroscopic stress tensor $\boldsymbol{\Sigma}$. The definition of $\boldsymbol{\Sigma}_d$ is analogous to equation (5.22).

In particular, strength model (5.27) will be evaluated for stress states related to uniaxial compression $\boldsymbol{\Sigma} = \Sigma\,\boldsymbol{e}_1 \otimes \boldsymbol{e}_1$, yielding an estimate for the macroscopic uniaxial compressive strength

$$\boldsymbol{\Sigma}_{pred}^{ult,c} = \frac{\left[9(2\nu_{hom} - 1)^2\frac{\partial k_{hom}}{\partial \mu_S} + 12(\nu_{hom} + 1)^2\frac{\partial \mu_{hom}}{\partial \mu_S}\right]^{1/2}(1 - \varphi)^{1/2}E_{hom}\tau^{ult}}{\left[3(2\nu_{hom} - 1)^2\frac{\partial k_{hom}}{\partial \mu_S} + 4(2\nu_{hom} + 1)^2\frac{\partial \mu_{hom}}{\partial \mu_S}\right]\mu_S} \tag{5.28}$$

In equation (5.28), ν_{hom} is Poisson's ratio of the homogenised material

$$\nu_{hom} = \frac{3k_{hom} - 2\mu_{hom}}{6k_{hom} + 2\mu_{hom}} \tag{5.29}$$

5.4 Model validation

5.4.1 Strategy for model validation through independent test data

Validation of the micromechanical representation of CEL2-based biomaterials will rest on two independent experimental sets, related to dense CEL2 glass ceramics and to samples of (macro)porous biomaterials: biomaterial specific macroscopic (homogenised) Young's moduli E_{hom} and uniaxial compressive strengths $\Sigma_{pred}^{ult,c}$, predicted by the micromechanics model (see Section 5.3) on the basis of biomaterial independent ('universal') elastic and strength properties of pure CEL2-glass (experimental set I, see Section 5.4.2) for biomaterial specific porosities φ (experimental set IIa, see Section 5.4.3), are compared to corresponding biomaterial specific experimentally determined Young's moduli E_{exp} (experimental set IIb-1, see Section 5.4.4) and uniaxial compressive strength values $\Sigma_{exp}^{ult,c}$ (experimental set IIb-2, see Section 5.4.5).

5.4.2 'Universal' mechanical properties of dense CEL2 glass ceramics — experimental set I

Acoustic experiments (Kohlhauser et al. 2008) reveal the isotropic elastic constants for dense CEL2 glass ceramic, its Young's modulus $E_S = 85.3$ GPa, and its Poisson's ratio $\nu_S = 0.25$ (equivalent to bulk modulus $k_S = E_S/3/(1 - 2\nu_S) = 56.9$ GPa and shear modulus $\mu_S = E_S/2/(1 + \nu_S) = 34.1$ GPa (see also Table 5.1). The authors are not aware of reliable direct strength tests on dense CEL2 glass ceramics. However, ceramic biomaterials made of hydroxyapatite with a microporosity similar to that of the herein investigated materials exhibit a typical shear strength of $\tau^{ult} = 9.8$ MPa (Charrière et al. 2001), which will be considered as representative for dense (microporous) CEL2 glass ceramic (Table 5.1).

Table 5.1: 'Universal' (biomaterial-independent) isotropic phase properties of dense CEL2 glass ceramic (=solid phase in Figure 5.3)

Young's modulus E_S	85.3 GPa	from (Kohlhauser et al. 2008)
Poisson's ratio ν_S	0.25	from (Kohlhauser et al. 2008)
Shear strength τ_S^{ult}	9.8 MPa	from (Charrière et al. 2001)

5.4.3 Sample specific porosities of CEL2-based biomaterials — experimental set IIa

The porosity of the investigated CEL2-based samples was determined from measurements of their masses M and volumes V, according to

$$\varphi = 1 - \frac{M}{V\,\rho_S} \tag{5.30}$$

whereby $\rho_S = 2.6$ g/cm³ is the mass density of the dense CEL2 glass ceramic (Kohlhauser et al. 2008) (see Table 5.2). Samples denoted A-E in this table were cubes with an edge length of about 5 mm, while the rest of the samples collected in Table 5.2 were cuboid shaped, with dimensions between 10x10x10 mm and 10x10x50 mm. Equation (5.30) was also used for the estimation of the porosity of the scaffolds soaked in SBF and tris (see Section 5.2 for details):

this is equivalent to approximating the mass density of the soaking induced, newly formed phases, such as hydroxyapatite with density between 2.61 and 3.16 g/cm^3 in biological systems (Dorozhkin and Epple 2002) by the mass density of CEL2 glass.

Table 5.2: Porous CEL2-based biomaterial samples: Young's modulus E_{exp} determined from propagation velocity v_{bar} of bar waves with a signal frequency f=0.1 MHz: a is a typical cross-sectional dimension, ρ is the mass density, and φ the porosity of the sample; λ denotes the wavelength

Specimen	a	ρ	φ	v_{bar}	λ	a/λ	E_{exp}
	measured	measured	Eq. (5.30)	Eq. (5.31)	Eq. (5.32)	-	Eq. (5.33)
nr.	[mm]	[g/cm^3]	[%]	[km/s]	[mm]	-	[GPa]
A	5.22	0.84	67.3	3.96	39.6	0.13	13.10
B	5.35	0.87	66.2	4.09	40.9	0.13	14.50
C	4.33	0.97	62.3	3.94	39.4	0.11	15.00
D	5.22	0.80	68.7	3.06	30.6	0.17	7.50
E	5.14	0.58	77.5	2.97	29.7	0.17	5.10
1	15.27	1.47	42.4	4.71	47.1	0.32	32.73
2	13.34	1.45	43.5	4.31	43.1	0.31	26.87
3	9.78	1.35	47.1	4.09	40.9	0.24	22.61
4	9.74	1.32	48.3	4.16	41.6	0.23	22.85
5	9.85	1.40	45.3	4.08	40.8	0.24	23.28
6	9.59	1.30	49.3	4.08	40.8	0.24	21.58
7	9.5	1.88	26.7	4.73	47.3	0.20	42.02
8	9.5	1.59	37.9	4.43	44.3	0.21	31.13
9	10.39	0.88	65.4	4.34	43.4	0.24	16.70
10	9.74	0.89	65.1	4.24	42.4	0.23	16.10
11	24.75	0.88	65.4	4.25	42.5	0.58	16.00
12	21.6	0.89	65.1	4.13	41.3	0.52	15.30

5.4.4 Sample specific elasticity experiments on CEL2-based biomaterials — experimental set IIb-1

Elastic properties of porous CEL2-based biomaterials were determined through acoustical testing. The used ultrasonic device is composed of a pulser-receiver Panametrics-NDT 5077 PR, of an oscilloscope, and of several ultrasonic transducers; the pulser unit can emit a square pulse of up to 400 V, with frequencies from 0.1 to 20 MHz. The piezoelectric elements in the transducers are able to transform electrical signals into mechanical ones, or mechanical signals into electrical ones (see Figure 5.5).

The receiver unit has a bandwidth of 0.1-35 MHz and a voltage gain until 59 dB. The signal is displayed on an oscilloscope Lecroy Waverunner 62Xi, which allows for estimating the time of flight t of the acoustic wave through the specimen along a path of length l; t and l give access to the velocity v of the wave, via

$$v = \frac{l}{t} \tag{5.31}$$
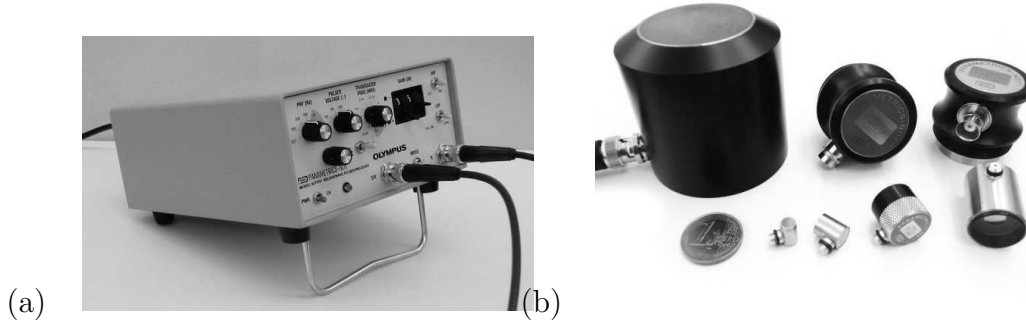
Figure 5.5: Equipment for acoustical testing: (a) pulser-receiver, (b) ultrasonic transducers

Velocity v and frequency f of the acoustic signal yield the wavelength λ as

$$\lambda = \frac{v}{f} \tag{5.32}$$

If the wavelength l is considerably larger than the diameter or another typical cross-sectional dimension a of the specimen, a bar wave propagates with velocity v_{bar} (Fedorov 1968; Ashman et al. 1984). This is the case for the herein employed 0.1 MHz signals propagating through CEL2-based biomaterial samples (see Table 5.2). There, the theory of elastodynamics (Fedorov 1968; Ashman et al. 1984) allows for the determination of Young's modulus from the velocities of bar waves

$$E = \rho v_{bar}^2 \tag{5.33}$$

Given $\lambda \approx 40$ mm (see Table 5.2) $\gg l_{RVE} = 5$ mm (see Section 5.2), these values for Young's modulus actually refer to the (macro)porous biomaterial scaffolds (and not to the dense CEL2 glass ceramic between the macropores).

5.4.5 Comparison between sample specific stiffness predictions and corresponding experiments

The stiffness values predicted by the homogenisation scheme for elastic properties (described in Section 5.3) for biomaterial specific porosities (experimental set IIa) on the basis of biomaterial independent ('universal') stiffness of CEL2 biomaterials (experimental set I) are compared to corresponding experimentally determined biomaterial specific stiffness values from experimental set IIb-1. To quantify the model's predictive capabilities, the mean and the standard deviation of the normalised error e, between predictions and experiments $\bar{e}$ and e_S, are considered

$$\bar{e} = \frac{1}{n}\sum_{i=1}^{n} e_i = \frac{1}{n}\sum_{i=1}^{n} e_i \frac{E_{hom,i} - E_{exp}}{\bar{E}_{exp}} \tag{5.34}$$

$$e_S = \left[\frac{1}{n-1}\sum_{i=1}^{n}(e_i - \bar{e})^2\right]^{\frac{1}{2}} \tag{5.35}$$

with summation over n values E_{exp}. $\bar{E}_{exp}$ is the mean over all experimental values.

Insertion of biomaterial specific porosities (fourth column of Table 5.2) and 'universal' stiffness constants (Table 5.1) into equation (5.18) delivers, together with equation (5.19), sample specific

stiffness estimates for the effective Young's modulus E_{hom}. These stiffness predictions are compared to corresponding experimental stiffness values E_{exp} (Figure 5.6 and last column of Table 5.2). The satisfactory agreement between model predictions and experiments is quantified by prediction errors of $-9 \pm 16\%$ (mean value±standard deviation).
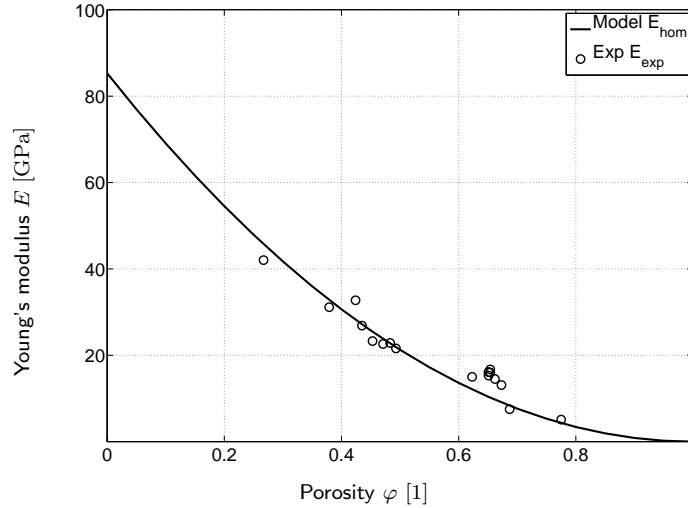
Figure 5.6: Comparison between model predictions and experiments for stiffness of porous CEL2 glass ceramic scaffolds

5.4.6   Sample specific strength experiments on CEL2-based biomaterials — experimental set IIb-2

Ultimate properties of CEL2-based biomaterials were determined by uniaxial, compressive, quasistatic testing. The five cubic samples A-E (see also Table 5.2 and Section 5.4.3) were suitable for measurements in an electromechanical testing stand (MTS QTest 10, see Figure 5.7). A 1000 N range force transducer was used. Compression tests were performed in a displacement control mode with 0.015 mm/s speed (strain rate $\sim 3 \cdot 10^{-3}$/s). Corresponding stress strain curves of the specimens are characterised by pronounced softening after a first stress peak. The latter was identified as ultimate strength (see Table 5.3).

Table 5.3: Experimental compressive strength $\Sigma_{exp}^{ult,c}$ of CEL2-based biomaterial samples as function of porosity φ (see Table 5.2)

Sample	φ	$\Sigma_{exp}^{ult,c}$
	[-]	[MPa]
A	0.67	1.85
B	0.66	4.58
C	0.62	4.40
D	0.69	2.11
E	0.77	1.91

Figure 5.7: Electromechanical testing stand for compression tests on CEL2-based biomaterial samples

5.4.7 Comparison between sample specific strength predictions and corresponding experiments

The strength values predicted by the upscaling relations described in Section 5.3, for sample specific porosities (experimental set IIa) on the basis of sample independent ('universal') elasticity and shear strength characteristics of dense CEL2 glass ceramic (experimental set I) are compared to corresponding experimentally determined sample specific uniaxial compressive strength values from experimental set IIb-2.

Insertion of biomaterial specific porosities (second column of Table 5.3) into equation (5.28), together with equations (5.24), (5.25) and (5.18), delivers, together with E_S, ν_S and τ_S^{ult} (Table 5.1), sample specific strength estimates for uniaxial compressive strength ($\Sigma_{pred}^{ult,c}$). These strength predictions are compared to corresponding experimental strength values $\Sigma_{exp}^{ult,c}$ (Figure 5.8 and third column of Table 5.3). The satisfactory agreement between model predictions and experiments is quantified by prediction errors of 3±34% [mean value±standard deviation, in analogy to equations (5.34)-(5.35)].

5.5 Conclusions

A continuum micromechanical concept has been developed for the elasticity and strength of porous biomaterials made of CEL2, which was verified through independent experimental sets. The latter were gained from the authors' own experiments. The predictions of the porosity based micromechanics model agree well with the corresponding experimentally determined mechanical properties of samples produced by both the replication technique and the burning-out method: this underlines the relevance of the Differential Scheme for microstructures with interconnected pores, irrespective of the actual sphere or strut type microstructural morphology. The good agreement of the model with the corresponding elasticity and strength experiments of samples of both the unmodified and the bioactivity tested biomaterials indicates that the bioactivity tests primarily increased the porosity of the scaffolds, while the newly formed chemical phases exhibit mechanical properties which are more or less similar to the original glass ceramic phase.
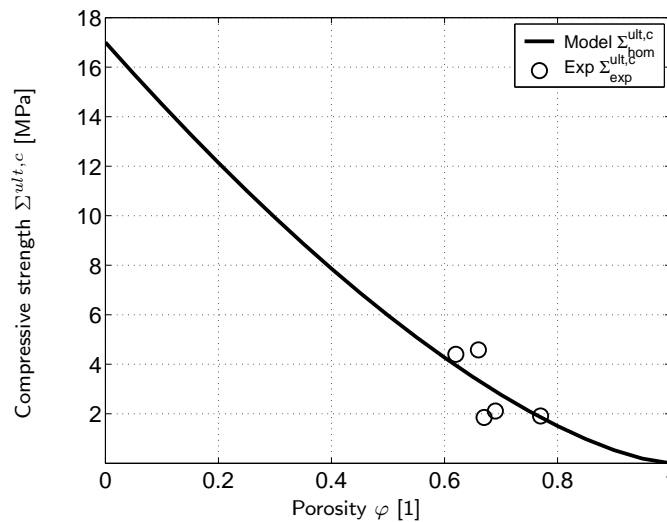
Figure 5.8: Comparison between model predictions and experiments for compressive strength of porous CEL2 glass ceramic scaffolds

The suitability of the differential scheme to predict the elasticity properties of porous CEL2 glass ceramic scaffolds for tissue engineering is consistent with the earlier finding (Zimmermann 1991) that this scheme appropriately predicts the elastic properties of sintered glass (Walsh et al. 1965) of various porosities with nearly spherical pore shape.

Conclusively, it is proposed that micromechanical models have a considerable potential for improving biomaterial design. Nowadays, the latter is largely done in a trial-and-error procedure. Based on a number of mechanical and/or acoustical tests, new material design parameters are guessed. On the other hand, with well validated micromechanical models, the mechanical implications of changes in the microstructure can be predicted so that minimisation of material failure risk allows for the optimisation of key design parameters, such as porosities or geometries of microstructures. Hence, it is believed that micromechanical theories can considerably speed up the future development of tissue engineering scaffolds.

Acknowledgements

Appendix **A**

Literature review

Several theortical works on wave propagation phenomena in the early times of ultrasonic methods deal with isotropic materials (Hearmon 1946; Kolsky 1953). Later anisotropic materials, where energy flux deviation and group velocity must be taken into account when determining the complete stiffness tensor, were investigated (Hayes and Musgrave 1979). Extensive literature can be found on the propagation of elastic waves in anisotropic media, e.g. Auld (1990); Carcione (2001); Helbig (1994); Kolsky (1953); Markham (1970). Whereas anelastic waves are covered by far less authors, e.g. Kolsky (1953); Carcione (2001).

In the following, short literature reviews on (i) wave propagation in bars and (ii) wave scattering in multi-phase media are given.

A.1 Wave propagation in bars

In the majority of ultrasonic experiments on small specimen some influence of the side boundaries of the specimen exists and often the complete wave is guided by the boundaries, i.e. guided waves propagate that travel a zigzag path along the waveguide by successive reflections at the boundaries (Redwood 1963). A clear distinction between this propagation type and bulk wave propagation is difficult because of coupling of the longitudinal and transversal waves at boundaries and interfaces in bounded media (Redwood 1963; Thurston 1978). Depending on different reflection types for longitudinal and transversal waves, different propagation modes are possible, which are assigned to modes called compression, shear, torsional or flexural and, depending on the particle displacement, are termed symmetric or asymmetric. For some higher modes of guided waves the plane wave assumption also breaks down, but these are connected with velocities that are not directly related to elastic stiffnesses (Redwood 1963).

The first mathematical description of high frequency waves in (circular) bars based on the solution of a boundary value problem in the theory of elasticity go back to Pochhammer (1876) and Chree (1889). For a short history of research on wave propagation in bars see McSkimin (1956) and Kolsky (1964). The solutions of the dispertion relation for a high frequency continuous wave propagating in isotropic, infinte, circular bar are usually presented in plots of phase or group velocity against frequency f or wavelength λ parameters that include the diameter of the bar a, e.g. a/λ. Of all (infinite) modes of wave propagation, i.e. real solutions of the dispertion relation, only three extend to zero frequency, i.e. $a/\lambda = 0$. These are the lowest (fundamental)

axial-radial, i.e. longitudinal, and the lowest torsional mode (both axial-symmetric modes) and the lowest flexural mode (Thurston 1978). The torsional wave propagation is govern by a single elastic constant, the shear modulus G, while the two other modes are govern by two elastic constants, e.g. Young's modulus E and Poisson's ratio ν, i.e. plots are usually given for fixed Poisson's ratio ν.

The (lowest) longitudinal mode propagates at the extensional wave velocity, which is govern by Young's modulus E in the low-frequency limit, reaching $v_E = \sqrt{E/\rho}$ at $a/\lambda = 0$, where ρ is the mass density of the bar (Kolsky 1964; Thurston 1978). This special symmetrical mode is also called the Young's modulus mode, which is (not exactly) plane and dispersive (Redwood 1963). With decreasing wavelength the (phase and group) velocity drops to the Rayleigh velocity between $a/\lambda \approx 0.2$–2 (reaching it at $a/\lambda = \infty$). Except for the Young's modulus mode, all axial-radial modes have cut-off frequencies, at which the displacements are independent of the length of the bar (Thurston 1978).

The (lowest) flexural mode can be described by the elementary flexure theory for $a/\lambda \lesssim 0.03$, i.e. at vanishingly small velocities at infinite wavelength ($a/\lambda = 0$). With increasing frequency the (phase and group) velocity tends to the Rayleigh velocity, reaching it approximately at $a/\lambda \approx 1$ and reaching it exactly at $a/\lambda = \infty$ (Kolsky 1964). For higher 'flexural' modes at high frequencies, $a/\lambda \ll 1$, wave propagation can be described as nearly transverse shear waves, i.e. waves that are nearly linearly polarized, with phase and group velocity nearly equal to the transversal wave velocity v_T (Thurston 1978).

The velocity of the (lowest) torsional mode is nondispersive, i.e. the wave velocity is constant for all values of a/λ, and equal to the transversal wave velocity v_T, showing dispersion only at higher modes (Kolsky 1964). The (phase and group) velocities of all higher axi-symmetric and flexural modes tend to the transversal wave velocity at zero wavelengths (Thurston 1978). Generally phase and group velocities in the long and short wavelength limits of the fundamental modes are equal. Only the transition behavior is slightly different, with the longitudinal mode and the flexular modes exhibiting a minimum of $0.38\,v_E$ and a maximum of $0.64\,v_E$, respectively, at $\approx 0.4\,a/\lambda$, i.e. no smooth transition to the Rayleigh velocity exists.

The phase velocity of the first mode of shear wave propagtion of small wavelength in a bar was found to be slightly greater than the bulk transversal wave velocity (McSkimin 1956). Solutions for long wavelength of transverse wave motion are described by the flexural mode.

As the velocity, also the displacement distribution across the cross-section of the bar changes with frequency. At very long wavelengths the cross-section oscillates essentially rigidly, while the axial displacements vary linearly from the neutral plane or remain constant for the fundamental flexural mode or longitudinal mode, respectively. At very small wavelengths the disturbance at the fundamental longitudinal and flexural modes is concentrated near the bar surface, similar to Rayleigh waves (Thurston 1978). Transversal waves at small wavelengths exhibit a predominantly transverse displacement distribution with only very small axial displacements. The displacements in the center of the bar are principally unidirectional, but radial and tangential displacements reverse their direction along axes in and normal to the excitation direction, respectively (McSkimin 1956).

It is important to realize, that experimentally obtained ultrasonic velocities are measurements of pulse wave propagation in bars of finite length. The dispersion curves ignore boundary conditions (because they are obtained for infinite bars), but these do not influence the velocity solutions for high frequencies when the wavelength is smaller than the length of the bar. The Pochhammer-Chree theory can also be applied to determine resonance frequencies of finite bars (Thurston 1978). Moreover, pulse propagation in a bar of low frequency, i.e. the extensional velocity at $a/\lambda < 1$ may be discribed by the theoretical solutions for continuous waves, but fail to describe the propagation of high frequency pulses ($a/\lambda > 10$), where the velocity of the first

pulse is equal to the longitudinal bulk wave velocity v_L in an unbounded medium (Redwood 1959). The theoretic high frequency limiting velocities of longitudinal wave modes (Rayleigh and transversal velocity) could not be confirmed in experiments with very high frequency waves (e.g. pulses), where longitudinal bulk wave velocity in bars was observed (Tu et al. 1955). This discrepancy is related to the coupling of transversal and longitudinal waves at the boundaries (Thurston 1978).

Normally the fundamental mode is excited by a pulse propagating in a bar. A small part of a pulse in a bar propagates with longitudinal bulk wave velocity, but its amplitude becomes extremely small when $a/h < 0.1$ (Kolsky 1964). Diffraction phenomena can occure when the wavelength of a pulse is in the same order of magnitude as the characteristic lateral dimension (i.e. $a/\lambda \approx 1$).

Tu et al. (1955) measured the group velocity in circular rods (diameter $a = 3 - 25$ mm, $f = 0.2 - 2.5$ MHz) within a range of $a/\lambda = 0 - 3.2$. The pulse-transmission technique and the standing wave technique (continuous sinusoidal wave) were used for the lower ($a/\lambda < 1$) and upper ($a/\lambda > 1$) range. Around $a/\lambda = 1$ neither technique was successfull. For $a/\lambda > 2.5$ bulk wave velocity and at $a/\lambda = 0$ extensional wave velocity was measured. The group velocities measured with the pulse technique increased steadily with increasing frequency from half of the longitudinal bulk wave velocity at $a/\lambda \approx 1.2$. This is not conform with solutions for a continous wave (Thurston 1978). Within the region measured with the standing wave technique ($a/\lambda = 0 - 0.8$) the group velocity follows the solution of a continous wave, i.e. it drops down to approximately $0.3\,v_L$ at $a/\lambda = 0.4$. Using the standing wave method, the extensional wave velocity approaches the Rayleigh velocity from $a/\lambda = 0$ to $a/\lambda \approx 1$ (Morse 1948, 1950), which follows the solution for the phase velocity of a continous wave. If the edge-length of a square is equal to the diameter of circular cross-section no difference in phase velocity measured in a bar was found (Morse 1948). For the shear pulse velocity in a bar no dependency on a/λ was found (Tu et al. 1955).

Besdo et al. (2007) showed with a 3D finite element model of a circular bar that inducing a sudden transversal displacement in the form of a ramp function, yields a flexural and a shear wave propagating in the bar ($a/\lambda \approx 1$). They also mention that it is usually impossible to separate these waves in experiments.

Hayashi et al. (2003) found good agreement (for both, phase and group velocities) between theoretical and experimental dispersion curves [characterize the frequency dependence of (guided) wave velocities] of a square bar obtained in experiments with $a/h = 0.002$ and a contact transducer with a center frequency $f = 50$ kHz. Later Hayashi et al. (2006) gave wave structures (discribe displacement distributions in a bar cross-section) for longitudinal, flexural and torsional vibration modes in bar. For the longitudinal vibration, a transition from extensional velocity v_E to bulk longitudinal velocity v_L with increasing a/λ can be observed, reaching v_L at $a/\lambda \approx 2$.

In an infinite isotropic medium phase and group velocity are equal. In a waveguide group and phase velocity differ, the former being the velocity of the pulse, i.e. the velocity along the traveled path within the waveguide and the later the velocity along the propagation direction, i.e. the longitudinal direction of the waveguide (Redwood 1963). Because in typical experimental setups, velocity is determined by dividing the direct travel distance, i.e. height or length of the specimen, by the time of flight through the specimen, it is evident that the determined velocity is the phase velocity in an (isotropic) bulk medium as well as in waveguide, e.g. in a bar.

A.2   Wave scattering in multi-phase media

Two essentially different methods can be applied to obtain the homogenized (effective) elastic stiffness of microstructured materials: (i) (multi-step) homogenization of elastic stiffnesses and (ii) modelling of plane wave propagation considering scattering effects. Homogenization techniques predict the overall behavior, e.g. linear elasticity, of heterogeneous materials from their constituents (Zaoui 2002). With this methods for materials with several different inclusions, an hierarchical microstructure, and with other more complex microstructures an excellent approximation of elastic stiffnesses (over the complete porosity or concentration range) can be given. Effective wave propagation techniques predict the scattering behavior over a certain frequency range (Yang and Mal 1994). The effective stiffnesses computed from effective (phase) velocities converge for zero frequency, i.e. in the long-wavelength-limit, to the static limit case of elastic stiffness. These methods give access to the frequency dependency of attenuation, velocities and (complex) elastic stiffnesses, i.e. results may be obtained for any desirable wavelength. Most models consider relatively simple microstructures (spherical or cylindrical inclusions). Recently, models for composites with complex (two-dimensional) microstructure were developed (Parnell and Abrahams 2008). Strict upper and lower bounds on the effective stiffnesses can be derived by variational principles (Hashin and Shtrikman 1962a,b).

When applying ultrasonic methods to determine elastic stiffnesses of microstructured materials it is essential to know the correct applicable frequency to obtain the correct homogenized stiffnesses and/or the stiffnesses of the matrix material in a single phased material. Using dynamic models (effective wave propagation techniques) to obtain solutions for velocities (and thus stiffnesses) is much more complex, due to the underlying theoretical and computational expenses. Furthermore, due to the complexity of some microstructures, presently not all materials can be modeled with such techniques. Homogenization techniques on the other hand are available for very complex materials (e.g. strut-like scaffolds) and allow for the backcalculation of velocities (in the static limit).

First theoretical descriptions of the propagation of multiple-scattered waves were given for point scatters (Foldy 1945; Waterman and Truell 1961) and polycrystalline metals (Mason and McSkimin 1948; Huntington 1950). Three different scattering regimes (Rayleigh, stochastic and diffusive or geometric region), accompanied by different energy losses, are identified by the ratio of grain or inclusion (i.e. scatter) dimension d to the wavelength λ (d/λ). For large wavelengths ($d/\lambda < 1/3$) Rayleigh scattering of waves occures, where energy losses are proportional to d^3/λ^4. Transmission at small wavelengths ($d/\lambda > 3$) leads to a diffusion of waves (compareable to the propagation of heat waves) in the geometric region with losses proportional to $1/d$ (Mason and McSkimin 1948). In the intermediate range ($d/\lambda \approx 1$), the stochastic region, the losses are proportional to d/λ^2 (Huntington 1950). Ayrault and Griffiths (2006) proposed a method to seperate viscothermal losses and losses due to scattering for frequencies in the Rayleigh scattering regime.

Stanke and Kino (1984) developed a model covering all three scattering regimes for (single phase) polycrystalline materials with small single crystal anisotropy. The dispersion curves and the maximal differences in longitudinal and transversal velocities were given for two isotropic metals (aluminum and iron) with single crystals of cubic symmetry (see Table A.1). The magnitudes of order of d/λ-ratios between the different scattering regimes (see Table A.1) are the same as the ratios given by Mason and McSkimin (1948) (see previous paragraph). d/λ-ratios at which a steep increase in velocity difference is observeable are given in brackets in Table A.1. At small d/λ-ratios the velocity difference is less than 1% (for aluminum even less than 0.1%). The steep increase in the velocity difference in the diffusive region is due to higher perturbations of the velocity, i.e. the acoustic rays can bend and thereby 'weight' the effective (average) inhomogenity. Stanke and Kino (1984) mention that longitudinal waves in

a polycrystalline media with single crystals of cubic symmetry travel along the stiffer grains in the diffusive scattering region. In all other cases they travel along weaker grains. They do not give an explantion for this effect.

Table A.1: d/λ-limits determined from single crystal properties at scattering regions in polycrystalline aluminum and iron [values extracted from dispersion curves given by Stanke and Kino (1984)].

scattering region:		Rayleigh	diffusive	max. velocity
material	velocity	d/λ [-]	d/λ [-]	difference [%]
aluminum	v_L	$< 0.2(20)$	> 100	1
	v_T	$< 0.2(4)$	> 20	3
iron	v_L	$< 0.2(2)$	> 20	6
	v_T	$< 0.02(1)$	> 10	10

Several works on ultrasonic wave scattering in heterogeneous materials were published on fibrous (Yang and Mal 1994) and on particulate (Yang 2003; Wei and Huang 2004) two phase composite materials. Also several experimental studies (Kinra et al. 1982; Kinra and Anand 1982; Datta and Ledbetter 1983; Ledbetter and Fortunko 1991) on such transversal isotropic and isotropic materials were published. Multiple-scattering theories for elastic waves considering (i) the 'quasi-crystalline approximation' (Lax 1952) — to obtain average wave propagation constants — and (ii) a 'pair correlation function' (Bose and Mal 1973) — to account for the (random) geometric correlations between the inclusions (i.e. scatters) — accurately predict wave propagation at low frequencies and low inclusion concentrations (Bose and Mal 1973, 1974; Datta 1977; Varadan et al. 1978; Willis 1980; Ledbetter and Datta 1986). Some multiple-scattering models do not predict static limits at the zero-frequency or long-wavelength-limit correctly because their formulation is based on an isolated scatter (Yang and Mal 1994). At high inclusion concentrations, the multiple-scattering models become sensitive to the choice of the pair correlation function (Yang and Mal 1994), i.e. the interaction of inclusions is not correctly described. The effective medium approach (Berryman 1980; Sabina and Willis 1988; Yang and Mal 1994; Yang 2003) solves this problem by implementing a micromechanical homogenization technique. Yang and Mal (1994) used the generalized self consistent model of Christensen and Lo (1979) for high (fiber) concentrations. Sabina and Willis (1988) showed that the effective medium scattering models are valid for wavelengths greater than four times the diameter of (spherical) inclusions ($\lambda > 4\,d$). More recent studies include effects due to imperfect (e.g. viscoelastic) interphases between inclusions and matrix materials (Wei and Huang 2004). Wave scattering models (covering solid inclusions and small d/λ-ratios) are focused on the isotropic plane of transversal isotropic composites and rearly on wave propagation in the longitudinal direction of the composite. Only Murakami et al. (1979b) presented dispersion curves of longitudinal wave velocity in the direction of (solid) cylindrical inclusions embedded in an isotropic matrix. The dispersion increases as the stiffness of the fibers becomes much larger than that of the matrix and — in this case — decreases with increasing fiber volume fraction.

Yang and Mal (1994) verified their model for high frequencies for graphite-epoxy, boron-epoxy and silicon carbide-titanium (fiber) composites using inclusion diameters and fiber volume fractions of $d = 0.01$ mm, $d = 0.14$ mm, $d = 0.14$ mm and $\varphi = 0.65$, $\varphi = 0.54$, $\varphi = 0.35$, respectively. These values yield at a frequency of $f = 20$ MHz approximately $d/\lambda = 0.1$, $d/\lambda = 1.6$, and $d/\lambda = 0.7$, respectively. Comparing these values with the scattering regimes

of polycrystalline materials (see Table A.1), shows that measurements and models used for composite materials generally cover the Rayleigh regime (long-wavelength regime). Therefore, as expected, velocities (and thus stiffnesses) measured in this range are approximately constant [compare Yang and Mal (1994), Figures six, ten and eleven] and correspond to the homogenized stiffnesses. Only in the case of boron-epoxy,the model shows an increase in velocity [compare Yang and Mal (1994), Figure ten], indicating that the stochastic scattering regime is reached and thus related stiffnesses do not correspond to the homogenized material. Datta and Ledbetter (1983) showed good agreement in elastic stiffness constants between measurements of a boron-aluminum alloy composite at $d/\lambda = 0.14$ ($d = 0.14$ mm, $f = 10$ MHz, $\varphi = 0.48$) and different models (Bose and Mal 1973, 1974; Hlavacek 1975).

The work of Kinra and Anand (1982) seems to be the only experimental study of (particulate) composites investigating the problem of wave propagation at small (and long) wavelengths. Ultrasonic velocities of glass-epoxy composites with different glass-inclusion diameters ($d = 1, 2, 3$ mm) and inclusion volume fractions ($\varphi = 0.05 - 0.45$) were measured at different frequencies ($f = 0.3 - 3$ MHz). Velocities at long wavelengths ($d/\lambda_L < 0.8$) agree well with (static) bounds (being closer to the lower bound) given for the static limit case (see also Kinra et al. (1982)). The values move, with increasing inclusion volume fraction and smaller d/λ_L-ratios, closer the upper bound. For short wavelength ($d/\lambda > 1.2$) the measured velocities were all located above the upper bound, again with smaller differences to the bound, as inclusion volume fraction increases. Both observations lead to the assumption that at short wavelength (i.e. in the stochastic to the diffusive scattering regime) the wave propagation becomes more influenced by the (much stiffer) inclusions (ratio of longitudinal velocity of inclusion to that of the matrix equals 2.1), especially at high inclusion volume fractions. Later, Kinra (1985) showed experimentally that at high frequencies (stiffer) inclusions move out of phase with the matrix.

Gubernatis and Domany (1984) derived a unified theory for effective (elastic) wave propagation in an isotropic medium containing spherical pores. They show, that a porosity of 10% yields an (effective medium) velocity 7.5% less than the velocity of the solid material at $d/\lambda \approx 0.04$. Ratios of $d/\lambda < 0.06$ also yielded the effective velocity within deviations of less than 10% (rising constantly from the minimum at $d/\lambda \approx 0.04$). Ratios of $d/\lambda > 0.2$ resulted in the solid wave velocity with deviations smaller than 1%. Gubernatis and Domany (1984) also found that the significant (spherical) void diameter (in porous materials with different distributions of inclusion diameters) is the most probable one, and that the wave propagation (velocity and attenuation) is quite insensitive to the distribution of inclusion diameters.

Numerical modeling of wave scattering in composites with finite difference equations, employing space and time discretization (Ruffino and Delsanto 2000), allows for detailed investigation of interferences and mode conversion patterns in (reflected) waves. The problem of shear wave propagation in scaffolds was investigated by Besdo et al. (2007) by means of finite element models, without considering the frequency dependency of wave propagation.

If the influence of inclusion diameter to wavelength ratios (or other micromechanical parameters) on the different tensor components of a (general) anisotropic material are of interest, application of a continuum (micro)mechanical homogenization techniques and backcalculation of the appropriate frequency (and thus wavelength) to obtain the desired stiffness, is recommended. Especially for large inclusion diameter or, more precisely,at higher d/λ-ratios (i.e. in the diffusive scattering regime) these methods are of advantage.

Another concept for (micro)mechanical homogenization for periodic heterogeneous materials defines a material volume as a repeating unit cell (RUC). In contrast to the micromechanical analysis of an RVE, which is based on the equivalence of homogeneous traction and displacement boundary conditions, the analysis of an RUC is based on combined periodic displacement and

traction boundary conditions (Drago and Pindera 2007). Drugan and Willis (1996) showed that the minimum size of an RVE for any reinforcement type of (spherical) inclusions (including voids and rigid particles) is approximately $\ell_{RVE} \approx 2\,d$, up to an inclusion volume fraction of $\varphi = 0.4$ (error of effective stiffnesses $< 5\%$; for errors $< 1\%$: $\ell_{RVE} \approx 4.5\,d$). To obtain the same accuracy in normal and shear stiffnesses, the RVE for normal straining must approximately be twice the size necessary for shear straining. According to Kanit et al. (2003) the size of an RVE is a function of the physical property, the contrast of properties, the volume fractions of components, the wanted relative precision for the estimation of the effective properties, and the number of realizations of the microstructure associated with computations to be performed. Due to the dependency of the RVE size on all of these parameters, model and chosen ℓ_{RVE} are in general experimentally validated. Exemplarily the work of Jeong and Hsu (1996) shall be mentioned, which combines ultrasonic measurements and the Mori-Tanaka homogenization scheme (Mori and Tanaka 1973) to predict the effective porosity and elastic stiffness of porous ceramics.

Dimensional analysis of wave propagation in two-phase materials

Wave propagation in any direction in an two-phase, isotropic material, and in the principle material directions of an two-phase, anisotropic material, the wave (longitudinal or transversal) velocity only depends on a single (normal or shear) stiffness tensor component [compare Eqs. (1.15) and Eqs. (2.10)]. Therefore, an independent investigation of longitudinal and transversal wave propagation is possible in these cases. The experimentally measured wave velocities $v_{i,exp}$ ($i = L, T$) are hence a function of four material properties [mass density of matrix ρ and inclusion ρ^{inc}, normal or shear stiffness component of matrix C_{ijij} and inclusion C_{ijij}^{inc} ($ij = 11, 12$)], of one wave property (frequency f), of two geometrical properties (characteristic cross-sectional dimension a, height h), and of two microstructural properties (characteristic inclusion dimension d, volume fraction of inclusion φ), i.e.

$$v_{i,exp} = F(C_{ijij}, \, C_{ijij}^{inc}, \, \rho, \, \rho^{inc}, \, f, \, a, \, h, \, d, \, \varphi) \,. \tag{B.1}$$

Note that φ is related [e.g. for porous media via (1.29)] to material (ρ) and effective material (ρ_{app}) properties and to the characteristic inclusion dimension d [e.g. for hexagonal cylindrical pore inclusions via (1.30)]. The (matrix) material properties ($C_{ijij}, \, \rho$) are related via Eq. (1.15)$_1$ [or Eq. (1.15)$_2$] to the (matrix) wave velocities ($v_i, \, i = L, T$) and furthermore via (1.9) to the (matrix) wavelength ($\lambda_i, \, i = L, T$), which thus depends on wave (f) *and* material properties. Except for the geometry-related properties, the variables in (B.1) are the same as for determining the length of a representative volume element [see Kanit et al. (2003) and Appendix A].

To extract relevant parameters of this physical problem we apply dimensional analysis (Buckingham 1914; Barenblatt 1996). In dimensional analysis a functional relation [e.g. (B.1)] between one physical quantity (the dependent variable, here $v_{i,exp}$) and several other physical quantities (the independent variables, here $N = 9$ quantities), is simplified through the study of the dimensions of all involved quantities, while making sure that the newly extracted functional relationship does not depend on the units of measurements chosen to assign quantitative value to the physical quantities (Buckingham 1914). Using an L(ength)M(ass)T(ime)-class of systems of units, the dimension of each physical quantity Q_i can be written as a power-law monomial in the form

$$[Q_i] = L^{\alpha_i} M^{\beta_i} T^{\gamma_i} \,, \tag{B.2}$$

where L, M, and T are abstract positive numbers which describe the factor by which the fundamental units of length, mass, and time decrease upon passage from one system of units of measurements to an other one. In our case, these dimension functions read as $[v_i] = L\,T^{-1}$, $[\rho] = [\rho^{inc}] = L^{-3}\,M$, $[C_{ijij}] = [C_{ijij}^{inc}] = L^{-1}\,M\,T^{-2}$, $[f] = T^{-1}$, $[a] = [h] = [d] = L$ and $[\varphi] = 1$. The rank of the dimensional exponent matrix (see Table B.1) is $k = 3$, i.e. three of the nine independent physical quantities are dimensionally independent and $N - k = 6$ quantities are dimensionally dependent. These three dimensionally independent quantities can

Table B.1: Dimensional exponent matrix.

unit	Q_i	v_i	ρ	ρ^{inc}	C_{ijij}	C_{ijij}^{inc}	f	a	h	d	φ
L	α_i	1	-3	-3	-1	-1	0	1	1	1	0
M	β_i	0	1	1	1	1	0	0	0	0	0
T	γ_i	-1	0	0	-2	-2	-1	0	0	0	0

be chosen freely from the nine independent physical quantities. Here, we choose C_{ijij}, ρ and f as dimensionally independent quantities. Next, six ($N - k + 1 = 7$ and φ is omitted due to $[\varphi] = 1$) dimensionless forms i are constructed by dividing the dimensionally dependent quantities through powers of the dimensionally independent quantities, according to:

$$[\Pi_i] = \frac{[Q_i]}{[C_{ijij}]^{n_1^i}[\rho]^{n_2^i}[f]^{n_3^i}} \qquad i = \{\rho^{inc}, C_{ijij}^{inc}, a, h, d, v_i\}. \tag{B.3}$$

Inserting the dimension functions of all involved quantities into (B.3) yields an equation for each dimensionally dependent quantity, which has to be fulfilled for any abstract positive numbers L, M, and T and thus yielding $n_1^\rho = 0$, $n_2^\rho = 1$, and $n_3^\rho = 0$ for Π_ρ, $n_1^C = 1$, $n_2^C = 0$, and $n_3^C = 0$ for Π_C, $n_1^a = n_1^h = n_1^d = 1/2$, $n_2^a = n_2^h = n_2^d = -1/2$, and $n_3^a = n_3^h = n_3^d = -1$ for Π_a, Π_h, and Π_d, respectively, and $n_1^v = 1/2$, $n_2^v = -1/2$, and $n_3^v = 0$ for Π_v. The (dimensionless) physical relation expressed in dimensionless variables only, i.e. $\Pi_v = \mathcal{F}\left(\Pi_\rho, \Pi_C, \Pi_a, \Pi_h, \Pi_d, \Pi_\varphi\right)$ reads

$$\frac{v_{i,exp}}{\sqrt{C_{ijij}/\rho}} = \mathcal{F}\left(\frac{\rho^{inc}}{\rho}, \frac{C_{ijij}^{inc}}{C_{ijij}}, \frac{a\,f_i}{\sqrt{C_{ijij}/\rho}}, \frac{h\,f_i}{\sqrt{C_{ijij}/\rho}}, \frac{d\,f_i}{\sqrt{C_{ijij}/\rho}}, \varphi\right), \tag{B.4}$$

with $i = \{L, T\}$ and $ij = \{11, 12\}$. Using the requations Eq. (1.15)$_1$ [or Eq. (1.15)$_2$] and Eq. (1.9) yields

$$\frac{v_{i,exp}}{v_i} = \mathcal{F}\left(\frac{\rho^{inc}}{\rho}, \frac{C_{ijij}^{inc}}{C_{ijij}}, \frac{a}{\lambda_i}, \frac{h}{\lambda_i}, \frac{d}{\lambda_i}, \varphi\right) \qquad i = \{L, T\} \quad ij = \{11, 12\}. \tag{B.5}$$

The ratio of a measured (longitudinal or transversal) wave velocity to the (corresponding) bulk velocity of the matrix, i.e. a material parameter, is therefore depending on two inclusion material parameters, two geometry-wave parameters and two microstructural-wave parameters, namely the ratios of the inclusion density and stiffness to matrix density and (corresponding) stiffness, respectively, of geometrical and inclusion dimensions to the (corresponding) matrix wavelength, and the porosity. Using dimensional analysis the number of arguments in the function describing the physical problem of wave propagation in a two-phase material was reduced significantly from nine (dimensionful) to six (dimensionless). Further simplifications

for porous (i.e. pore inclusions) materials with $\rho^{inc} = 0$ and thus $C_{ijij}^{inc} = 0$ yield

$$\frac{v_{i,exp}}{v_i} = \mathcal{F}\left(\frac{a}{\lambda_i}, \frac{h}{\lambda_i}, \frac{d}{\lambda_i}, \varphi\right) \qquad i = \{L, T\}. \tag{B.6}$$

For wave propagation in (approximately) solid (single-phase) specimens (e.g. polycrystaline metals) the dimensionless physical relation (B.6) further simplfies with $\varphi = 0$ and consequently $d = 0$ to (see also Section 1.6)

$$\frac{v_{i,exp}}{v_i} = \mathcal{F}\left(\frac{a}{\lambda_i}, \frac{h}{\lambda_i}\right) \qquad i = \{L, T\}. \tag{B.7}$$

Hence, we obtained the ratio of measured to bulk velocities as a function of only two geometry-over-wave property parameters, i.e. characterisitc cross-sectional-dimension-over-wavelength a/λ and height-over-wavelength h/λ parameters. A similar functional relation to (B.7) is obtained when h instead of f is chosen as one of the dimensionally independent quantities, i.e. the two arguments of $\mathcal{F}$ in (B.7) become a/h and h/λ_i. Hence, a purely geometrical parameter and the same height-over-wavelength parameter. Considering (1.19) and (1.9) in the definition of the geometry-over-wavelength parameters a/λ_i and h/λ_i yields

$$\frac{a}{\lambda_i} = \frac{a}{h} f\, t_{f,i} \qquad \text{and} \qquad \frac{h}{\lambda_i} = f\, t_{f,i}, \tag{B.8}$$

respectively. From (B.8) follows that the parameter a/λ_i passes into the purely geometric parameter a/h by division of the parameter the $h/\lambda_i = f\, t_{f,i}$. If the influence of geometries can be neglected, i.e. if bulk wave propagation is ensured, the dimensionless physical relation (B.6) can be reduced to (see also Section 1.7)

$$\frac{v_{i,exp}}{v_i} = \mathcal{F}\left(\frac{d}{\lambda_i}, \varphi\right) \qquad i = \{L, T\}. \tag{B.9}$$

Hence, we obtained the ratio of measured to bulk velocities as a function of only one microstructure-over-wave property parameter, d/λ_i, and one microstructure property parameter, φ.

When investigating a two-phase material with solid inclusions a distinction (at high frequencies) between the wave velocity of the matrix and the wave velocity of the inclusions, is not easily possible (e.g. as in the work of Kinra and Anand (1982) mention in Section A.2). Besides this advantage of pore inclusions, several problems occure when investigating porous materials: The lower limits for d/λ_i to achieve effective wave propagation given in Section 1.7 as compared to values observed for different composites [e.g. by Datta and Ledbetter (1983)], are attributed to the limit case of void inclusions, which can not transmit any wave paths yielding much higher scattering. Thus larger wavelengths must be used to account for a propagation medium with inclusions that do not allow ultrasonic wave propagation, i.e. voids. This is also supported by results of Gubernatis and Domany (1984), which found similar (small) values of d/λ_i-ratios for spherical voids. Moreover, effective stiffnesses of materials with void inclusions are smaller than with solid inclusions, yielding smaller effective wave velocities and hence smaller wavelength at equal frequencies.

Appendix $\mathbf{C}$

Kelvin-Christoffel equation

The Kelvin-Christoffel equation gives the relationship between a stress wave propagating within a solid and the (elastic) material stiffness. Combination of the conservation law of linear momentum, of the generalized Hooke's law, of the linearized strain tensor, and of the general plane wave solution for the displacements inside an infinite solid medium yields the elasticity tensor components as functions of the material mass density and the wave propagation velocity. The derivation of this basic equation is given in several books on the topic of elastic waves in solids, among which are books by Auld (1990), Carcione (2001), and Helbig (1994). Kolsky (1953) solves the wave equation directly with isotropic constitutive relations and does not give the Kelvin-Christoffel equation specifically. Here, a detailed step-by-step derivation of the Kelvin-Christoffel equation is given, with a subsequent solution (giving the Kelvin-Christoffel matrix components) for the elastic waves in an isotropic material.

Extension of the periodic plane wave disturbance in a one-dimensional space [Eq. (13)] to a general plane wave solution for the displacement vector u_i of body waves in three-dimensional space yields

$$u_i(x_i, t) = u_{0,i}\,\sin(k_j\,x_j - \omega\,t) \qquad i, j = x, y, z\,, \tag{C.1}$$

where $k_i = k\,n_i$ is the wave vector and $u_{0,i} = u_0 p_i$ is the particle vector. The wave vector is a representation of the wave, with the wave number k as its magnitude and the direction of wave propagation n_i, which reads in vector notation

$$\mathbf{n} = n_x\,\mathbf{e}_z + n_y\,\mathbf{e}_y + n_z\,\mathbf{e}_z = \left\{ \begin{array}{c} n_x \\ n_y \\ n_z \end{array} \right\}\,, \tag{C.2}$$

where the components are the direction cosines with respect to the basis unit vectors $\mathbf{e}_x$, $\mathbf{e}_y$ and $\mathbf{e}_z$ of an arbitrary Cartesian coordinate system. The particle vector is a representation of the particle vibration, with the size of the displacement, i.e. the amplitude, u_0 and the particle vibration direction or polarization direction p_i. The vectors n_i and p_i are unit vectors. The space vector x_i defines a point in a three-dimensional space for which the displacement due to the wave propagation are given. Elucidations of time t and of angular frequency ω are given in the Introduction. The relationship for the phase velocity v_p [Eq. (14)] can be used to define the phase velocity vector

$$v_{p,i} = v_p\,n_i\,. \tag{C.3}$$

The phase function $\Theta(x_i, t) = k_i\, x_i - \omega\, t$ contains all information of the wave regarding its distribution in space $(k_i\, x_i)$ and time $(\omega\, t)$. The term $u_0\, p_i$ contains information regarding the particle vibration. Thus the displacement caused by a plane elastic stress wave is fully described by the function $u_i(x_i, t)$ [Eq. (C.1)] in time, space and magnitude. This function can also be expressed using the exponential function and an imaginary exponent

$$u_i(x_j, t) = u_0\, p_i\, \exp[i\, k(n_j\, x_j - v_p\, t)]. \tag{C.4}$$

This alternative form to (C.1) is used in the following derivations because it is easier to differentiate.

Starting point for the derivation of the Kelvin-Christoffel equation is the equation of motion,

$$\partial_j \sigma_{ij} + f_i = \rho\, b_i\,, \tag{C.5}$$

where σ_{ij} is the Cauchy stress tensor, f_i are the body forces, ρ is the mass density of the material and b_i is the particle acceleration. The displacements induced by an ultrasonic wave are small compared to the dimensions of solids. The derivation of displacements with respect to space coordinates is small compared to one. Thus the two prerequisites for using a geometrical linearized theory are fulfilled and the linearized strain tensor

$$\varepsilon_{ij} = \frac{1}{2}(\partial_j u_i + \partial_i u_j) \tag{C.6}$$

can be used. Assuming the materials under investigation have a linear stress-strain relationship within the displacement regime of ultrasonic waves a physical linearized theory can be applied. Therefore the relationship between stresses and strains can be described with the generalized Hooke's law

$$\varepsilon_{ij} = D_{ijkl}\, \sigma_{kl} \tag{C.7}$$

and its inverse form

$$\sigma_{ij} = C_{ijkl}\, \varepsilon_{kl}\,, \tag{C.8}$$

where $\mathbb{D}$ is the compliance tensor and

$$\mathbb{C} = \mathbb{D}^{-1} \tag{C.9}$$

is the stiffness tensor.

Substitution of the linearized strain tensor (C.6) into (C.8) and considering the symmetry of this tensor, i.e. $\varepsilon_{ij} = \varepsilon_{ji}$ and thus $C_{ijkl} = C_{ijlk}$, yields

$$\sigma_{ij} = C_{ijkl}\, \frac{1}{2}(\partial_l u_k + \partial_k u_l) = C_{ijkl}\, \partial_l u_k\,. \tag{C.10}$$

Inserting this expression in the first term of the equation of motion (C.5) and considering $\partial_j C_{ijkl} = 0$ for homogeneous materials yields

$$\partial_j(C_{ijkl}\, \partial_l u_k) = C_{ijkl}\, \partial_{lj}^2 u_k\,, \tag{C.11}$$

whereas

$$\partial_{lj}^2 u_k = -k^2\, n_l\, n_j\, u_k\,. \tag{C.12}$$

The particle velocity and particle acceleration are given by time derivatives of the particle displacement vector u_i [Eq. (C.4)] to

$$v_i = \partial_t u_i = \dot{u}_i = -i\, \omega\, u_i \qquad \text{and} \qquad b_i = \partial_{tt}^2 u_i = \ddot{u}_i = -\omega^2\, u_i = -k^2\, v_p^2\, u_i\,. \tag{C.13}$$

Neglecting the body forces acting on the solid ($f_i = 0$) and inserting (C.10) and the second equation (C.13) in the equation of motion (C.5) yields

$$C_{ijkl}\, k^2\, n_l\, n_j\, u_0\, p_k\, \exp[i\, k(n_j\, x_j - v_p\, t)] = \rho\, k^2\, v_p^2\, u_0\, p_i\, \exp[i\, k(n_j\, x_j - v_p\, t)] \tag{C.14}$$

and further

$$C_{ijkl}\, n_l\, n_j\, p_k - \rho\, v_p^2\, p_i\,. \tag{C.15}$$

Using $p_i = \delta_{ik}\, p_k$ one gets

$$(C_{ijkl}\, n_l\, n_j - \rho\, v_p^2\, \delta_{ik})\, p_k = 0\,, \tag{C.16}$$

with

$$\Gamma_{ik} = C_{ijkl}\, n_l\, n_j \tag{C.17}$$

as the symmetric Kelvin-Christoffel matrix one obtains the Kelvin-Christoffel equation

$$(\Gamma_{ik} - \rho\, v_p^2\, \delta_{ik})\, p_k = 0\,. \tag{C.18}$$

The Kelvin-Christoffel equation is an eigenvalue problem with three eigenvalues $(\rho\, v_p^2)^n$ and the associated eigenvectors p_i^n. The three solutions of the Kelvin-Christoffel equation correspond to three body waves $n = 1, 2, 3$ propagating in an unbounded medium. For a non-trivial solution of (C.18) the coefficient determinate must vanish, i.e. we obtain the dispersion relation

$$\left|\Gamma_{ik} - \rho\, (v_p^n)^2\, \delta_{ik}\right| = 0\,, \tag{C.19}$$

that gives $\omega = \omega(k)$ with the definition of the phase velocity (14). The three eigenvalues obtained from (C.19) correspond to the three phase or wave velocities v_p^n of the waves and the three eigenvectors obtained from (C.18) to the polarization directions p_i^n. The Kelvin-Christoffel matrix is real and symmetric, thus the eigenvalues are real and the eigenvectors are mutually perpendicular, i.e. the polarization directions of the three body waves for one propagation direction are mutually perpendicular. If two or three eigenvalues are equal, the Kelvin-Christoffel matrix is singular, i.e. of rank one, or of rank zero, respectively, and the corresponding eigenvectors do not have fixed directions (Helbig 1994). For double roots the two corresponding eigenvectors can be chosen within a plane perpendicular to the third eigenvector. Since all eigenvectors are mutually perpendicular these two must be mutually perpendicular. For triple roots three mutually orthogonal eigenvectors can be chosen completely arbitrarily. For comparison we mention another well-known eigenvalue problem in solid mechanics,

$$(\sigma_{ij} - \sigma\, \delta_{ij})\, n_j = 0\,, \tag{C.20}$$

which is used for the determination of principal normal stresses σ and their orientations n_j.

By using the kinetic, the kinematic, constitutive relations, and the general plane wave solution, we obtained a relationship between the stiffness and mass density of a material and the phase velocities v_p^n and polarization directions p_i^n of a stress wave propagating in a direction n_i within this material. The unit vector for the propagation direction n_i is normal to the wavefront of the wave, whereas the polarization direction p_i can have angles between $0°$ and $90°$ to the propagation direction (see Section 2.3). The inverse of the phase velocity is defined as slowness

$$s = \frac{k}{\omega} = \frac{1}{\lambda\, f} = \frac{1}{v_p}\,. \tag{C.21}$$

Thus the slowness vector can be computed as

$$s_i = \frac{k_i}{\omega} = \frac{k\, n_i}{\omega} = s\, n_i\,. \tag{C.22}$$

In matrix notation the Kelvin-Christoffel equation (C.18) reads

$$\begin{bmatrix} \Gamma_{11} - \rho v^2 & \Gamma_{12} & \Gamma_{13} \\ \Gamma_{21} & \Gamma_{22} - \rho v^2 & \Gamma_{23} \\ \Gamma_{31} & \Gamma_{32} & \Gamma_{33} - \rho v^2 \end{bmatrix} \cdot \left\{ \begin{array}{c} p_1 \\ p_2 \\ p_3 \end{array} \right\} = \left\{ \begin{array}{c} 0 \\ 0 \\ 0 \end{array} \right\}. \tag{C.23}$$

with the components of the Kelvin-Christoffel matrix in in explicit form

$$\Gamma_{11} = C_{1111}\, n_1^2 + C_{1212}\, n_2^2 + C_{1313}\, n_3^2 + 2\, C_{1312}\, n_2\, n_3 + 2\, C_{1113}\, n_3\, n_1 + 2\, C_{1112}\, n_1\, n_2$$

$$\Gamma_{22} = C_{1212}\, n_1^2 + C_{2222}\, n_2^2 + C_{2323}\, n_3^2 + 2\, C_{2223}\, n_2\, n_3 + 2\, C_{2312}\, n_3\, n_1 + 2\, C_{2212}\, n_1\, n_2$$

$$\Gamma_{33} = C_{1313}\, n_1^2 + C_{2323}\, n_2^2 + C_{3333}\, n_3^2 + 2\, C_{3323}\, n_2\, n_3 + 2\, C_{3313}\, n_3\, n_1 + 2\, C_{2313}\, n_1\, n_2$$

$$\Gamma_{12} = C_{1112}\, n_1^2 + C_{2212}\, n_2^2 + C_{2313}\, n_3^2$$

$$+ \ (C_{2312} + C_{2213})\, n_2\, n_3 + (C_{1123} + C_{1312})\, n_3\, n_1 + (C_{1122} + C_{1212})\, n_1\, n_2 \tag{C.24}$$

$$\Gamma_{13} = C_{1113}\, n_1^2 + C_{2312}\, n_2^2 + C_{3313}\, n_3^2$$

$$+ \ (C_{2313} + C_{3312})\, n_2\, n_3 + (C_{1133} + C_{1313})\, n_3\, n_1 + (C_{1123} + C_{1312})\, n_1\, n_2$$

$$\Gamma_{23} = C_{1312}\, n_1^2 + C_{2223}\, n_2^2 + C_{3323}\, n_3^2$$

$$+ \ (C_{2323} + C_{2233})\, n_2\, n_3 + (C_{3312} + C_{2313})\, n_3\, n_1 + (C_{2213} + C_{2312})\, n_1\, n_2 \,.$$

Due to the symmetry of the strain and stress tensors and the independency of the order of derivation of the strain energy density with respect to the strain tensor, the number of independent stiffness tensor components reduces from $3^4 = 81$ to 21. Giving these components in an contracted symmetric 6×6 matrix we have

$$\{C_{ijkl}\} = \begin{bmatrix} C_{1111} & C_{1122} & C_{1133} & C_{1123} & C_{1113} & C_{1112} \\ C_{2211} & C_{2222} & C_{2233} & C_{2223} & C_{2213} & C_{2212} \\ C_{3311} & C_{3322} & C_{3333} & C_{3323} & C_{3313} & C_{3312} \\ C_{2311} & C_{2322} & C_{2333} & C_{2323} & C_{2313} & C_{2312} \\ C_{1311} & C_{1322} & C_{1333} & C_{1323} & C_{1313} & C_{1312} \\ C_{1211} & C_{1222} & C_{1233} & C_{1223} & C_{1213} & C_{1212} \end{bmatrix}. \tag{C.25}$$

Reducing a pair of subscripts (ij) to a single subscript I or J according to the correspondence

$$\begin{array}{lll} (11) \rightarrow 1\,, & (22) \rightarrow 2\,, & (33) \rightarrow 3\,, \\ (23) = (32) \rightarrow 4\,, & (13) = (31) \rightarrow 5\,, \quad \text{and} \quad (12) = (21) \rightarrow 6\,, \end{array} \tag{C.26}$$

yields the shortend matrix notation or Voigt notation (Carcione 2001). Using contracted matrix and contracted subscripts yields the stiffness tensor $\mathbb{C}$ as

$$\{C_{IJ}\} = \begin{bmatrix} c_{11} & c_{12} & c_{13} & c_{14} & c_{15} & c_{16} \\ c_{21} & c_{22} & c_{23} & c_{24} & c_{25} & c_{26} \\ c_{31} & c_{32} & c_{33} & c_{34} & c_{35} & c_{36} \\ c_{41} & c_{42} & c_{43} & c_{44} & c_{45} & c_{46} \\ c_{51} & c_{52} & c_{53} & c_{54} & c_{55} & c_{56} \\ c_{61} & c_{62} & c_{63} & c_{64} & c_{65} & c_{66} \end{bmatrix}. \tag{C.27}$$

When the shortend matrix notation is used for the stiffness tensor C_{IJ}, the components of the

Kelvin-Christoffel matrix according to (C.24), become

$$
\begin{aligned}
\Gamma_{11} &= c_{11}\, n_1^2 + c_{66}\, n_2^2 + c_{55}\, n_3^2 + 2\, c_{56}\, n_2\, n_3 + 2\, c_{15}\, n_3\, n_1 + 2\, c_{16}\, n_1\, n_2 \\
\Gamma_{22} &= c_{66}\, n_1^2 + c_{22}\, n_2^2 + c_{44}\, n_3^2 + 2\, c_{24}\, n_2\, n_3 + 2\, c_{46}\, n_3\, n_1 + 2\, c_{26}\, n_1\, n_2 \\
\Gamma_{33} &= c_{55}\, n_1^2 + c_{44}\, n_2^2 + c_{33}\, n_3^2 + 2\, c_{34}\, n_2\, n_3 + 2\, c_{35}\, n_3\, n_1 + 2\, c_{45}\, n_1\, n_2 \\
\Gamma_{12} &= c_{16}\, n_1^2 + c_{26}\, n_2^2 + c_{45}\, n_3^2 + (c_{46} + c_{25})\, n_2\, n_3 + (c_{14} + c_{56})\, n_3\, n_1 + (c_{12} + c_{66})\, n_1\, n_2 \\
\Gamma_{13} &= c_{15}\, n_1^2 + c_{46}\, n_2^2 + c_{35}\, n_3^2 + (c_{45} + c_{36})\, n_2\, n_3 + (c_{13} + c_{55})\, n_3\, n_1 + (c_{14} + c_{56})\, n_1\, n_2 \\
\Gamma_{23} &= c_{56}\, n_1^2 + c_{24}\, n_2^2 + c_{34}\, n_3^2 + (c_{44} + c_{23})\, n_2\, n_3 + (c_{36} + c_{45})\, n_3\, n_1 + (c_{25} + c_{46})\, n_1\, n_2\,.
\end{aligned}
\tag{C.28}
$$

The non-zero stiffness tensor components for materials with isotropic, transversal isotropic and orthotropic symmetry class are

$$
\{C_{IJ}\} =
\begin{bmatrix}
c_{11} & c_{12} & c_{13} & 0 & 0 & 0 \\
c_{21} & c_{22} & c_{23} & 0 & 0 & 0 \\
c_{31} & c_{32} & c_{33} & 0 & 0 & 0 \\
0 & 0 & 0 & c_{44} & 0 & 0 \\
0 & 0 & 0 & 0 & c_{55} & 0 \\
0 & 0 & 0 & 0 & 0 & c_{66}
\end{bmatrix}.
\tag{C.29}
$$

One can recognize from (C.29) and Hooke's law in Voigt notation

$$
\sigma_I = C_{IJ}\, \varepsilon_J
\tag{C.30}
$$

that for these material symmetries axial stresses only cause axial strains and vice versa. A certain shear stress only depends on the respective shear strain. With (C.29) the components of the Christoffel matrix (C.28) reduce to

$$
\begin{aligned}
\Gamma_{11} &= c_{11}\, n_1^2 + c_{66}\, n_2^2 + c_{55}\, n_3^2 \\
\Gamma_{22} &= c_{66}\, n_1^2 + c_{22}\, n_2^2 + c_{44}\, n_3^2 \\
\Gamma_{33} &= c_{55}\, n_1^2 + c_{44}\, n_2^2 + c_{33}\, n_3^2 \\
\Gamma_{12} &= (c_{12} + c_{66})\, n_1\, n_2 \\
\Gamma_{13} &= (c_{13} + c_{55})\, n_3\, n_1 \\
\Gamma_{23} &= (c_{44} + c_{23})\, n_2\, n_3\,.
\end{aligned}
\tag{C.31}
$$

For an isotropic elastic solid not only the stiffness tensor components, but also the components of the stiffness matrix must be independent of the chosen coordinate system, because the material properties are equal in all directions. This leads to

$$
c_{11} = c_{22} = c_{33}\,, \quad c_{44} = c_{55} = c_{66}\,, \quad \text{and} \quad c_{12} = c_{13} = c_{23}\,,
\tag{C.32}
$$

and the other components, as given in (C.29), equal to zero. Using the unity constrain for the direction vector

$$
\|n_i\| = n_1^2 + n_2^2 + n_3^2 = 1\,,
\tag{C.33}
$$

we further have

$$
\begin{aligned}
\Gamma_{11} &= c_{11}\, n_1^2 + c_{44}\, (n_2^2 + n_3^2) = c_{11}\, n_1^2 + c_{44}\, (1 - n_1^2) \\
\Gamma_{22} &= c_{11}\, n_2^2 + c_{44}\, (n_1^2 + n_3^2) = c_{11}\, n_2^2 + c_{44}\, (1 - n_2^2) \\
\Gamma_{33} &= c_{11}\, n_3^2 + c_{44}\, (n_1^2 + n_2^2) = c_{11}\, n_3^2 + c_{44}\, (1 - n_3^2) \\
\Gamma_{12} &= (c_{12} + c_{44})\, n_1\, n_2 \\
\Gamma_{13} &= (c_{12} + c_{44})\, n_3\, n_1 \\
\Gamma_{23} &= (c_{12} + c_{44})\, n_2\, n_3 \,.
\end{aligned}
\tag{C.34}
$$

In an isotropic medium the material properties, and thus the wave solutions, are the same for all directions of propagation. Therefore an arbitrary direction can be chosen, e.g. the x-axis direction with a direction vector $\mathbf{n} = \{1, 0, 0\}^T$ leads to

$$
\Gamma_{11} = c_{11}\,, \qquad \Gamma_{22} = c_{44}\,, \qquad \text{and} \qquad \Gamma_{44} = c_{44}\,,
\tag{C.35}
$$

and the off-diagonal terms $\Gamma_{12} = \Gamma_{13} = \Gamma_{23} = 0$. Then the Kelvin-Christoffel equation (C.23) becomes

$$
\begin{bmatrix}
c_{11} - \rho\, (v_p^n)^2 & 0 & 0 \\
0 & c_{44} - \rho\, (v_p^n)^2 & 0 \\
0 & 0 & c_{44} - \rho\, (v_p^n)^2
\end{bmatrix}
\cdot
\begin{Bmatrix} p_1^n \\ p_2^n \\ p_3^n \end{Bmatrix}
=
\begin{Bmatrix} 0 \\ 0 \\ 0 \end{Bmatrix} .
\tag{C.36}
$$

From the dispersion equation (C.19) one dispersion relation is obtained, i.e.

$$
\left[c_{11} - \rho\, (v_p^n)^2 \right] \left[c_{44} - \rho\, (v_p^n)^2 \right] \left[c_{44} - \rho\, (v_p^n)^2 \right] = 0\,,
\tag{C.37}
$$

giving the three eigenvalues of the Kelvin-Christoffel matrix

$$
c_{11} = \rho\, (v_p^1)^2\,, \qquad c_{44} = \rho\, (v_p^2)^2\,, \quad \text{and} \quad c_{44} = \rho\, (v_p^3)^2\,,
\tag{C.38}
$$

from which the phase velocities are computed. The corresponding eigenvectors p_i^n are obtained by inserting each eigenvalue in the Kelvin-Christoffel equation (C.36). Solving a system of three equations consiting of two equations from (C.36) and the unity constrain $\|p_i^n\| = 1$ [see Eq. (C.33)] yields the three components of the polarization vector p_i^n. Because two eigenvalues coincide, the two corresponding eigenvectors can be chosen arbitrary as mutually perpendicular vectors within a plane that is perpendicular to the third eigenvector. For the first eigenvalue in (C.38) the resulting set of equations is

$$
\begin{aligned}
(c_{44} - c_{11})\, p_2^1 &= 0 \\
(c_{44} - c_{11})\, p_3^1 &= 0 \\
(p_1^1)^2 + (p_2^1)^2 + (p_3^1)^2 &= 1\,,
\end{aligned}
\tag{C.39}
$$

with the solution

$$
\mathbf{p}^1 = \begin{Bmatrix} 1 \\ 0 \\ 0 \end{Bmatrix} = \mathbf{n}\,,
\tag{C.40}
$$

i.e. the polarization direction of the first wave is parallel to the propagation direction. Two arbitrary eigenvectors may be chosen in the plane perpendicular to this eigenvector, e.g. one in the vertical plane containing the propagation direction and one perpendicular to this plane.

Thus the three waves propagating in an isotropic medium are

- one longitudinal (or compressional) wave at a phase velocity v_L with particle displacement in direction of propagation and

- two transversal (or shear) waves at equal phase velocities v_T with particle displacements perpendicular to the direction of propagation (in-plane and out-of-plane polarization).

The velocities of the three body waves are therefore

$$v_p^1 = v_L \qquad \text{and} \qquad v_p^2 = v_p^3 = v_T\,, \tag{C.41}$$

and the relationship between stiffness tensor components and velocities can be rewritten from (C.38)

$$C_{1111} = \rho\,v_L^2 \qquad \text{and} \qquad C_{1212} = \rho\,v_T^2\,. \tag{C.42}$$

The stiffness tensor for isotropic materials reads (in index and matrix notation)

$$C_{ijkl} = \lambda\,\delta_{ij}\,\delta_{kl} + \mu\,(\delta_{ik}\,\delta_{jl} + \delta_{il}\,\delta_{jk}) \quad \text{and} \quad \mathbb{C} = \lambda\,\mathbf{1}\otimes\mathbf{1} + \mu\,\mathbb{I}\,, \tag{C.43}$$

where $\mathbf{1}$ is the second and $\mathbb{I}$ the forth order unity tensor. An isotropic material is fully characterized by two independent engineering material constants. In (C.43) Lame's parameters

$$\lambda = c_{12} = c_{13} = c_{23} \quad \text{and} \quad \mu = G = c_{44} = c_{55} = c_{66} \tag{C.44}$$

are used, where the latter is equal to the shear modulus G. The third non-zero stiffness tensor component is related to the two others, and thus to Lame's elastic constants, by

$$c_{11} = c_{22} = c_{33} = c_{12} + 2\,c_{44} = \lambda + 2\,\mu\,. \tag{C.45}$$

The compliance tensor $\mathbb{D}$ as a function of the Young's modulus E and Poisson's ratio ν is given to

$$\{D_{ijkl}\} = \frac{1}{E}\begin{bmatrix} 1 & -\nu & -\nu & 0 & 0 & 0 \\ -\nu & 1 & -\nu & 0 & 0 & 0 \\ -\nu & -\nu & 1 & 0 & 0 & 0 \\ 0 & 0 & 0 & 2\,(1+\nu) & 0 & 0 \\ 0 & 0 & 0 & 0 & 2\,(1+\nu) & 0 \\ 0 & 0 & 0 & 0 & 0 & 2\,(1+\nu) \end{bmatrix}, \tag{C.46}$$

where the second equation of (C.44) can be verified by $G = E/2/(1+\nu)$ and (C.9).

The velocities expressed as a function of the mass density and stiffness tensor components or [using (C.45) and the expression for the bulk modulus $K = \lambda - 2/3\,G$] engineering elastic constants are given as

$$v_L = \sqrt{\frac{C_{1111}}{\rho}} = \sqrt{\frac{\lambda + 2\,\mu}{\rho}} = \sqrt{\frac{K + 4/3\,G}{\rho}} \qquad \text{and} \qquad v_T = \sqrt{\frac{C_{1212}}{\rho}} = \sqrt{\frac{G}{\rho}}\,. \tag{C.47}$$

Using the relationships between Lame's constants and the Young's modulus and Poisson's ratio

$$E = \frac{\mu\,(3\,\lambda + 2\,\mu)}{\lambda + \mu} \qquad \text{and} \qquad \nu = \frac{\lambda}{2\,(\lambda + \mu)}\,, \tag{C.48}$$

and the relationships between Lame's constants and the longitudinal and shear velocities, that

follow directly from (C.47)

$$\lambda = \rho \left(v_L^2 - 2\, v_T^2 \right) \qquad \text{and} \qquad \mu = \rho\, v_T^2 \,, \tag{C.49}$$

formulas for E and ν are obtained

$$E = \rho\, \frac{v_T^2 \left(3\, v_L^2 - 4\, v_T^2 \right)}{v_L^2 - v_T^2} \qquad \text{and} \qquad \nu = \frac{v_L^2/2 - v_T^2}{v_L^2 - v_T^2}\,. \tag{C.50}$$

Appendix **D**

Matrix notation of forth order elasticity tensors

The generalized Hooke's law and its inverted form are given to

$$\sigma^{ij} = C^{ijkl}\varepsilon_{kl} \quad \text{and} \quad \varepsilon_{ij} = D_{ijkl}\sigma^{kl}, \tag{D.1}$$

respectively. $\boldsymbol{\sigma}$ and $\boldsymbol{\varepsilon}$ are the second order stress and strain tensors and $\mathbb{C}$ and $\mathbb{D}$ are the forth order stiffness and complinace tensors, respectively. Subscripts indicate covariant coordinates, superscripts indicate contravariant coordinates of the tensorial basis (Helnwein 2001). The 6×6 matrix representation of $\mathbb{C}$ and $\mathbb{D}$ for materials with orthotropic symmetry is given to

$$\{C_{ijkl}\} = \begin{bmatrix} C_{1111} & C_{1122} & C_{1133} & 0 & 0 & 0 \\ C_{2211} & C_{2222} & C_{2233} & 0 & 0 & 0 \\ C_{3311} & C_{3322} & C_{3333} & 0 & 0 & 0 \\ 0 & 0 & 0 & c\,C_{2323} & 0 & 0 \\ 0 & 0 & 0 & 0 & c\,C_{1313} & 0 \\ 0 & 0 & 0 & 0 & 0 & c\,C_{1212} \end{bmatrix},$$

$$\{D_{ijkl}\} = \begin{bmatrix} D_{1111} & D_{1122} & D_{1133} & 0 & 0 & 0 \\ D_{2211} & D_{2222} & D_{2233} & 0 & 0 & 0 \\ D_{3311} & D_{3322} & D_{3333} & 0 & 0 & 0 \\ 0 & 0 & 0 & d\,D_{2323} & 0 & 0 \\ 0 & 0 & 0 & 0 & d\,D_{1313} & 0 \\ 0 & 0 & 0 & 0 & 0 & d\,D_{1212} \end{bmatrix}. \tag{D.2}$$

The constant c depends on the used tensorial basis. Most commonly used in engineering mechanics is the convention, to use contravariant coordinates for the second order stress tensor $\boldsymbol{\sigma}$ and covariant coordinates for the second order strain tensor $\boldsymbol{\varepsilon}$. Therefore $\mathbb{C}$ is given in contravariant and $\mathbb{D}$ is given in covariant coordinates, yielding $c = 1$ and $d = 4$. A more general formulation is obtained if a normalized tensorial basis is used to represent second and fourth order tensors (Helnwein 2001), yielding $c = d = 2$. No distinction between covariant and contravariant representation is required in this notation and the norm of a second order tensor is defined correctly.

Comparison of Eqs. (D.1) gives

$$\mathbb{D} = \mathbb{C}^{-1} \, . \tag{D.3}$$

The tensor of elastic constants must, by definition of the positive definitness of the strain energy density, be symmetric and positive definite. This implies the necessary but not sufficient condition that all diagonal terms must be positive, i.e.

$$C_{1111} > 0 \, , \quad C_{2222} > 0 \, , \quad C_{3333} > 0 \, , \quad C_{2323} > 0 \, , \quad C_{1313} > 0 \, , \quad C_{1212} > 0 \, . \tag{D.4}$$

The necessary and sufficient condition for C_{ijkl} to be positive definite is that the sequential principal minors must be positive, i.e. for orthorhombic symmetry

$$
\begin{aligned}
A_{11} &= C_{1111} > 0 \\[4pt]
A_{22} &= C_{1111}\, C_{2222} - C_{1122}^2 > 0 \\[4pt]
A_{33} &= C_{1111}\, C_{2222}\, C_{3333} + 2\, C_{1122}\, C_{1133}\, C_{2233} - C_{1111}\, C_{2233}^2 - C_{2222}\, C_{1133}^2 - C_{3333}\, C_{1122}^2 > 0 \\[4pt]
A_{44} &= C_{2323}\, A_{33} > 0 \\[4pt]
A_{55} &= C_{1313}\, C_{2323}\, A_{33} > 0 \\[4pt]
A_{66} &= |C_{ijkl}| = C_{1212}\, C_{1313}\, C_{2323}\, A_{33} > 0 \, .
\end{aligned}
\tag{D.5}
$$

Single crystal and polycrystal material properties of aluminum

Elastic material properties of certrain materials are unaltered by certain transformations — so-called symmetry transformations. These symmetry properties are usually described by symmetry classes used to characterize crystal symmetry. Out of two basic types of transformations — rotation and mirror reflection — all symmetries can be generated. These transformations are denoted by $k = 1$, 2, 3, 4, or 6 for rotations (where $2\,\pi/k$ is the angle of the rotation) and m for a mirror plane. The simplest repeating unit in a crystal is called unit cell, which is defined by a certain arrangement of lattice points. The lattice points in 3D-space are the points around which the particles (set of atoms) are free to vibrate. All crystals can be classified in terms of 14 different unit cells, which fall into seven crystal systems (triclinic, monoclinic, orthorhombic, tetragonal, rhombohedral, hexagonal, and cubic). Each of the seven crystal systems consists of a discrete number of point groups that sum up to a total of 32 crystal classes. Materials in the most general, the triclinic system do not have any symmetry and are described by 21 elastic constants. The istropic symmetry, belonging to the cubic crystal system, is unchanged by any transformation and is thus the highest possible symmetry, with two independent elastic constants. Besides the isotropic symmetry, the transversal isotropic (hexagonal crystal system) and the orthotropic (orthorhombic crystal system) symmetry are of importance in this work (see Section 2.3 for details on their independent elastic constants). The latter requires either three twofold axes of rotation, one twofold axis of rotation and two mirror planes, or three mirror planes, denoted by 222, $2mm$, and mmm, respectively.

Aluminum is used for different investigations in Publications 1 and 2. In the following the difference in aluminum single crystal and alumnium (polycrystals) alloy (see Table 1.7 for material properties of alloy EN AW-5083-H111) is elucidated. Major component of the chemical composition of aluminum alloy 5083 (Table E.1) is (pure) aluminum (≈ 94 %), with, according to EN-485-2 (2006), a magnesium content of 4.5 % and a manganese content of 0.4 %. The temperature dependency of aluminum alloy 5083 was found to be the highest for Young's modulus and shear modulus and the lowest for bulk modulus and Poisson's ratio, with changes from liquid-helium to room temperature of 14% and 4%, respectively (Weston et al. 1975).

Aluminum is a metal with a face-centred cubic crystal structure (closest packing possible) with a lattice constant of 0.40494 nm (Kamm and Alers 1964). In single crystal materials only one orientation of the crystal lattice is present in a specimen, whereas in a material consisting of

Table E.1: Range of chemical composition of aluminum alloy 5083.

Al [%]	Mg [%]	Mn [%]	Si [%]	Fe [%]	Zn [%]	Ti [%]	Cr [%]	Cu [%]
balance	$4.0-4.9$	$0.4-1.0$	0.4	0.4	0.25	0.15	$0.05-0.25$	0.1

grains each of these has a certain orientation of the crystal lattice. Spherical grains would have the lowest surface to volume ratio, i.e. lowest energy usage to form a material, but do not fill completely the space. Thus, polygonal grains are formed. The elastic properties of such polycrystal materials are influenced by their microstructure and the crystallography of the single crystal (Markham 1962). The elastic stiffness of cubic (single) crystal structure is defined by three independent stiffness tensor components. However, in a polycrystalline (aluminum) alloy, the properties of a single crystal are homogenized over single crystals with a quasi-isotropic orientation distribution. Hence, the alloy is an (quasi-)isotropic material with two independent stiffness tensor components.

The single crystal adiabatic elastic constants of aluminum have been determined by several authors (Goens 1933; Lazarus 1949; Sutton 1953; Schmunk and Smith 1959; Kamm and Alers 1964; Chung and Buessem 1968; Thomas 1968; Ho and Ruoff 1969) to a relatively high precision, by dynamic methods — mostly using ultrasonic wave propagation (see Table E.2 for average values and standard deviations in percent of average at room temperature). The standard deviation of these eight different sources are maximal only 1% and 2% for ultrasonic velocities (in principal material directions) and cubic stiffness tensor components, respectively. The component C_{1122} has a standard deviation nearly twice as high, indicating that the determination of off-diagonal stiffness tensor components is not possible with an equally high precision. This stems from the much higher impact of measurement errors in velocities of waves propagating in non-principal material directions, used to determine the off-diagonal stiffness components. Obviously, the stability criteria for a cubic crystal, namely the spinodal, shear and Born criteria, i.e. (Karki et al. 2001)

$$C_{1111} + 2\,C_{1122} > 0\,, \qquad C_{1212} > 0\,, \quad \text{and} \quad C_{1111} - C_{1122} > 0\,, \tag{E.1}$$

are fullfilled by the stiffness components given in Table E.2.

Table E.2: Elastic constants of cubic aluminum single crystal from literature (Goens 1933; Lazarus 1949; Sutton 1953; Schmunk and Smith 1959; Kamm and Alers 1964; Chung and Buessem 1968; Thomas 1968; Ho and Ruoff 1969) [average values ± standard deviation in percent of average; ultrasonic velocities derived via (1.15)].

ρ [g/cm^3±%]	v_L [km/s±%]	v_T [km/s±%]	C_{1111} [GPa±%]	C_{1212} [GPa±%]	C_{1122} [GPa±%]	n [-]
2.699±0.03	6.316±1.0	3.237±0.3	107.69±2.1	28.28±0.7	62.03±3.5	8

The strength of aluminum alloys is two orders of magnitude higher than of single crystal aluminum, whereas the difference in elastic stiffness is marginal (see Tables 1.7 and E.2). Single crystal aluminum is only slighly anisotropic (compare C_{1122} in Tables 1.7 and E.2), thus even a strongly textured polycrystalline aggregate of aluminum would be nearly isotropic (Naimon

et al. 1975). The elastic constant of polycrystalline materials could also be determined by computational averaging of the single crystal properties. Ledbetter (1980) showed that the errors of computational homogenization for copper was within the (ultrasonic) measurement uncertainties of the polycrystaline material. The grain size, i.e. the inhomogeneity d of pure Aluminum is approximately 300 μm (Hansen and Huang 1998), the average grain size of Aluminum alloy 5083 is approximately 100 μm (Llorca-Isern et al. 2005). Comparing $d/\lambda_L = 0.3$ and $d/\lambda_T = 0.6$ of the highest deployed frequency $f = 20$ MHz (see Table 1.1 for wavelengths) with d/λ-values obtained for aluminum alloy (see Table A.1), confirms that all our ultrasonic measurements were clearly performed in the Rayleigh scattering regime and thus the average (static limit case) stiffness constants of the aluminum alloy were determined (without induced deviations from single crystal properties). Young's modulus of aluminum oxide (alumina) was found to be independent of grain size [1-200 μm, Spriggs et al. (1986)].

For an isotropic material, such as aluminum alloy, the combination of the wave velocities in an infinite isotropic medium (1.15) with the isotropic stiffness tensor $\mathbb{C}$ written in terms of engineering elastic constants (C.43), and using $C_{1111} = C_{1122} + 2\,C_{1212}$ [see Eq. (C.45)] yields Lame's parameters ($\lambda\;(=C_{1122})$ and $\mu\;(=C_{1212})$) in terms of (isotropic) wave velocities [see Eq. (C.49)]. Using relationships between the isotropic stiffness tensor components and engineering elastic constants Young's modulus E and Poisson's ratio ν

$$\frac{C_{1111}}{E} = \frac{v_L^2}{v_E^2} = \frac{1-\nu}{(1+\nu)\,(1-2\,\nu)} \qquad \text{and} \qquad \frac{C_{1212}}{E} = \frac{v_T^2}{v_E^2} = \frac{1}{2\,(1+\nu)}\,, \tag{E.2}$$

the latter can be written in terms of wave velocities [see Eq. (C.50)]. The ratio of longitudinal to transversal stiffness tensor components is given to

$$\frac{C_{1212}}{C_{1111}} = \frac{v_T^2}{v_L^2} = \frac{1/2-\nu}{1-\nu}\,. \tag{E.3}$$
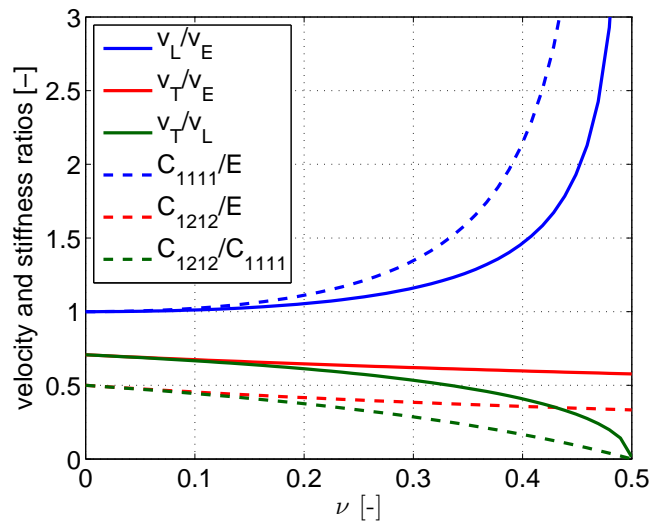
Figure E.1: Dependency of the ratio of bulk longitudinal (v_L) and transversal (v_T) wave velocities to extensional wave velocity v_E (blue and red solid line, respectively), of the normal (C_{1111}) and shear (C_{1212}) stiffnesses to Young's modulus E (blue and red dashed line, respectively), of bulk longitudinal wave velocity (v_L) to transversal wave velocity (v_T) (solid green line), and of normal stiffness (C_{1111}) to shear stiffness (C_{1212}) (dashed green line) on Poisson's ratio ν.

An stronger influence of Poisson's ratio on both, velocity and stiffness, in longitudinal than in transversal direction is evident from equations (E.2) (compare blue and red curves in Figure E.1). For lower Poisson's ratios ($\nu < 0.2$) the difference of C_{1111} and E is less than 10%, thus

the stiffness deduced from a bulk wave propagation may be approximated with a extensional wave. This can be of importance if an estimation of Young's modulus E needs to be determined by only longitudinal (bulk) wave propagation. The higher Poisson's ratio, the higher the error in stiffness determination ($\approx 50\%$ for aluminum) when the propagation mode is not correctly considered. The ratio of the bulk longitudinal velocity to the bulk transversal velocity is always smaller than 0.7 for the physical admissible range of positive Poisson's ratios in isotropic materials ($\nu = 0-0.5$) and approximately 0.5 in aluminum [Eq. (E.3); see solid green curve in Figure E.1].

Appendix **F**

Sample-specific wave propagation — bulk waves and extensional waves: Alternative representation

In Publication 1 the dependceny of sample specific (longitudinal and transversal) wave velocity with respect to the edge-length-over-height parameter a/h and the height-over-wavelength parameters h/λ_i ($i = \{L,\,T\}$) was given (see Section 1.6). Here, the same measurement results are presented with respect to the edge-length-over-wavelength parameters a/λ_i and the height-over-wavelength parameters h/λ_i (see Figures F.1 and F.2, and Figure F.3 for a sectional view along a/λ_i of specimen *set A1*; sectional views along h/λ_i of Figures F.1 and F.2 and Figures 1.9, 1.10, 1.11, and 1.12 are identical). Also, the 2D-cross-sections through Figures 1.11 and 1.12 for transversal waves are presented (see Figures F.4 to F.6). Finally, the effect of using delay lines with longitudinal waves in elucidated (see Figure F.7).

Investigated specimen geometry and deployed ultrasonic transducers, i.e. ultrasonic pulse frequencies yield the geometry parameters a/λ_i, h/λ_i in a range of five orders of magnitude (see Figures F.1 and F.2). Data points in Figures F.1 and F.2 belonging to specimen *sets A1, A2*, and *B* are for clarity connected with blue, green, and red lines, respectively, while data points belonging to *set R* are not interconnected. To retaine clarity, sectional views only display each specimen *set A1* (constant h/λ_i), *set A2* (constant a/λ_i), and *set B* (constant a/λ_i).

It should be noted, that the physical realizability of measurements in regions not covered by data points in Figures F.1 and F.2 (very long bars or very thin plates), is very limited or only possible with extensive complexity in the experimental realization. In this cases, generally, measurement possibilities other than (contact) ultrasonic pulse-transmission should be considered.

(a) 3D-representation

(b) Top view
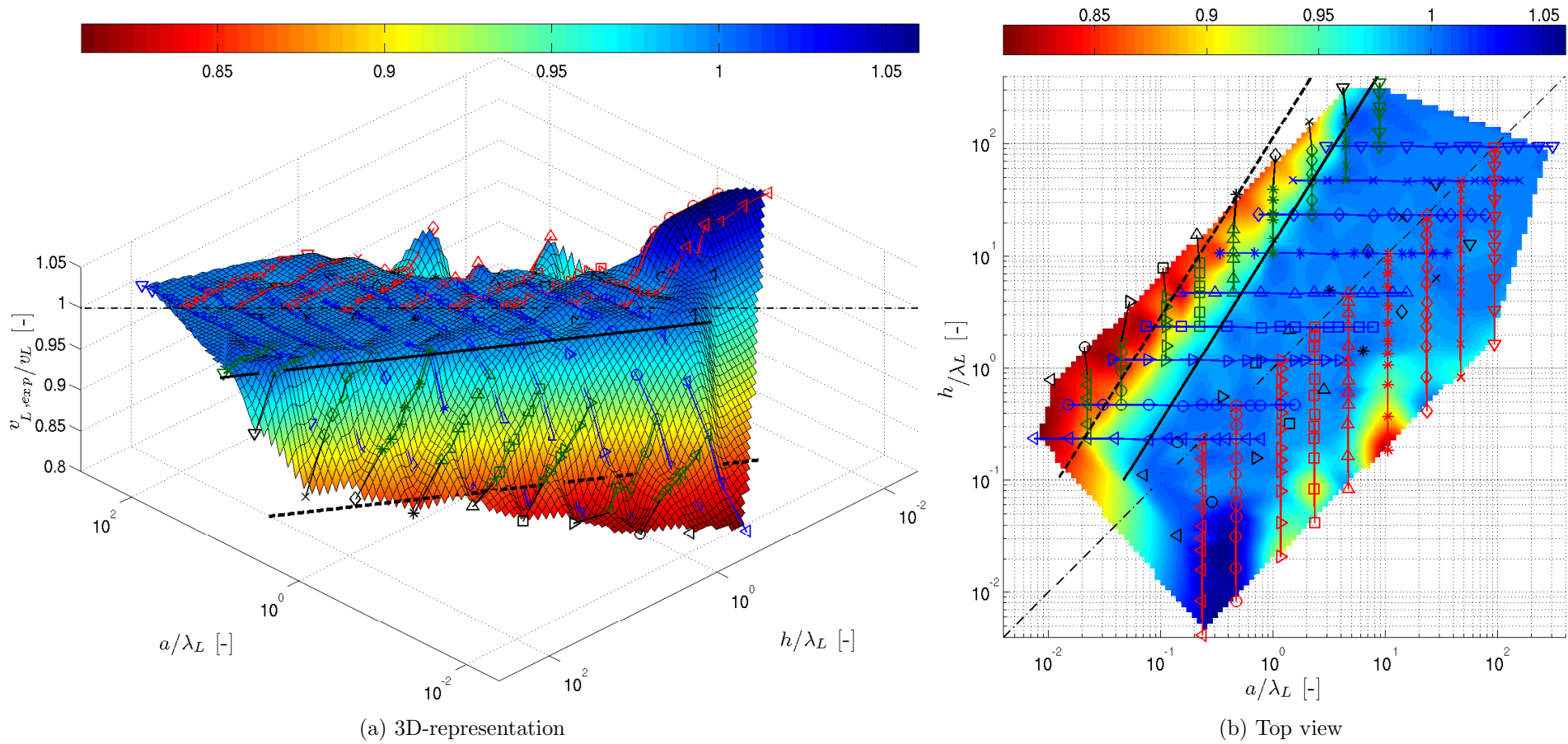
Figure F.1: Specimen *sets A, B, R* (according to Table 1.5): Dependency of dimensionless longitudinal wave velocity ($v_{L,exp}/\sqrt{C_{1111}/\rho} = v_{L,exp}/v_L$), on specimen geometry, and on wave frequency (in terms of edge-length-over-wavelength parameter a/λ_L and height-over-wavelength parameter h/λ_L).

(a) 3D-representation

(b) Top view
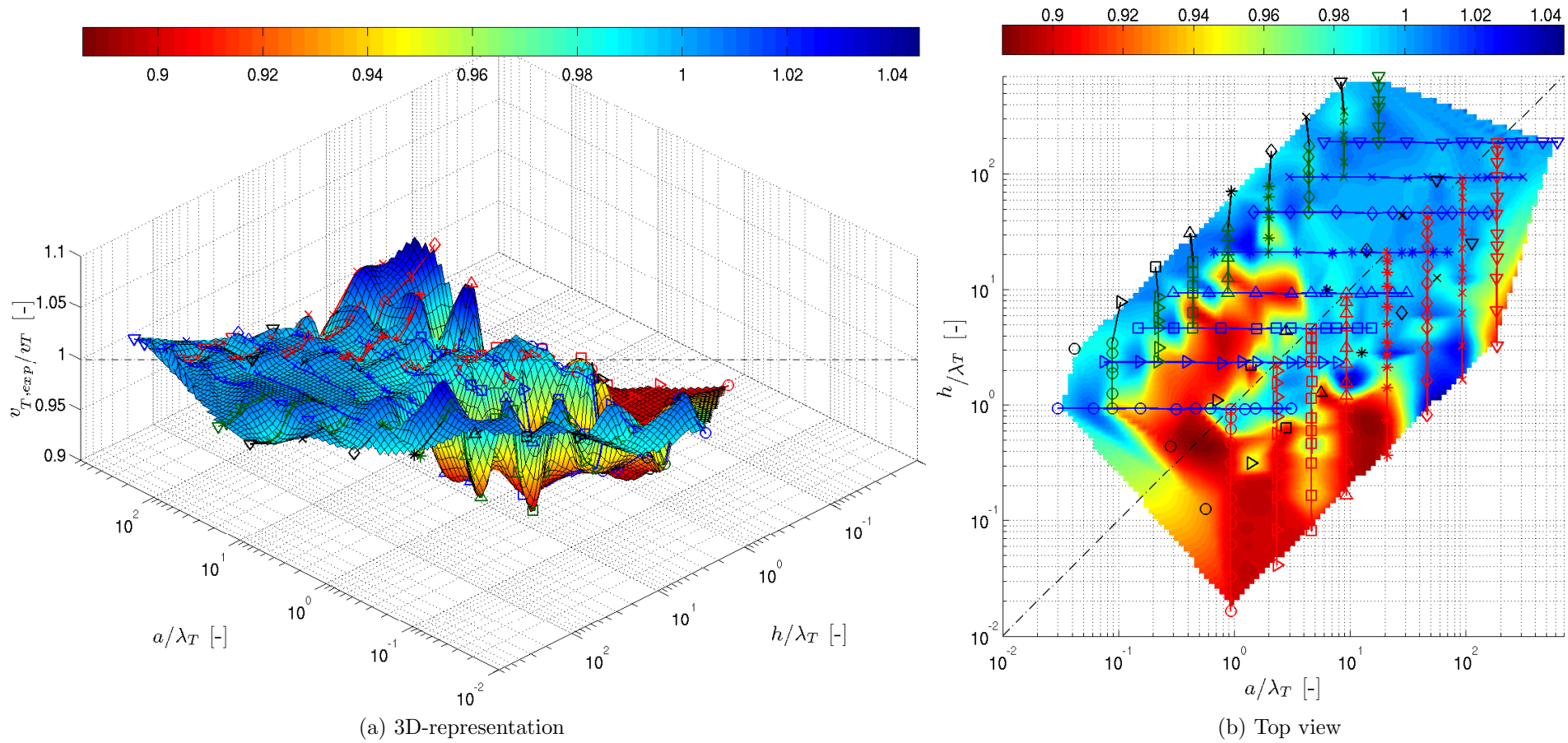
Figure F.2: Specimen *sets A, B, R* (according to Table 1.5): Dependency of dimensionless transversal wave velocity ($v_{T,exp}/\sqrt{C_{1212}/\rho} = v_{T,exp}/v_T$), on specimen geometry, and on wave frequency (in terms of edge-length-over-wavelength parameter a/λ_T and height-over-wavelength parameter h/λ_T).

The four corners of the Figures F.1 and F.2 represent limit cases of wave propagation (assuming a finite wavelength λ_i). Constant values of a/h are located on parallel lines to the diagonal defined by $a/\lambda_i = h/\lambda_i$ (equivalent to cubic specimens, i.e. $a/h = 1$; see dash-dotted lines in Figures F.1 and F.1), i.e. identical specimen, measured at different frequencies. Along this diagonal the *worst case* (pertaining to wave propagation) at the lower end with $a/\lambda_i = h/\lambda_i \to 0$ and the *best case* at the upper end with $a/\lambda_i = h/\lambda_i \to \infty$ are located. These cases refer to wave propagation in an infinitely small to infinitely large (cubic) specimen assuming a fixed finite wavelength, or refer to an infinitely large to infinitely small wavelength assuming a (cubic) specimen with fixed finite dimensions. Perpendicular to this diagonal the *bar case* with $a/\lambda_i \to 0$ and $h/\lambda_i \to \infty$ and the *plate case* with $a/\lambda_i \to \infty$ and $h/\lambda_i \to 0$ are located. The directions normal to the diagonal $a/\lambda_i = h/\lambda_i$ refer to geometry transition from bar via cube to plate, while the directions parallel to the diagonal $a/\lambda_i = h/\lambda_i$ refer to wave transition from larger to smaller wavelength, i.e. from lower to higher frequencies. In Figures 1.9, 1.10, 1.11, and 1.12 these limit cases of wave propagation refer to a finite height h. The geometry limit cases of *bar case* and *plate case* with $a/h \to 0$ and $a/h \to \infty$, respectively are here separated from the wave limit cases of zero to infinite wavelength, i.e. $h/\lambda_i \to \infty$ and $h/\lambda_i \to 0$, respectively. The *best case* and *worst case* are located along $a/h = 1$ at $h/\lambda_i \to \infty$ and $h/\lambda_i \to 0$, respectively.
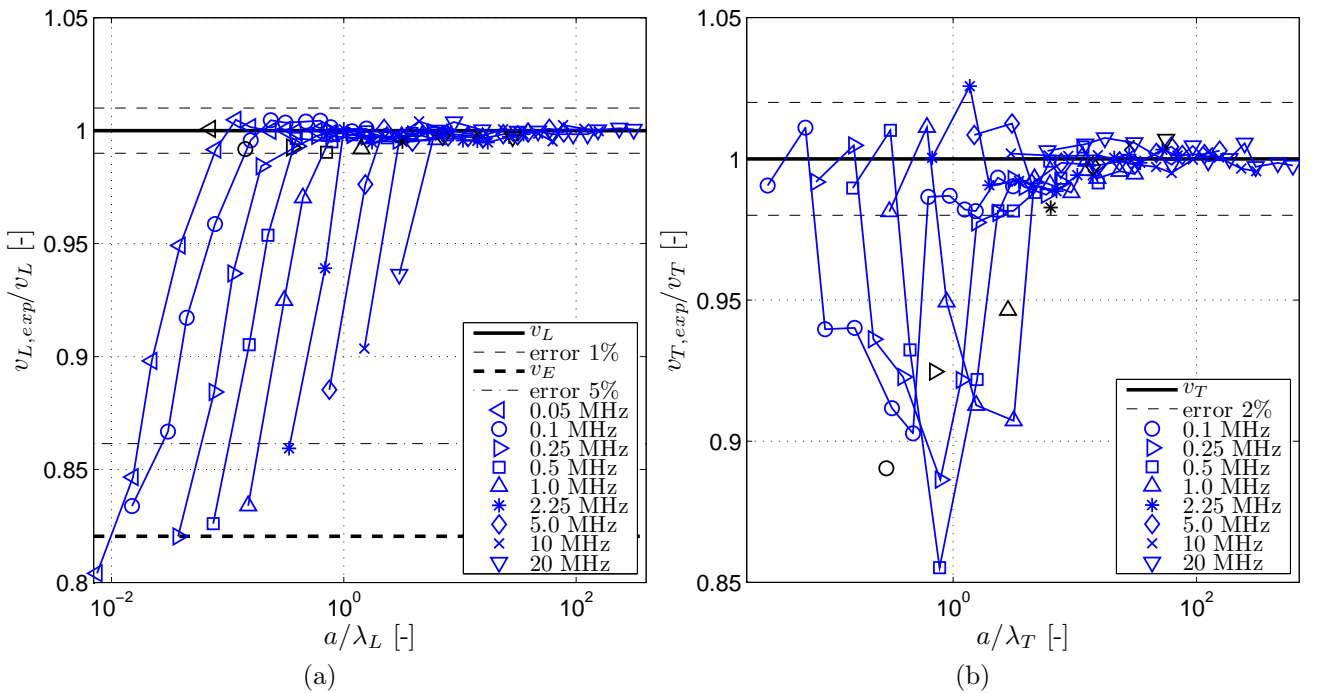
Figure F.3: Specimen *set A1, R-2* (according to Table 1.5): Dependency of dimensionless (a) longitudinal wave velocity $(v_{L,exp}/\sqrt{C_{1111}/\rho} = v_{L,exp}/v_L)$ and (b) transversal wave velocity $(v_{T,exp}/\sqrt{C_{1212}/\rho} = v_{T,exp}/v_T)$ on edge-length-over-wavelength parameter $(a/\lambda_L, a/\lambda_T)$; data points relating to the same $h/\lambda_L(a/\lambda_T)$-ratio are connected by solid lines.

Five major regions of a/λ_i (or a/h) and h/λ_i values are identified for longitudinal wave propagation in Figures F.1, which are regions of

- extensional (or bar) wave propagation,
- transition between bulk and extensional wave propagation,
- bulk wave propagation,
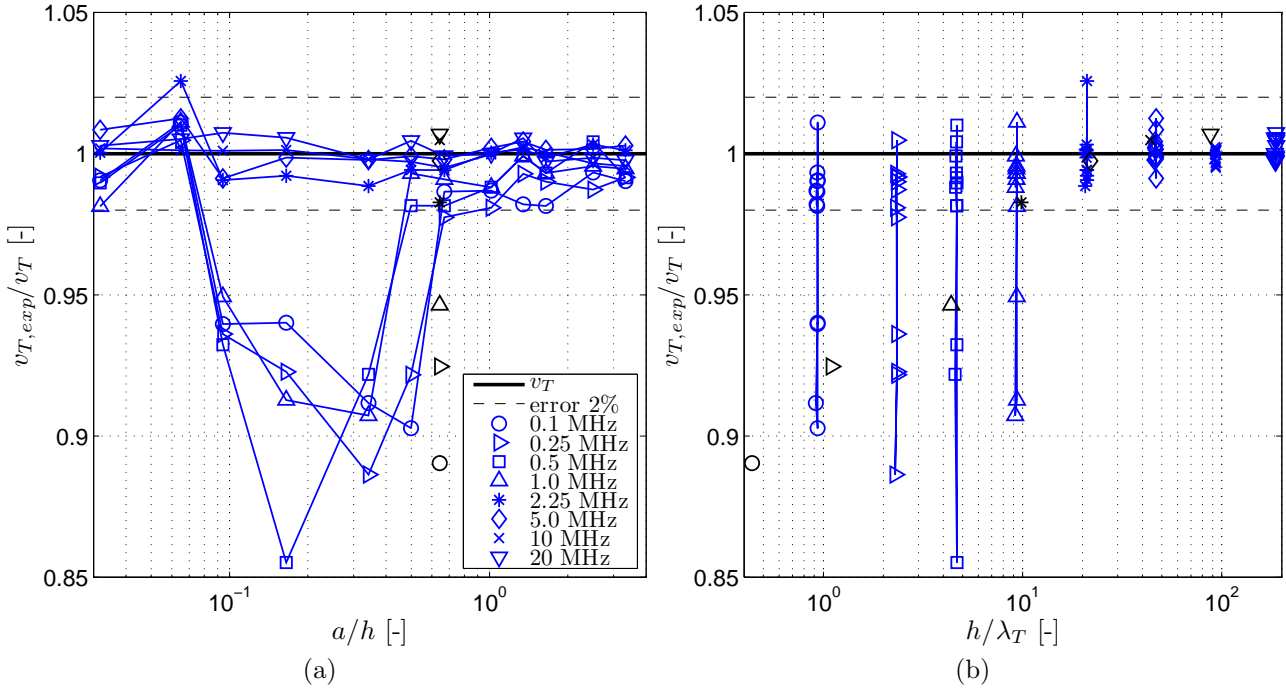
Figure F.4: Specimen *set A1, R-2* (according to Table 1.5): Dependency of dimensionless transversal wave velocity ($v_{T,exp}/\sqrt{C_{1212}/\rho} = v_{T,exp}/v_T$), on (a) edge-length-over-height parameter (a/h), and on (b) height-over-wavelength parameter (h/λ_L); data points relating to the same h/λ_T-ratio are connected by solid lines.

- measurement accuracy limit of wave velocity, and

- ultrasonic frequencies limit,

whereas for transversal wave propagation in Figures F.2 only the latter three regions are present. In the following this different regions shall be discussed.

Bulk wave propagation (blue area in Figures F.1) occures for geometry to wavelength ratios that are located around the diagonal $a/\lambda_i = h/\lambda_i$, where the deviation from the diagonal becomes larger with increasing ratios. This means that bulk wave propagations becomes easier with increasing frequency for both, lower specimen geometry ratios a/h (rising deviation from cube to bar) and higher ratios a/h (rising deviation from cube to plate). Longitudinal wave velocities deviate from bulk wave velocities in regions where changes to a bar-like geometry and thus to Young's modulus mode become pronounced (see Figures 1.6 and 1.7), and where changes to a plate-like geometry and to thus very short propagation times (see Figures 1.8) become pronounced. For transversal waves there is no theoretical reason for deviation from the bulk wave velocity. Deviations from the transversal (bulk) wave velocity are due to problems in determining the correct transversal velocity at low frequencies at plate-like (see Figures F.6), as well as at bar-like (see Figures F.4 and F.5) geometries.

Extensional wave propagation (red area beyond thick dashed line in Figures F.1) occures for combinations of small ratios a/λ_L with larger ratios h/λ, e.g. $a/\lambda_L < 0.1$ and $h/\lambda_L > 1$ or $a/\lambda_L < 1$ and $h/\lambda_L > 100$, where the best pre-conditions are combinations of low ratios. The lower the ratios, the larger the extensional wave region becomes with respect to the bulk wave region (see Figures F.1). Generally, specimen geometry ratios $a/h < 0.01$ lead to extensional wave propagation for all frequencies, wheres for $a/h > 0.01$ only very low frequencies yield this type of wave (see Figure 1.10). Extensional wave propagation seems to be influenced
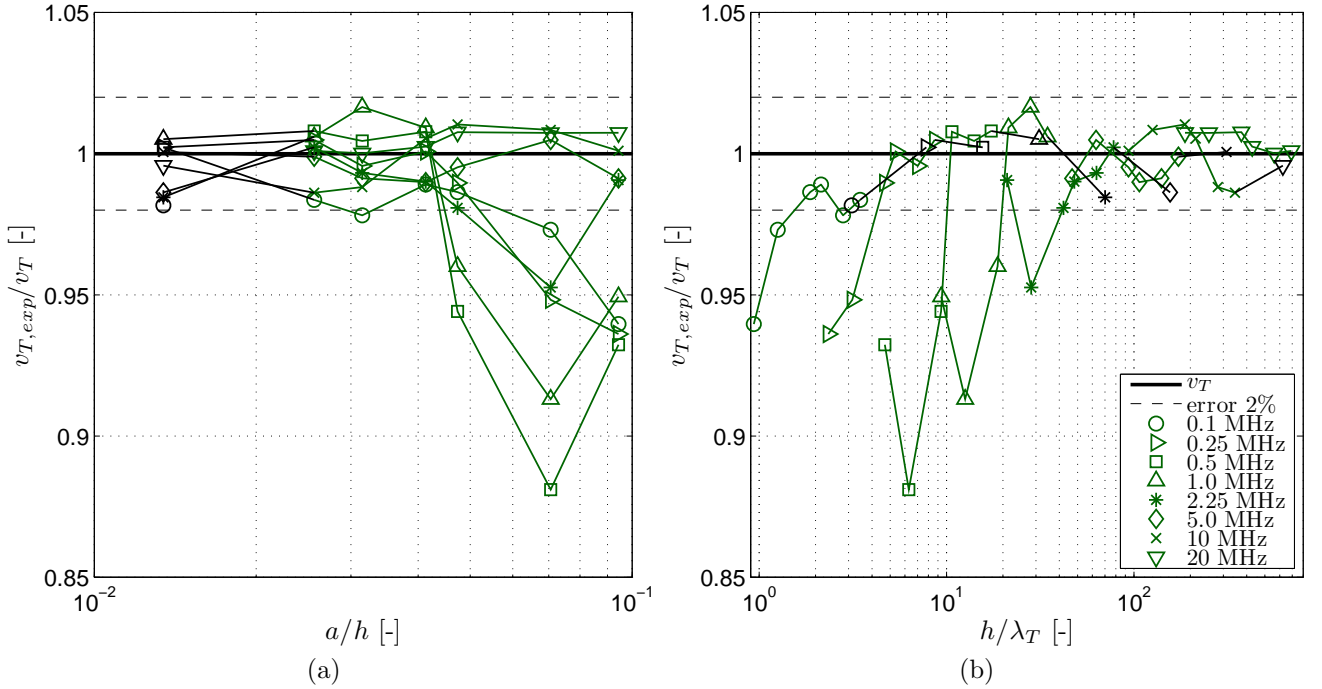
Figure F.5: Specimen *set A2, R-1* (according to Table 1.5): Dependency of dimensionless transversal wave velocity $(v_{T,exp}/\sqrt{C_{1212}/\rho} = v_{T,exp}/v_T)$, on (a) edge-length-over-height parameter (a/h), and on (b) height-over-wavelength parameter (h/λ_T); data points relating to the same a/λ_T-ratio are connected by solid lines.

not only by the (generally accepted) ratio of a/λ_L, but also by the ratio h/λ_L, i.e. also the slenderness ratio a/h. Hence, for a given (bar-like) specimen (i.e. constant a/h) extensional wave propagation is more difficult to achieve with increasing frequency (see Figure 1.10). Or, in other words, a measurement in (bar-like) specimen at a given frequency (i.e. constant λ_L) will more likely lead to extensional wave propagation if its height (or length) is short in comparison to the wavelength. Increasing slenderess, i.e. smaller ratio a/h $(0.02 - 0.06)$, and decreasing ratios a/λ_L $(0.01 - 0.5)$ and h/λ_L $(0.2 - 10)$ yield extensional wave propagation (compare with Figures F.3 (a), 1.6, and 1.7). The preferable frequencies to transmit extensional waves in bars $(a/h \to 0)$ are low, as to obtain wavelengths that are equally long or longer than the bar $(h/\lambda_L \to 0)$.

Transition between bulk and extensional wave propagation (area between thick dashed line and thick solid line in Figures F.1) occures between the regions mentioned above, with an approximately constant width over the complete frequency range (see Figures F.1, 1.9, and1.10). Transition in Figures F.3 (a), 1.6, and 1.7 from extensional to bulk wave propagation is related to transition from slender and long bars (small a/h) measured at low frequencies (small a/λ_L) to squat and short bars (slighly larger a/h) measured at higher frequencies (large a/λ_L) at increasing h/λ_L. Measurements of bars with a slenderness ratio a/h between 0.01 to 0.2, i.e. the slim to squat bars of *set A1* (see Figures F.3 (a) and 1.6) and the long to short bars of *set A2* (see Figures 1.7) are located in the transition region. Specimen with equal ratio a/h are approximately (deviation within experimental errors) located on parallel lines (see Figures F.3 (a), 1.6, and 1.7), indicating that the transition region is an inclined plane in the double logarithmic $a/\lambda_L - h/\lambda_L$ space. We note for comparison that a change in $v_{L,exp}/v_L$ in this region $(h_{min} = 30 \text{ mm})$ of 0.01 (1% change of $v_{L,exp}$) refers to a difference in time of flight readings of $\Delta t_f \approx 0.05 \ \mu s$, which is due to difficulties in extensional wave measurements and measurement errors (see Table 1.4) a relatively low value. At low values of a/λ_L $(a/\lambda_L < 1)$
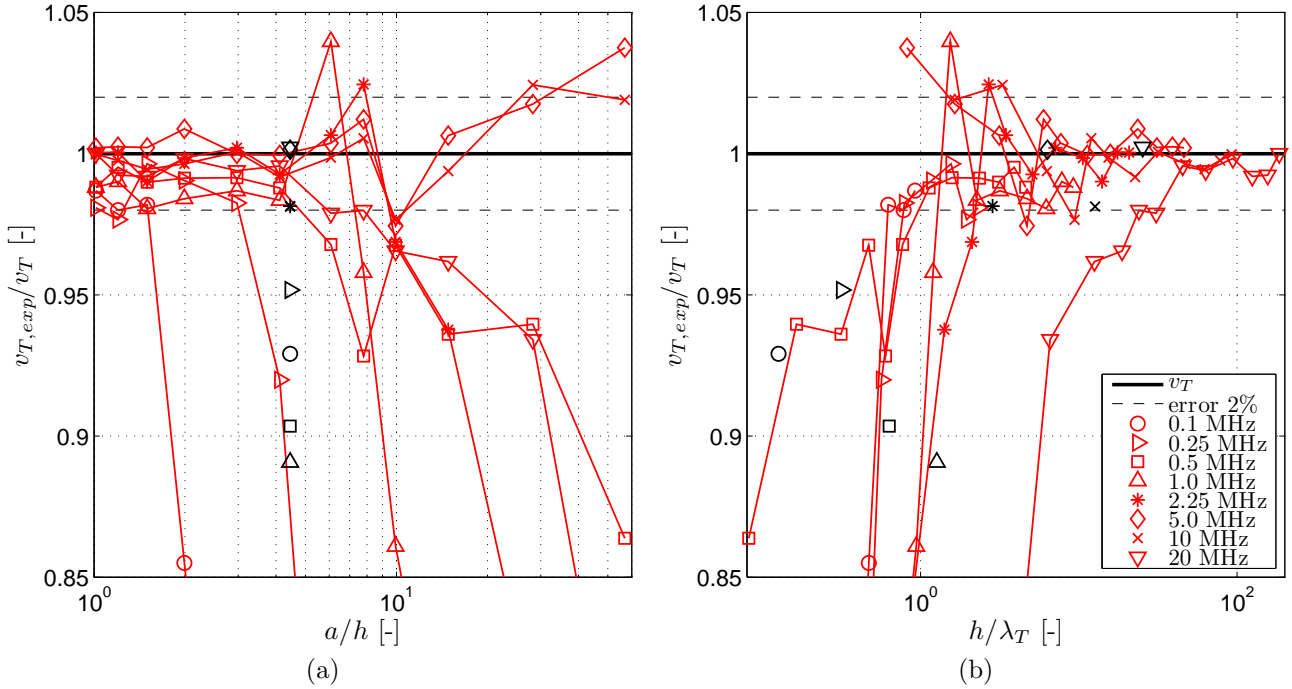
Figure F.6: Specimen *set B, R-3* (according to Table 1.5): Dependency of dimensionless transversal wave velocity $(v_{T,exp}/\sqrt{C_{1212}/\rho} = v_{T,exp}/v_T)$, on (a) edge-length-over-height parameter (a/h), and on (b) height-over-wavelength parameter (h/λ_T); data points relating to the same a/λ_T-ratio are connected by solid lines.

the energy is divided among a large number of modes and thus the transmitted pulse becomes weak and blurred and hence difficult to detect (Tu et al. 1955). The high pulse voltage used in our experimental setup enabled us to detect longitudinal pulses at values as low as $a/\lambda_L = 0.01$. Several works on stiffness determination of porous materials with the pulse-transmission technique (Ashman et al. 1987; Ashman and Rho 1988; Kohlhauser et al. 2008) use the unverified assumption that for $\lambda_L \ll a$ extensional wave propagation is present in a sample regardless its height and thus Young's modulus can be determined directly via (1.18). Our results show that extensional wave propagation is only possible in very slender bars at low frequencies indicating this assumption is not correct. Williams (1992) excluded the possibility, by using Biot's theory to describe wave propagation, that extensional wave propagation on struts within the microstructure of bone occures.

Measurements at the accuracy limit of the wave velocity [dark blue, green, yellow. and red area to the lower right of the dash-dotted line in Figure F.1 (b)], i.e. of the time of flight t_f and of the specimen height h (h to a lesser extent, see Section 1.3.3), may yield to considerable errors (see Figures 1.8 and F.6). In very thin specimens waves propagate as bulk waves, but when the thickness h in comparison to the time of flight t_f becomes very small [compare with equation (1.19)], v_i can not be determined accurately enough (see also Table 1.4). This circumstance is not correctly displayed by the given illustration based on h/λ_i and a/λ_i (or a/h), as the dimensional analysis only considers changes in the velocity due to *physical* reasons and not to, e.g., reasons related to experimental realizations. Thus, no clear limit of h/λ_i can be identified in Figures F.1 (b) and F.2 (b). Considers a relatively thick specimen, say $h/\lambda_i > 1$, and a very large characteristic cross-section dimension a, e.g. $a/\lambda_i > 100$, it becomes clear that the dimensional analysis, i.e. given illustration, do not reproduce this effect for all sets of h/λ_i and a/λ_i. Clearly, velocity measurements at medium frequencies would be accomplishable to a high accuracy, but the corresponding data point would be positioned in the accuracy limit

(a) with delay line   (b) without delay line
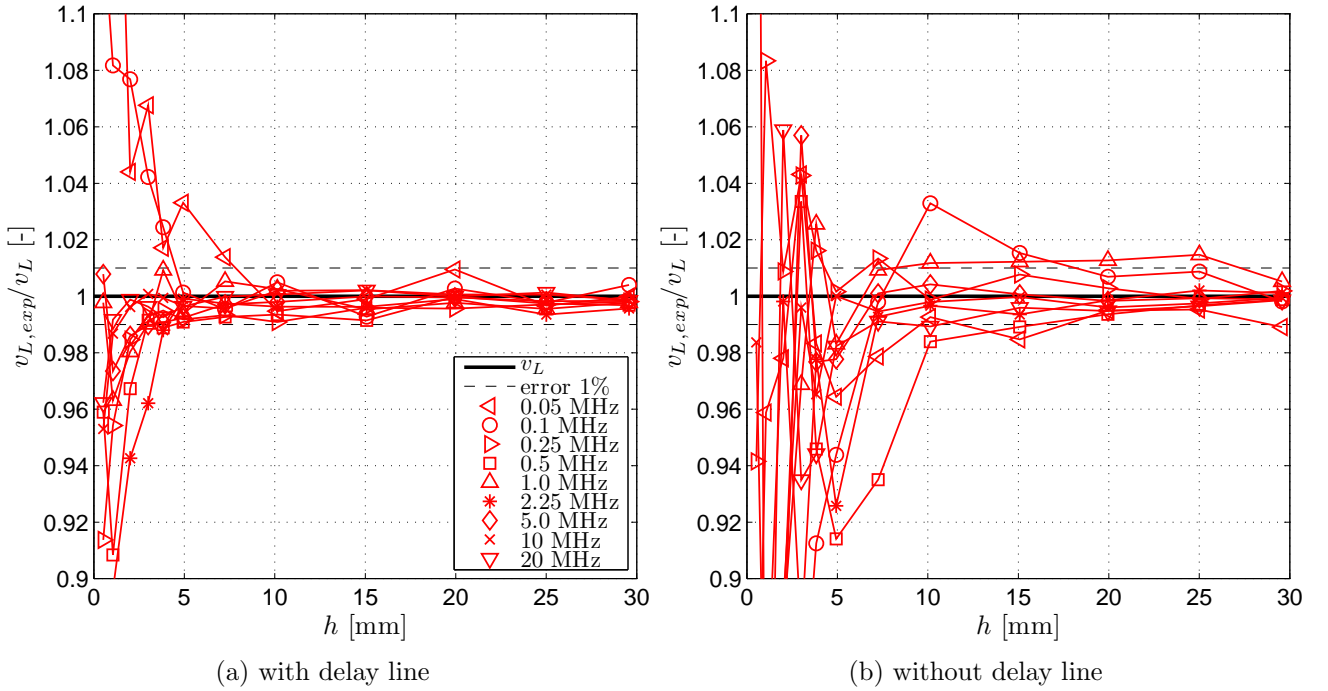
Figure F.7: Dependency of dimensionless longitudinal wave velocity ($v_{L,exp}/\sqrt{C_{1111}/\rho} = v_{L,exp}/v_L$), i.e. error of $v_{L,exp}$, of specimen *set B* over specimen height h for different frequencies.

region. Hence, the accuracy limit region depends on the ratio h/λ_i, i.e. $f\,t_{f,i}$, but is independent from a/λ_i, and is not a wave propagation phenomena.

Longitudinal velocity were determined using delay lines to improve accuracy of measurements and to allow for measurements in very thin samples. Comparison of Figures F.7 shows that the velocity deviation was reduced from 2% (for specimen with $h > 10$ mm) to 1% (for specimen with $h > 5$ mm) for all frequencies. Velocity measurements of very thin specimens ($h \geq 1$ mm) with an error of 2% were possible at high frequencies ($f \geq 5$ MHz). Generally, accurate measurements were possible for $h/\lambda_L \gtrsim 0.1$ to $h/\lambda_L \gtrsim 1$ [see Figures 1.8 (b)] and for $h/\lambda_T \gtrsim 1$ to $h/\lambda_T \gtrsim 10$ [see Figures F.6 (b)] at low to high frequencies, respectively.

Application limits of (ultrasonic) frequencies [white area in lower left corner in Figures F.1 (b) and F.2 (b)] are reached for typical specimen dimensions at low values of both geometry related parameters ($a/\lambda_L = h/\lambda_L \lesssim 0.1$), e.g. a or h equal to 30 mm for aluminum alloy (limit ultrasonic frequency $f_{min} = 20$ kHz yields $\lambda_{L,max} \approx 320$ mm). Due to the lack of ultrasonic transducer at frequencies that close to the ultrasonic limit no measurements were performed in this region.

Appendix **G**

Graphical representation of Poisson's ratio ranges

Ultrasonic velocity measurements are commonly used to determine elastic stiffnesses of (fiber) composite materials. Comparison of the resulting engineering elastic constants with other (measurement) methods is often limited to Young's modulus, while comparing Poisson's ratios directly, is neglected. Complete sets of elasticity components of materials of hexagonal, orthorhombic, or lower symmetry class determined by both mechanical and ultrasonic tests are very scarce in literature. In addition to the aluminum-silica fiber composite [see Section 2.5.2 and Figure G.1 (a)] ultrasonic measurement results from two other transversal isotropic aluminum matrix-fiber composites with different fibers are taken from literature and the Poisson's ratios from ultrasonic measurements are compared with results obtained from combined ultrasonic-mechanical testing (see Publication 2) of normal elastic stiffnesses constants.

If C_{1111}, C_{2222}, and E_1 are known, Poisson's ratios of transveral isotropic materials depend [on the basis of Eqs. (2.30)] on the missing normal stiffness, i.e. Young's modulus E_2 [transversal shear stiffness in the isotropic plane follows from Eq. (2.31) and the fifth unknown is the shear stiffness in longitudinal direction]. Thus, Poisson's ratios then cannot be directly computed from Eqs. (2.30), based on given values for C_{1111}, C_{2222}, E_1, and E_2, but these equations need to be seen as functions of a single variable L,

$$\nu_{ij} = \mathcal{F}_{trans} \left(L \right)_{C_{1111}, C_{2222}, E_1 \text{ fixed}} , \tag{G.1}$$

with the longitudinal-to-radial ratio of normal stiffnesses to Young's modulus ratios L according to Eq. (2.36)$_1$, in order to give ranges with respect to the missing normal stiffness (see Figure G.1 for visual representations of $\mathcal{F}_{trans}$). In addition to the discussion of Poisson's ratios determination of orthotropic stainless-steel weld metal in Section 2.5.3, the graphical representation of the Poisson's ratio ranges according to Eqs. (2.35) and (2.36) in Section 2.6 is given and discussed in here.

G.1 Transversely isotropic aluminum-carbon fiber composite

Mouchtachi et al. (2004) determined the elastic constants of transversely isotropic fiber composites, consisting of carbon (C) fibers embedded into a matrix made of aluminum alloy AS7G0.3; characterized by a fiber diameter $d_F = 7$ μm and a fiber volume fracion of $f_F = 0.58$. Elasticity tensor components related to normal strains and stresses (see Table G.1, row three) and to shear strains and stresses (see Table G.1, row eight) were measured on plate-like specimens, by means of an automated, computer-assisted, immersion device, based on (quasi-)longitudinal and (quasi-)transversal waves propagating in the principle material directions as well as in several different angles to these directions. Young's modulus in longitudinal direction E_1 was determined by means of mechanical tests for this composite (see Table G.1, row seven). The measured modulus agrees well (1% difference) with the result obtained by the rule of mixture model approach (Mouchtachi et al. 2004). Inversion of ultrasonic results yield a deviation of more than 8% of the longitudinal Young's modulus between mechanical and ultrasonic tests, indicating measurement erros in ultrasonically determined off-diagonal stiffnesses tensor components.

Table G.1: Elastic constants of fiber composite Al-C from mechanical, ultrasonic and combined tests (bold values from direct measurements).

elastic stiffness tensor constants	C_{1111} [GPa]	C_{2222} [GPa]	C_{3333} [GPa]	C_{1122} [GPa]	C_{1133} [GPa]	C_{2233} [GPa]
ultrasonic	**165.30**	**42.90**	**39.50**	**22.60**	**24.40**	**18.70**
combined	**165.30**	**41.20**	**41.20**	11.46	11.46	8.33
engineering elastic constants	E_1 [GPa]	E_2 [GPa]	E_3 [GPa]	G_{23} [GPa]	G_{13} [GPa]	G_{12} [GPa]
mechanical	**160.00**	–	–	–	–	–
ultrasonic	146.64	33.23	29.97	**10.70**	**20.70**	**22.30**
combined	**160.00**	39.00	39.00	16.43	–	–
normal stiffness ratios & fraction	f_F [-]	L [-]	T [-]	C_{1111}/E_1 [-]	C_{1111}/C_{2222} [-]	C_{2222}/C_{3333} [-]
ultrasonic	0.58	0.87	0.98	1.13	3.85	1.09
combined	–	0.98	1.00	1.03	4.01	1.00
Poisson's ratios	ν_{32} [-]	ν_{31} [-]	ν_{21} [-]	ν_{23} [-]	ν_{13} [-]	ν_{12} [-]
ultrasonic	0.428	0.464	0.325	0.386	0.095	0.074
combined	0.187	0.231	0.231	0.187	0.056	0.056

Using normal stiffnesses C_{iiii} and longitudinal Young's modulus E_1 from mechanical tests, Poisson's ratios ν_{ij} are given in Figure G.1 (b) as a function of L. A large deviation in the longitudinal Poisson's ratios is evident from this function, as the maximum values for ν_{21} and ν_{12} are approximately 0.24 and 0.06, respectively (compare with ν_{ij} in Table G.1, row 16). Moreover, even though $C_{2222} \approx C_{3333}$ (difference is 8%, which is small compared to the four times higher value of stiffness C_{1111}) and $T \approx 1$ (see Table G.1) ν_{31} deviates by $\approx 40\%$ from

ν_{21} (see Table G.1, row 16). This, too, is an indicator that the off-diagonal stiffnesses tensor components are not correct.

To obtain results for Poisson's ratios from normal stiffnesses, the transversal modulus given in Mouchtachi et al. (2004), which was nummerically determined (using an Eshelby-type model), and the average of C_{2222} and C_{3333} were used (assuming perfect transversal isotropy). These Poisson's ratios, which make use of the mechanical result for E_1, strongly deviate from the ones obtained from ultrasonic tests (compare Table G.1, rows 16 and 17), but both the transverse and the larger longitudinal Poisson's ratio are in accordance with Poisson's ratios for the similarly buildup composite with alumina-silica fibers (see Table 2.2, row 17 and Section 2.5.2). The difference in Poisson's ratios is due to the difference in the ratio C_{1111}/E_1 (see Table G.1, rows twelve and 13), whereas the negative Poisson's ratio obtained for aluminum-silica fibers (see Table 2.2) were due to the ratio $T = 0.85$ that is too far off the value of 1 (transversal isotropy) to result in positive solutions (see Figures G.3 and 2.3 for a typical complete three-dimensional representation of $\nu_{ij} = \nu_{ij}(L, T)$ for orthotropic symmetry and the related discussion).

(a) Al$_2$O$_3$-SiO$_2$ fibers   (b) C fibers   (c) Al$_3$Ni fibers
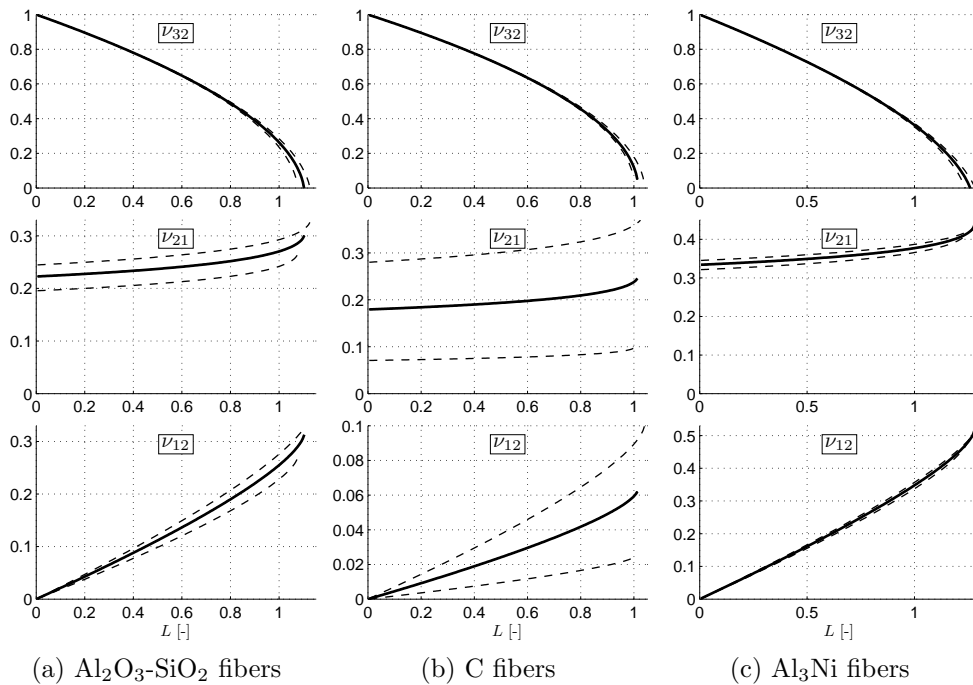
Figure G.1: Poisson's ratios as a function of longitudinal-to-radial ratio of normal stiffnesses to Young's modulus ratios L for transversal isotropic aluminum matrix composites (dashed lines indicate new ranges for deviations of C_{1111}/E_1 of $\pm 5\%$).

G.2 Transversely isotropic aluminum-nickel fiber composite

An unidirectionally-solidified eutectic composite of aluminum nickel (Al$_3$Ni) fibers in an α-aluminum matrix was tested with an ultrasonic pulse-echo-overlap method by Grabel and Cost (1972). Velocity measurements were performed on five specimen (composite density $\rho = 2.84$ g/cm^3), which were cut at different angles to the fiber direction to obtain the complete stiffness tensor (precision of stiffnesses $\approx 0.6\%$). Ultrasonic frequencies between 2 and 30 MHz were used — most measurements were performed at 5 MHz, yielding a ratio of inhomogenity d to wavelength λ of $d/\lambda \approx 10^{-3}$, i.e. small enough to ensure homogeneous material behavior

in terms of wave propagation [compare (1.1) and Kohlhauser and Hellmich (2009b)] and thus measuring average stiffness properties and not stiffnesses of composite constituents (Table G.2, rows three, seven, and eight). Using the average fiber diameter of 0.7 μm and the inter-fiber spacing of 1.7 μm, the fiber volume fraction is estimated via Eq. (1.30) to be $f_F \approx 15\%$ — considering a hexagonal fiber arrangement, which was observed in some regions (Grabel and Cost 1972). The fiber length was approximately 100 times larger than the fiber diameter. The average longitudinal Young's modulus from mechanical tests was given to $E_1 = 78$ GPa [Grabel and Cost (1972); see Table G.2, row seven]. Longitudinal Young's modulus from ultrasonic measurements overestimates this value by 9.6%.

Table G.2: Elastic constants of fiber composite Al-Al$_3$Ni from mechanical, ultrasonic and combined tests (bold values from direct measurements).

elastic stiffness tensor constants	C_{1111} [GPa]	C_{2222} [GPa]	C_{3333} [GPa]	C_{1122} [GPa]	C_{1133} [GPa]	C_{2233} [GPa]
ultrasonic	**132.60**	**122.30**	**122.30**	**66.50**	**66.50**	**65.30**
combined	**132.60**	**122.30**	**122.30**	72.36	72.36	69.49
engineering elastic constants	E_1 [GPa]	E_2 [GPa]	E_3 [GPa]	G_{23} [GPa]	G_{13} [GPa]	G_{12} [GPa]
mechanical	**78.00**	–	–	–	–	–
ultrasonic	85.45	77.47	77.47	**28.40**	–	–
combined	**78.00**	71.94	71.94	26.40	–	–
normal stiffness ratios & fraction	f_F [-]	L [-]	T [-]	C_{1111}/E_1 [-]	C_{1111}/C_{2222} [-]	C_{2222}/C_{3333} [-]
ultrasonic	0.15	0.98	1.00	1.55	1.08	1.00
combined	–	1.00	1.00	1.70	1.08	1.00
Poisson's ratios	ν_{32} [-]	ν_{31} [-]	ν_{21} [-]	ν_{23} [-]	ν_{13} [-]	ν_{12} [-]
ultrasonic	0.359	0.354	0.354	0.359	0.321	0.321
combined	0.362	0.377	0.377	0.362	0.348	0.348

Using normal stiffnesses C_{iiii} and longitudinal Young's modulus E_1 from mechanical tests, Poisson's ratios ν_{ij} are given in Figure G.1 (c) as a function of L. Figure G.1 (c) indicates similar Poisson's ratios as obtained from ultrasonic tests (compare with Table G.2, row 16). Using $L = 1.00$ — $L = 0.98$ from ultrasonic measurements; aluminum composites in the previous Section and Section 2.5.2 exhibit similar values; see Tables G.1 and 2.2 — Poisson's ratios show good agreement with ultrasonically determined ratios (see Table G.2, row 16 and 17). The ultrasonically determined constants of this composite are less prone to measurement errors because of its low acoustical damping. The larger deviation of longitudinal Poisson's ratios (ν_{21} and ν_{12}) is due to the lower value of E_1 — yielding a higher C_{1111}/E_1-ratio — obtained from mechanical tests, which is used in the combined method.

Generally, when using normal stiffnesses to compute Poisson's ratios, a low C_{1111}/E_1-ratio (close to one) yields higher errors for Poisson's ratio of longitudinal planes $\nu_{21} = \nu_{31}$ and $\nu_{12} = \nu_{13}$ [compare dashed lines in Figures G.1 (a) – (c), which indicate 5% change in C_{1111}/E_1], while the transverse Young's moduli, i.e. L, mostly influences the result of Poisson's ratios in the transverse plane $\nu_{32} = \nu_{23}$ and of $\nu_{12} = \nu_{13}$ (see Figures G.1, row one and two).

G.3 Orthotropic stainless-steel weld metal

Dewey et al. (1977) determined the elastic stiffness tensor constants by means of mechanical and ultrasonic tests (see Section 2.5.3, Table 2.3). In Dewey et al. (1977) average values — assuming transversal isotropy in the plane $1-2$ — of the elastic constants obtained from these two measurement methods are given. For normal components the average of ultrasonic and mechanical results, for off-diagonal components the mechanical results, and for shear components the ultrasonic results were used. The latter two selections were argued with the use of transformation relations (using, besides measurement values associated with this components, also measurement results of other components) to determine these components with ultrasonic tests [see Eqs. (2.12) to (2.14)] and mechanical tests, respectively. Young's moduli in the transverse directions 2 and 3 differ by 7 and 26%, respectively, from the longitudinal moduli, while the deviations of stiffness tensor components in the transverse directions compared to the longitudinal direction 1 are 13 and 20%, respectively. As these differences between the normal stiffnesses in the three principal directions are in the same order of magnitude and not negligible small, orthotropic — and not transversal isotropic — symmetry should be considered for this material.

(a) cross-section at $T = 0.86$ (b) cross-section at $L = 1.07$
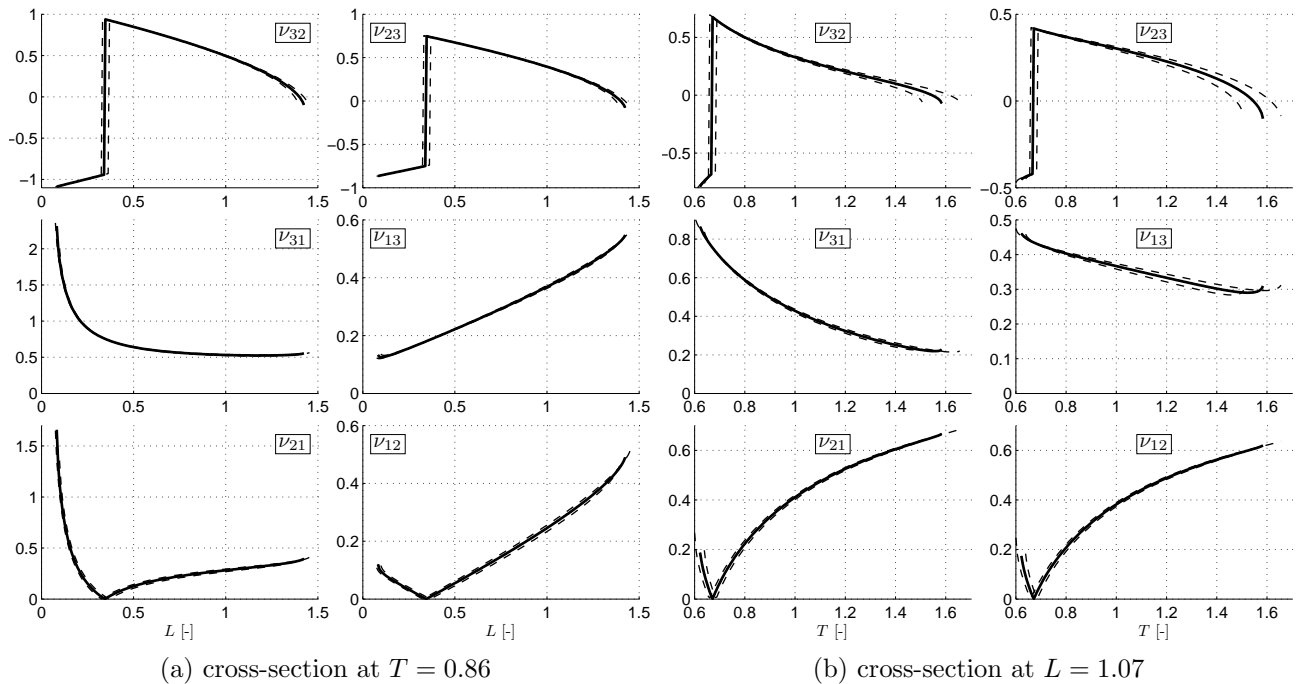
Figure G.2: Cross-sections through Figures G.3 at relevant values of L and T for orthotropic stainless-steel weld metal (see Table 2.3; dashed lines indicate new ranges for deviations of C_{1111}/E_1 of $\pm 5\%$).

Using the normal stiffness tensor components and longitudinal Young's modulus, i.e. known ratios C_{1111}/E_1, C_{1111}/C_{2222}, and C_{2222}/C_{3333}, Poisson's ratios ν_{ij} can be given as function of L and T (see Figures G.3 and G.4 for 3D and top views of this 3D representations, respectively). It is evident from cross-sections through Figures G.3 and G.4 (see Figures G.2) that L and T, i.e. E_2 and E_3, have a strong influence on the resulting Poisson's ratios when determined from normal stiffnesses (see Table 2.3, row 20 for results when using all six normal stiffnesses). They are not, on the other hand, sensitive to changes in the C_{1111}/E_1-ratio — see dashed lines in Figures G.2 for a change of 5% — because this ratio is not close to one. Ratios C_{1111}/C_{2222} and C_{2222}/C_{3333} are, even if they are close to one, of lesser influence on the results.
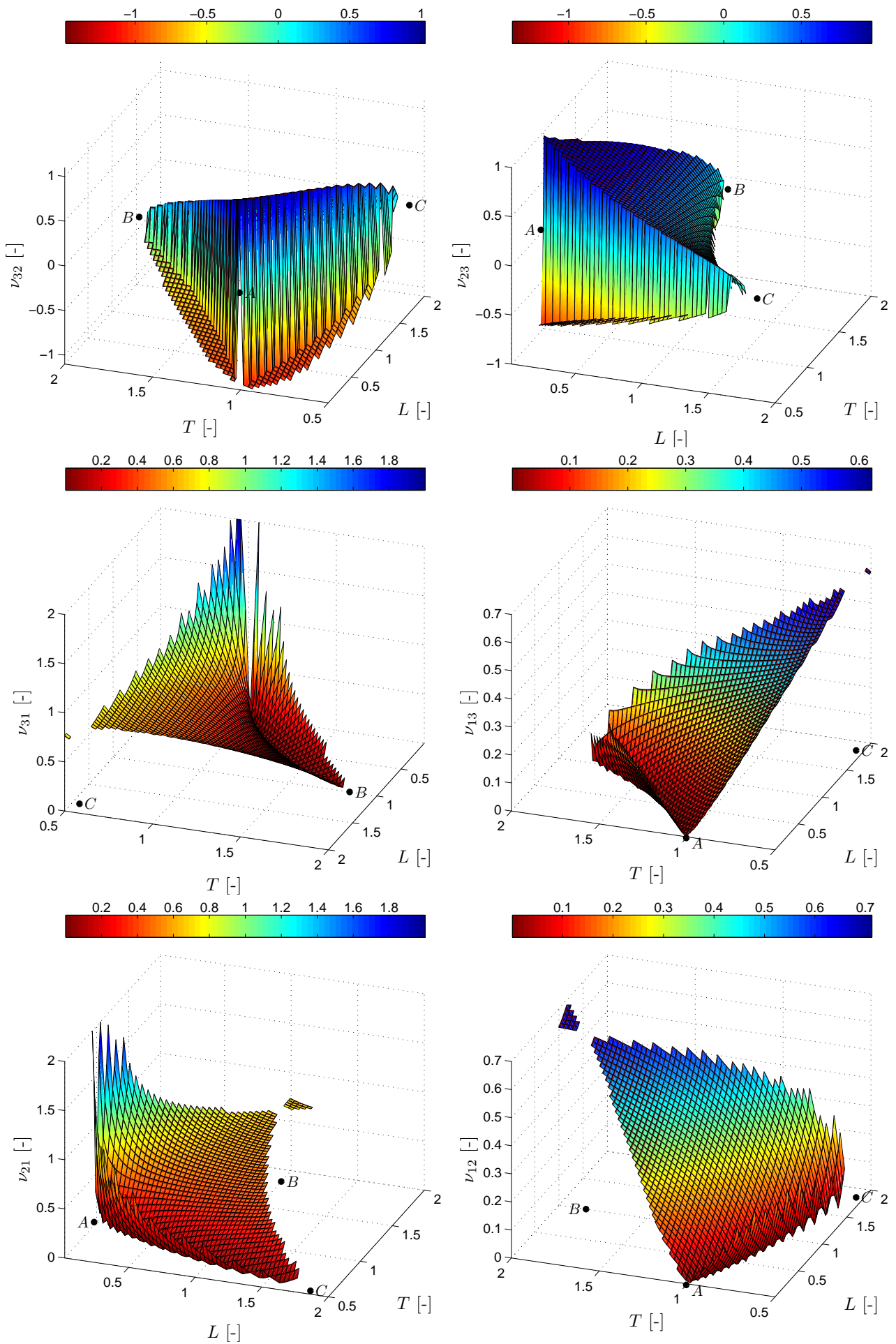
Figure G.3: Poisson's ratios of stainless-steel weld as function of ratios L and T (see Table 2.3).
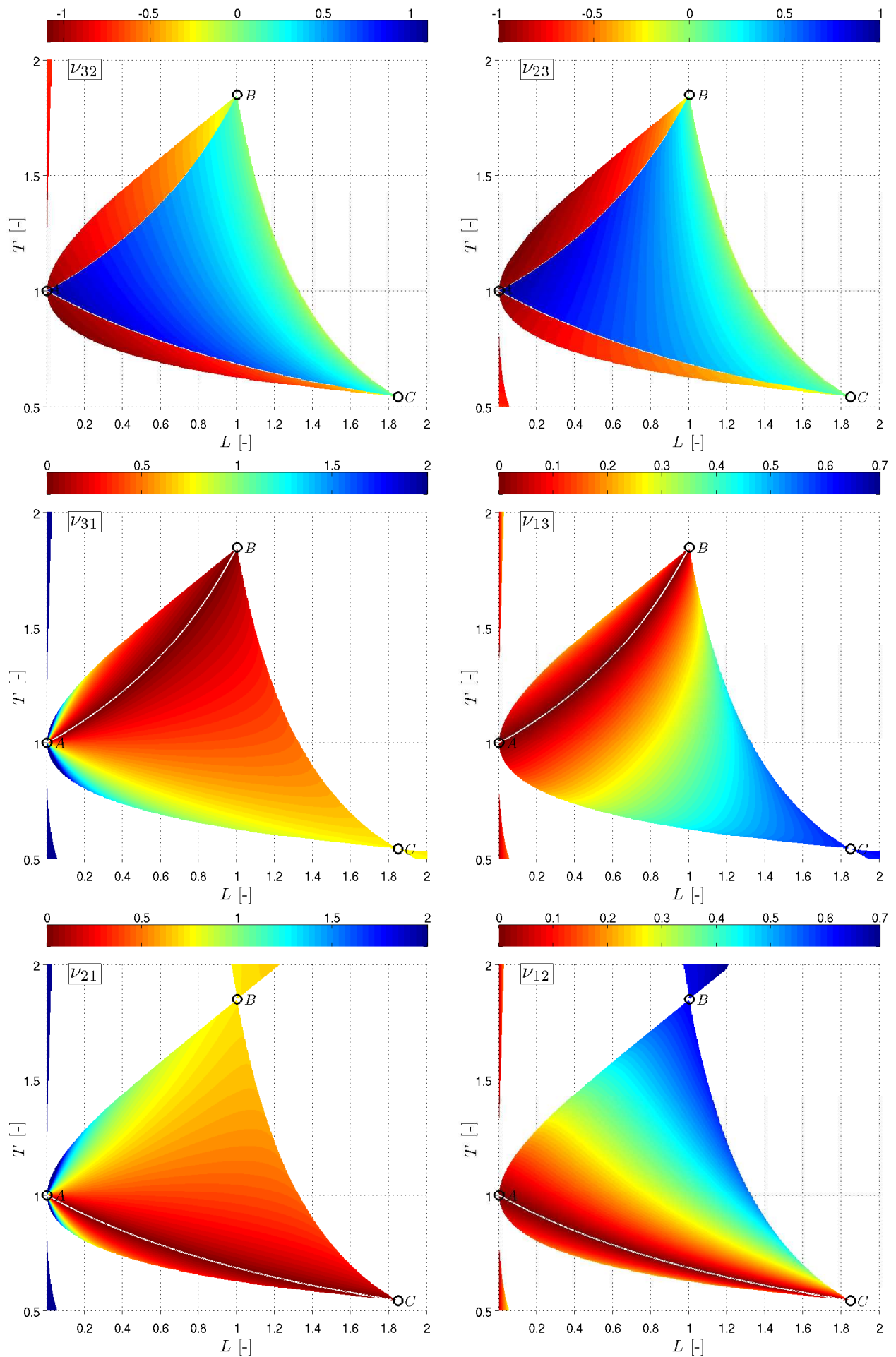
Figure G.4: Poisson's ratios of stainless-steel weld as function of ratios L and T (see Table 2.3) — top view.

Appendix H

Group velocities and energy deviation angles in bone, wood, and a fiber composite

Ultrasonics determination of material elasticity has become a classical technique, with plane wave theory as its theoretical fundament. However, from a general physics viewpoint, it is generally accepted that waves travel in the form of packets with more than one frequency, rather than in that of a shape with one single frequency. This also holds for mechanical (pulse) waves such as the ones employed for ultrasonic measurements. Velocities of wave packets are referred to as *group* velocities, while (plane) wave velocities (as standardly considered in ultrasonics) are referred to as *phase* velocities. The energy velocity (defines the wave front, which in the elastic range is equal to the wave surface) of the amplitude of a pulse, i.e. wave packet (superposition of harmonic components), is equal to the group velocity (Lighthill 1965; Auld 1990; Carcione 2001), which in lossless (non-attenuating, non-dispersive) media is equal to the envelope velocity (velocity of the envelope of plane waves) (Shercliff 1970; Carcione 2001). The group velocity is the velocity of the modulation envelope, while the carrier waves of the wave packet travel with the phase velocity, i.e. the velocity of a certain state — the phase — of a material point ('representative volume element'). In general each component of a pulse can travel at a different phase velocity, but in a homogeneous elastic media the phase velocity is frequency-independent — compare Eqs. (2.8), which are only functions of C_{ijij} and ρ, and the linear dispersion relation (2.7), which is a characteristic of continuum elasticity theory (Wolfe 1998) — and thus the pulse travels at the same velocity as each component.

Materials with microstructure can be considered as homogeneous in terms of wave propagation if the scale of the characteristic loading of the medium, here the wavelength λ, is much larger than the representative volume element (characteristic length ℓ_{RVE}), which must be considerably larger than the inhomogeneities d inside the RVE (Zaoui 2002), i.e. $d \ll \ell_{RVE} \ll \lambda$. If this is not fullfilled, phase velocities are frequency-dependent, i.e. the wave is dispersive. In anisotropic materials, energy (defined by the energy flux vector, also referred to as ray direction) does not necessarily propagate with the phase velocity in the direction the wave normal $\mathbf{n}$ (wave propagation direction) as it does in isotropic materials (Musgrave 1970). Experimentally one always receives the displacement or energy of a wave (pulse). A discussion of the interpredation of the resulting time measurement is given in Section 2.8. In short, it follows that the *projection*

of the signal vector to the wave normal is equal to the phase velocity, thus allowing for certain experimental set-ups to directly measure the phase velocity from time delay measurements (Sahay et al. 1992; Every 1980).

Next, we re-call the relationships between phase velocity and group velocity, and we re-evaluate experimental data published in the open literature as to show the difference between these velocities for anisotropic materials, more precisely for bone, wood, and a fiber composite.

Group velocity is the velocity of the amplitude of a wave packet, i.e. of a puls [for details on the theory of pulse propagation, see Norris (1978)]. The propagation velocity of modulation or envelope on a wave is defined as the group velocity (Lighthill 1965; Hayes and Musgrave 1979; Carcione 2001) (see also Section 2.8)

$$\mathbf{v}_g = \frac{\partial \omega}{\partial \mathbf{k}} = \frac{\partial v_p}{\partial \mathbf{n}} \,. \tag{H.1}$$

We will verify the relationship (Fedorov 1968; Auld 1990; Wolfe 1998; Carcione 2001)

$$\mathbf{v}_g \cdot \mathbf{n} = v_p \,, \tag{H.2}$$

using dispersion relations $\omega = \omega(\mathbf{k})$ to obtain an explicit form of $\mathbf{v}_g$ in terms of stiffness tensor components. The right part of (H.1) is obtained using (2.7), $\mathbf{k} = k\,\mathbf{n}$, and the fact that $\mathbf{v}_p = v_p\,\mathbf{n}$ is a homogeneous function of degree one in the components of $\mathbf{n}$ (Fedorov 1968; Every 1980).

Substituting v_p in Eq. (2.8) (quasi-longitudinal and quasi-transversal wave in the symmetry plane $1-2$) according to the definition of the phase velocity $v_p = \omega/k$ [Eq. (2.7)] and considering that $\mathbf{k} = k\,\mathbf{n}$ we obtain

$$\omega^{(1,2)} = \sqrt{\frac{C_{1111}\,k_1^2 + C_{2222}\,k_2^2 + C_{1212}\,k^2 \pm c_k}{2\,\rho}} \tag{H.3}$$

$$c_k = \sqrt{\left[(C_{2222} - C_{1212})\,k_2^2 - (C_{1111} - C_{1212})\,k_1^2\right]^2 + 4\left[(C_{1122} + C_{1212})\,k_1\,k_2\right]^2} \,.$$

Derivation with respect to k_i under consideration of $k^2 = k_1^2 + k_2^2 + k_3^2$ and backsubstituting v_p gives the group velocity vector $\mathbf{v}_g$ for the quasi-longitudinal and quasi-transversal wave in the symmetry plane $1-2$ as a function of the mass density ρ, the stiffness tensor components C_{ijkl} and the propagation direction n_i

$$\mathbf{v}_g^{(1,2)} = \frac{d\omega^{(1,2)}}{d\mathbf{k}} = \frac{1}{2\,\rho\,v_p^{(1,2)}} \left\{ \begin{array}{c} (C_{1111} + C_{1212})\,n_1 \pm c^{-1}\,c_a \\ (C_{2222} + C_{1212})\,n_2 \pm c^{-1}\,c_b \\ 0 \end{array} \right\} \,, \tag{H.4}$$

where

$$c_a = -(C_{2222} - C_{1212})\,(C_{1111} - C_{1212})\,n_1\,n_2^2 + (C_{1111} - C_{1212})^2\,n_1^3$$

$$+ 2\,(C_{1122} + C_{1212})^2\,n_1\,n_2^2 \,, \tag{H.5}$$

$$c_b = (C_{2222} - C_{1212})^2\,n_2^3 - (C_{1111} - C_{1212})\,(C_{2222} - C_{1212})\,n_1^2\,n_2$$

$$+ 2\,(C_{1122} + C_{1212})^2\,n_1^2\,n_2 \,, \tag{H.6}$$

and c according to (2.8). From Eq. (2.9) we obtain the group velocity vector $\mathbf{v}_g$ for the purely

transversal wave as

$$\mathbf{v}_g^{(3)} = \frac{d\omega^{(3)}}{d\mathbf{k}} = \frac{1}{\rho \, v_p^{(3)}} \left\{ \begin{array}{c} C_{1313} \, n_1 \\ C_{2323} \, n_2 \\ 0 \end{array} \right\} . \tag{H.7}$$

Eqs. (H.4) and (H.7) are also obtained via [see Section 2.8, Eq. (**??**); (Fedorov 1968; Every 1980)]

$$\mathbf{v}_g = \frac{\partial v_p}{\partial \mathbf{n}} . \tag{H.8}$$

In the case of a deviation between the propagation direction (or phase velocity direction, or wave normal) and the energy flux direction (group velocity direction), that is, in anisotropic materials in non-principle material directions, it is the projection of the group velocity into the direction of the wave normal (propagation direction), that is measured in an ultrasonic contact pulse transmission experimental setup [with finite dimensions of the (ultrasonic) wave source and receiver (i.e. no point source or receiver), and with $\mathbf{n}$ being normal to the (parallel) specimen surfaces, where the transducers are applied], i.e.

$$\mathbf{v}_g \cdot \mathbf{n} = v_{g,1} \, n_1 + v_{g,2} \, n_2 + v_{g,3} \, n_3 . \tag{H.9}$$

For quasi-longitudinal and quasi-transversal waves [Eq. (H.4)] this yields

$$\mathbf{v}_g^{(1,2)} \cdot \mathbf{n} = \frac{1}{2 \, \rho \, v_p^{(1,2)}} \left[(C_{1111} + C_{1212}) \, n_1^2 + (C_{2222} + C_{1212}) \, n_2^2 \pm c^{-1}(c_a \, n_1 + c_b \, n_2) \right] . \tag{H.10}$$

With $c_a \, n_1 + c_b \, n_2 = c^2$, $n_1^2 + n_2^2 = 1$, and the square of the phase velocity $v_p^{(1,2)}$ [Eq. (2.8)], the latter equation becomes

$$\mathbf{v}_g^{(1,2)} \cdot \mathbf{n} = \frac{1}{2 \, \rho \, v_p^{(1,2)}} \left[C_{1111} \, n_1^2 + C_{2222} \, n_2^2 + C_{1212} \pm c \right] = v_p^{(1,2)} . \tag{H.11}$$

For the out-of-plane pure transversal wave [Eq. (H.7)], Eq. (H.9) yields, using the square of the phase velocity $v_p^{(3)}$ [Eq. (2.9)],

$$\mathbf{v}_g^{(3)} \cdot \mathbf{n} = \frac{1}{\rho \, v_p^{(3)}} (C_{1313} \, n_1^2 + C_{2323} \, n_2^2) = v_p^{(3)} . \tag{H.12}$$

From (H.11) and (H.12) follows, that for contact pulse transmission time of flight measurements in any direction within symmetry planes of orthotropic media it is the phase velocity that is measured. This result is also obtained from geometrical arguments and is valid for *any* direction in an anisotropic material (Musgrave 1954; Sahay et al. 1992; Every 1994; Wolfe 1998). Furthermore, Eq. (H.2) is verified via (H.11) and (H.12) for symmetry planes. Eq. (H.2) holds for all directions in a fully anisotropic material (Fedorov 1968; Auld 1990; Wolfe 1998; Carcione 2001).

The group velocity is given through the norm of the group velocity vector,

$$v_g = \|\mathbf{v}_g\| , \tag{H.13}$$

the deviation angle Δ_v between the group and phase velocity vectors can be computed from vector calculus,

$$\Delta_v = \cos^{-1} \left(\frac{\mathbf{v}_p \cdot \mathbf{v}_g}{v_p \, v_g} \right) , \tag{H.14}$$

with $\mathbf{v}_p = v_p \, \mathbf{n}$, and the difference between the phase velocity and the group velocity is given

to

$$\Delta v = \frac{v_g - v_p}{v_g} \,. \tag{H.15}$$

Four stiffness tensors of three different materials were taken from the open literature. Two biological materials which are considered to be of orthorhombic symmetry (bone and wood) and one transversely isotropic material (artificial fiber composite) (for stiffness tensor components and densities see Table H.1). From these stiffness tensor components the phase velocities in the principle material directions (see Table H.2), and the phase and group velocities in symmetry planes in directions inclined 45° to the two other symmetry planes (see Tables H.3 and H.4), were computed.

Table H.1: Density [g/cm^3] and stiffness tensor components [GPa] of different anisotropic materials: human femoral bone (Ashman et al. 1984), pine (Bucur and Archer 1984), spruce (Jenkin 1920; Hearmon 1948), carbon-epoxy fiber composite (Dean and Turner 1973; Kriz and Stinchcomb 1979).

material	bone human femoral	wood pine	wood spruce	composite carbon-epoxy
ρ	1.9	0.383	0.43	1.61
C_{1111}	27.6	10.202	14.0648	161
C_{2222}	18.0	2.472	1.1030	14.5
C_{3333}	20.2	0.903	0.5929	14.5
C_{2323}	4.52	0.073	0.0320	3.63
C_{1313}	6.23	0.683	0.5000	7.10
C_{1212}	5.61	0.925	0.7200	7.10
C_{1122}	10.1	2.864	0.6845	6.50
C_{1133}	10.7	1.785	0.4747	6.50
C_{2233}	9.98	1.393	0.3451	7.24

Ashman et al. (1984) determined the complete stiffness tensor of human femoral bone by a continuous ultrasonic wave technique (see Table H.1, column two).

Bucur and Archer (1984) determined the complete stiffness tensor of six different wood species by the ultrasonic contact pulse transmission method at frequencies of 0.5 and 1 MHz (moisture content was not specified). Both, the diagonal and off-diagonal stiffness components of pine were taken from measurements at a pulse frequency of 0.5 MHz (see Table H.1, column three). For the latter an optimum value was used by rejecting values with extreme error estimates and taking the midpoint of the remaining values (Bucur and Archer 1984). Stiffness tensors determined via ultrasonic methods yielded negative Poission ratio's and several stiffness tensors had a determinant close to zero, i.e. were nearly singular. See Section 2.6 for resulting errors in stiffness tensor components and for a reliable method to determine complete stiffness tensors of wood.

Tests on different wood species performed by different authors were collected by Hearmon (1948). The engineering elastic constants of spruce (at moisture content 12%) determined by Jenkin (1920), defined the compliance tensor, which was inverted to obtain the stiffness tensor (see Table H.1, column four). Jenkin (1920) and Carrington (1923) were the first to give full elasticity tensors of wood (Hearmon 1948).

The stiffness tensor components of the transversely isotropic carbon-epoxy fiber composite (see Table H.1, column five) were obtained by curve-fitting ultrasonic data (Kriz and Stinchcomb

Table H.2: Phase velocities [km/s] in principle material directions of different anisotropic materials computed from data in Table H.1.

material	bone	wood	wood	composite
	human femoral	pine	spruce	carbon-epoxy
$v_{1,1}^{p,L}$	3.811	5.161	5.719	10.000
$v_{2,2}^{p,L}$	3.078	2.541	1.602	3.001
$v_{3,3}^{p,L}$	3.261	1.535	1.174	3.001
$v_{2,3}^{p,T}$	1.542	0.437	0.273	1.502
$v_{1,3}^{p,T}$	1.811	1.335	1.078	2.100
$v_{1,2}^{p,T}$	1.718	1.554	1.294	2.100

1979; Dean and Turner 1973). The composite is made up of transversly isotropic Modmor type 2 carbon fibers, which are uniaxially aligned and embedded in an Ciba LY558 epoxy resin (Dean and Turner 1973). The volume fractions of the fibers was $f_F = 0.67$.

Table H.3: Phase and group velocities [km/s] of human femur bone and pine wood in symmetry planes in directions inclined 45° to the two other symmetry planes computed from data in Table H.1.

material	bone — human femoral				wood — pine			
quantity	v_p	v_g	Δv	α_v	v_p	v_g	Δv	α_v
	[km/s]	[km/s]	[%]	[°]	[km/s]	[km/s]	[%]	[°]
$v_{12,12}^{qL}$	3.435	3.516	2.4	12.36	4.068	4.764	17.1	31.38
$v_{13,13}^{qL}$	3.534	3.578	1.2	8.95	3.875	4.910	26.7	37.90
$v_{23,23}^{qL}$	3.169	3.174	1.7E-1	3.30	2.114	2.320	9.7	24.31
$v_{12,12}^{qT}$	1.776	1.776	1.7E-2	1.07	1.554	1.554	1.6E-6	0.01
$v_{13,13}^{qT}$	1.835	1.835	1.6E-3	0.33	1.126	1.196	6.2	19.73
$v_{23,23}^{qT}$	1.546	1.546	5.1E-6	0.02	0.357	0.367	2.7	13.09
$v_{12,3}^{T}$	1.682	1.703	1.3	9.04	0.993	1.277	28.5	38.90
$v_{13,2}^{T}$	1.633	1.642	5.8E-1	6.14	1.141	1.501	31.5	40.49
$v_{23,1}^{T}$	1.765	1.768	1.4E-1	3.00	1.449	1.465	1.1	8.56

The three phase velocities of waves propagating in each principle material direction (which are equal to the group velocities in these directions) were back-calculated from the elastic constants in Table H.1 via Eqs. (2.10) (see Table H.2; for transversal waves $v_{i,j} = v_{j,i}$ is valid, thus only six values are given). The three phase velocities of waves propagating in the three non-principle material directions under investigation, namely $\mathbf{n} = \{1/\sqrt{2},\ 1/\sqrt{2},\ 0\}^T$ in symmetry plane $1-2$, $\mathbf{n} = \{1/\sqrt{2},\ 0,\ 1/\sqrt{2}\}^T$ in symmetry plane $1-3$, and $\mathbf{n} = \{0,\ 1/\sqrt{2},\ 1/\sqrt{2}\}^T$ in symmetry plane $2-3$, i.e. three quasi-longitudinal wave velocities $v_{ij,ij}^{p,qL}$, three quasi-transversal wave velocities $v_{ij,ij}^{p,qT}$, and three purely transversal wave velocities $v_{ij,k}^{p,T}$, are computed via Eqs. (2.8) and (2.9), and similar equations for symmetry planes $1-3$ and $2-3$ (see Tables H.3 and H.4, columns two and six). The respective nine group velocities, $v_{ij,ij}^{g,qL}$, $v_{ij,ij}^{g,qT}$, and $v_{ij,k}^{g,T}$, are computed via Eqs. (H.4), (H.7) and (H.13) (see Tables H.3 and H.4, columns three and seven). The differences

Table H.4: Phase and group velocities [km/s] of spruce wood and carbon-epoxy fiber composite in symmetry planes in directions inclined 45° to the two other symmetry planes computed from data in Table H.1.

material	wood — spruce				fiber composite — carbon-epoxy			
quantity	v_p	v_g	Δv	α_v	v_p	v_g	Δv	α_v
	[km/s]	[km/s]	[%]	[°]	[km/s]	[km/s]	[%]	[°]
$v_{12,12}^{qL}$	4.167	5.560	33.4	41.45	7.252	9.760	34.6	42.01
$v_{13,13}^{qL}$	4.125	5.611	36.0	42.68	7.252	9.760	34.6	42.01
$v_{23,23}^{qL}$	1.246	1.412	13.3	28.07	3.001	3.001	0.0	0.00
$v_{12,12}^{qT}$	1.395	1.407	9.2E-1	7.74	2.514	2.622	4.3	16.55
$v_{13,13}^{qT}$	1.091	1.091	2.4E-2	1.26	2.514	2.622	4.3	16.55
$v_{23,23}^{qT}$	0.703	0.778	10.7	25.45	1.502	1.502	0.0	0.00
$v_{12,3}^{T}$	0.787	1.048	33.2	41.34	1.825	1.919	5.1	17.92
$v_{13,2}^{T}$	0.935	1.267	35.5	42.46	1.825	1.919	5.1	17.92
$v_{23,1}^{T}$	1.191	1.210	1.6	10.22	2.100	2.100	0.0	0.00

between phase and group velocities Δv are computed via Eq. (H.15) (see Tables H.3 and H.4, columns four and eight) and the angle Δ_v between the directions of these two velocities in the non-principle material directions is computed via Eq. (H.14) (see Tables H.3 and H.4, columns five and nine).

The difference between phase and group velocity in certain directions strongly depends on the difference between stiffness components of anisotropic materials. A high difference in the absolute value of the two velocities is always accompanied by a large angle of deviation between the two velocity vectors, i.e. a large energy beam deviation from the wave normal (see Tables H.3 and H.4, columns four and five, eight and nine). This is also an indication for highly anisotropic material behavior. Human femoral bone has the lowest deviation angles Δ_v ($\Delta_{v,max} = 12°$; see Table H.3, column five). Among the two wood spieces investigated, spruce is slighlty more anisotropic ($\Delta_{v,max} = 43°$; see Table H.4, column five). Still, beam deviations in wood are very strong and are between 10° and 45° for most velocities in the non-principle material direction investigated (see Tables H.3 and H.4, columns nine and five, respectively). The carbon-epoxy fiber composite is characterized by a strong (energy) beam deviation in longitudinal directions ($\Delta_{v,max} = 42°$), but due to its isotropic nature in the transversal plane, beam deviation is zero in this plane (see Table H.4, column nine).

For certain ultrasonic measurement setups the difference of group and phase velocity is not relavant for (phase) velocity measurements (e.g. for the contact pulse transmission technique and others, see Section 2.8. It is nevertheless important to be aware of this deviation in order to allow for a correct physical interpretation of measurement results (e.g. strong beam deviations can yield to unintended reflections at specimen surfaces).

Bibliography

Akao, M., Aoki, H., and Kato, K. (1981). Mechanical properties of sintered hydroxyapatite for prosthetic applications. *Journal of Materials Science*, 16:809 – 812.

ANSI/IEEE-Std-176 (1987). IEEE Standard on Piezoelectricity. American National Standard.

Arenberg, D. (1948). Ultrasonic solid delay lines. *Journal of the Acoustical Society of America*, 20(1):1 – 26.

Ashman, R., Corin, J., and Turner, C. (1987). Elastic properties of cancellous bone: measurement by an ultrasonic technique. *Journal of Biomechanics*, 20(10):979 – 986.

Ashman, R., Cowin, S., Van Buskirk, W., and Rice, J. (1984). A continuous wave technique for the measurement of the elastic properties of cortical bone. *Journal of Biomechanics*, 17(5):349 – 361.

Ashman, R. and Rho, J. (1988). Elastic modulus of trabecular bone material. *Journal of Biomechanics*, 21(3):177 – 181.

Auld, B. (1990). *Acoustic Fields and Waves in Solids*, volume I. John Wiley & Sons, Toronto, Canada, 2nd edition.

Authier, A. and Zarembowitch, A. (2006). *International Tables for Crystallography*, volume D, chapter 1.3.4.6. Experimental determination of elastic constants, pages 88 – 89. International Union of Crystallography.

Ayrault, C. and Griffiths, S. (2006). Separation of viscothermal losses and scattering in ultrasonic characterization of porous media. *Ultrasonics*, 45:40 – 49.

Barenblatt, G. (1996). *Scaling, self-similarity, and intermediate asymptotics*. Cambridge University Press, Cambridge, England, 1 edition.

Barthélémy, J.-F. and Dormieux, L. (2003). Determination of the macroscopic strength criterion of a porous medium by nonlinear homogenization. *Comptes Rendus Mecanique*, 331:271 – 276.

Barthélémy, J.-F. and Dormieux, L. (2004). A micromechanical approach to the strength criterion of Drucker-Prager materials reinforced by rigid inclusions. *International Journal for Numerical and Analytical Methods in Geomechanics*, 28(7-8):565 – 582.

Baughman, R., Shacklette, J., Zakhidov, A., and Stafström, S. (1998). Negative Poisson's ratios as a common feature of cubic metals. *Nature*, 392:362 – 365.

Benck, R. and Filbey, G. (1976). Elastic constants of aluminum alloys 2024-T3510, 5083-H131, and 7039-T64 as measured by a sonic technique. Memorandum report no. 2649, USA Ballistic Research Laboratories.

Benveniste, Y. (1987). A new approach to the application of Mori-Tanaka's theory in composite materials. *Mechanics of Materials*, 6:147 – 157.

Berryman, J. (1980). Long-wavelength propagation in composite elastic media I. Spherical inclusions. *Journal of the Acoustical Society of America*, 68(6):1809 – 1819.

Besdo, D., Besdo, S., Behrens, B.-A., and Bouguecha, A. (2007). Problems with ultrasonic measurements of shear modulus of structred media. *Acta Biomaterialia*, 3:723 – 733.

Boccaccini, A., Blazer, J., Maquet, V., Day, R., and Jérôme, R. (2005). Preparation and characterisation of poly(lactide-co-glycolide) (PLGA) and PLGA/Bioglass® composite tubular foam scaffolds for tissue engineering applications. *Materials Science and Engineering C*, 25:23 – 31.

Bodig, J. and Jayne, B. (1993). *Mechanics of wood and wood composites.* Krieger, Malabar, Florida, USA.

Böhm, H. (2004). A short introduction to continuum micromechanics. In Böhm, H., editor, *Mechanics of Microstructured Material*, pages 1 – 40. Springer, Wien – New York. CISM Lecture Notes No. 464.

Bose, S. and Mal, A. (1973). Longitudinal shear waves in a fiber-reinforced composite. *International Journal of Solids and Structures*, 9:1075 – 1085.

Bose, S. and Mal, A. (1974). Elastic waves in a fiber-reinforced composite. *Journal of Mechanics and Physics of Solids*, 22:217 – 229.

Boucher, S. (1976). Modules effectifs de matériaux composites quasi homogènes et quasi isotropes, constitués d'une matrice élastique et d'inclusions élastiques. II. Cas des concentrations finies en inclusions. *Revue M*, 22(1):31 – 36.

Boulanger, P. and Hayes, M. (1998). Poissons ratio for orthorhombic materials. *Journal of Elasticity*, 50:87 – 89.

Briggs, A. (1992). *Acoustic Microscopy.* Clarendon Press, Oxford University Press, Oxford, England.

Buckingham, E. (1914). On physically similar systems. Illustrations of the use of dimensional analysis. *Physical Review*, 4(4):345 – 376.

Bucur, V. and Archer, R. (1984). Elastic constants for wood by an ultrasonic method. *Wood Science and Technology*, 18:255 – 265.

Cancedda, R., Cedola, A., Giuliani, A., Komlev, V., Lagomarsino, S., Mastrogiacomo, M., Peyrin, F., and Rustichelli, F. (2007). Bulk and interface investigations of scaffolds and tissue-engineered bones by X-ray microtomography and X-ray microdiffraction. *Biomaterials*, 28:2505 – 2524.

Carcione, J. (2001). *Wave Fields in Real Media: Wave Propagation in Anisotropic, Anelastic and Porous Media*, volume 31 of *Handbook of Geophysical Exploration – Seismic Exploration*. Pergamon, Elsevier Science Ltd., Oxford, United Kingdom, 1st edition.

Carrington, H. (1923). The elastic properties of spruce. *Philosophical Magazine*, 45:1055 – 1057.

Castagende, B., Kim, K., W., S., and Thompson, M. (1991). Determination of the elastic constants of anisotropic materials using laser-generated ultrasonic signals. *Journal of Applied Physics*, 70:150 – 157.

Charrière, E., Terrazzoni, S., Pittet, C., Mordasini, P., Dutoit, M., Lemaître, J., and Zysset, P. (2001). Mechanical characterization of brushite and hydroxyapatite cements. *Biomaterials*, 22:2937 – 2945.

Chen, Q., Thompson, I., and Boccaccini, A. (2006). 45s5 Bioglass-derived glass-ceramic scaffolds for bone tissue engineering. *Biomaterials*, 27:2414 – 2425.

Chree, C. (1889). The equations of an isotropic elastic solid in polar and cylindrical coordinates, their solutions and applications. 14:250 – 369.

Christensen, R. and Lo, K. (1979). Solutions for effective shear properties in three phase sphere and cylinder models. *Journal of Mechanics and Physics of Solids*, 27:315 – 330.

Christoffel, E. (1877a). Über die Fortpflanzung von Stößen durch elastische feste Körper. *Annali di Mathematica Pura ed Applicata*, 8(II):193 – 243. in German.

Christoffel, E. (1877b). Untersuchungen über die mit dem Fortbestehen linearer partieller Differentialgleichungen verträglichen Unstetigkeiten. *Annali di Mathematica Pura ed Applicata*, 8(II):81 – 112. in German.

Chung, D. and Buessem, W. (1968). The elastic anisotropy of crystals. In *Anisotropy in single-crystal refractory compounds*, volume 2, pages 217 – 245, Dayton, Ohio, USA. Plenum Press, New York.

Coussy, O. (2004). *Poromechanics*. Wiley, Chichester, NJ.

Cowin, S. (2003). A recasting of anisotropic poroelasticity in matrices of tensor components. *Transport in Porous Media*, 50:35 – 56.

Cowin, S. and Mehrabadi, M. (1992). The structure of the linear anisotropic elastic symmetries. *Journal of Mechanics and Physics of Solids*, 40(7):1459 – 1471.

Crank, J. (1975). *The mathematics of diffusion*. Oxford Science Publications, New York, USA, 2 edition.

Dahl, K. and Malo, K. (2008). Planar strain measurements on wood specimens. *Experimental Mechanics*, pages DOI: 10.1007/s11340–008–9162–0.

Datta, S. (1977). Self-consistent approach to multiple scattering by elastic ellipsoidal inclusions. *American Society of Mechanical Engineers*, 77:657 – 662.

Datta, S. and Ledbetter, H. (1983). Elastic constants of fiber-reinforced boron-aluminum: Observation and theory. *International Journal of Solids and Structures*, 19(10):885 – 894.

Dean, G. and Turner, P. (1973). The elastic properties of carbon fibers and their composites. *Composites*, 4(4):174 – 180.

Degtyar, A. and Rokhlin, S. (1997). Comparison of elastic constant determination in anisotropic materials from ultrasonic group and phase velocity data. *Journal of the Acoustical Society of America*, 102(6):3458 – 3466.

Dewey, B., Adler, L., King, R., and Cook, K. (1977). Measurements of anisotropic elastic constants of type 308 stainless-steel electroslag welds. *Experimental Mechanics*, 17(11):420 – 426.

Dormieux, L. (2005). Poroelasticity and strength of fully or partially saturated porous materials. In Dormieux, L. and Ulm, F.-J., editors, *CISM Vol. 480 — Applied Micromechanics of Porous Media*, pages 109 – 152. Springer, Wien.

Dormieux, L., Kondo, D., and Ulm, F.-J. (2006). *Microporomechanics.* Wiley.

Dormieux, L. and Lemarchand, E. (2001). Homogenization approach of advection and diffusion in cracked porous material. *Journal of Engineering Mechanics (ASCE)*, 127(8):1267 – 1275.

Dormieux, L., Molinari, A., and Kondo, D. (2002). Micromechanical approach to the behavior of poroelastic materials. *Journal of the Mechanics and Physics of Solids*, 50:2203 – 2231.

Dorozhkin, S. and Epple, M. (2002). Biological and medical significance of calcium phosphates. *Angewandte Chemie International Edition*, 41:3130 – 3146.

Doyle, D.V. abd Drow, J. and McBurney, R. (1946). The elastic properties of wood. *US Department of Agriculture, Forest Products Laboratory*, Mimeo 1528:Supplement A and B.

Drago, A. and Pindera, M. (2007). Micro-macromechanical analysis of heterogeneous materials: Macroscopically homogeneous vs periodic microstructures. *Composites Science and Technology*, 67:1243 – 1263.

Drugan, W. and Willis, J. (1996). A micromechanics-based nonlocal constitutive equation and estimates of representative volume element size for elastic composites. *Journal of Mechanics and Physics of Solids*, 44(4):497 – 524.

Eberhardsteiner, J. (2002). *Mechanisches Verhalten von Fichtenholz — Experimentelle Bestimmung der biaxialen Festigkeitseigenschaften.* Springer, Vienna, Austria.

EN-485-1 (2007). Aluminum and aluminum alloys – Sheets, strip and plate – Part 1: Technical conditions for inspection and delivery. German version.

EN-485-2 (2006). Aluminum and aluminum alloys – Sheets, strip and plate – Part 2: Mechanical properties. German version.

Eshelby, J. (1957). The determination of the elastic field of an ellipsoidal inclusion, and related problems. *Proceedings of the Physical Society of London*, A241:376 – 396.

Every, A. (1980). General closed-form expressions for acoustic waves in elastically anisotropic solids. *Physical Review B*, 22(4):1746 – 1760.

Every, A. (1994). Determination of the elastic constants of anisotropic solids. *NDT & E International*, 27(1):3 – 10.

Every, A. and Sachse, W. (1990). Determination of the elastic constants of anisotropic solids from acoustic wave group velocity measurements. *Physical Review B*, 42:8196 – 8205.

Every, A. and Sachse, W. (1992). Sensitivity of inversion algorithms for recovering elastic constants of anisotropic solids from longitudinal wavespeed data. *Ultrasonics*, 30:43 – 48.

Fedorov, F. (1968). *Theory of Elastic Waves in Crystals.* Plenum Press, New York, USA.

Fengel, D. and Wegener, G. (2003). *Wood. Chemistry, Ultrastructure, Reactions.* Verlag Kessel, Remagen.

Firestone, F. and Frederick, J. (1946). Refinements in supersonic reflectoscopy. Polarized sound. *Journal of the Acoustical Society of America*, 18(1):200 – 211.

Foldy, L. (1945). The multiple scattering of waves. *Journal of Theoretical Biology*, 67(3):107 – 119.

Fritsch, A., Dormieux, L., Hellmich, C., and Sanahuja, J. (2007a). Micromechanics of crystal interfaces in polycrystalline solid phases of porous media: fundamentals and application to strength of hydroxyapatite biomaterials. *Journal of Materials Science*, 42(21):8824 – 8837.

Fritsch, A., Dormieux, L., Hellmich, C., and Sanahuja, J. (2007b). Micromechanics of hydroxyapatite-based biomaterials and tissue engineering scaffolds. In Boccaccini, A. and Gough, J., editors, *Tissue engineering using ceramics and polymers*, chapter 25, pages 529 – 565. Woodhead Publishing, Cambridge, U.K.

Fritsch, A., Dormieux, L., Hellmich, C., and Sanahuja, J. (2009). Mechanical behaviour of hydroxyapatite biomaterials: An experimentally validated micromechanical model for elasticity and strength. *Journal of Biomedical Materials Research Part A*, 88A:149 – 161.

Fritsch, A. and Hellmich, C. (2007). 'universal' microstructural patterns in cortical and trabecular, extracellular and extravascular bone materials: Micromechanics-based prediction of anisotropic elasticity. *Journal of Theoretical Biology*, 244(4):597 – 620.

Goens, E. (1933). Elastizitätskonstanten des Aluminiumeinkristalls. *Annalen der Physik*, 17(5):233 – 242. in German.

Grabel, J. and Cost, J. (1972). Ultrasonic velocity measurement of elastic constants of Al-Al3Ni unidirectionally solidified eutectic. *Metallurgical Transactions*, 3(7):1973 – 1978.

Grimm, M. and Williams, J. (1997). Measurements of permeability in human calcaneal trabecular bone. *Journal of Biomechanics*, 30:743 – 745.

Gubernatis, J. and Domany, E. (1984). Effects of microstructure on the speed and attenuation of elastic waves in porous materials. *Wave Motion*, 6:579 – 589.

Hansen, N. and Huang, X. (1998). Microstructure and flow stress of polycrystals and single crystals. *Acta Metallurgica*, 46(5):1827 – 1836.

Hartmann, B. and Jarzynski, J. (1974). Immersion apparatus for ultrasonic measurements in polymeres. *Journal of the Acoustical Society of America*, 56(5):1469 – 1477.

Hashin, Z. (1983). Analysis of composite materials – A survey. *Journal of Applied Mechanics*, 50:481 – 505.

Hashin, Z. and Rosen, B. (1964). The elastic moduli of fibre-reinforced media. *Journal of Applied Mechanics*, 31:223 – 232.

Hashin, Z. and Shtrikman, S. (1962a). On some variational principles in anisotropic and non-homogeneous elasticity. *Journal of Mechanics and Physics of Solids*, 10:335 – 342.

Hashin, Z. and Shtrikman, S. (1962b). A variational approach to the theory of the elastic behavior of polycrystals. *Journal of Mechanics and Physics of Solids*, 10:343 – 352.

Hassel, B., Berard, P., Modén, C., and Berglund, L. (2009). The single cube apparatus for shear testing — Full-field strain data and finite element analysis of wood in transverse shear. *Composites Science and Technology*, 69:877 – 882.

Hayashi, T., Song, W., and Rose, J. (2003). Guided wave dispersion curves for a bar with an arbitrary cross-section, a rod and rail example. *Ultrasonics*, 41:175 – 183.

Hayashi, T., Tamayama, C., and Murase, M. (2006). Wave structure analysis of guided waves in a bar with an arbitrary cross-section. *Ultrasonics*, 44:17 – 24.

Hayes, M. and Musgrave, M. (1979). On energy flux and group velocity. *Wave Motion*, 1(1):75 – 82.

Hearmon, R. (1946). The elastic constants of anisotropic materials. *Reviews of Modern Physics*, 18(3):409 – 440.

Hearmon, R. (1948). The elasticity of wood and plywood. In *Special Report 7*, London, England. Department of Scientific and Industrial Research, Forest Product Research.

Hearmon, R. (1965). The assessment of wood properties by vibrations and high frequency acoustic waves. In *Proceedings of the 2nd symposium on nondestructive testing of wood*, pages 49 – 67, Pullman, Washington, USA. Washington State University.

Helbig, K. (1994). *Foundations of Anisotropy for Exploration Seismics*, volume 22 of *Handbook of Geophysical Exploration*. Pergamon Press, Oxford, England, 1st edition.

Hellmich, C. (2005). Microelasticity of bone. In *Applied Micromechanics of Porous Materials*, pages 289 – 331, Udine, Italy. CISM, SpringerWienNewYork.

Hellmich, C., Barthelemy, J., and Dormieux, L. (2004). Mineral-collagen interactions in elasticity of bone ultrastructure – a continuum micromechanics approach. *European Journal of Mechanics A/Solids*, 23:783 – 810.

Hellmich, C. and Ulm, F.-J. (2005a). Drained and undrained poroelastic properties of healthy and pathological bone: a poro-micromechanical investigation. *Transport in Porous Media*, 58:243 – 268.

Hellmich, C. and Ulm, F.-J. (2005b). Micro-porodynamics of bones: prediction of the 'Frenkel-Biot' slow compressional wave. *Journal of Engineering Mechanics (ASCE)*, 131(9):918 – 927.

Helnwein, P. (2001). Some remarks on the compressed matrix representation of symmetric second-order and fourth-order tensors. *Computer Methods in Applied Mechanics and Engineering*, 190:2753 – 2770.

Hench, L. and Jones, J., editors (2005). *Biomaterials, artificial organs and tissue engineering.* Woodhead Publishing, Cambridge, U.K.

Hiki, Y. (1981). Higher order elastic constants of solids. *Annual Review of Materials Science*, 11:51 – 73.

Hill, R. (1963). Elastic properties of reinforced solids: some theoretical principles. *Journal of the Mechanics and Physics of Solids*, 11:357 – 362.

Hirose, A. (2009). Waves, fields, and optics. University of Saskatchewan, Lecture Notes EP225.3.

Hlavacek, M. (1975). A continuum theory for fibre-reinforced composites. *International Journal of Solids and Structures*, 11:199 – 211.

Ho, P. and Ruoff, A. (1969). Pressure dependence of the elastic constants for Aluminum from 77 to 300 K. *Journal of Applied Physics*, 40(8):3151 – 3156.

Hofstetter, K., Hellmich, C., and Eberhardsteiner, J. (2005). Development and experimental validation of a continuum micromechanics model for the elasticity of wood. *European Journal of Mechanics A/Solids*, 24:1030 – 1053.

Holt, A. and Ford, J. (1967). Theory of ultrasonic pulse measurements of third-order elastic constants for cubic crystals. *Journal of Applied Physics*, 38(1):42 – 50.

Hörig, H. (1935). Anwendung der Elastizitätstheorie anisotroper Körper auf Messungen an Holz. *Ingenieur-Archiv*, 6:8 – 14. in German.

Hosoda, H., Kinoshita, Y., Fukui, Y., Inamura, T., Wakashima, K., Kim, H., and Miyazaki, S. (2006). Effects of short time heat treatment on superelastic properties of a TiNbAl biomedical shape memory alloy. *Materials Science and Engineering A*, 438-440:870 – 874.

Hueter, T. (1950). Ultrasonic velocity dispersion in solid rods. *Journal of the Acoustical Society of America*, 22:514 – 515.

Huntington, H. (1947). Ultrasonic measurements on single crystals. *Physical Review*, 72(4):321 – 331.

Huntington, H. (1950). On ultrasonic scattering by polycrystals. *Journal of the Acoustical Society of America*, 22(3):362 – 364.

Itskov, M. and Aksel, N. (2002). Elastic constants and their admissible values for incompressible and slightly compressible anisotropic materials. *Acta Mechanica*, 157:81 – 96.

Ivey, D., Mrowca, B., and Guth, E. (1949). *Journal of Applied Physics*, 20:486 – 492.

Jenkin, C. (1920). Report on materials used in the construction of aircraft and aircraft engines. Technical report, H.M. Stationery Office, London.

Jeong, H. and Hsu, D. (1996). Quantitative estimation of material properties of porous ceramics by means of composite micromechanics and ultrasonic velocity. *NDT & E International*, 29(2):95 – 101.

Jernkvist, L. and Thuvander, F. (2001). Experimental determination of stiffness variation across growth rings in Picea abies. *Holzforschung*, 55:309 – 317.

Jones, J. (2005). Scaffolds for tissue engineering. In Hench, L. and Jones, J., editors, *Biomaterials, artificial organs and tissue engineering*, pages 201 – 214. Woodhead Publishing, Cambridge, U.K.

Kamioka, H. (1988). Effects of ultrasonic bonding materials on velocity and attenuation of sound in red lauan wood. *Japanese Journal of Applied Physics*, 27(2):188 – 191.

Kamm, G. and Alers, G. (1964). Low-temperature elastic moduli of aluminum. *Journal of Applied Physics*, 35(2):327 – 330.

Kanit, T., Forest, S., Galliet, I., Mounoury, V., and Jeulin, D. (2003). Determination of the size of the representative volume element for random composites: statistical and numerical approach. *International Journal of Solids and Structures*, 40:3647 – 3679.

Karki, B., Stixrude, L., and Wentzcovitch, R. (2001). High-pressure elastic properties of major materials of earth's mantle from first principles. *Reviews of Geophysics*, 39(4):507 – 534.

Kazemi-Najafi, S., Bucur, V., and Ebrahimi, G. (2005). Elastic constants of particleboard with ultrasonic technique. *Materials Letters*, 59:2039 – 2042.

Kim, K. (1994). Analytic relations between the elastic constants and the group velocity in an arbitrary direction of symmetry planes of media with orthorhombic or higher symmetry. *Physical Review B*, B49(6):3713 – 3724.

Kim, K., Wu, T., and Sachse, W. (1997). Group velocity formulas for the symmetry planes of a stressed anisotropic elastic solid. *Journal of the Acoustical Society of America*, 102(6):3333 – 2301.

Kino, G. (1987). *Acoustic Waves: Devices, Imaging, and analog processing*. Englewood Cliffs, New Jersey, USA.

Kinra, V. (1985). Dispersive wave propagation in random particulate composites. *ASTM Special Technical Publication*, pages 309 – 325.

Kinra, V. and Anand, A. (1982). Wave propagation in a random particulate composite at long and short wavelengths. *International Journal of Solids and Structures*, 18(5):367 – 380.

Kinra, V., Petraitis, M., and Datta, S. (1982). Ultrasonic wave propagation in a random particulate composite. *International Journal of Solids and Structures*, 16:301 – 312.

Kobayashi, K., Sakai, J., and Sakamoto, M. (2001). Strength criterion for bovine tibial trabecular bone under multiaxial stress. *Theoretical and Applied Mechanics*, 50:91 – 96.

Kohlhauser, C. and Hellmich, C. (2009a). Determination of Poisson's ratios in isotropic, transversely isotropic, and orthotropic materials by means of combined ultrasonic-mechanical testing of normal stiffnesses: Application to metals and wood. *European Journal of Mechanics A/Solids*, submitted for publication.

Kohlhauser, C. and Hellmich, C. (2009b). Ultrasonic contact pulse transmission for elastic wave velocity and stiffness determination: Influence of specimen geometry and porosity. *Ultrasonics*, submitted for publication.

Kohlhauser, C., Hellmich, C., Vitale-Brovarone, C., Boccaccini, A., Rota, A., and Eberhardsteiner, J. (2008). Ultrasonic characterisation of porous biomaterials across different frequencies. *Strain*, 45(1):34 – 44.

Kollmann, F. (1982). *Technologie des Holzes und der Holzwerkstoffe*, volume 1. Springer Verlag, Berlin, Heidelberg, New York, 2nd edition.

Kollmann, F. and Côté (1968). *Principles of wood science and technology*, volume 1. Springer, Berlin, Germany.

Kolsky, H. (1953). *Stress Waves in Solids*. Oxford University Press, London, United Kingdom.

Kolsky, H. (1964). Stress waves in solids. *Journal of Sound and Vibration*, 1:88 – 110.

Koponen, T., Karppinen, T., Haggstrom, E., Saranpaa, P., and Serimaa, R. (2005). The stiffness modulus in norway spruce as a function of year ring. *Holzforschung*, 59(4):451 – 455.

Krautkrämer, J. and Krautkrämer, H. (1986). *Werkstoffprüfung mit Ultraschall*. Springer Verlag, Berlin, Germany, 5th edition. in German.

Kreher, W. (1990). Residual stresses and stored elastic energy of composites and polycrystals. *Journal of the Mechanics and Physics of Solids*, 38(1):115 – 128.

Kriz, R. and Stinchcomb, W. (1979). Elastic moduli of transversly isotropic graphite fibers and their composites. *Experimental Mechanics*, 19(2):41 – 49.

Lakes, R. (1987). Foam structures with negative Poisson's ratio. *Science*, 235:1038 – 1040.

Langer, R. and Vacanti, J. (1993). Tissue engineering. *Science*, 260:920 – 926.

Lax, M. (1952). Multiple scattering of waves. II. The effective field in dense systems. *Physical Review*, 85(4):621 – 629.

Lazarus, D. (1949). The variation of the adiabatic elastic constants of KCl, NaCl, CuZn, Cu, and Al with pressure to 10,000 bars. *Physical Review*, 76(4):545 – 553.

Ledbetter, H. (1980). Sound velocities and elastic-constant averaging for polycrystalline copper. *Journal of Physics D: Applied Physics*, 13:1879 – 1884.

Ledbetter, H. and Datta, S. (1986). Effective wave speeds in an SiC-particle-reinforced Al composite. *Journal of the Acoustical Society of America*, 79(2):239 – 248.

Ledbetter, H. and Fortunko, C. (1991). Dynamic Young modulus of a ceramic-aluminum particle-reinforced composite: Measurement and modeling. *IEEE Ultrasonics Symposium*, pages 1065 – 1067.

Ledbetter, H., Frederick, N., and Austin, M. (1980). Elastic-constant variability in stainless-steel 304. *Journal of Applied Physics*, 51(1):305 – 309.

Ledbetter, H. and Kriz, R. (1982). Elastic-wave surface in solids. *Physica Status Solidi B*, 114:475 – 480.

Lee, I. (1958). A non-destructive methode for measuring the elastic anisotropy of wood using an ultrasonic pulse technique. *Journal of the Institute of Wood Science*, 43(1):1 – 15.

Lees, S., Heeley, J., and Cleary, P. (1979). A study of some properties of a sample of bovine cortical bone using ultrasound. *Calcified Tissue International*, 29:107 – 117.

Lei, M., Ledbetter, H., and Xie, Y. (1994). Eastic constants of a material with orthorhombic symmetry: An alternative measurement approach. *Journal of Applied Physics*, 76(5):2738 – 2741.

Leong, K. and Jin, L. (2006). Characteristics of oscillating flow through a channel filled with open-cell metal foam. *International Journal of Heat and Fluid Flow*, 27:144 – 153.

Li, G., Bronk, J., An, K.-N., and Kelly, P. (1987). Permeability of cortical bone of canine tibiae. *Microvascular Research*, 34:302 – 310.

Li, S. (2000). General unit cells for micromechanical analyses of unidirectional composites. *Composites*, A32:815 – 826.

Lichtenegger, H. (1999). *The composite architecture of the wood cell wall*. Doctoral thesis, University of Vienna, Vienna, Austria.

Lighthill, M. (1965). Group velocity. *Journal of the Institute of Mathematics and its Applications*, 1(1 – 28).

Lim, T.-H. and Hong, J. (2000). Poroelastic properties of bovine vertebral trabecular bone. *Journal of Orthopaedic Research*, 18:671 – 677.

Llorca-Isern, N., Luis-Pérez, C., González, P., Laborde, L., and Patiño, D. (2005). Analysis of structure and mechanical properties of AA 5083 aluminum alloy processed by ECAE. *Rev. Adv. Mater. Sci.*, 10:473 – 478.

Love, A. (1906). *A Treatise on the Mathematical Theory of Elasticity*. University Press, 2nd edition.

Lynnworth, L., Rea, W., and Papadakis, E. (1981). Continuous wave transmission techniques for measuring ultrasonic phase and group velocities in dispersive materials and composites. *Journal of the Acoustical Society of America*, 70(6):1699–1703.

Malasoma, A., Fritsch, A., Kohlhauser, C., Brynk, T., Vitale-Brovarone, C., Pakiela, Z., Eberhardsteiner, J., and Hellmich, C. (2008). Micromechanics of bioresorbable porous cel2 glass ceramic scaffolds for bone tissue engineering. *Advances in Applied Ceramics*, 107(5):277–286.

Markham, M. (1957). Measurements of elastic constants by the ultrasonic pulse method. *British Journal of Applied Physics*, 8(S6):56–63.

Markham, M. (1962). Correlation between the elastic constants of polycrystalline aggregates and single crystals. *Materials Research*, 1(2):107–114.

Markham, M. (1970). Measurements of the elastic constants of fibre composites by ultrasonics. *Composites*, 1:145–149.

Mason, W. and McSkimin, H. (1948). Energy losses of sound waves in metals due to scattering and diffusion. *Journal of Applied Physics*, 19:940–946.

Matweb (2007). Automations Creations Inc., Material type: Titanium alloy.

Matweb (2009). Automations Creations Inc., Material type: Aluminum alloy 5083-H112.

McLaughlin, R. (1977). A study of the differential scheme for composite materials. *International Journal of Engineering Science*, 15:237–244.

McNeil, D. and Stuart, A. (2004). Vertically upward two-phase flow with a highly viscous liquid-phase in a nozzle and orifice plate. *International Journal of Heat and Fluid Flow*, 25:58–73.

McSkimin, H. (1956). Propagation of longitudinal waves and shear waves in cylindrical rods at high frequencies. *Journal of the Acoustical Society of America*, 28(3):484–494.

Miyauchi, K. and Murata, K. (2007). Strain-softening behavior of wood under tension perpendicular to the grain. *Journal of Wood Science*, 53:463–469.

Mizuno, S., Watanabe, S., and Takagi, T. (2004). Hydrostatic fluid pressure promotes cellularity and proliferation of human dermal fibroblasts in a three-dimensional collagen gel/sponge. *Biochemical Engineering Journal*, 20:203–208.

Modén, C. and Berglund, L. (2008). Elastic deformation mechanisms of softwoods in radial tension — Cell wall bending or stretching? *Holzforschung*, 62:562–568.

Molinari, A. and El Mouden, M. (1996). The problem of elastic inclusions at finite concentration. *International Journal of Solids and Structures*, 33:3131–3150.

Morgan, E., Lee, J., and Keaveny, T. (2005). Sensitivity of multiple damage parameters to compressive overload in cortical bone. *Journal of Biomedical Engineering*, 127:557–562.

Mori, T. and Tanaka, K. (1973). Average stress in matrix and average elastic energy of materials with misfitting inclusions. *Acta Metallurgica*, 21(5):571–574.

Morse, R. (1948). Dispersion of compressional waves in isotropic rods of rectangular cross section. *Journal of the Acoustical Society of America*, 20(6):833–838.

Morse, R. (1950). The velocity of compressional waves in rods of rectangular cross section. *Journal of the Acoustical Society of America*, 22(2):219 – 223.

Mouchtachi, A., El Guerjouma, R., Baboux, J., Santini, P., Merle, P., and Bouami, D. (2004). Ultrasonic study of elastic anisotropy of material composite. *Applied Composite Materials*, 11:341 – 351.

Müller, J. (1979). Some second thoughts on error statements. *Nuclear Instruments and Methods*, 163:241 – 251.

Müllner, H., Fritsch, A., Kohlhauser, C., Reihsner, R., Hellmich, C., Godlinski, D., Rota, A., Slesinski, R., and Eberhardsteiner, J. (2007). Acoustical and poromechanical characterization of titanium scaffolds for biomedical applications. *Strain*, 44(2):153 – 163.

Murakami, H., Maewal, A., and Hegemier, G. (1979a). Mixture theory for longitudinal wave propagation in unidirectional composites with cylindrical fibers of arbitrary cross section — I. Formulation. *International Journal of Solids and Structures*, 15:325 – 334.

Murakami, H., Maewal, A., and Hegemier, G. (1979b). Mixture theory for longitudinal wave propagation in unidirectional composites with cylindrical fibers of arbitrary cross section — II. Computational procedure. *International Journal of Solids and Structures*, 15:335 – 357.

Musgrave, M. (1954). On the propagation of elastic waves in aeolotropic media — i. Gerneral principles. *Proceedings of the Royal Society of London*, A226:339 – 355.

Musgrave, M. (1970). Deviation of ray from wave normal for elastic waves in principal planes of crystal symmetry. *Journal of Mechanics and Physics of Solids*, 18:207 – 211.

Musgrave, M. (1981). On an elastodynamic classification of orthorhombic media. *Proceedings of the Royal Society of London*, A374:401 – 429.

Naimon, E., Ledbetter, H., and Weston, W. (1975). Low-temperature elastic properties of four wrought and annealed aluminium alloys. *Journal of Materials Science*, 10(8):1309 – 1316.

Neuhaus, F. (1981). *Elastic constants of wood depending on wood moisture*. Masters Thesis, Ruhr-Universitt Bochum, Institut fr konstruktiven Ingenieurbau. in German.

Newton, I. (1687). *Philosophiae Naturalis Principia Mathematica*. Royal Society, London, United Kingdom, 1st edition. in Latin.

Nicholson, P. and Strelitzki, R. (1999). On the prediction of Young's modulus in calcaneal cancellous bone by ultrasonic bulk and bar velocity measurements. *Clinical Rheumatology*, 18:10 – 16.

Niemz, P. and Caduff, D. (2008). Untersuchungen zur Bestimmung der Poissonschen Konstanten an Fichtenholz. *Holz als Roh- und Werkstoff*, 66:1 – 4. in German.

Norris, A. (1978). A theory of pulse propagation in anisotropic elastic solids. *Wave Motion*, 9:509 – 532.

Northwood, T. (1947). Velocity of dilatational waves in rods. *Journal of the Acoustical Society of America*, 19:505.

Ochoa, J., Sanders, A., Heck, D., and Hilberry, B. (1991). Stiffening of the femoral head due to intertrabecular fluid and intraosseous pressure. *Journal of Biomechanical Engineering*, 113:259 – 261.

Ouis, D. (2002). On the frequency dependence of the modulus of elasticity of wood. *Wood Science and Technology*, 36:335–346.

Papadakis, E., Patton, T., Tsai, Y., Thompson, D., and Thompson, R. (1991). The elastic moduli of a thick composite as measured by ultrasonic bulk wave pulse velocity. *Journal of the Acoustical Society of America*, 89(6):2753–2757.

Parnell, W. and Abrahams, I. (2008). Homogenization for wave propagation in periodic fibre-reinforced media with complex microstructure. I. Theory. *Journal of Mechanics and Physics of Solids*, 56:2521–2540.

Paschalis, P. (1978). Bestimmung der korrelation zwischen ausgewählten festigkeitseigen-schaften und strukturmerkmalen von holz mit anwendung des resonanz- und ultraschallver-fahrens. *Holztechnologie*, 19:14–17.

Payton, R. (2003). Wave fronts in wood. *Quarterly Journal of Mechanics and Applied Mathematics*, 56(4):527–546.

Pochhammer, L. (1876). Über die Fortpflanzungsgeschwindigkeiten kleiner Schwingungen in einem unbegrenzten isotropen Kreiszylinder. *Zeitschrift für reine und angewandte Mathematik*, 81:325–336.

Rao, M. and Prasanna Lakshmi, K. (2003). Shear-wave propagation in rocks and other lossy media: An experimental study. *Current Science*, 85(8):1221–1225.

Redwood, M. (1959). Velocity and attenuation of a narrow-band, high-frequency compressional pulse in a solid wave guide. *Journal of the Acoustical Society of America*, 31(4):442–448.

Redwood, M. (1963). Ultrasonic waveguides — a physical approach. *Ultrasonics*, 1(2):99–105.

Rokhlin, S. and Wang, W. (1989). Ultrasonic evaluation of in-plane and out-of-plane elastic properties. *Review of Progress in Quantitative Nondestructive Evaluation*, 8B:1489–1496.

Rokhlin, S. and Wang, W. (1992). Double through-transmission bulk wave method for ul-trasonic phase velocity measurement and determination of elastic constants of composite materials. *Journal of the Acoustical Society of America*, 91(6):3303–3312.

Rossi, G. (2007). Measurability. *Measurement*, 40:545–562.

Rovati, M. (2003). On the negative Poisson's ratio of an orthorhombic alloy. *Scripta Materialia*, 48:235–240.

Ruffino, E. and Delsanto, P. (2000). Scattering of ultrasonic waves by void inclusions. *Journal of the Acoustical Society of America*, 108(4):1941–1945.

Rydberg, K. (2001). Energy efficient water hydraulic systems. In *Proceedings of the Fifth International Conference on Fluid Power Transmission and Control*, pages 440–446, Zhejiang, China.

Sabina, F. and Willis, J. (1988). A simple self-consistent analysis of wave propagation in particulate composite. *Wave Motion*, 10:127–142.

Sahay, S., Kline, R., and Mignogna, R. (1992). Phase and group velocity considerations for dynamic modulus measurement in anisotropic media. *Ultrasonics*, 30:373–383.

Salençon, J. (2001). *Handbook of Continuum Mechanics*. Springer, Berlin Heidelberg, Germany.

Schmunk, R. and Smith, C. (1959). Pressure derivatives of the elastic constants of aluminum and magnesium. *Journal of Physics and Chemistry of Solids*, 9:100–112.

Shercliff, J. (1970). A note on the envelope construction for group velocity in dispersive, anisotropic wave systems. *Journal of the Institute of Mathematics and its Applications*, 6:91–95.

Soule, D. and Nezbeda, C. (1968). Direct basal-plane shear in single-crystal graphite. *Journal of Applied Physics*, 39(11):5122–5139.

Spriggs, R., Mitchell, J., and Vasilos, T. (1986). Mechanical properties of pure, dense aluminum oxide as a function of temperature and grain size. *Science of Sintering*, 18:41–49.

Stamer, J. (1935). Elastizitätsuntersuchungen an Hölzern. *Ingenieur-Archiv*, 6:1–8. in German.

Stanke, F. and Kino, G. (1984). A unified theory for elastic wave propagation in polycrystalline materials. *Journal of the Acoustical Society of America*, 75(3):665–681.

Suquet, P. (1987). Elements of homogenization for inelastic solid mechanics. In Sanchez-Palencia, E. and Zaoui, A., editors, *Homogenization Techniques for Composite Media*, pages 193–278. Springer, Wien – New York. Lecture Notes in Physics No. 272.

Suquet, P. (1997). Effective behavior of nonlinear composites. In Suquet, P., editor, *CISM Courses and Lectures 377 — Continuum Micromechanics*, pages 197–264. Springer, Wien/New York.

Sutton, P. (1953). The variation of the elastic constants of crystalline aluminum with temperature between 63°K and 773°K. *Physical Review*, 91(4):816–821.

Teischinger, A. and Patzelt, M. (2005). Characterisation of material parameters as basis for innovative processing methods and products made of large dimensioned wood aiming at economically sustainable use of austrian timber resources. Report, University of Natural Resources and Applied Life Sciences, Department of Material Sciences and Process Engineering. in German.

Thelen, S., Barthelat, F., and Brinson, L. (2004). Mechanics considerations for microporous titanium as an orthopedic implant material. *Journal of Biomedical Materials Research*, 69A:601–610.

Thomas, J. (1968). Third-order elastic constants of aluminum. *Physical Review*, 175(3):955–962.

Thurston, R. (1978). Elastic waves in rods and clad rods. *Journal of the Acoustical Society of America*, 64(1):1–37.

Ting, T. and Barnett, D. (2005). Negative Poissons ratios in anisotropic linear elastic media. *Journal of Applied Mechanics*, 72:929–931.

Ting, T. and Chen, T. (2005). Poissons ratio for anisotropic elastic materials can have no bounds. *Quarterly Journal of Mechanics and Applied Mathematics*, 58(1):73–82.

Tu, L., Brennan, J., and Sauer, J. (1955). Dispersion of ultrasonic pulse velocity in cylindrical rods. *Journal of the Acoustical Society of America*, 27(3):550–555.

Turner, C. and Cowin, S. (1988). Errors induced by off-axis measurement of the elastic properties of bone. *Journal of Biomechanical Engineering*, 110(3):213–215.

USDA (1999). *Wood handbook — wood as an engineering material.* Forest Products Society.

Varadan, V., Varadan, V., and Pao, Y. (1978). Multiple scattering of elastic waves by cylinders of arbitrary cross section. I. SH waves. *Journal of the Acoustical Society of America*, 63(5):1310 – 1319.

Verma, D., Katti, K., and D., K. (2006). Bioactivity in *in situ* hydroxyapatite-polycaprolactone composites. *Journal of Biomedical Materials Research A*, 78A:772 – 780.

Vitale-Brovarone, C., Verné, E., Robiglio, L., Appendino, P., Bassi, F., Martinasso, G., Muzio, G., and Canuto, R. (2007). Development of glass-ceramic scaffolds for bone tissue engineering: Characterisation, proliferation of human osteoblasts and nodule formation. *Acta Biomaterialia*, 3:199 – 208.

Wagenführ, R. (1989). *Anatomie des Holzes.* VEB Fachbuchverlag, Leipzig, 4th edition.

Walsh, J., Brace, W., and England, A. (1965). Effect of porosity on compressibility of glass. *Journal of the American Ceramic Society*, 48:605 – 608.

Waterman, P. and Truell, R. (1961). Multiple scattering of waves. *Journal of Mathematical Physics*, 2(4):512 – 537.

Wei, P. and Huang, Z. (2004). Dynamic effective properties of the particle-reinforced composites with the viscoelastic interphase. *International Journal of Solids and Structures*, 41:6993 – 7007.

Weinbaum, S., Cowin, S., and Zeng, Y. (1994). A model for the excitation of osteocytes by mechanical loading-induced bone fluid shear stresses. *Journal of Biomechanics*, 27:339 – 360.

Weston, W., Naimon, E., and Ledbetter, H. (1975). Low temperature elastic properties of aluminum 5083-0 and four ferritic nickel steels. In Kaufman, J., editor, *Properties of materials for liquefied natural gas tankage*, volume ASTM STP 579, pages 397 – 420, Boston, MA, USA. American Society for Testing and Materials.

Williams, J. (1992). Ultrasonic wave propagation in cancellous and cortical bone: Prediction of some experimental results by Biot's theory. *Journal of the Acoustical Society of America*, 91(2):1106 – 1112.

Willis, J. (1980). A polarization approach to the scattering of elastic waves — II. Multiple scattering from inclusions. *Journal of Mechanics and Physics of Solids*, 28:307 – 327.

Wolfe, J. (1998). *Imaging Phonons: Acoustic Wave Propagation in Solids.* Cambridge University Press.

Wolfe, J. and Hauser, M. (1995). Acoustic wavefront imaging. *Annalen der Physik (Leipzig)*, 4(2):99 – 126.

Wooh, S. and Daniel, I. (1991). Mechanical characterization of a unidirectional composite by ultrasonic methods. *Journal of the Acoustical Society of America*, 90(6):3248 – 3253.

Yang, R. (2003). A dynamic generalized self-consistent model for wave propagation in particulate composites. *Journal of Applied Mechanics*, 70:575 – 582.

Yang, R. and Mal, A. (1994). Multiple scattering of elastic waves in a fiber-reinforced composite. *Journal of Mechanics and Physics of Solids*, 42(12):1945 – 1968.

Zaoui, A. (1997). Structural morphology and constitutive behavior of microheterogeneous materials. In Suquet, P., editor, *Continuum micromechanics*, pages 291 – 347. Springer, Wien – New York.

Zaoui, A. (2002). Continuum micromechanics: Survey. *Journal of Engineering Mechanics*, 128(8):808 – 816.

Zhang, J., Zhang, Y., Xu, K., and Ji, V. (2008). Young's modulus surface and Poisson's ratio curve for orthorhombic crystals. *Journal of the Chemical Crystallography*, 38:733 – 741.

Zienkiewicz, O. and Taylor, R. (2000). *The Finite Element Method*, volume 1: The Basis. Arnold, London, England, 5th edition.

Zimmermann, R. (1991). Elastic moduli of a solid containing spherical inclusions. *Mechanics of Materials*, 12:17 – 24.

Dipl.-Ing. Christoph Kohlhauser Curriculum Vitæ

CONTACT INFORMATION	**Present address**	**Permanent address**
	Zollergasse 16/16	Laudach 11
	A-1070 Vienna, Austria	A-4817 St.Konrad, Austria
	mobile: +43 650 4475739	home: +43 7615 8163
	e-mail: christoph.kohlhauser@tuwien.ac.at	e-mail: gertlschuster@gmail.com

PERSONAL INFORMATION

Date of Birth: 17. July 1978
Place of Birth: Eberstalzell, Austria

EDUCATION

Vienna University of Technology, Vienna, Austria

Doktor der technischen Wissenschaften (Doctor of Philosophy)   **January 2005 – present**
- Dissertation at the Institute for Mechanics of Materials and Structures
- Advisor: Professor Christian Hellmich; Expected graduation date: July 2009

Diplom Ingenieur (graduate engineer)   **October 1998 – January 2005**
- Civil engineering, emphasis on structural engineering
- First diploma, second diploma, and final degree with distinction

University of Washington, Seattle, USA   **September 2002 – June 2003**
- Academic exchange year at the *Department for Civil and Environmental Engineering*
- Preparation of thesis in November 2003 and spring 2004

Höhere Technische Bundeslehranstalt, Linz, Austria   **September 1992 – July 1997**
- 5 year polytechnic college with emphasis on civil engineering
- Graduation in July 1997 with distinction

Gymnasium (grammar school), Linz-Auhof, Austria   **September 1988 – July 1992**

Elementary school, Gramastetten, Austria   **September 1984 – July 1988**

PROFESSIONAL EXPERIENCE

Vienna University of Technology, Vienna, Austria

Research Assistant   **January 2005 – March 2009**
Research assistant at the Institute for Mechanics of Materials and Structures. Teaching assistant, examination invigilator for the course mechanics of materials (civil engineering).

Johann Greindl (legally certified civil engineer), Linz, Austria

Stress analyst   **July 1997 – September 2001**
(FE-)Analysis and documentation (CAD) of steel structures. Parallel to civilian service and during summer breaks.

Civilian service, Linz, Austria

Paramedic   **October 1997 – September 1998**
Rescue service, first aid support for Arbeiter-Samariter Bund (Worker-Samaritan Union).

Delta – Dr. Shebl & Partner, Linz, Austria

Internship, structural draftsman   **Summer 1995, Summer 1996**

Raiffeisenbank, Linz, Austria

Internship, accounting   **Summer 1994**

Construction company Schütz, Gramastetten, Austria

Internship, carpenter   **Summer 1993**

AWARDS

awards for excellent performance as a student in 2002 and 2003 granted by the Department of Civil Engineering, Vienna University of Technology